Unravelling Contributions to the Dynamics of the Elastic Properties in Volcanic Environments

Towards Volcano Monitoring Using Passive Image Interferometry

A Dissertation

Submitted in Partial Fulfilment

of the Requirements for the Degree of

Doctor of Natural Sciences (Dr. rer. nat.)

to the Department of Earth Sciences

of Freie Universität Berlin

by

Peter Makus

Berlin, June 2024

Primary advisor Dr. Christoph Sens-Schönfelder

Secondary advisor Prof. Dr. Frederik Tilmann

Reviewers/Gutachter

Prof. Dr. Frederik Tilmann (FU Berlin, GFZ Potsdam)

Prof. Dr. Corentin Caudron (Université Libre de Bruxelles)

Date of defense 12th November 2024

Abstract

Volcanic eruptions pose a grave risk to metropolitan areas and the global economy. Improving the accuracy, reliability, and warning time of eruption forecasts opens avenues to make the lives of some 600 million people living at active volcanoes safer. An effective way of achieving these ends is diversifying current monitoring strategies. This thesis employs changes in the seismic wave propagation velocity (dv/v), retrieved from the ubiquitous ambient seismic noise, as a new measure to quantify alterations in the dynamics of the volcanic system.

We explore an easily automatable method to quantify seismic velocity changes from ambient seismic noise, which we implemented into the software suite SeisMIC. SeisMIC offers end-to-end processing of ambient seismic noise in an easy-to-use, well-documented, modular, and adaptable Python software suite. Compared to other ambient seismic noise software solutions, SeisMIC offers improved computational performance and is particularly suited to satisfy the extraordinarily variable processing needs for ambient noise volcano monitoring. We apply this method to two datasets at active volcanoes: The Klyuchevskoy Volcanic Group (KVG), in Kamchatka, Russia, and Mount St. Helens (MSH), in the United States of America.

At the KVG, we analyse data recorded during the KISS project, which consists of one year of seismic data recorded by over 110 stations. On Kamchatka, the constant volcanic tremor causes fluctuations in the wavefield, violating the assumption of source stationarity in our method. We address these fluctuations using a hierarchical clustering algorithm to identify times with stationary noise fields, for which we can create shorter dv/v time series. Coincident with the first inflation at Bezymianny volcano and 11 months before its eruption, we observe a dv/v increase. Furthermore, we find evidence for a higher damage susceptibility of volcanic rock following the M7.2 Zhupanov earthquake and, with the help of a simple empirical model, link changes in rainfall and snow depth to dv/v changes.

The long-standing seismic network at MSH has recorded continuous seismic waveform data for over 25 years. We use this unique dataset to investigate changes in the seismic velocity during, before, and after MSH's 2004-2008 eruption period. Over time, new seismic stations are deployed, while old ones are removed, destroyed, or upgraded. This poses a particular challenge when creating long-term dv/v time series as the normalisations for time series of station combinations recording during different times diverge. We overcome this challenge using an innovative approach that predicts dv/v at new station combinations from data from pre-existing stations and their spatial sensitivity kernels. The average dv/v time series exhibits two marked increases. Together with the first explosions of the 2004-2008 eruption and a GNSS downward movement, we find a sudden velocity increase caused by the pressure drop and unplugging of the volcanic conduit. Between 2017 and 2020, we detect a large-scale velocity increase below the volcanic edifice focused on the location of MSH's plumbing system. From the dv/v increase, a temporal gravity anomaly, and the GNSS observations, we infer a slowing or stopping of MSH's post-eruptive reinflation during this interval.

This thesis paves the way towards automated volcanic eruption forecasting using seismic velocity changes by distributing a software suite well suited to monitor seismic velocity changes in a breadth of environments in real-time and by demonstrating that the seismic velocity can be employed to quantify volcanic dynamics at various active volcanoes, even when technical and environmental conditions are unideal. Future work should focus on implementing seismic velocity change monitoring at volcano observatories and strengthening the physical links between various environmental, tectonic, and volcanic forcings to the seismic velocity.

Kurzfassung

Vulkanausbrüche stellen eine große Bedrohung für Ballungsräume und die Weltwirtschaft dar. Die Verbesserung der Genauigkeit, Zuverlässigkeit und Vorwarnzeit von Eruptionsvorhersagen eröffnet Möglichkeiten, das Leben von etwa 600 Millionen Menschen, die an aktiven Vulkanen leben, sicherer zu machen. Ein wirkungsvoller Weg, diese Ziele zu erreichen, ist die Diversifizierung der derzeitigen Überwachungsstrategien. Diese Arbeit befasst sich mit Veränderungen der seismischen Wellenausbreitungsgeschwindigkeit (dv/v), die aus dem allgegenwärtigen seismischen Umgebungsrauschen abgeleitet werden, als neues Maß zur Quantifizierung von Veränderungen in der Dynamik des vulkanischen Systems.

Eine leicht automatisierbare Methode zur Quantifizierung seismischer Geschwindigkeitsänderungen aus seismischem Hintergrundrauschen wird entwickelt und in das Softwarepaket SeisMIC integriert. SeisMIC bietet eine Komplettverarbeitung von seismischem Hintergrundrauschen in einer benutzerfreundlichen, gut dokumentierten, modularen und anpassungsfähigen Python-Software-Suite. Im Vergleich zu anderen Softwarelösungen zur Prozessierung von seismischem Hintergrundrauschen bietet SeisMIC eine bessere Rechenleistung und ist besonders geeignet, um die außerordentlich variablen Anforderungen bei der Vulkanüberwachung zu erfüllen. Wir wenden diese Methode auf zwei Datensätze an aktiven Vulkanen an: Die Klyuchevskoy Vulkangruppe (KVG), in Kamtschatka, Russland, und Mount St. Helens (MSH), in den Vereinigten Staaten von Amerika.

An der KVG analysieren wir Daten, die im Rahmen des KISS-Projekts aufgezeichnet wurden, das aus einem Jahr seismischer Daten besteht, die von über 110 Stationen aufgezeichnet wurden. Auf Kamtschatka verursacht der konstante vulkanische Tremor Fluktuationen im Wellenfeld, die die Annahme der Quellenstationarität in unserer Methode verletzen. Wir gehen auf diese Fluktuationen mit Hilfe eines hierarchischen Clustering-Algorithmus ein, um Zeiten mit stationären Wellenfeldern

zu identifizieren, für die wir kürzere dv/v-Zeitreihen erstellen können. Zeitgleich mit der ersten Inflation am Vulkan Bezymianny und 11 Monate vor dessen Ausbruch beobachten wir einen dv/v Anstieg. Darüber hinaus finden wir Belege für eine höhere Schadensanfälligkeit von Vulkangestein nach dem M7,2 Zhupanov Erdbeben und stellen mit Hilfe eines einfachen empirischen Modells einen Zusammenhang zwischen Änderungen der Niederschlagsmenge und der Schneetiefe und dv/v Änderungen her.

Das seit langem bestehende seismische Netzwerk am MSH zeichnet seit über 25 Jahren kontinuierliche seismische Wellenformdaten auf. Wir nutzen diesen einzigartigen Datensatz, um die Veränderungen der seismischen Geschwindigkeit während, vor und nach der Eruptionsperiode des MSH zwischen 2004 und 2008 zu untersuchen. Im Laufe der Zeit werden zusätzliche seismische Stationen aufgestellt, während alte Stationen entfernt, beschädigt oder modernisiert werden. Dies stellt eine besondere Herausforderung bei der Erstellung langfristiger und kontinuierlicher dv/v-Zeitreihen dar, da die Normalisierungen für Zeitreihen von Stationskombinationen, die zu unterschiedlichen Zeiten aufgezeichnet haben, divergieren. Wir überwinden diese Herausforderung mit einem innovativen Ansatz, der dv/v an neuen Stationskombinationen aus Daten von bereits bestehenden Stationen und deren räumlichen Wahrscheinlichkeitsdichtekerneln vorhersagt. Die gemittelte dv/v-Zeitreihe weist zwei deutliche Anstiege auf. Zusammen mit den ersten Explosionen der 2004-2008 Eruption und einer GNSS Abwärtsbewegung stellen wir einen abrupten Geschwindigkeitsanstieg fest, der durch den Druckabfall und die Öffnung des vulkanischen Gangsystems verursacht wird. Zwischen 2017 und 2020 stellen wir einen großflächigen Geschwindigkeitsanstieg unterhalb des Vulkangebäudes fest, der sich auf MSH Kammernsystem konzentriert. Der dv/v-Anstieg, eine zeitliche Schwereanomalie und die GNSS-Beobachtungen lassen auf eine Verlangsamung oder ein Anhalten der post-eruptiven Reinflation in diesem Zeitraum schließen.

In dieser Arbeit ebnen wir den Weg für eine automatisierte Prognose von Vulkanausbrüchen anhand von seismischen Geschwindigkeitsänderungen, indem wir eine Software bereitstellen, die geeignet ist, seismische Geschwindigkeitsänderungen in einer Vielzahl von Umgebungen in Echtzeit zu überwachen, und indem wir zeigen, dass die seismische Geschwindigkeit dazu verwendet werden kann, die vulkanische Dynamik an verschiedenen aktiven Vulkanen zu quantifizieren, selbst wenn die technischen und Umweltbedingungen nicht optimal sind. Künftige Arbeiten sollten sich darauf konzentrieren, die Echtzeitüberwachung seismischer Geschwindigkeitsänderungen in Vulkanobservatorien zu implementieren und die physikalischen Verbindungen zwischen verschiedenen umweltbedingten, tektonischen und vulkanischen Einflüssen auf die seismische Geschwindigkeit zu stärken.

Acknowledgements

To me, this is probably the most challenging to write but also the most intimate part of the thesis. As I know that it will likely also be the most-read part, I will try my best to do it justice. This thesis would not have been possible without the help of numerous people, some of whom I would like to name in particular.

First and foremost, I would like to thank my advisor, Christoph Sens-Schönfelder. You have helped me find motivation and inspiration through the trying lockdown times and taught me everything I know about ambient seismic noise. Also, thank you for allowing me to venture into a breadth of directions and explore research far beyond the scope of this thesis. Certainly, there will be further opportunities for collaborations, runs, and climbs soon! On this note, I am also grateful to my second PhD advisor, Frederik Tilmann. Thank you for responding to my "urgent" last-minute emails at inhumane times, providing an external, much more holistic view of our research, and guiding me through the jungle of quantitative analyses that would otherwise have been far too mathematical to grasp.

Thank you, Thomas Walter, for letting me see this project through more volcanological lenses than were at my disposal. My particular thanks go to the seismology section of the GFZ Potsdam - both former and current members, who have been great friends and colleagues - I could not have asked for any better. I would also like to thank the people from the University of Washington (friends and colleagues likewise), who, during my research stay, have made me feel welcome from the first moment. In particular, I would like to acknowledge Marine Denolle for immediately answering my request to stay in Seattle and helping me to finance said stay. Marine, I wish I had half your enthusiasm and energy, and your spirits keep amazing me!

All the field campaigns, workshops and conferences I had the privilege to participate in will always remain in fond memory. I would, therefore, in no particular order, like to thank the people from the SPIN ITN, who adopted me into their family, the

UPFLOW team, the people who partook in the Albanian AdriaArray deployment, the Cargese folks, Jannes Münchmeyer for tackling the Irpinia deployment road trip together, and all the people I met on the many other occasions. Also, outside of this PhD project, but within science, I would like to thank Marthe Faber, Charlotte Bruland, and Eldert Fokker for our fun little side-project on probing environmental parameters using seismological methods. As my scientific journey started long before my time in Potsdam, I would like to extend my thanks to my Master's advisor, Stéphane Rondenay. Your constant enthusiasm has inspired me to pursue a career in science. Finally, I would like to thank the DFG for financing the SAMOVAR project - without pay, this PhD would have felt a lot longer.

While it took a large chunk of it, my life these past three years did, of course, not only consist of research. So, on a more personal note, I would like to thank the many old and new friends who supported me throughout this episode of my life. So here it goes: I thank the 7a+ and Kahleberg team for the many climbing-related and unrelated activities. My old childhood friends, Mandy, Thomas, and Amarin, for keeping in touch with me, although I am quite bad at reaching out. Speaking of reaching out - to those of you still in Norway: Tiffany, Bård, Camena, Ida, Victoria, Erik, and Rachel, for the regular and irregular exchanges and for providing me with refuge whenever I needed it. Thanks to Marcus and Alina, the best Aachen Geosciences group! To those of you (temporarily) in Potsdam: Thank you, Luc, for welcoming me in Potsdam during such dystopic and unwelcoming times and for the little craziness that I so desperately needed. Fiona, for always offering your ear in good as in bad times. To Donovan, for occasionally making me feel like an intellectual. To Jannes and Emma, for always sharing accommodation, laughs, and great times at the other ends of this world. To Stefan, Sergio, Manuel, Marianne, Kim, Violeta, and Laura for times of games and fun! Also, a special mention to the Seattle folks - Audrey, Max, Julia, Matt, Manuela, Dominik, Irene, and Quibin. And

thanks to so many more people with whom I have crossed paths and who have given me warmth.

So, finally, before this acknowledgement section turns out to be longer than the following thesis, I would like to conclude by thanking my family. To my parents - for always encouraging my curiosity to explore the natural world and supporting me in all my decisions, whether you liked them or not. To Madita, Arthur, Amelie, and Erik for showing that there can be so much love in the world.

Contents

List of Figures

List of Tables

Acronyms

dv/v seismic velocity change. ii–v, xii, xiii, xv, xvii, xix–xxiii, xxv, xxxix, xli, xlii, 15–24, 28, 31–33, 36, 42–45, 47, 51, 55, 57, 58, 60–62, 64–70, 72–77, 79, 80, 82, 83, 85, 86, 88, 89, 91, 95–101, 103–115, 117–122, 165, 225, 228–231, 243, 244, 247, 248

API application programming interface. 5, 117

CCC cumulative correlation coefficient. xx–xxiii, 65, 68, 69, 80, 82, 83, 99, 100

CF correlation function. xvi–xviii, xxiii, xxv, xxviii–xxx, xxxviii, 7, 13–15, 26–29, 31, 32, 34, 37, 40–43, 45, 56–64, 81, 94–98, 105, 107, 117, 119, 174–180, 222, 225, 234

CKD Central Kamchatka Depression. xix, xx, 52, 66–69, 71, 77

CWI coda wave interferometry. 16, 91, 107, 109, 114, 120

DEM digital elevation model. 87

ERidge eastern ridge. xix, 66, 67, 77

FDSN International Federation of Digital Seismograph Networks. 25, 36, 48, 57, 86, 115

GNSS global navigation satellite system. iii, v, xxii, xxiii, xli, 10, 89, 93, 95, 99–101, 104, 106, 108, 111, 113, 115, 122, 219, 245

GPU graphic processing unit. 35, 47

HPC high-performance computing. 31

ICA independent component analysis. 60, 61

INSAR Interferometric Synthetic Aperture Radar. xiv, 11, 90, 122

IRIS Incorporated Research Institutions for Seismology. 92

KBGS Kamchatka Branch of the Geophysical Survey of the Russian Academy of Sciences. 55

KVG Klyuchevskoy Volcanic Group. ii, iv, xii, xix–xxi, 5, 7, 50, 52, 54, 64, 66–71, 77–80, 84, 85, 118

MPI message passing interface. 31, 33, 40

MSH Mount St. Helens. ii–v, xxii–xxv, xxxviii, xxxix, xlii, 6–8, 89–93, 95, 98, 100, 101, 103, 105–114, 118, 123, 219, 225, 226, 231, 233, 235, 247

PGV peak ground velocity. xxi, 76–78

PII passive image interferometry. 4, 5, 15, 16, 19, 21, 22, 37, 44, 50, 51, 54, 64, 65, 72, 84, 85, 91, 109, 114, 116–119, 121–123

PNSN Pacific Northwest Seismic Network. 92, 95, 98, 114, 224

RAM random access memory. 31, 34

RSAM Real-time Seismic-Amplitude Measurement. 122

SAGE Seismological Facility for the Advancement of Geoscience. 114

SAR synthetic aperture RADAR. xxii, 80, 83

SHZ St. Helens Seismic Zone. xxiv, 89, 101, 102, 109, 113

TADR time-averaged lava discharge rate. xx, xxi, 68, 69, 82, 86

TSPII time-segmented passive image interferometry. 64, 72, 84

USGS United States Geological Survey. 57, 86, 95, 115

CHAPTER 1

Introduction

1.1 Motivation

Volcanic eruptions are among the most spectacular but also the most hazardous phenomena in the natural world. Volcanic risk is not only limited to the increasing population of more than 600 million living in the vicinity of active volcanoes (Chester et al., 2000) but also has a global component due to far-reaching effects such as tsunamis or ash clouds that can have global impacts for several years after the eruption (Jenkins et al., 2015, see, e.g., photo in Figure 1.1). A powerful reminder of such global risk was the 2010 Eyjafjallajökull eruption in Iceland that, despite its intermediate size, caused significant disruptions in the European air traffic (e.g., Petersen, 2010). Eruption early warning allows for warning, preparation, and evacuation of the local population and infrastructure, thereby mitigating the socioeconomic impact of volcanic events (Wilson et al., 2014).

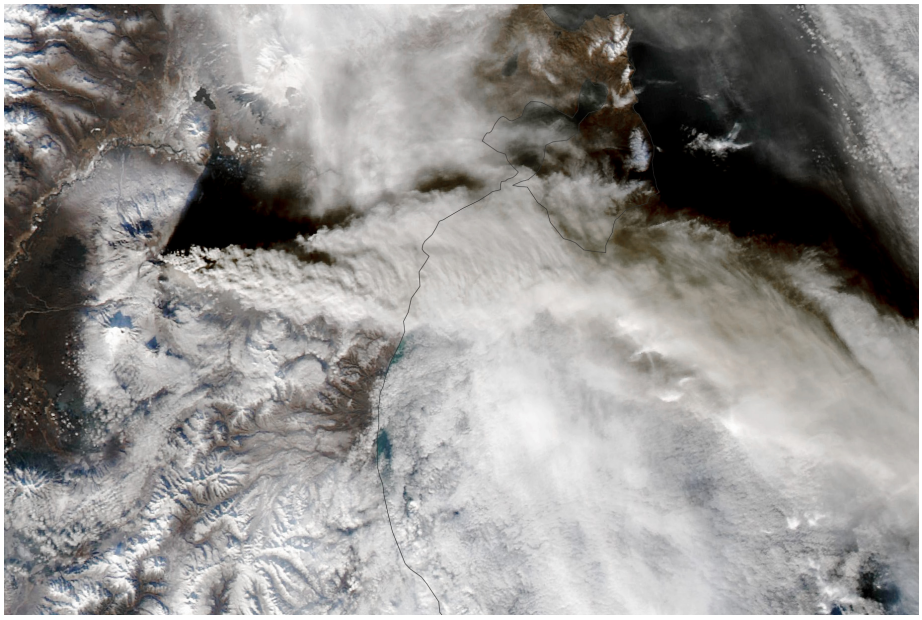

Figure 1.1: Satellite image of Klyuchevskoy volcano in Kamchatka, Russia, in November 2023. An ash cloud reaching hundreds of kilometres over the Pacific Ocean (outlined in black) is visible. Image obtained from the NASA Earth Observatory at https://earthobservatory.nasa.gov/.

The data used to create eruption forecasts and inform early warning is mostly of geophysical and geochemical nature. Consequently, geophysical real-time monitoring of volcanoes is at the heart of volcanic risk mitigation. Using continuous observations, scientists attempt to identify deviations from a baseline behaviour indicating an impending eruption (Tilling, 2008). However, due to drastic individual variations in plumbing systems and eruption mechanisms, volcanic precursors are often not transferable from one volcano to another. Especially at explosive volcanoes, identifying volcanic precursors and, thus, eruption forecasting remains a challenge (Scarpa & Gasparini, 1996). In addition, remote and difficult-to-access terrain often complicates volcano monitoring.

To date, geophysical volcano monitoring exploits a multitude of techniques and

datasets. Ideal monitoring techniques afford a high temporal resolution and sensitivity to the targeted volcanic processes. On the other hand, they should be insensitive to signals overlaying the target signal (i.e., noise). Cost efficiency, low maintenance, and easy installation of the field equipment are desirable qualities, especially in remote areas. Monitoring techniques that at least partially fulfil these requirements are, for example, satellite-born techniques (Mania et al., 2019; Massonnet et al., 1995) or tiltmeters (Fontaine et al., 2014; Peltier et al., 2005) used to detect surface deformation induced by inflation of the volcanic edifice. In many cases, increased seismicity, recorded with the help of seismometers, also precedes eruptions (e.g., Budi-Santoso et al., 2013; Chouet, 1996; Droznin et al., 2015; Soubestre et al., 2021). As described above, the various precursors are differently pronounced from volcano to volcano and may not occur at all. Therefore, scientists strive to explore new volcanic precursors (Brenguier, Shapiro, et al., 2008; Brenguier et al., 2016; Tilling, 2008).

All monitoring techniques will inevitably record signals unrelated to volcanic forcing, although their influence can often be mitigated by taking appropriate precautions. Therefore, it is essential to understand which other environmental mechanisms may introduce additional signals into the geophysical dataset at hand but also quantify their respective contributions. Such quantification requires a deep understanding of the physical relationships governing those environmental contributions. By unravelling the individual contributions, the volcanic component to the composite signal may ultimately be isolated and, subsequently, interpreted.

Traditionally, one can broadly divide seismological tools into two categories: (1) tools that focus on analysing seismic sources and (2) methodologies that allow for structural imaging of the subsurface. While source-focussed seismology accounts for time dependency, subsurface structures are mostly assumed to be temporally invariant on non-geological time scales. Consequently, resolving structures temporally was often neglected - except for 4D active source surveys in exploration seismology (see,

e.g., Jack, 2017). While this might be reasonable for the Earth's deeper and less dynamic parts, its shallower and more active parts can exhibit rapid dynamics on virtually all time scales.

Over the past decades, the increasing availability of digital storage has enabled the scientific community to obtain and archive continuous seismic recordings. Simultaneously, the ever-growing computational power allowed for more complex exploration and analysis of such large data amounts. Consequently, seismologists developed new processing techniques and obtained new derived data products from these continuous recordings. One family of these methods exploits the energy of the ubiquitous ambient seismic noise, a constant background chatter present in all seismic recordings (e.g., Nakata et al., 2019).

This thesis will focus on the analysis of time-varying structures at volcanoes using seismological tools. To this end, I will employ a tool called passive image interferometry (PII), exploiting properties of the ubiquitous ambient seismic field (Sens-Schönfelder & Wegler, 2006). In addition, I will present auxiliary geophysical and environmental observables, set them in context to seismological observations, and, thereby, shed light on the volcanic contribution to the final data product with the ultimate goal to contribute to establish and consolidate PII as a tool to compliment existing volcano monitoring techniques.

1.2 Outline

This thesis consists of six chapters, including this introduction. Three of these chapters present individual studies.

Before diving into the details of those studies, I will briefly review the required background knowledge in Chapter 2. Therein, we will explore signs and phenomena accompanying volcanic crises and outline the status quo of volcano monitoring (Sec-

tion 2.1). Section 2.2 examines the properties and origin of the ambient seismic noise, a background signal present in all seismic recordings. Here, we will also learn about a technique called passive image interferometry (PII). Finally, Section 2.3 discusses the measurement of seismic velocity changes in the solid Earth, what they represent, and the state-of-the-art research employing seismic velocity change time series.

Chapter 3 presents a research software called SeisMIC, which enables end-to-end processing of seismic velocity change time series. Here, we[1] will elaborate on the finer methodological details concerning PII and show how SeisMIC contributes to the ambient noise research community. The software's highlights include fast and efficient processing routines, an intuitive and easy-to-learn application programming interface (API), and the ability to map seismic velocity changes in space. We also include a minimal example supplemented by a software tutorial. This chapter was published as Makus and Sens-Schönfelder (2024) in SEISMICA.

In Chapter 4, we apply the method described in the preceding chapter to one year of seismic waveform data recorded by a large seismometer array at the Klyuchevskoy Volcanic Group (KVG) in Kamchatka, Russia. In this chapter, we demonstrate how to employ PII in the context of the fluctuating noise field impacted by the quasi-ubiquitous volcanic tremors prevailing around the KVG. Exploiting these high-energy tremors, we extract high-resolution velocity change time series dominated by the impacts of regional weather variations. Following a large regional earthquake, we infer very heterogeneous damage reactions across the network, which we attribute to the strongly varying geology at the different sites. Almost one year before an eruption at Bezymianny volcano initiates and coincident with satellite-observed deformation of the volcanic edifice, we find a velocity increase, which we link to a pressure change within the volcano's magma conduits. This chapter was published as Makus, Sens-

[1]The first person plural is used to emphasise that the presented research is the product of the collaboration of several authors rather than attributed to a single person.

Schönfelder, et al. (2023) in the Journal of Geophysical Research - Solid Earth.

Following the application to a temporary deployment of large spatial extent, we present a long-term analysis of the evolution of the seismic velocity at Mount St. Helens (MSH) in Chapter 5. At MSH, continuous seismic data has been recorded for over 25 years, including during its 2004-2008 eruption cycle. Exploiting this dataset, we investigate how long-term changes in the magma supply rate influence the seismic velocity. Coincident with the first explosions in 2004, we find marked velocity decreases, which we interpret as signs of unplugging associated with pressure drops within the volcanic plumbing system. After 2008, vertically positive ground displacement implies a reinflation of magma and gas chambers below the volcanic system. From the velocity change times series, we infer a slowing or potentially even an end to this reinflation after 2017. We conclude that groundwater fluctuations dominate the seasonal cycles of the seismic velocity. Furthermore, we find contrasting responses to environmental forcing on the volcanic edifice compared to its foot, indicating that ground freezing might inhibit groundwater infiltration at higher altitudes. This chapter has been accepted for publication in Seismological Research Letters.

Finally, in Chapter 6, I will draw some conclusions from the work and outline how it complements the current understanding of the dynamics of the seismic velocity at volcanoes. In addition, I will pose open questions and suggest ways in which they could be addressed by future research.

1.3 Prior Published Work and Contribution Statements

This thesis contains chapters based on work published in various scientific journals. The software description of "SeisMIC" in Chapter 3 has been published as:

> Makus, P., & Sens-Schönfelder, C. (2024). SeisMIC - an Open Source Python Toolset to Compute Velocity Changes from Ambient Seismic Noise. *Seismica*, *3*(1). https://doi.org/10.26443/seismica.v3i1.1099

Chapter 4, containing the investigation of medium changes at the Klyuchevskoy Volcanic Group (KVG), has been published as:

> Makus, P., Sens-Schönfelder, C., Illien, L., Walter, T. R., Yates, A., & Tilmann, F. (2023). Deciphering the Whisper of Volcanoes: Monitoring Velocity Changes at Kamchatka's Klyuchevskoy Group With Fluctuating Noise Fields. *Journal of Geophysical Research: Solid Earth*, *128*(4), e2022JB025738. https://doi.org/10.1029/2022JB025738

The analysis of the spatiotemporal evolution of the seismic velocity over 25 years at Mount St. Helens (MSH) in Chapter 5 has been published as:

> Makus, P., Denolle, M. A., Sens-Schönfelder, C., Köpfli, M., & Tilmann, F. (2024). Analyzing Volcanic, Tectonic, and Environmental Influences on the Seismic Velocity from 25 Years of Data at Mount St. Helens. *Seismological Research Letters*, *95*(5), 2674–2688. https://doi.org/10.1785/0220240088

For the listed works, Peter Makus wrote the manuscripts and designed, conducted, and interpreted the data analyses. All accompanying research codes and programmes were written, tested, and are maintained by Peter Makus. Some of the algorithms used in Chapter 3 were developed by Christoph Sens-Schönfelder. He also contributed to the manuscript design. Thomas Walter processed the satellite aperture radar data in Chapter 4. In the same chapter, Luc Illien contributed to the conceptualisation of the models describing the environmental impact on the seismic velocity. Finally, Alexander Yates introduced some of the ideas of the hierarchical clustering of correlation functions (CFs) into the study. Christoph Sens-Schönfelder contributed to the

overall study and manuscript design. For Chapter 5, Christoph Sens-Schönfelder and Marine A. Denolle helped design the final study and manuscript. Manuela Köpfli contributed to the discussion of volcanic and source mechanisms at Mount St. Helens (MSH). For Chapter 4 and 5, Frederik Tilmann contributed to the manuscript designs and proposed ideas towards improving the respective experiments.

CHAPTER 2

Theory

2.1 Monitoring Volcano Dynamics

Volcanic eruptions result from a pressure imbalance following the upward migration of magma from the mantle and the deep crust towards the surface. When rising to shallower depths with lower confining pressures, the magma exsolves gas bubbles, the so-called volatiles, further increasing the overpressure in the magmatic conduit and accelerating the speed of the upwards-migration. Finally, the eruption occurs when the pressure is high enough for the magma to breach the surface. We classify eruptions as effusive or explosive depending on the rate and violence with which material extrudes, which is governed by the magma's chemical composition. Silicic magmas and those with a large fraction of dissolved fluids produce more explosive eruptions than basaltic magmas and magmas with a small fluid fraction (e.g., Cassidy et al., 2018; La Spina et al., 2022; Sparks, 2003; Woods, 1995).

The upward transport of the magma causes deformation that, above the brittle-ductile transition, can induce so-called volcano-tectonic earthquakes. While extrusion leads to deflation, the accumulation of magma in the conduit may inflate the volcanic edifice and the surrounding areas. This inflation is expressed as an extension of the surface, often centripetal to the inflating magma body (see Figure 2.1). The opening of new dykes and sills fractures the surrounding rock and triggers volcano-tectonic earthquakes. Besides volcano-tectonic earthquakes, long-period seismicity or volcanic tremor is commonly observed at active volcanoes. This tremor is assumed to result from resonances within the magmatic plumbing system. Perhaps unsurprisingly, ground deformation monitoring via ground-based global navigation satellite system (GNSS), tiltmeters, or space-born satellite system and seismic monitoring have evolved to be two of the principal techniques used for short-term volcano monitoring (McNutt & Roman, 2015; Segall, 2013; Sparks et al., 2012).

While many monitoring methods investigate induced signals like seismicity or surface deformation, other methods allow for a direct investigation of structural changes in the volcanic plumbing system. For example, repeated gravimetry surveys can detect mass increases below a volcano (Battaglia et al., 2008; Greco et al., 2012). Also, repeated electrical resistivity measurements were used to infer structural changes (e.g., Aizawa et al., 2011; Utada, 2003). Similarly, seismic waves can measure medium changes. For example, Titzschkau et al. (2010) and Caudron et al. (2019) observed modifications in the seismic attenuation that preceded eruptions. Recently, studies that link relative changes in the seismic velocity to volcanic dynamics have become more common (e.g., Brenguier, Shapiro, et al., 2008; Donaldson et al., 2017; Ratdomopurbo & Poupinet, 1995; Rivet et al., 2014; A. S. Yates et al., 2019). This thesis focuses on analysing seismic velocity changes at volcanoes retrieved from ambient seismic noise.

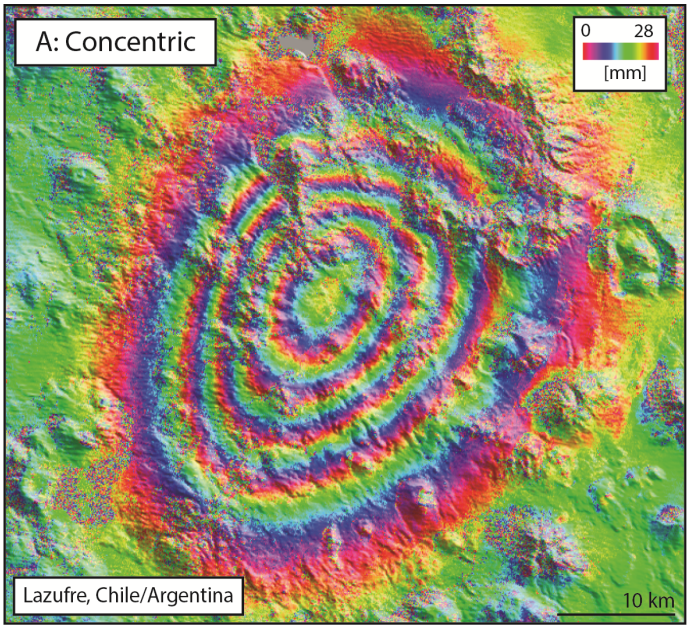

Figure modified from Biggs, J., & Pritchard, M. E. (2017). Global Volcano Monitoring: What Does It Mean When Volcanoes Deform? *Elements*, *13*(1), 17–22. https://doi.org/10.2113/gselements.13.1.17 / Reprinted with permission from the Mineralogical Society of America.

Figure 2.1: Ground deformation around the inflating Lazufre volcano as measured by Interferometric Synthetic Aperture Radar (INSAR). The deformation shows a characteristic concentric pattern around the inflating magma body. Original study by Fournier et al. (2010).

2.2 Ambient Seismic Noise and Passive Image Interferometry

Ambient seismic noise is a ubiquitous background chatter on all seismic recordings caused by a wide range of natural and artificial phenomena. Physically, it can be considered the composite sum of signals with amplitudes too small to make them emerge and stand out from the rest of the recording. As we will see, ambient seismic noise

can be exploited for many practical applications, often very similar to active (i.e., artificial) and natural seismological sources. Hence, nowadays, many seismologists perceive the term "ambient seismic *noise*" as a misnomer.

While, as a whole, the ambient seismic field is a composite signal, it is dominated by different physical mechanisms dependent on frequency, recording location, time of the day, and season. Particularly in urban environments, shorter periods below one second are dominated by cultural noise, whereas longer periods contain the natural secondary and primary microseismic peaks at seven and 14 s, respectively (Ardhuin et al., 2019). These peaks are due to ocean-wave-induced excitation. Consequently, long periods contain more energy at seismic stations[1] close to coastlines (consult, e.g., McNamara & Boaz, 2019, for a detailed review of the physics of ocean noise generation).

Many of the mechanisms constituting the spectrum of the ambient field also have temporal dependencies and periodicities. For example, in the northern hemisphere, the signal of ocean-generated noise is more pronounced in the winter months, November to March. This is due to large winter storms. Similarly, cultural noise, as human activity, has a diurnal pattern. Interestingly, during the CoViD-19 pandemic, a marked difference in the energy content of urban ambient seismic noise was visible as compared to pre-pandemic levels (e.g., Lecocq et al., 2020; Piccinini et al., 2020). In Figure 2.2, I visualise the probability density function of the power spectral density separately for the summer and winter months at station IU.HRV in Massachusetts, USA, demonstrating the discussed properties of the ambient seismic noise spectrum.

Since the ambient seismic "noise" is a deterministic signal, it must be coherent over different sensors. Indeed, the fact that recordings of seismic noise can be correlated over several stations had been demonstrated well before any theories concerning its

[1]For the sake of conciseness, I will from now on refer to these simply as stations, unless the context requires otherwise.

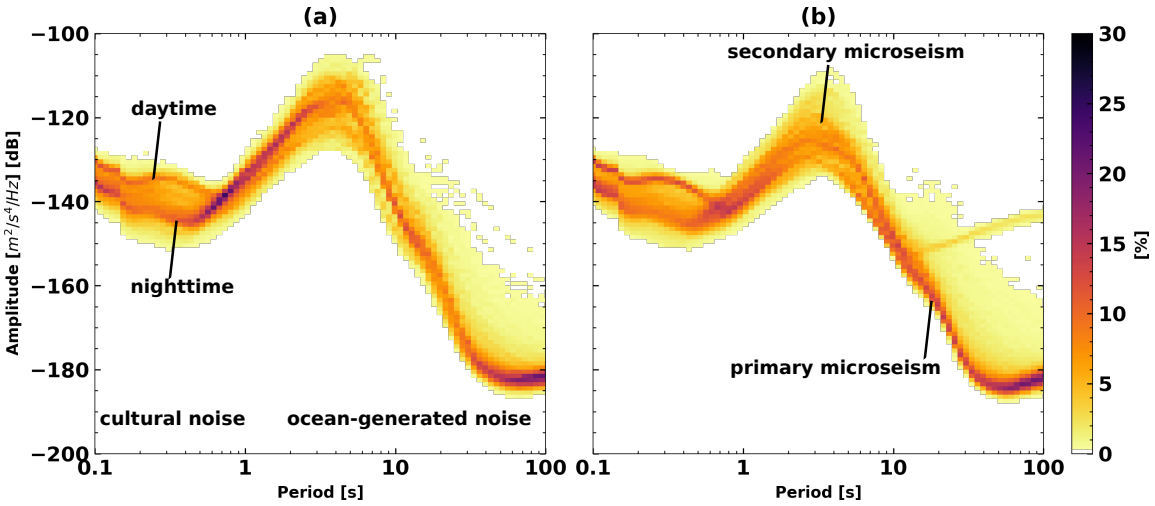

Figure 2.2: The probability function of the power spectral density from data recorded at IU.HRV.BHZ between **(a)** November and February 2017 and **(b)** April and August 2017. In periods<1 s dominated by cultural noise, a clear diurnal division is visible. The ocean-wave-dominated energy content in periods>1 s is higher in the winter (a) than in summer (b).

generation were developed (e.g., Aki, 1957). If ambient noise sources were distributed homogeneously in space and uniform in time, the resulting correlation functions (CFs), computed via a cross-correlation (equation 2.1), would correspond to the Green's function describing the impulse response of the subsurface between the two sensors. This is practically never the case. Nonetheless, as we will discover, with the appropriate preprocessing (Bensen et al., 2007), there are numerous ways to exploit this property. Figure 2.3 illustrates the coherence of the ambient seismic noise across time and space.

Mathematically, we can retrieve the CF using a simple cross-correlation:

$$C_{1|2}(\tau) = (s_1 \star s_2)(\tau) = \int_{-\infty}^{\infty} \overline{s_1(t)} s_2(t+\tau) \mathrm{d}t, \tag{2.1}$$

where $s_1(t)$ and $s_2(t)$ are the waveforms recorded at the two stations. The cross-correlation is a function of the time lag between the two signals τ rather than the

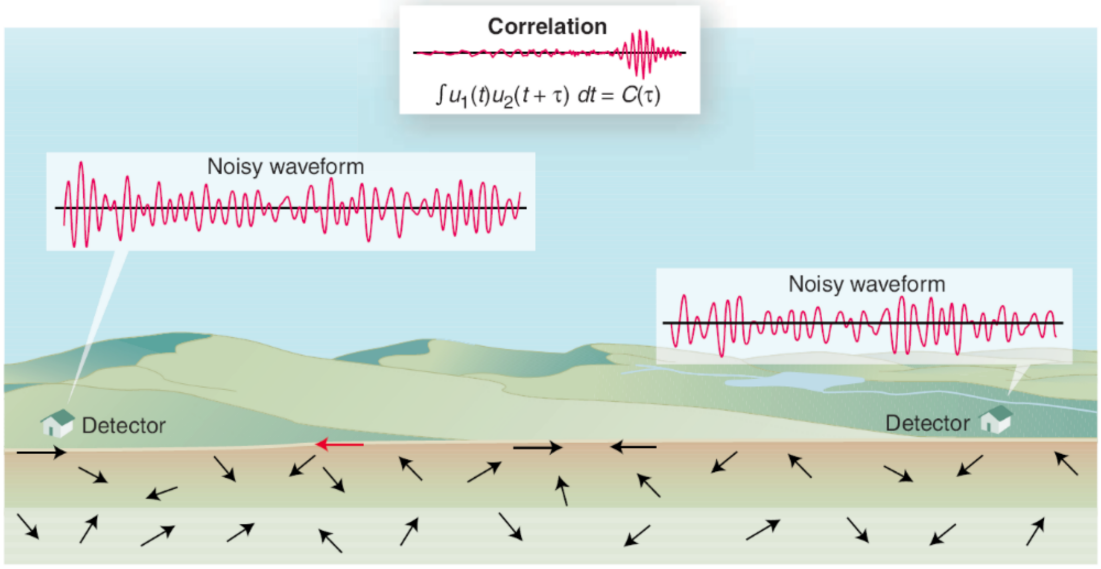

From Weaver, R. L. (2005). Information from Seismic Noise. *Science*, *307*(5715), 1568–1569. https://doi.org/10.1126/science.1109834 / Reprinted with permission from AAAS.

Figure 2.3: Conceptual illustration of the cross-correlation of ambient seismic noise recordings between two stations (each labelled "Detector"). While the two stations by themselves record seemingly random waveforms, their recordings can be correlated to obtain the coherent waveforms travelling from one station to the other.

recording time t. For practical purposes, one usually computes the CFs in the frequency rather than the time domain. In the given example, we would treat station 1, recording s_1, as a virtual source. For all but very late lag times τ, the coherent wavefield between the virtual source and the receiver is dominated by the so-called surface waves (Obermann, Planès, Larose, Sens-Schönfelder, & Campillo, 2013), a family of waves that occur at seismic interfaces with high impedance contrasts (e.g., Shearer, 2019).

Seismologists exploit the similarity between the CF and the medium's Green's

function to extract information about the medium that the noise's energy passes on the way from the virtual source to the receiver. These noise-based interferometric methodologies are especially useful in seismically quiet regions where seismic events occur infrequently. Ambient noise tomography (see, e.g., Nicolson et al., 2012) is an example of this, where seismologists use methods similar to those employed in earthquake surface wave tomographies to invert for the seismic velocity structure between the virtual source(s) and receiver(s). They usually obtain data from large station arrays, allowing for numerous source-receiver combinations. The theoretical foundation of seismic interferometry is also valid for auto-correlations, for which the virtual source and receiver are identical. In such cases, the coherent wavefield is equivalent to the energy portion scattered back to the virtual source's position.

As the ambient field is ubiquitous through time and space, one can repeatedly retrieve CFs (or empirical Green's functions) of the medium and, thereby, quantify potential velocity changes that a region might undergo. In a study using data recorded at Merapi Volcano, Sens-Schönfelder and Wegler (2006) proposed a method called passive image interferometry (PII) to retrieve a seismic velocity change (dv/v) time series from ambient seismic noise. Chapter 3 provides a quantitative description of PII's algorithm. In the following section, I will discuss the state of the art of research employing dv/v time series.

2.3 The Impact of External Forcing on the Seismic Velocity

The fact that the seismic velocity varies over time raises a simple question whose answer is surprisingly complex: "Why?". In other words: "Which physical processes impact the seismic velocities, and what are the material properties they influence?" To answer this question, let us go back to the basics and examine the propagation

velocity of shear or S-waves (e.g., Shearer, 2019):

$$v_S = \sqrt{\frac{\mu}{\rho}}, \tag{2.2}$$

where ρ is the mass density of the propagation material and μ is the shear modulus describing the material's resistance to shearing. As v_S primarily governs the surface wave phase velocity (or dispersion), all phenomena causing a measurable velocity change must impact either μ or ρ. Seismological field experiments investigate large volumes. Consequently, changes in the mean of ρ would have to translate to volume changes, which are not observed in the expected magnitude. Therefore, the bulk of velocity changes are due to changes in the shear modulus.

As with seismic tomography, the first studies that investigated changes in the seismic velocity did not rely on noise interferometry but on the energy emitted by controlled sources (e.g., De Fazio et al., 1973; Eisler, 1967). Poupinet et al. (1984) proposed to use the whole waveform, rather than just the first ballistic arrival, of repeating earthquake doublets to determine dv/v, using a method called coda wave interferometry (CWI) (see Singh et al., 2019; Snieder et al., 2019), and observed a decreased seismic velocity following a M5.9 earthquake. Note that, because of the different nature of the correlated wavefield, CWI tends to be sensitive to deeper properties with a high-frequency coda dominated by body waves (Sheng et al., 2021), and PII tends to use lower frequency surface waves (Obermann et al., 2016; Viens et al., 2022).

Following Poupinet et al. (1984)'s observation, a large number of publications presented evidence for dv/v decreases shortly after large earthquakes using CWI or PII (e.g., Brenguier, Campillo, et al., 2008; Hobiger et al., 2012; Hotovec-Ellis et al., 2014; Minato et al., 2012; Richter et al., 2014; Schaff & Beroza, 2004, and numerous others). Furthermore, these studies established that these damage-induced changes can last over many years and only recover slowly following a logarithmic law. However, while the occurrence of "healing" and damage has been demonstrated, the

underlying physical processes are still subject to scientific discussion. Recently, Sens-Schönfelder et al. (2019) proposed that thermal and chemical microscopic healing of cracks based on contact ageing leads to an overall stiffening following the damage-induced material softening. Their model appears to deliver accurate predictions for damage and recovery in laboratory experiments (Simpson et al., 2023).

Another family of mechanisms impacting the seismic velocity can be summarised as modifications in the confining pressure. For example, snow loads increase the confining pressure and cause increases in the seismic velocity (Donaldson et al., 2019; Guillemot et al., 2020; Hotovec-Ellis et al., 2014; Q. Y. Wang et al., 2017). Increases in pore pressure, on the other hand, for example, by refilling of groundwater, leads to decreases in dv/v (Andajani et al., 2020; Barajas et al., 2021; Sens-Schönfelder & Wegler, 2006). Many studies found hydrological effects to be the dominant mechanism in dv/v time series and controlling seasonal cycles as shown in Figure 2.4. Therefore, several authors have proposed using dv/v as a proxy for groundwater levels (Clements & Denolle, 2021; Lecocq et al., 2017; Mao et al., 2022). Usually, such studies invoke the opening and closing of cracks and pores caused by decreasing and increasing confining pressure, respectively, to explain the velocity changes associated with changes in the confining pressure (O'Connell & Budiansky, 1974).

Particularly for granular media, the rigidity and shear modulus and, thereby, v_S change significantly with the freezing or thawing of pore waters. This leads to sudden dv/v jumps at soil-covered sites whenever the temperature falls below 0 °C (Gassenmeier et al., 2015; Steinmann et al., 2021). Conversely, thawing, for example, associated with permafrost degradation, leads to decreasing seismic velocity (Albaric et al., 2021; Lindner et al., 2021; Zimmerman & King, 1986).

Along with these very commonly observed factors influencing dv/v, many more exotic ones were observed. Particularly in arid settings, temperature changes induce thermal strain (e.g., Oakley et al., 2021). For example, in Chile's Atacama

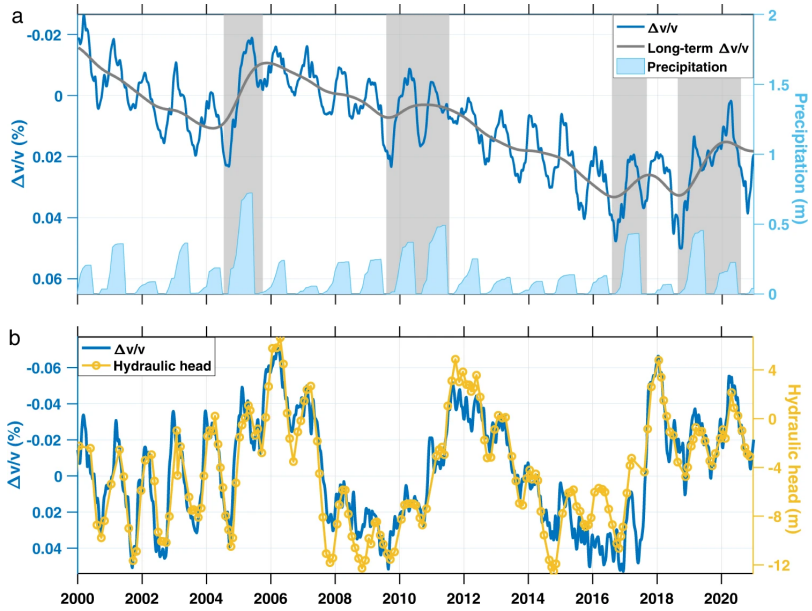

This figure was obtained from Mao, S., Lecointre, A., van der Hilst, R. D., & Campillo, M. (2022). Space-time monitoring of groundwater fluctuations with passive seismic interferometry. *Nature Communications*, *13*(1), 4643. https://doi.org/10.1038/s41467-022-32194-3

Figure 2.4: Anti-correlation between dv/v and hydraulic parameters observed in southern California. **a** dv/v in comparison to precipitation. **b** dv/v set in context to the hydraulic head. Note that dv/v is labelled Δv/v. For further details, refer to the original publication.

.

desert, the seismic velocity exhibits patterns that Richter et al. (2014) traced back to temperature diffusion in the subsurface. Sens-Schönfelder and Larose (2010) even demonstrated that drastic temperature changes on the lunar surface are responsible for velocity changes observed in the seismic data collected by the Apollo 17 mission. Additionally, the impact of solar and lunar tidal stresses was identified in some dv/v time series (Sens-Schönfelder & Eulenfeld, 2019).

To monitor active volcanoes, temporally dense and continuous monitoring techniques are particularly desired. Therefore, PII established itself as a suitable mean to quantify changes in the volcanic edifice and its vicinity before, during, and after an eruption cycle. However, the physical relationship between volcanic deformation and dv/v is complex, non-linear, and, as a result, still poorly understood. The complexity of the relationship also explains the multitude of recorded observations, which reach from co-eruptive velocity decreases (e.g., Brenguier et al., 2011, 2016; De Plaen et al., 2016, 2019; Machacca-Puma et al., 2019; Takano et al., 2017) over velocity increases (e.g., Caudron et al., 2021, 2022; Donaldson et al., 2019; Donaldson et al., 2017; Hotovec-Ellis et al., 2015; A. S. Yates et al., 2019) to no detected velocity changes. Overprinting signals from mechanisms with a more significant impact on the seismic velocity may also obscure volcanic influence on dv/v.

Moreover, ambient noise studies at very active volcanoes suffer from strong contaminations of the ambient seismic field by volcanic tremors (Gómez-García et al., 2018; A. Yates et al., 2023). PII requires a stationary spatio-temporal distribution of the wavefield as fluctuations alter the shape of the cross-correlation and, thereby, lead to modulations in the dv/v estimate that do not correspond to any physical changes in the medium but could be misinterpreted as such (Hadziioannou et al., 2011).

Due to all these complexities and challenges, volcano observatories do not yet employ dv/v modulations as precursory signals for imminent volcanic activity. Instead, all so-far published studies utilise datasets available after a volcanic crisis and aim to establish links to estimated velocity changes, thereby paving the way towards eruption forecasts using ambient seismic noise (Brenguier, Shapiro, et al., 2008). This thesis will expand on existing research in a similar spirit. While doing so, we will explore a manifold of other physical mechanisms impacting dv/v present in complex volcanic and environmental settings. Understanding and unravelling all physical con-

tributions to dv/v is crucial to making meaningful quantitative statements about the volcanic impact on seismic velocity.

CHAPTER 3

End-to-End Processing of Ambient Seismic Noise:

From Raw Noise Recordings to Time-Dependent Velocity Change Maps

This chapter[1] revolves around the methodological aspects of ambient seismic noise monitoring and, more specifically, passive image interferometry (PII). In it, we present SeisMIC, a fast, versatile, and adaptable open-source software to estimate seismic velocity changes (dv/v) from ambient seismic noise. SeisMIC includes a broad set of tools and functions to facilitate end-to-end processing of ambient noise data, from data retrieval and raw data analysis via spectrogram computation, over waveform coherence analysis, to post-processing of the final velocity change estimates. A

[1]This chapter has been published as [Makus, P., & Sens-Schönfelder, C. (2024). SeisMIC - an Open Source Python Toolset to Compute Velocity Changes from Ambient Seismic Noise. *Seismica*, *3*(1). https://doi.org/10.26443/seismica.v3i1.1099]. This work is licensed under a Creative Commons Attribution 4.0 International License. Compared to the published article, I replaced the introduction to fit into the context of this thesis. Minor modifications were introduced to the remaining text and the mathematical notation to preserve consistency across the thesis.

particular highlight of the software is its ability to invert velocity change time series onto a spatial grid, making it possible to create maps of velocity changes. With the software, we implement new data formats, ensuring uniformity, flexibility, interoperability, and integrity. To tackle the challenge of processing large continuous datasets, SeisMIC can exploit multithreading at high efficiency with an about five-time improvement in compute time compared to MSNoise, probably the most widespread ambient noise software. In this chapter, we provide a short tutorial and tips for users on how to employ SeisMIC most effectively. Extensive and up-to-date documentation is available online. Its broad functionality combined with easy adaptability and high efficiency make SeisMIC a well-suited tool for studies across all scales. Furthermore, we will outline and discuss some more theoretical aspects of PII and describe and derive the assumptions underlying to the method.

As I discussed in Section 2.3, dv/v is used in a host of applications to changes in the subsurface induced, for example, by environmental, tectonic, or volcanic processes. Estimates of dv/v time series can be obtained from the ubiquitous ambient seismic noise (see Section 2.2). Recordings of ambient seismic noise are only retained on continuous seismic data, as opposed to triggered data, which, for the sake of storage efficiency, contain only recordings of events such as earthquakes. Nowadays, it has become common practice to preserve continuous waveform recordings, opening a path for a focus on noise-based methods.

Processing and analysing continuous waveforms comes with multiple challenges due to the large amount of raw and derived data, such as the need for efficient processing and storage strategies (Arrowsmith et al., 2022). Still today, many authors use unpublished codes to produce results for later publication and interpretation, making it difficult for fellow researchers to reproduce or adapt the analyses. Using community codes published in the spirit of the FAIR principles (Barker et al., 2022) can facilitate the reproducibility of research, exchange in the community, and

progress in science. Only a few software solutions exist for ambient noise seismology. Perhaps the most popular among these are MSNoise (Lecocq et al., 2014) and NoisePy (Jiang & Denolle, 2020). However, as we will show and discuss in this chapter, the existing software still leaves a niche to fill. For example, MSNoise is more specialised for end-to-end workflows and automated monitoring solutions, lending it more towards applications in large observatories, whereas, recently, NoisePy has undergone development towards cloud computing. To fill the remaining gap, we introduce SeisMIC (Seismological Monitoring using Interferometric Concepts) (Makus & Sens-Schönfelder, 2022), a fast, robust, flexible, and easily-adapted Python tool to compute, process, and analyse dv/v. Due to these attributes, SeisMIC especially excels in the analysis of campaign data, where both ease of use and flexibility are crucial.

3.1 Modular Structure

3.1.1 Whom is it for? - The Philosophy behind SeisMIC

As outlined above, monitoring surveys are applied to a broad spectrum of research scopes resulting in a high diversity of requirements for research software. With that in mind, we developed SeisMIC to be flexible and adaptable to user needs. As opposed to working with a black box, users work close to the source code, making it easy to develop individualised workflows. Modules, submodules, or even single objects and functions of the code can also be used individually. Yet, the software remains a light and fast package, in which we avoid overhead due to non-essential functionality. For example, in contrast to MSNoise, we avoid heavy database management structure for continuous observatory monitoring, resulting in a significantly faster processing (see Section 3.1.3) and giving SeisMIC an advantage in the analysis of campaign based data.

Learning to use a new code and even only determining whether a code satisfies one's need is a large time investment. To guarantee a fast start and a steep learning curve, we aligned SeisMIC closely with ObsPy (Beyreuther et al., 2010), with whose syntax almost all seismologists are familiar. In addition, we host tutorials and extensive, regularly-updated documentation at https://petermakus.github.io/SeisMIC/. All objects, methods, and functions have documentation strings according to the Sphinx standard.

As developers, we follow the FAIR principles (Barker et al., 2022). That is, we make SeisMIC findable, accessible, interoperable, and reusable. SeisMIC is a community code with clearly communicated community standards, and users can discuss or report issues, suggest changes, or submit pull requests via GitHub. We distribute SeisMIC under the European Union Public License 1.2.

Lastly, we keep up to high standards regarding functional robustness. We test functional integrity using a combination of integral and unit tests. To date, SeisMIC has successfully been applied to a broad range of applications, such as volcanic environments (Makus, Denolle, et al., 2023; Makus, Sens-Schönfelder, et al., 2023), lab-scale applications (Asnar et al., 2023), and cryoseismological analyses (Nanni et al., 2023).

3.1.2 Implementation

As commonplace in Python, we structure SeisMIC in a modular fashion. We divide the program into clear modules, which, in turn, are subdivided into submodules. These modules can either be used separately or connected into a workflow/pipeline, starting from data retrieval and concluding with the computation, plotting, and post-processing of dv/v objects. We show a chart with a simplified overview of SeisMIC's modular structure in Figure 3.1.

As shown in Figure 3.1, SeisMIC consists of four main modules. `seismic.trace_-`

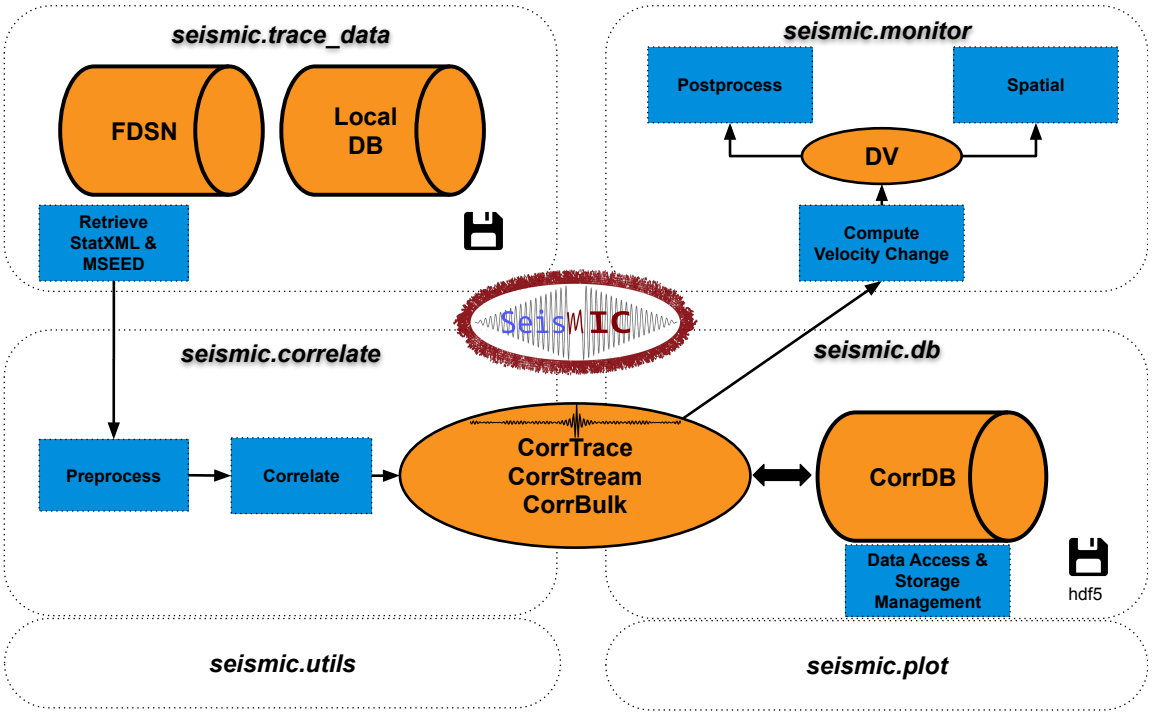

Figure 3.1: A flowchart summarising SeisMIC's modules and their purposes. A general workflow starts with data retrieval, continues with the computation of correlation functions, from which a velocity change time series can subsequently be estimated. We illustrate this with the example given in Section 3.2. The depicted floppy disk marks database management modules. Operations and processes are shown in blue, whereas objects and databases are shown in orange. For the sake of simplicity, we omit non-essential objects and functions, instead, the flowchart focuses on the core processes.

`data` hosts the code for reading raw waveform data and station information. Alternatively, it can request data from FDSN servers. SeisMIC handles waveform data in *miniseed* format in daily chunks, while it saves station information in *StationXML* format. Generally, station response information is only necessary if the user opts to remove the station response before correlating. However, basic station information, such as the station's geographic coordinates, is always required.

All objects and functions to preprocess waveform data and compute correlation functions (CFs) are located in `seismic.correlate`. We include commonly used preprocessing functions such as detrending, tapering, amplitude clipping, sign-bit-normalisation, or spectral whitening (Bensen et al., 2007). For a complete and up-to-date list of preprocessing functions, consult SeisMIC's documentation. Users can easily import custom processing functions into the workflow. We compute CFs by transferring traces to matrices, computing the Fourier transform, and then computing their cross-correlation in the frequency domain. Suppose we want to calculate all available correlations from a dataset of M waveforms, of which each has N samples (indices m and n, respectively). Then, the respective mathematical operations can be expressed as follows:

First, we compute the discrete Fourier transform of the matrix $\mathbf{s}$ containing the waveforms in the time domain:

$$S_{m,k} = \sum_{n=1}^{N} s_{m,n} e^{-\frac{i2\pi}{N}kn}, \tag{3.1}$$

where $i = \sqrt{-1}$ and k is the sample index of the signal in the frequency domain. Secondly, we obtain the correlation matrix $\mathbf{C}$ by computing the product of the matrix with the complex conjugate of itself. We then repeat the operation M times, each time rolling the complex conjugate matrix by $j = \{1, 2, .., M\}$ lines:

$$C_{o,k} = S_{m,k}\overline{S_{m+j,k}}, \tag{3.2}$$

where the bar indicates the complex conjugate and o indexes the station pair. In the described scenario, we obtain M^2 CFs, which are subsequently transferred back to the time domain:

$$C_{o,n} = \frac{1}{N} \sum_{k=1}^{N} C_{o,k} e^{\frac{i2\pi}{N}kn} \tag{3.3}$$

The CFs are then stored as special objects with attributes, plotting and post-processing methods. Finally, SeisMIC writes the CFs to a storage- and computationally-efficient *HDF5* container (Koranne, 2011).

All functionality to estimate velocity changes from the CFs resides in `seismic.monitor`. Currently, SeisMIC supports the estimation of velocity changes using the stretching technique (Sens-Schönfelder & Wegler, 2006) and we are implementing the wavelet-cross-spectrum analysis (Mao et al., 2020).

The stretching technique compares a reference correlation function $\tilde{C}_n$ to a CF C_n^l computed from data at an arbitrary subwindow l of the total time series. Note that we omit the index o indicating the station pair since this operation is independently executed for each station pair. There are several approaches to obtaining $\tilde{\mathbf{C}}$, all with their unique advantages, SeisMIC supports the use of single or multiple references (Sens-Schönfelder, Pomponi, & Peltier, 2014). In SeisMIC, we implemented a grid search, in which we evaluate $\tilde{\mathbf{C}}$ at a new time vector $\tilde{\tau}$ stretched (or compressed) with the stretching factor κ_j:

$$\tilde{\tau}_j = \tau e^{-\kappa_j} \tag{3.4}$$

Note that we base the exponential stretching on a Taylor extension for small velocity changes. This assumption is more accurate than the more common $\tilde{\tau}_j \approx \tau(1 + \kappa_j)$ and has the advantage of yielding linearly reversible stretched functions. In Appendix A, we provide a derivation.

Using our stretched time vector, we obtain a stretched reference correlation matrix with J lines, where J is the total number of tested stretch factors. Afterwards, we compute the zero-lag correlation (i.e., the normalised dot product) between each stretched reference and $\mathbf{C}^l$:

$$R_j^l = \sum_{n=1}^{N} \tilde{C}_n^j C_n^l \left(\sum_{n=1}^{N} (\tilde{C}_n^j)^2 \sum_{n=1}^{N} (C_n^l)^2 \right)^{-1/2} \tag{3.5}$$

The stretching factor $\hat{\kappa}_j = -dv/v$ resulting in the maximum R_j^l corresponds to the negative apparent velocity change at time step l. The maximum value of R measures the velocity change estimate's stability and is often referred to as coherence. We then compute R_j^l for all time steps resulting in the similarity matrix $\mathbf{R}$, the final velocity change time series, and a corresponding coherence time series. Note that $\mathbf{R}$ is usually not computed for the whole coda, but just for a user-defined subset of lag time samples. In SeisMIC, dv/v can either be jointly inverted from causal (right) and acausal (left side) or estimated from either side, which might be desirable for active source experiments or if one side of the CF exhibits a superior signal-to-noise-ratio.

Finally, the computed velocity change time series can be post-processed and plotted using pre-implemented or custom functions. In addition, SeisMIC can invert a set of velocity change time series from different stations onto a map using the inversion method described by Obermann, Planès, Larose, and Campillo (2013). To our knowledge, SeisMIC is currently the only publicly available software that supports spatial inversion of velocity change time series.

The workflow steps outlined above rely entirely on well-known Python libraries, including *NumPy* (Harris et al., 2020), *SciPy* (Virtanen et al., 2020), *ObsPy* (Beyreuther et al., 2010), *Matplotlib* (Hunter, 2007), and *h5py* (Collette et al., 2020). To ensure the best stability, we only utilise the most well-maintained projects and keep the number of dependencies to a minimum. Some of SeisMIC's core functionalities are based on the MIIC software project (Sens-Schönfelder, Flores-Estrella, et al., 2014). SeisMIC's latest beta version 0.5.23 is compatible with Python 3.10 and 3.11.

Data Formats and Standards

At the time of writing, there are no established standards for data handling in ambient noise seismology that would facilitate the exchange of correlation functions and subsequent processing with different tools. In the seismological community, excellent examples of well-designed data representations that developed into quasi-standards are the ObsPy (Beyreuther et al., 2010) trace and stream classes for waveform data and the inventories for station metadata. Such successful representations require some core attributes:

1. Uniformity: Various datasets have the same set of attributes, making them directly comparable.

2. Easy and flexible I/O (i.e., input/output), where data can be read, modified and stored later. Reading and writing operations are fast and easy. Modifications can be stored safely.

3. Interoperability: Data can easily be imported and exported into broadly used applications or libraries, facilitating data exchange.

4. Integrity: The data format must contain all information required for later processing, analysis, or cataloguing. No crucial information should be lost.

With SeisMIC, we suggest a representation of noise correlation functions implementing these attributes. For correlation functions, we base our data representation on the successful ObsPy streams and traces by introducing the `CorrTrace` and `CorrStream` classes that incorporate the specific requirements of CFs to ensure uniformity and integrity.

For the storage of CFs, the seismological standard for waveform data, MiniSEED, is not appropriate since it does not allow for the storage of the required meta information. The solution provided in SeisMIC stores the data itself in the form of a NumPy

array complemented with a header containing information about the recording and correlation computation, such as sample rate, start and duration of the correlated time windows, minimum and maximum lag times, seed identifiers of the used stations, and coordinates of these stations. We show an extract of the header fields for an exemplary dataset in Table 3.1. `CorrTrace` headers also contain information about executed processing steps, such as filtering or tapering. The naming of stations follows the SEED convention. To ensure interoperability, data and header can easily be converted into NumPy arrays and Python dictionaries, respectively. The objects come with processing and plotting methods. As outlined above, SeisMIC saves `CorrStreams` in hdf5 containers, from which they can later be read, modified, and saved again.

Table 3.1: Extraction from the header of a correlation function computed in Section 3.2.

Field name	Value	Explanation
network	X9-X9	SEED network codes, dash-separated
station	IR1-IR1	SEED station codes, dash-separated
channel	HHE-HHE	SEED channel codes, dash-separated
location	-	SEED location codes, dash-separated (may be empty)
corr_start	2016-01-25T01...	UTC start time of the correlated traces
corr_end	2016-02-25T01...	UTC end time of the correlated traces
start_lag	-25.0	computed start lag in seconds
⋮	⋮	⋮

3.1.3 Benchmark and Performance

In ambient noise seismology, it is not uncommon to work with data volumes in the order of terabytes. We address the arising computational and storage challenges with efficient and high-performance computing (HPC) compatible code design. To this end, SeisMIC enables parallel computing of correlations, velocity change estimates and spatial inversions, where the computation of CFs is the most expensive operation by a large margin. We implement parallel computing using *mpi4py* (Dalcin & Fang, 2021), which relies on the message passing interface (MPI). In contrast to other Python multi-threading solutions, MPI-based solutions work seamlessly on HPC and cluster solutions.

In SeisMIC, the computationally most expensive parts of the workflow described in Section 3.1.2 are the calculation of correlation functions, the associated preprocessing, and the estimation of the final velocity change time series. Therefore, an effective parallelisation scheme matters the most in these steps. For users, it is also important to understand how memory requirements scale. For the computation of CFs and the preprocessing of raw data, each core reads different raw data in chunks of equal length (see Listing 3.3 for details). Subsequently, the same core performs the preprocessing. For the cross-correlation operation, each core is responsible for a different component combination. This implementation makes the random access memory (RAM) usage practically independent of the number of cores used. Thus, RAM usage will mainly depend on the length of the raw data chunks read in each step (i.e., a smaller read length will lead to lower memory usage) and its sampling rate (i.e., a lower sampling rate will lead to lower memory usage). Resulting CFs are written to h5 files immediately after correlation or stacking and the memory is freed. In contrast, SeisMIC computes the final dv/v estimate with "1-core per component combination". Here, a single core loads all available CFs for one component combination and executes the stretching algorithm and the associated processing. Therefore,

for the final dv/v calculation, the memory requirement scales with the number of employed cores.

Multicore Scaling

To test how SeisMIC's computational performance scales with the number of used threads, we compute autocorrelations from three component data on a single cluster node featuring an Intel Cascadelake CPU structure that is equipped with 2 CPU sockets, each holding 20 physical cores that can each execute two threads in parallel. For our test, we compute CFs from 30 days of waveform data. SeisMIC reads daily chunks of miniseed files, which it subsequently decimates, here to a sampling rate of 25 Hz, after imposing an anti-alias filter. The daily waveforms are then detrended, tapered, and filtered with a pass band between 0.01 and 12 Hz. The data is then sliced into hourly traces, which are again linearly detrended, filtered between 2 and 8 Hz, and clipped if the amplitude exceeds a threshold of 2.5 times its standard deviation. Then, SeisMIC computes hourly CFs in the frequency domain and saves them in a customised HDF5 container after performing an inverse Fourier transform. We provide the *YAML* file containing the processing parameters in the digital supplement. We execute this operation using 1, 2, 4, 8, 16, 32, and 64 threads for data from 1, 2, 4, and 8 stations (i.e., 3, 6, 12, and 24 channels and component combinations). For each configuration, we repeat the computation ten times.

Figure 3.2 shows the mean processing time and standard deviation over the ten operations per unique $n_{threads}$-$n_{stations}$-combination. We normalise the processing times by the time required for $n_{threads} = 1$ and $n_{stations} = 1$. While $n_{threads} \leq n_{channels}$, where, in our case, $n_{channels} = 3n_{stations}$, the processing time scales close to linearly with the number of used threads, indicating an excellent parallel computing performance. As most of the parallel processing in SeisMIC works on a one-core-per-channel basis, only very little increase can be expected beyond this threshold.

Indeed, for $n_{channels} < n_{threads}$, the code reaches a performance plateau. From here on, the processing time increases with a further increase of $n_{threads}$, probably due to MPI's communication overhead. Based on the shown results, we would discourage hyperthreading (i.e., using more threads than available physical cores), which leads to a significant performance drop. Generally, one should not employ more threads than the total number of available channels for the computation of correlation functions or the total number of channel combinations for the dv/v estimation.

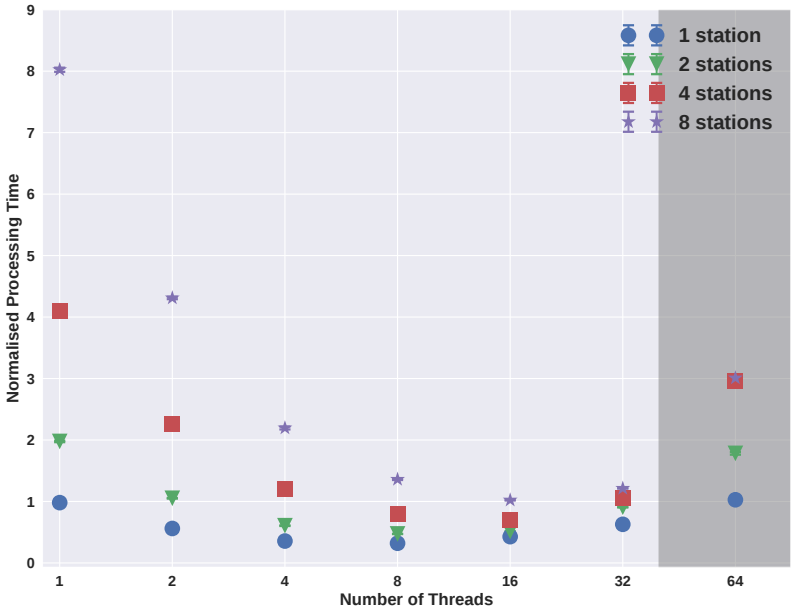

Figure 3.2: Multi-core scaling properties of SeisMIC. We show compute times for auto-correlations as a function of number of three-component datasets and number of parallel processing threads. The data points correspond to the mean processing time and the error bars to its standard deviation for ten operations (mostly too small to be visible). The processing times are normalised by the time needed to compute the correlations for one station using only one thread. The shaded area marks the area where the number of threads exceeds the number of physical cores, 40, i.e., the area where hyperthreading is employed.

Comparison with MSNoise

To analyse how SeisMIC's processing speed compares to the latest release of MSNoise (Lecocq et al., 2014), 1.6.3, we choose to calculate cross-correlations, which is the most expensive operation in a standard workflow, taking up more than 95 % of the total compute time. In this benchmark, we retrieve hourly cross-correlations for 14 days of raw waveform data between eight 3-component broadband seismometers sampling at 100 Hz. We set the preprocessing to be identical for both programs. First, the data are decimated to 25 Hz. Subsequently, we detrend, taper, and band-pass filter the data between 2 and 4 Hz. Before computing the CFs, we apply one-bit normalisation and spectral whitening. We do not remove the instrument response. Note, however, that both MSNoise and SeisMIC execute the response removal using ObsPy (Beyreuther et al., 2010) and will therefore take the same amount of compute time and resources. Finally, we save the hourly CFs and daily CF stacks for all six unique component combinations with a length of 50 s. We perform the benchmark on the same Intel-Cascadelake-based node that we use in Section 3.1.3.

We show the processing times required by MSNoise and SeisMIC for the outlined operation as a function of employed threads in Figure 3.3. Despite having received a significant performance boost with the update to version 1.6.x, MSNoise still needs about five times as long and thrice as much RAM as SeisMIC to execute the cross-correlation workflow, putting SeisMIC at a similar efficiency level as NoisePy (see Jiang & Denolle, 2020). In addition, SeisMIC offers a broader range of preprocessing options than NoisePy or MSNoise. MSNoise creates one miniseed file per CF, resulting in less complex writing operations, which are more evenly distributed across the cores. For this benchmark, this translates to a slightly better scaling between the number of cores and the computational time but also in a high number of files, which can be undesirable for large datasets. SeisMIC, on the other hand, creates one file per component combination. In every case, MSNoise remains more than twice as

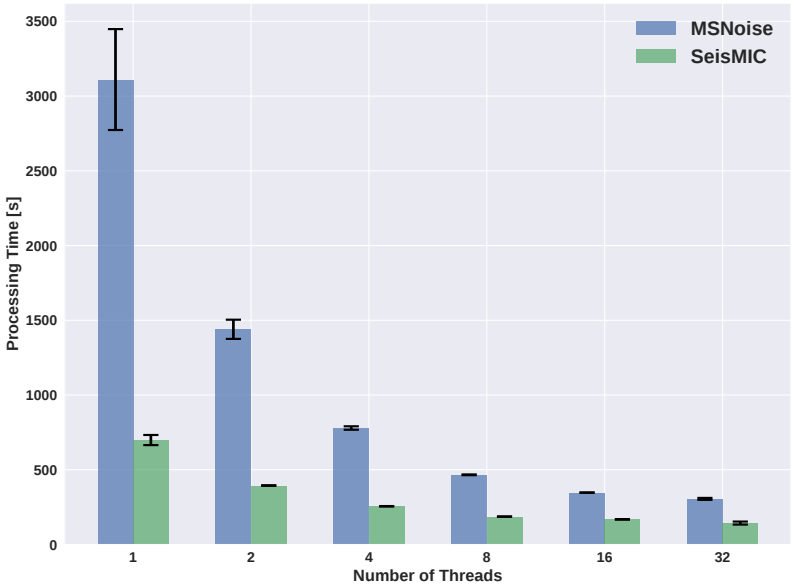

Figure 3.3: Compute times for a cross-correlation workflow for all six unique component combinations between eight seismic stations using MSNoise 1.6.3 (Lecocq et al., 2014) and SeisMIC 0.5.3. The height of the bars indicates the mean processing time over five iterations with the error bars representing the standard deviation. For hardware information and the exact parametrisation of the workflows, consult the text body.

slow as SeisMIC. Note that the shown times do not include the time that MSNoise takes to set up a database and scan new data, which can take a significant amount of time, whereas these operations are practically instantaneous in SeisMIC.

While the presented results are encouraging, we remark that we could decrease compute times even further by exploiting the potential of modern graphic processing units (GPUs), which can correlate ambient seismic noise with high efficiency (Clements & Denolle, 2021; Wu et al., 2022). Implementing such algorithms belongs to the intermediate-term goals of SeisMIC's development.

3.2 A Practical Example of a Workflow: From Raw Waveform Data to a Velocity Change Time Series

In this section, we demonstrate how to obtain a dv/v time series using a minimal workflow in SeisMIC. In the digital supplement, we provide two Jupyter notebooks containing the source code used for this workflow. The exemplary data are recorded by station X9.IR1 around the date of the M7.2 Zhupanov earthquake in Kamchatka, Russia. In the following, we investigate the impact of the event on the seismic velocity in the station's vicinity. A discussion of the result is performed in Chapter 4. We conducted this analysis using SeisMIC's implemented workflow, which is parametrised using a simple *YAML* file (see digital supplement). In the following, we will take a step-by-step tour through said workflow and provide some minimal code examples. For further examples, we advise the reader to consult SeisMIC's documentation and our GitHub page.

3.2.1 Data Retrieval

To start, we download data from an FDSN-compatible server. In our case, we download data from station X9.IR1, available over the GEOFON FDSN service (Quinteros et al., 2021). For conciseness, we restrict this example to 11 days of data from 25 January to 5 February 2016. In Section 3.1.3, we show how SeisMIC performs when confronted to larger datasets recorded on several stations and how compute time scales when employing multiple cores. Our exemplary time window comprises the 28 January Zhupanov earthquake, whose coseismic velocity drop we want to investigate. In SeisMIC, we can initiate the data download using the `Store_Client` class and its method `download_waveforms_mdl`:

Listing 3.1: Downloading data using SeisMIC

```
from obspy import UTCDateTime

from seismic.trace_data.waveform import Store_Client

starttime = UTCDateTime(2016, 1, 25)
endtime = UTCDateTime(2016, 2, 5)

# Decide where data are stored
sc = Store_Client('GEOFON', '/path/to/project', read_only=False)
sc.download_waveforms_mdl(
starttime, endtime, clients=['GEOFON'], network='X9',
station='IR1', location='*', channel='HHE')
```

Under the hood, this will initiate ObsPy's (Beyreuther et al., 2010) `MassDownloader` to download continuous waveform data from the specified station if not already present locally. Here, we will compute autocorrelations using only the east component of the seismogram. We can use SeisMIC to get a first idea of the spectral content of our waveform and to investigate in which frequency bands we might find stable noise sources suitable for PII. We show a spectrogram computed using Welch windows (see, e.g., Barbe et al., 2010) as implemented in SeisMIC in Figure 3.4.

3.2.2 Computing Autocorrelations

After downloading the waveforms, we can correlate them to obtain CFs. When computing correlations, we have ample preprocessing options, which, for brevity, we will not discuss here in detail. Most fundamentally, we must set the correlation length, `corr_len`, (i.e., the duration of the time windows to be correlated), the

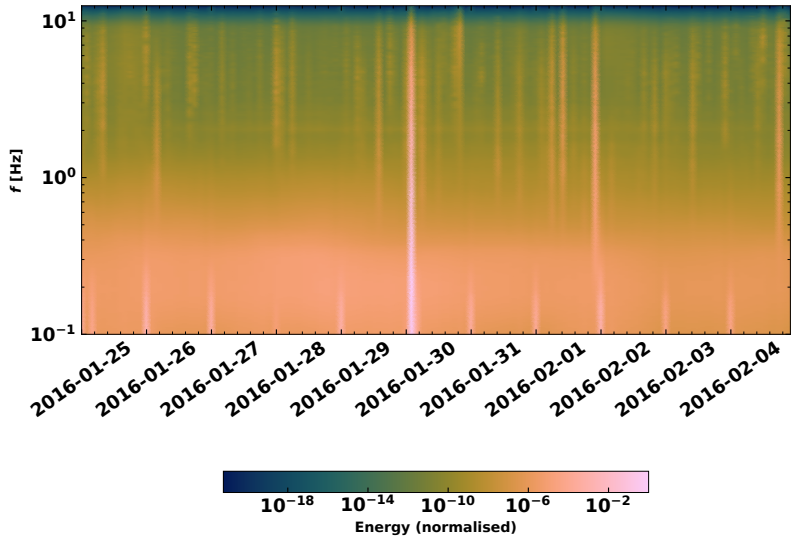

Figure 3.4: Time dependent spectrogram of the raw waveform at X9.IR1. We compute the spectrogram after removing the instrument response using 2-hours Welch windows. Note the energy spike caused by the Zhupanov earthquake. The energy amplitude is normalised by its maximum.

increment between these time windows, `corr_inc`, the correlation method (in our case, autocorrelation), and the frequency window to be filtered. The user defines all options in the *YAML* file, but they can also provide parameters in a Python dictionary. For this example, we choose a correlation length of one hour and a frequency band between 2 and 4 Hz. In SeisMIC, the `Correlator` class handles the correlation workflow.

Listing 3.2: Downloading data using SeisMIC

```
from seismic.correlate.correlate import Correlator

# sc is the previously initatied Store_Client
c = Correlator(sc, options='path/to/params.YAML')
st = c.pxcorr()
```

To illustrate the syntax of the parameter file, we show an extract of it below. Note that the keys `preProcessing`, `TDpreProcessing`, and `FDpreProcessing` can also import custom, external functions as long as input arguments and return objects follow a predefined syntax.

Listing 3.3: params.YAML

```
...
read_start : '2016-01-25 00:00:01.0'
read_end : '2016-02-05 00:00:00.0'
sampling_rate : 25
remove_response : False
combination_method : 'autoComponents'
preProcessing : [
{'function':'seismic.correlate.preprocessing_stream.detrend_st',
        'args':{'type':'linear'}},
{'function':'seismic.correlate.preprocessing_stream.cos_taper_st',
        'args':{'taper_len': 100,
                'lossless': True}},
{'function':'seismic.correlate.preprocessing_stream.stream_filter',
        'args':{'ftype':'bandpass',
                'filter_option':{'freqmin':0.01, 'freqmax':12.49}}}]
subdivision:
corr_inc : 3600
corr_len : 3600
...
corr_args : {'TDpreProcessing':[
        {'function':'seismic.correlate.preprocessing_td.detrend',
                'args':{'type':'linear'}},
```

```
        {'function':'seismic.correlate.preprocessing_td.TDfilter',
                'args':{'type':'bandpass','freqmin':2,'freqmax':4}},
        ],
        'lengthToSave':25,
        'center_correlation':True,
        'normalize_correlation':True,
        ...
}
...
```

Its `pxcorr` method will internally handle preprocessing and correlation. It will also initiate MPI to enable parallel processing. In Figure 3.5, we plotted the CFs using SeisMIC's plotting tools. Due to the high noise level in the chosen time window and frequency band, a well-defined coda emerges from the CFs (see Makus, Sens-Schönfelder, et al., 2023, or Chapter 4 for details).

3.2.3 Waveform Coherence

For a first assessment of which frequency bands are well-suited for a velocity change analysis, we can use a spectrogram like the one we show in Figure 3.4. Additionally, one can use SeisMIC's waveform coherence function. The waveform coherence corresponds to the averaged zero-lag cross-correlation between a reference CF and CFs at time t (Steinmann et al., 2021). In Figure 3.6, we show the waveform coherence for our exemplary dataset computed between hourly CFs and the average CF as a reference. We determine the coherence for 5 s long lapse-time windows and one-octave-wide frequency bands jointly for positive (causal) and negative (acausal) lag times. SeisMIC computes waveform coherence using the `Monitor` class and its `compute_waveform_coherence_bulk()` method (see digital supplement).

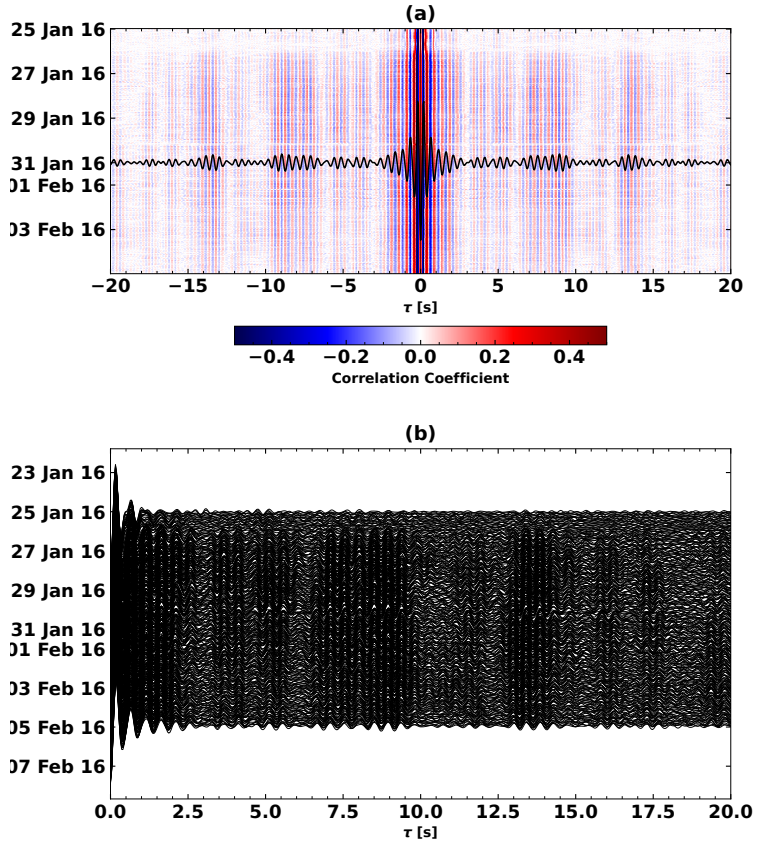

Figure 3.5: Hourly autocorrelations of ambient noise recorded by the east component of X9.IR1. This plot showcases two styles to plot correlations in SeisMIC. **(a)** Autocorrelations plotted as a colour image. The colours scale with the amplitude of the correlation. We superimpose the average of all shown autocorrelations on top of the heatmap. **(b)** Autocorrelations plotted as a section plot. In this plot, each hourly CF corresponds to one curve. Here, we only show the causal side of the CF.

Figure 3.6 leads us to infer a high stability and energy content between 0.5 and 4 Hz. The coherence remains high until late lag times, e.g. for 3 Hz centre frequency,

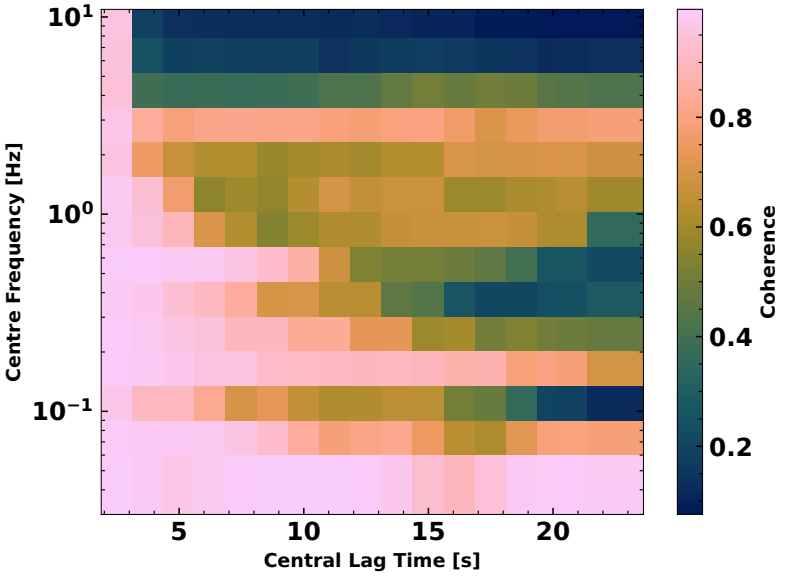

Figure 3.6: The waveform coherence as a function of lag time and frequency for the dataset from station X9.IR1 and channel HHE. For details, consult the text body.

up to 75 periods. From this, we infer a highly scattering medium paired with a high energy content in this frequency band originating from the volcanic system (see Makus, Sens-Schönfelder, et al., 2023, or Chapter 4). Therefore, we henceforth focus on the analysis of dv/v between 2 and 4 Hz.

3.2.4 Computing Velocity Changes Using the Stretching Method

Using the procedure theoretically outlined in Section 3.1.2, we can estimate the evolution of the seismic velocity in the study period. Like previously, the parametrisation is handled over the *YAML* file (see digital supplement). Before computing dv/v, we smooth the one-hour CFs with a 4-hour long Hanning window. As reference CF, we use the mean of all CFs. Then, we compute dv/v for lag times between 3.5 s and 12 s simultaneously from the causal and acausal parts of the coda. We plot the resulting velocity change time series using one of SeisMIC's standard plotting templates in

Figure 3.7.

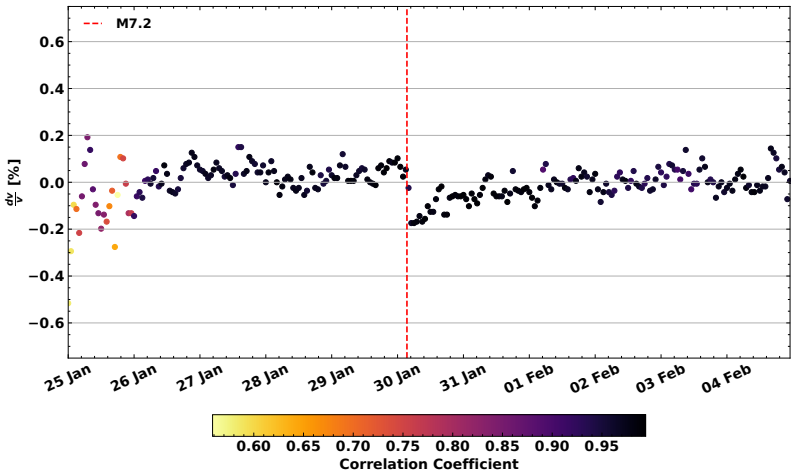

Figure 3.7: Velocity change time series estimated from the CFs shown in Figure 3.5. The increment between each data point is one hour and the shown dv/v is derived from CFs that are smoothed over 4 hours. The points' colour scales with the correlation coefficient (coherence) between the stretched CF and the reference CF. We plotted the origin time of the M7.2 Zhupanov earthquake, which occurred on 28 January 2016, as a vertical red line. An obvious velocity drop coinciding with the event can be identified. A subsequent recovery and more subtle differences in seismic velocity between day- and nighttime are visible.

Even though we do not focus on data interpretation in this article, we should take a brief look at the presented results. Most notably, we identify a clear velocity drop coinciding with the regional M7.2 Zhupanov earthquake. Interestingly, the resolution of the dv/v time series is high enough to identify a diurnal cycle that could be caused by air temperature and pressure variations, for example, observed by B. Wang et al. (2020), or might be due to lunar and solar tides as reported by Yamamura et al. (2003) and Sens-Schönfelder and Eulenfeld (2019). Lastly, we note that the correlation coefficient is significantly lower before 26 January 2016. We

link this observation to a transient change in the wavefield as described by (Makus, Sens-Schönfelder, et al., 2023, Chapter 4) and Steinmann et al. (2023).

3.2.5 Spatial Imaging of Velocity Changes

Velocity change estimates like the one presented in Figure 3.7 show dv/v as a function of time but do not directly yield insight into the spatial distribution of these velocity changes. Coda waves, as used in PII, sample the medium at a high spatial extent. While this allows to detect distributed weak velocity changes or changes located away from the path of direct waves, it prevents a simple inference of the affected location along a ray path or Fresnel volume. The affected location can, however, be estimated using sensitivity kernels that describe the time-dependent energy distribution of the wavefield for a statistically uniform medium. For a theoretical derivation of the sensitivity kernels based on the Radiative Transfer Theory, refer to Mayor et al. (2014), Margerin et al. (2016), and Zhang et al. (2022).

In SeisMIC, we implemented a simplified approach relying on sensitivity kernels derived from an approximate solution of the Boltzmann equation for a homogeneous medium (Paasschens, 1997) describing isotropic scattering of acoustic waves. Using these sensitivity kernels and a linearised inversion scheme proposed by Obermann, Planès, Larose, and Campillo (2013), we can map a 2-dimensional distribution of dv/v at a fixed time t_i resulting in $dv/v(t_i, x, y)$.

In SeisMIC, the module `seismic.monitor.spatial` contains the necessary functions for the outlined approach. To illustrate the procedure and make our example easily adaptable and reproducible, we create a synthetic velocity-change model, which we then forward model onto a random station configuration. After adding noise to the synthetic data, we try to recover the initial model using the inverse algorithm. In detail, we proceed as follows: First, we create a synthetic velocity change model with an extent of 40 km×40 km and a spatial resolution of 1 km (Figures 3.8 (b) and (d)).

The background medium has a homogeneous velocity of 3 $\frac{\text{km}}{\text{s}}$ and a transport mean free path l_0 of 30 km. Then, we place an arbitrary number of stations on random positions along the grid. Using sensitivity kernels of cross- and autocorrelations, we solve the forward problem to compute dv/v, as it would be obtained from the CFs in the presence of the spatial velocity variations. The sensitivity kernels are computed for lapse time windows between 14 and 34 s. To the dv/v values, we add random noise. This noise follows a Gaussian distribution around 0 % velocity change with a standard deviation of 0.1 %. Finally, we invert for the synthetic model employing the damped linearised inversion (Tarantola & Valette, 1982). We show the results of this inversion in Figures 3.8(a) and (c) for 4 and 32 stations, respectively. There, we also indicate the used damping parameters. The optimal damping parameters minimise both the misfit between the initial and the retrieved model and the model complexity and can be found using the L-curve criterion, as discussed by Obermann, Planès, Larose, and Campillo (2013). This inversion relies on two damping parameters, the correlation length λ determining how strongly related neighbouring grid cells are and the model variance σ_m that the model may assume.

The results demonstrate that increasing the number of stations is the most powerful tool to decrease the misfit between the inversion result and the input model. While the geometry of the synthetic model is poorly retrieved for a configuration using only four stations, we can reproduce the model quite accurately with 32 stations.

The digital supplement contains a Jupyter notebook to reproduce or modify these results with an arbitrary number of stations, velocity change model, and damping parameters. We also include options to invert for dv/v only utilising data from auto- or cross-correlations and using sensitivity kernels from split coda windows (i.e., with lapse time windows sliced into narrow sub-windows). In Appendix A, we show results that exploit these options. Based on these, we argue that adding dv/v information from auto- and cross-correlations, improves the accuracy of the result

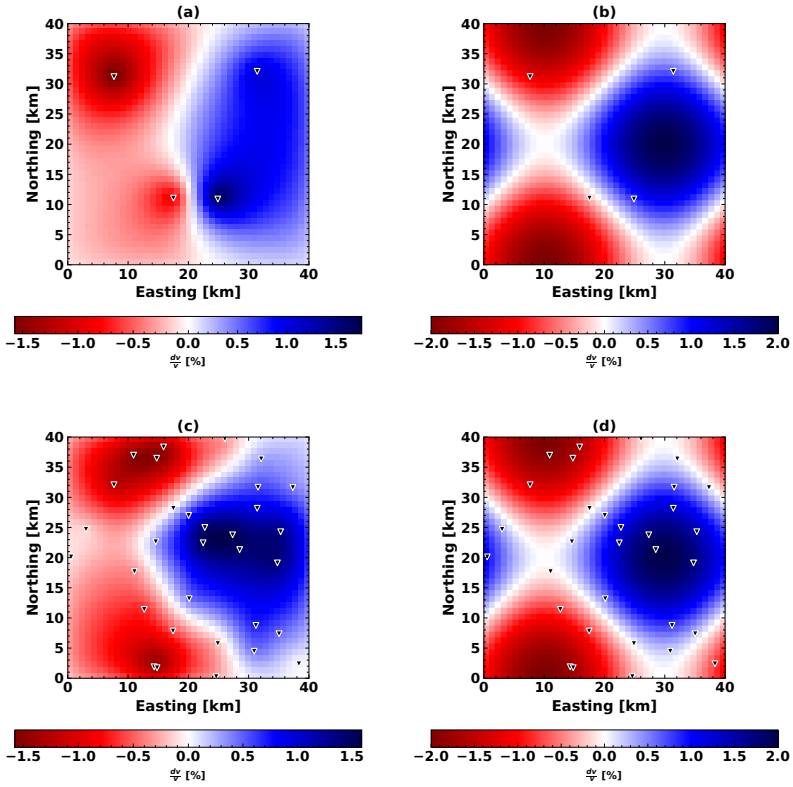

Figure 3.8: Two examples of the spatial inversion using different parametrisations and station configurations. **(a)** Result of the spatial inversion algorithm using four stations, a model variance $\sigma_m = 0.1\ \frac{\text{km}}{\text{km}^2}$, and a correlation length $\lambda = 2$ km. **(b)** The synthetic velocity model and station configuration used to obtain (a). **(c)** Result of the spatial inversion algorithm using 32 stations, $\sigma_m = 0.01\ \frac{\text{km}}{\text{km}^2}$, and $\lambda = 2$ km. **(d)** The synthetic velocity model and station configuration used to obtain (c). For an exhaustive description of the parametrisation and the inversion steps, consult the text body.

notably, whereas splitting the coda yields only minor improvements.

3.3 Conclusion and Outlook

We presented SeisMIC, a software to estimate changes in the seismic propagation velocity from continuous records of seismic ambient noise. SeisMIC contains functionalities for the end-to-end processing of velocity-change time series, including data retrieval, the computation of correlation functions, calculating velocity change time series using the stretching method, and postprocessing as well as inverting dv/v time series onto a spatial grid. While these functions can be part of a workflow, they are also intended to be used separately and can easily be altered and adapted to individual processes. In SeisMIC, we implement a new data format for correlation functions, which provides uniformity, flexibility, interoperability, and integrity. Thereby, we hope to foster a broader discussion in the community regarding data standards, which, we believe, would aid data exchange, efficiency, and reproducibility of ambient noise studies.

In the near future, we will release versions capable of estimating dv/v employing algorithms other than the stretching method, like the wavelet-cross-spectrum analysis (Mao et al., 2020). Other future milestones include exploiting the computational power of GPUs to decrease the compute time of noise correlations even further and adding solutions that automatically update correlation function databases.

SeisMIC complements existing software to process ambient noise. Highlights are its broad functionality, high efficiency, and versatility applicable to local small-scale studies on a laptop computer as well as surveys using large-N arrays processed on computer clusters. SeisMIC is available on GitHub as a well-documented and regularly maintained open-source software.

Data and Code Availability

This chapter is distributed with a supplementary document in Appendix A. Aside from this appendix, we provide Jupyter notebooks, computing scripts, and the main program "SeisMIC" as a digital supplement. For SeisMIC, however, we strongly encourage the reader to obtain the code's latest version, for example, from GitHub. The digital supplement includes SeisMIC 0.5.3 and is available at https://doi.org/10.5281/zenodo.8283683.

The SeisMIC data from the KISS experiment (N. Shapiro et al., 2017) used in Section 3.2 can be obtained from the GEOFON webservice (Quinteros et al., 2021). For the benchmarks in 3.1.3, we used data from the Saxony Network (University of Leipzig, 2001) available from the EIDA FDSN service (Strollo et al., 2021).

CHAPTER 4

Creating High-Resolution Velocity Change Time Series with Fluctuating Noise Fields:

An Application to the Klyuchevskoy Volcanic Group

4.1 Introduction

4.1.1 Motivation for Noise Interferometry Studies at Active Volcanoes

In this chapter[1], we will turn towards a first application of PII to data recorded at active volcanoes. Specifically, we analyse seismic data recorded at the Klyuchevskoy

[1]This chapter has been published as [Makus, P., Sens-Schönfelder, C., Illien, L., Walter, T. R., Yates, A., & Tilmann, F. (2023). Deciphering the Whisper of Volcanoes: Monitoring Velocity Changes at Kamchatka's Klyuchevskoy Group With Fluctuating Noise Fields. *Journal of Geophysical Research: Solid Earth*, *128*(4), e2022JB025738. https://doi.org/10.1029/2022JB025738]. The article is open access under the terms of the Creative Commons Attribution-NonCommercial Li-

Volcanic Group (KVG) in Kamchatka, Russia, between the summer of 2015 and the summer of 2016 to study medium changes related to volcanic activity.

However, PII is not only sensitive to changes in the medium but is also impacted by fluctuations in the noise wavefield (Hadziioannou et al., 2011). Such fluctuations are particularly problematic in active volcanic regions as pervasive volcanic tremors cause constant changes in the spatio-temporal distribution of sources and frequency content of the noise field. In contrast to other causes of noise field fluctuations, such as cultural noise, seasonal changes, or weather-induced changes, these fluctuations are hard to predict and often last for extended periods of days and months.

In this chapter, we propose and demonstrate a technique to mitigate the impact of these fluctuations that we found particularly effective in the case of ubiquitous volcanic tremors. This approach relies on machine learning to find time segments with temporarily stationary noise fields and describe a non-linear spatial stack that further reduces uncertainty in the dv/v estimates. In our dv/v results, we find influences of a multitude of tectonic (e.g. a velocity drop following the M7.2 Zhupanov earthquake), environmental (e.g., rain and snow), and volcanic (i.e., a gradual velocity increase of about 0.3 % at Bezymianny Volcano coinciding with surface deformation observed using remote sensing techniques) processes. We further analyse these mechanisms by evaluating peak ground velocity/velocity change responses, developing a snow depth and precipitation dv/v coupling model, and discussing volcanic activity during the experiment. Finally, we draw some concluding remarks concerning our

 Compared to the original publication, the introduction has been modified. Figure 4.9 was moved from the supplementary material to the main manuscript. In the interest of conciseness, descriptions of procedures already described in Chapter 3 were condensed or replaced by references to said chapter. I also introduced minor changes in the mathematical notation and the text body. To ensure consistency across the thesis, I adapted the orthography according to the British/Canadian standard.

work's methodological novelties and geoscientific implications.

4.1.2 Kamchatka and the Klyuchevskoy Volcanic Group

Kamchatka is a peninsula situated in Russia's far east, west of the Aleutian Islands and north of the Kuril Islands. Even though Kamchatka is located at a latitude of about only 60° N, temperatures can reach down to -40° C and remain low around the year. On Kamchatka's east coast, the annual precipitation can be up to 2700 mm/yr. Together, these effects lead to thick snow covers for over six months per year, especially at higher altitudes (Hersbach et al., 2020).

The subduction of the Pacific Plate under the Okhotsk Microplate at a rate of about 80 mm/yr (Bürgmann et al., 2005) regularly causes large earthquakes, among them the magnitude 7.2 Zhupanov earthquake that struck on 30 January 2016 south of the study region (see Figure 4.1). The magmatic activity under Kamchatka has also been associated with this subduction. Despite its extraordinarily high productivity and almost constant activity, most of the volcanism on Kamchatka does not pose an immediate threat as the peninsula is only sparsely populated (Koulakov, 2021). However, eruptions may impact important aviation routes in the Western Pacific (Girina et al., 2019), and effects like ash clouds or tsunamis (Belousov et al., 2000) could reach far beyond Kamchatka's borders. Furthermore, knowledge gained from Kamchatka can be transferred to other volcanic systems posing threads for densely populated areas such as in Japan or Central and South America.

The Klyuchevskoy Volcanic Group (KVG) lies within the Central Kamchatka Depression (CKD) in central-east Kamchatka. While the KVG consists of dozens of volcanoes (see Figure 4.1), currently, only three of them are active: Bezymianny, Klyuchevskoy, and Tolbachik (Fedotov et al., 2010). During our study period, between the summer of 2015 and the summer of 2016, Klyuchevskoy exhibited high seismic activity with intermittent eruptions. In addition, Bezymianny showed signs

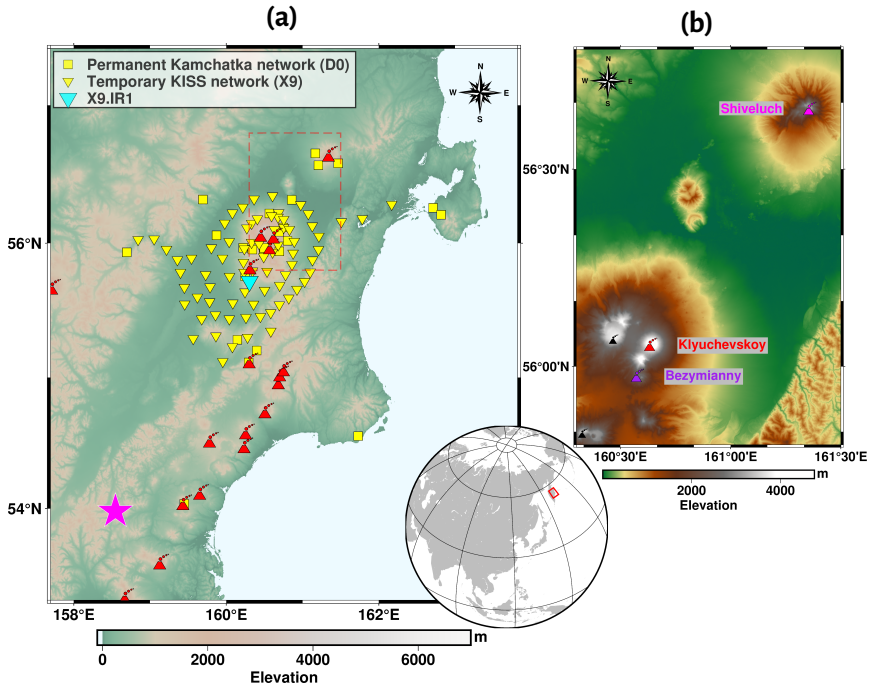

Figure 4.1: A map view of the study region. **(a)** The sites of permanent and temporary stations are represented by squares and triangles, respectively. We use data from station X9.IR1 (cyan) in Figures 4.2 and 4.3. The epicentre of the M7.2 Zhupanov earthquake is plotted as a magenta-coloured star. We depict the locations of volcanic centres active during the Holocene. **(b)** A zoom on the area marked by the dashed, red box shown in (a). The locations of the three volcanoes discussed here, Bezymianny, Klyuchevskoy, and Shiveluch are indicated and labelled.

of the initiation of an eruptive cycle, whereas Tolbachik remained inactive (Coppola et al., 2021; Journeau et al., 2022; Mania et al., 2021). Evidence from geophysical and petrological data suggests the existence of a common magma reservoir at about 30 km depth (Fedotov et al., 2010; Ozerov et al., 1997). However, the isotope composition of the magmas seems to contradict these findings (Dorendorf et al., 2000; Kayzar et al., 2014). The deeper magma reservoir feeds several complex systems of smaller shallow magma chambers at about 5 km depth and, in the case of Klyuchevskoy, directly into the volcano (Green et al., 2020; Journeau et al., 2022; Koulakov et al., 2017; N. Shapiro et al., 2017). Koulakov et al. (2021) proposed the existence of a separate gas-filled chamber responsible for Bezymianny's explosive activity. Recently, Coppola et al. (2021) showed that activities of Bezymianny and Klyuchevskoy are correlated, whereas activity at Tolbachik seems to reduce the output at the two other volcanoes, indicating a complex, interconnected volcanic plumbing system.

A number of publications focused on the spatio-temporal evolution of volcanic tremors and volcano-tectonic events at the KVG. Volcanic tremors are thought to result from fluid movements and pressure variations in the volcanic plumbing system (Chouet, 1996). For Kamchatka, Soubestre et al. (2019) and Journeau et al. (2022) show that tremors occurring below several active volcanoes migrate periodically between shallow and deep locations. These tremors dominate the noise field above $\sim$0.5 Hz (Gómez-García et al., 2018). As we will discuss later, this observation has important implications for noise interferometry studies.

Other studies have investigated the time-dependent variations of the subsurface properties. Koulakov et al. (2013) found velocity changes in the upper crust below the KVG using repeated 3D seismic tomography. They interpreted these changes as signs of magma migration preceding eruptive periods. However, due to its coarse temporal resolution, 4D earthquake tomography is only of limited use for eruption

early warning. Gómez-García et al. (2018) applied PII to data collected at the KVG. While they recovered long-term velocity changes from frequencies below 0.7 Hz, their algorithm showed limitations for higher frequencies due to strong fluctuations in the regional noise wavefield. dv/v time series retrieved from these lower frequencies are usually limited in their temporal resolution due to the high variability of the ocean-generated microseismic signals (e.g., weather and particularly storm dependence). Additionally, they are ill-suited to study shallow variations. In this chapter, we retrieve stable dv/v estimates for four one-octave-wide frequency bands between 0.5 and 8 Hz during shorter time segments by exploiting uniform noise fields that are temporarily stable and, thereby, obtain high-resolution dv/v time series that reveal fast-acting, shallow medium changes and their accurate timing.

4.2 Data and Preprocessing

4.2.1 Seismic Data

For this study, we use one year of seismic data from 101 broadband and short-period stations (Figure 4.1). Of these, 77 are part of the temporary KISS deployment (N. Shapiro et al., 2017) between summer 2015 and summer 2016. The remaining 24 stations are permanent stations operated by the Kamchatka Branch of the Geophysical Survey of the Russian Academy of Sciences (KBGS).

Before computing cross- (i.e., inter-station), self- (i.e., inter-component, see Hobiger et al. (2014)), and auto-correlations, we apply some common preprocessing steps to the seismic data: First, we load daily chunks of data that we subsequently downsample to 25 Hz, detrend, taper, and filter in octave wide passbands. For cross- and self-correlations, but not for auto-correlations, we whiten the spectrum in the frequency domain (i.e., dividing the traces' spectra by their amplitude spectra). We discard the traces' amplitude information while only keeping its sign (i.e., one-bit

or sign-bit normalisation), which we found to be the most effective way to mitigate the impact of high amplitude sources for our data. Afterwards, we slice the data into one-hour-long windows and compute correlation functions (CFs) as described in Chapter 3.1.2.

We retrieve our velocity change estimates by applying the trace stretching technique (Sens-Schönfelder & Wegler, 2006; Sens-Schönfelder & Brenguier, 2019). First, we select N subsets of all CFs (for details, see Section 4.3.3). From these subsets, we stack four-hourly noise correlations C_i every two hours (i.e., we smooth with a moving mean) to reduce random noise in the CFs. The stretching technique is described in greater detail in Chapter 3.1.2. We perform the stretching grid search for $-0.025 \leq \kappa \leq 0.025$ (i.e., up to 2.5 % deviation from the reference velocity) and coda times where the lag time is between $\tau_1 = 7.5T_1$ and $\tau_2 = 17.5T_1$ relative to the theoretical time of arrival, on both causal and acausal parts of the CF. T_1 corresponds to the long period corner period of the applied bandpass filter (Hobiger et al., 2014); for auto- and self-correlations, the reference time is accordingly 0. Ultimately, we retrieve N similarity matrices (see eq. 3.5) of the size $J \times I_n$ that relate the correlation coefficient R to the four-hour-long time sample i and the stretching factor κ. For each similarity matrix, we thus obtain a velocity change estimate time series $(dv/v)_i$.

To execute these steps, we employ SeisMIC (Makus & Sens-Schönfelder, 2022), a freely available open-source software suite written in Python. SeisMIC is available on GitHub and discussed in Chapter 3.

4.2.2 Complementary Data

To set our results in context to potential environmental and volcanological forcing, we retrieve snow load, precipitation, and temperature data from ERA5, a global climate reanalysis dataset. ERA5 is sampled every hour and is resolved on a 9×9 km grid

(Hersbach et al., 2020). While the precipitation data shows degraded accuracy on an hourly time scale (Tang et al., 2020), its performance is still sufficient for our purposes. For Kamchatka, ERA5 is exclusively based on satellite data.

We rely on infrared satellite measurements (Coppola et al., 2021) to compare the determined velocity changes to the lava output of the volcanoes.

The magnitudes and origin times for regional earthquakes were obtained from the USGS FDSN web service.

4.3 Stabilising Velocity Change Estimates

4.3.1 The Limitations of Passive Image Interferometry in Fluctuating Noise Fields

Ideally, each of our I CFs would correspond to a Green's function approximation at the time t_i. In practically all cases, however, non-uniform noise fields violate this assumption. While noise interferometry does not require an actual Green's function approximation, a stationary noise field is necessary for the study to succeed (Hadziioannou et al., 2011). Commonly, researchers apply a set of standard preprocessing techniques such as those described in Section 4.2 to mitigate the impact of this non-stationarity directly in the data (Fichtner & Tsai, 2019). Another standard approach is the temporal smoothing of CFs, which results in a trade-off between stability and temporal resolution. This approach assumes that rapid fluctuations between CFs retrieved from the noise of consecutive times are due to the stochastic character of the noise and, hence, can be reduced by temporal smoothing. Processing the dv/v observations can improve the monitoring further. Even though these steps aim to reduce the measurement noise, we try to avoid the term denoising as we find it ambiguous in the context of ambient noise seismology. Instead, we prefer the broader

term *stabilisation* of CFs and dv/v estimates.

For data from Kamchatka, Gómez-García et al. (2018) have already shown that standard preprocessing does not suffice to retrieve stable dv/v estimates. They proposed a different algorithm that exploits a Bayesian framework to estimate dv/v. However, their algorithm shows limitations for higher frequencies severely impacted by the pervasive fluctuation of volcanic tremors (see power spectrum in Figure 4.2 (a)). In addition, the proposed method is not suited to retrieve reliable long-term trends when properly parametrised for changing noise fields (Gómez-García et al., 2018). To illustrate the non-stationarity of the CFs, we show the east-north component of the self-correlation matrix of station X9.IR1 in Figure 4.2 (b). When the energy is high (e.g. December 2015), the corresponding CFs differ from other times. Journeau et al. (2022) showed that the intensity of the tremors fluctuates simultaneously, confirming that volcanic sources cause the changes in noise amplitudes and CFs. For illustrative purposes, we show a velocity change estimate using the standard trace stretching approach in Figure 4.2 (c). The resulting dv/v fluctuates strongly with abrupt changes in the associated correlation coefficient (i.e., the coherence), indicating that this measurement does not reflect physical changes in the subsurface and cannot be interpreted. Interestingly, the dv/v estimate has the highest correlation coefficient when volcanic tremors dominate the noise field. Hence, it seems as if phases that emerge in the CFs due to the high-energy tremor dominate the reference CF, which is a mean of all CFs.

4.3.2 Previous Approaches

Aside from standard preprocessing and Bayesian-type inversions (Gómez-García et al., 2018), several methods have been proposed to avoid instabilities due to non-stationary wavefields. Hadziioannou et al. (2011) utilised an adaptive filter to remove incoherent phases from CFs. Moreau et al. (2017) combined singular value

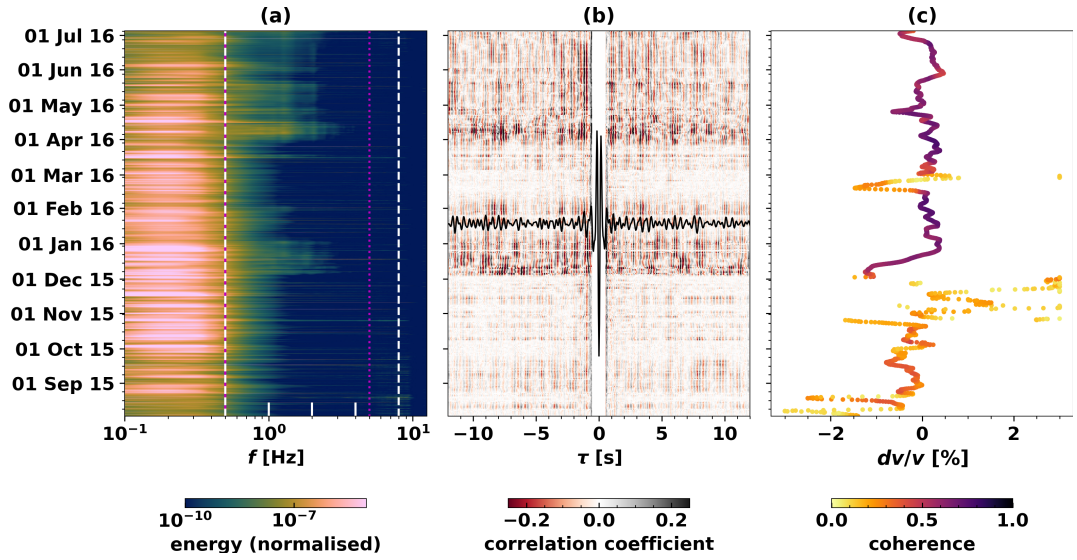

Figure 4.2: **(a)** Spectrogram of station's X9.IR1 N component calculated with a 4-hour-window. Volcanic tremors appear as obvious bright (i.e., high energy) spots between ∼0.5 and 5 Hz (frequency band marked with magenta dotted lines). We truncated the colour scale at both ends. In this work, we analyse velocity changes in octave bands between 0.5 and 8 Hz (marked by white dashed lines) **(b)** Daily self-correlation functions as calculated from station X9.IR1 between the E and N component created from preprocessed waveform data between 2 and 4 Hz. Note that the shape of the CFs (i.e., the Green's function estimate) changes significantly during the study. The average CF is plotted in black on top of the heatmap. We muted the daily correlation functions for $-0.5\,\mathrm{s} \leq \tau \leq 0.5\,\mathrm{s}$ to emphasise the shape of the coda. The colour scale is truncated to -0.25 and 0.25, respectively. **(c)** The velocity change estimated using the trace stretching method with the data from (b) and a smoothing of 2 days. We indicate the location of X9.IR1 in Figure 4.1.

decomposition with a Wiener filter to remove statistically and linearly independent components from the CFs. Schimmel et al. (2011) computed CFs using a phase cross-correlation rather than a conventional cross-correlation to suppress the impact of non-coherent high-amplitude phases. Viens and Van Houtte (2020) implemented an approach that employs deep learning to remove incoherences from CFs. Most of these solutions yield good results for noise that remains constant over the whole study period and distorts all CFs more or less equally. However, when the ambient wavefield changes entirely due to a shift of dominant sources over long periods, they become ineffective. In Kamchatka, volcanic tremors can last and remain stable for several months (Journeau et al., 2022; Soubestre et al., 2019), so we require a different approach to achieve stable dv/v estimates from ambient noise.

Recently, there has been a shift from more traditional filtering methods to methods using machine learning algorithms. Arguably the most popular choices among these are unsupervised clustering algorithms and unsupervised de-mixing algorithms. Both are particularly well-suited for large amounts of continuous data as they occur in ambient noise seismology. For example, Seydoux et al. (2020) clustered raw waveform data to differentiate ambient noise from earthquake signals. Similarly, Steinmann, Seydoux, Beaucé, and Campillo (2022) combined independent component analysis (ICA), a dimensionality reduction algorithm that separates statistically independent features, with hierarchical clustering. Thereby, they succeeded to discriminate time windows with different dominant sources. In another approach, they analysed the output features of the independent component analysis (ICA) and found a feature that closely resembles the velocity change of the medium (Steinmann, Seydoux, & Campillo, 2022). While this approach seems to retrieve very accurate and highly resolving dv/v estimates for their dataset, one must have successfully retrieved a low-resolution baseline estimate of dv/v using a conventional algorithm. Only then it is possible to evaluate that a feature of the decomposition corresponds to dv/v

and provide quantitative estimates of the velocity change, as the amplitude of the ICA coefficients is physically meaningless. These limitations reduce the applicability of the ICA-based method. In addition, in more complex datasets, like our datasets, dv/v does not seem to be confined to a single feature of the ICA decomposition rendering the output practically uninterpretable. A more general issue with approaches that rely entirely on machine learning is that the related physical processes remain elusive, often making a correct interpretation of the results challenging. In the following section, we will describe an approach that combines the advantages of machine learning and conventional noise interferometry to retrieve velocity change estimates for the Kamchatka dataset.

4.3.3 Clustering Noise Correlations

We address the varying noise conditions by splitting the experimental period into segments during which the ambient field is sufficiently stationary to observe temporal changes in the subsurface material. By clustering the CFs, we identify moments of change in the noise field that naturally separate the different segments. We use an agglomerative hierarchical clustering algorithm employing Ward's linkage algorithm with a Euclidean distance metric that minimises the variance in each cluster (Ward, 1963) to find CFs that are sufficiently similar to be used in the same interferometric analysis. For many clustering algorithms, such as K-means clustering, the user determines the number of clusters before assigning the data to these clusters. Hierarchical clustering, in contrast, returns a dendrogram representing possible clusters and subclusters and their respective (dis-)similarities (Müllner, 2013). Thereby, it helps avoiding an unsuitable choice of cluster numbers that would result in poorly defined clusters or too few clusters lumping together members with large differences. For a detailed discussion of hierarchical clustering of noise correlations, refer to A. Yates et al. (2023).

Similar to A. Yates et al. (2023), we cluster preprocessed CFs instead of raw waveform data to disregard factors such as amplitude variations in the ambient noise irrelevant to our study. Additionally, the cross-correlation serves as a dimensionality reduction that reduces the computational cost of the clustering. Instead of clustering CFs from all stations, we only use self-correlations from station X9.IR1 and component combination N-E that is sensitive to body, Love, and Rayleigh waves. As changes in the wavefield are regional, we do not obtain markedly different clusters for other stations and combinations (see Figure B.7). Also, using separate clusters would unnecessarily complicate the comparability of results between different stations.

We show the hierarchical dendrogram for data between 2 and 4 Hz in Figure 4.3 (a). As a compromise between stability and length of the dv/v time series, we split the dataset into five clusters. For 2-4 Hz, all clusters are highly dissimilar with a minimum cluster merging cost of about 9 (see Table B.1 for a merging cost-frequency overview).

We can assess the nature of each cluster by examining its temporal occurrence (see Figure 4.3 (b)) and the shape of its average CF (Figure 4.3 (c)). Most average CFs share some common features at early lag times, but their peaks differ later in the coda, confirming that they are ill-suited for an interferometry study based on a single reference trace and time window. Remarkably different from all other average CFs is group number 2 (green), which dominates during times of low volcanic activity. When comparing the temporal distribution of the clusters (Figure 4.3 (b)) to the volcanic tremor activity found by Journeau et al. (2022), it becomes evident that they directly correspond to the different dominating sources. During periods of low volcanic activity, cluster 2 (green) dominates. Clusters 3 and 4 correspond to periods at which volcanic tremors prevail. During the eruption at Klyuchevskoy volcano starting in April 2016, cluster 0 becomes active.

For the clustering, we focus on CFs created from the frequency band between 2

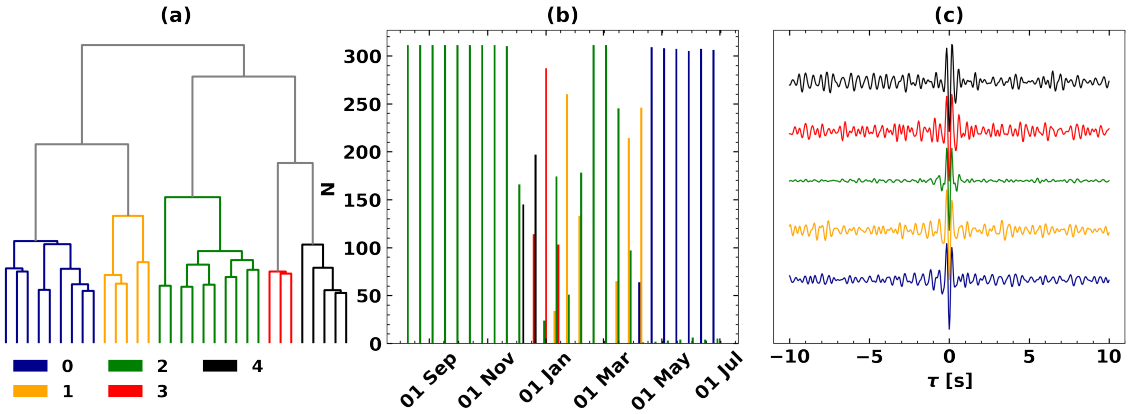

Figure 4.3: The output of the hierarchical clustering. As input data, we used one year of self-correlations between station's X9.IR1 (see Figure 4.1) east and north component created from waveform data between 2 and 4 Hz. Colours are used to identify the different clusters in the three panels. **(a)** A dendrogram that quantifies the similarity between the different clusters. The vertical distance of the branches scales with the dissimilarity of the clusters, i.e., their merging cost (see Table B.1). We show unclustered branches in grey. **(b)** The distribution of the clusters over the whole study period. The bars show the bi-weekly occurrence N of the respective cluster. **(c)** Averages of the CFs belonging to each of the five clusters.

and 4 Hz, which shows the greatest impact of volcanic tremors (see Figure 4.2 (a)). However, we remark that almost all frequency bands, particularly above 2 Hz, show similar patterns as the one under discussion, albeit not always as pronounced. Below 0.25 Hz, we find no temporal patterns attributed to volcanic activity. We provide additional clustering results in Figures B.1-B.7

To retrieve stable dv/v estimates for shorter periods, we apply the trace stretching algorithm to *all CFs* in time periods dominated by one (e.g., August 2015 to November 2015, April 2016 to July 2016, see Figure 4.3 (b)) or, in some cases, two clusters (time windows at the turn of the year, see Figure 4.3 (b)). Thus, instead of using CFs from only one cluster per dv/v estimation, we use all CFs for a given period. Applying interferometry to only one cluster could introduce a bias if the clustering algorithm splits the dataset due to changes in the medium (i.e., stretching of the CF), which we want to retain and analyse in PII, rather than changes in noise characteristics. For a much longer continuous dataset at Piton de la Fournaise, A. Yates et al. (2023) show that changes in the medium alter the dominant cluster permanently, whereas changes in the noise wavefield only lead to temporary variations. However, for the times available to us at KVG, making such an evaluation is challenging since varying tremors, which commence in late November 2015, last throughout the whole study period (Journeau et al., 2022).

For each period, we use the average CF as reference correlation function to measure changes in wave velocity. The same segments are chosen for all stations and station groups. In the following, we will refer to our described method as *time-segmented passive image interferometry (TSPII)*. We provide a complete overview of the chosen time segments in Table B.2.

An obvious drawback of TSPII is that it fails to track long-term changes of dv/v. Gómez-García et al. (2018) used data from lower, less tremor-affected frequencies to compute long-term velocity changes. For higher frequencies, however, the modifica-

tions in the noise wavefield will induce changes in the spatial sensitivity between the subsequent time segments. Therefore, the time segments quantify dv/v in different locations and they cannot be set in context to each other.

4.3.4 Spatial Stacking of Sequenced dv/v Time Series

Applying passive image interferometry to the selected time windows yields several dv/v time series, of which many show a significant amount of fluctuations that we regard as measurement noise. One strategy to stabilise the measurements is to apply smoothing in the time domain, as is commonplace in PII studies. In our case, however, this would degrade the time resolution and limit the usefulness of the already relatively short dv/v time series resulting from the time segmentation.

Statistical noise in dv/v measurements can be reduced by applying spatial stacking over results from several stations (Illien et al., 2023). We stack the similarity matrices that the trace stretching algorithm yields (see equation 3.5). Subsequently, we pick the location of the maxima on the stacked similarity matrix to find the apparent homogeneous velocity change. In comparison to directly averaging the dv/v time series, this strategy has the advantage that unstable estimates with low correlation coefficients are down-weighted. On the flip side, the non-linear nature of the stack makes it challenging to quantify uncertainties and the contribution of different areas to the obtained velocity changes. Due to the ergodic nature of ambient seismic noise, one faces a decision between temporal and spatial resolution by opting for a more aggressive smoothing in either domain to reach the same stability (Illien et al., 2023). As we are looking for rapid responses of the subsurface to volcanic processes in rather short dv/v time series, we opt for a high resolution in time rather than in space with two-hour increments and four-hour smoothing windows. We point out that the stacked correlation coefficient will almost always be lower than the correlation coefficient found from individual stations. To make a clear distinction between

the two, we refer to the stacked correlation coefficient as the *cumulative correlation coefficient (CCC)*.

When stacking similarity matrices, we need to find sites with similar velocity changes. Due to significant variations in topography and geology from site to site, these are not necessarily stations that are laterally closest to each other. To identify such stations, we employ an approach that combines visual inspection of the individual dv/v time series and a sequencing algorithm. Visually, we find that stations with a similar elevation and similar geology have similar dv/v curves for all examined frequencies (i.e., 0.5-8 Hz). To confirm this impression with an AI approach free of human bias, we use the TheSequencer algorithm (Baron & Ménard, 2021), which, in contrast to Ward's linkage algorithm, can quantify the distance between multi-dimensional data points (i.e., matrices). We chose the similarity matrices of each self-correlation from time segment 2015/07/01-2015/12/01 as our input data points. The algorithm then uses the Kullback-Leibler divergence and the Euclidean distance between the data points to find how the data is distributed in an N-dimensional space and sorts them by their respective distance. The closer two given data points are in said sequence, the more similar they are. We visualise the output of the algorithm in Figure 4.4 (a). As one should expect, results from correlations from different component combinations of the same station are close in the sequence in almost all cases (in the plot, circles on top of each other). Furthermore, the algorithm reveals a very similar pattern to our qualitative evaluation; it evaluates responses of stations around the KVG with high elevation as similar, whereas stations in the Central Kamchatka Depression (CKD), the regional sedimentary basin, and on the eastern ridge (ERidge) plot in different groups. Based on the resulting sequence, we decided to stack similarity matrices in the five groups shown in Figure 4.4 (b).

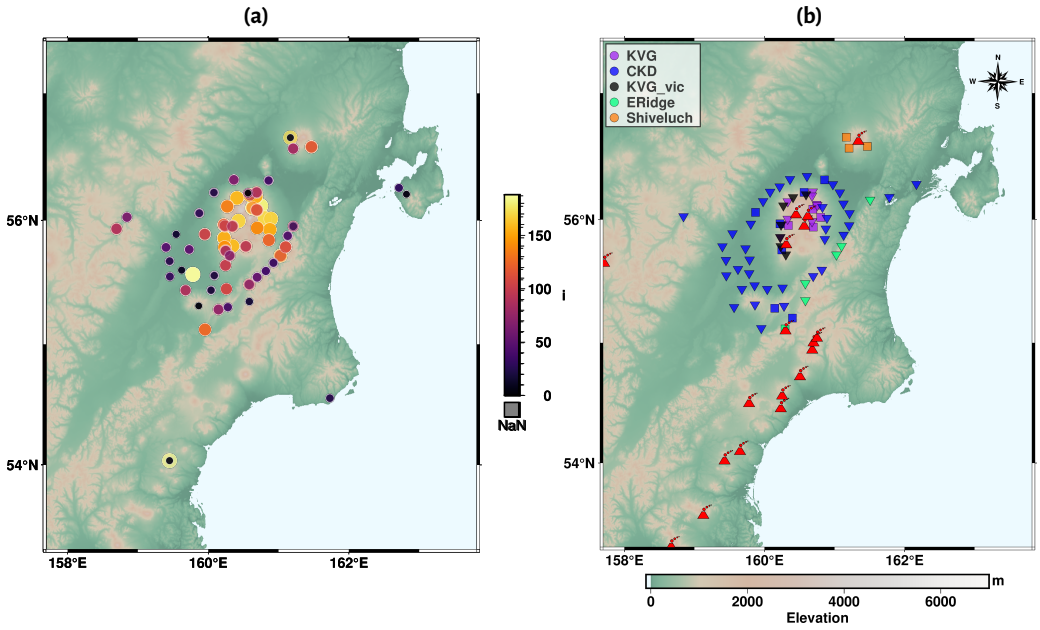

Figure 4.4: **(a)** The output of TheSequencer (Baron & Ménard, 2021). The closer two data points are in the sequence (i.e., similarly coloured and similarly sized circles) the more similar the algorithm deemed their dv/v responses as given by the similarity matrices. Note that data points in the sedimentary basin, on the KVG, and on the ridge in the East tend to build subgroups. **(b)** Groups that we use for the spatial stacking. Based on the results shown in panel (a) and on visual inspection of the dv/v time series, we divide our dataset into 5 subgroups. Each colour corresponds to a different subgroup. Inverted triangles represent stations belonging to the temporary KISS experiment, whereas squares are the locations of permanent stations. Note that we disregard some stations due to low data availability. We depict the locations of volcanic centres active during the Holocene. KVG: Klyuchevskoy Volcanic Group, CKD: Central Kamchatka Depression, ERidge: Eastern Ridge, KVG_vic: stations in the vicinity of the KVG.

4.4 Velocity Changes at the KVG

Using the method outlined above, we compute dv/v time series stacks for frequencies above 0.5 Hz, where volcanic tremor energy is generally very high (see Figure 4.2 (a)). For frequencies below 0.5 Hz, the statistical variation exceeds the amplitude of physical velocity changes over one year, even after introducing an aggressive temporal smoothing with a window length of 30 days. To remove these statistical variations and obtain interpretable results from these frequencies, we would require a longer continuous dataset. The most stable results were obtained from the averages of auto- and self-correlations of all components from the stations of each of the groups shown in Figure 4.4.

Figure 4.5 shows the estimated velocity variation for the station group CKD from July 2015 to December 2015 for 4-8 Hz. We set these in context to precipitation, snow depth, and large regional earthquakes. In addition, we provide the time-averaged lava discharge rate (TADR) for Klyuchevskoy and Bezymianny that Coppola et al. (2021) estimated from satellite data. Most notably, we can see a significant temporal correlation between precipitation events and drops in seismic velocity (e.g., in early September), followed by periods of velocity recovery. When precipitation comes in the form of snow (i.e., is accompanied by an increase in snow load) as on 19 October (feature 1, marked by an arrow), decorrelations (i.e., decreases in the CCC) occur. From late October, the temperatures remain below freezing and the snow load increases. Simultaneously, dv/v exhibits an almost monotonously increasing trend. For most earthquakes, we identify no correlated changes in dv/v - except for an event on 18 September that seems to be accompanied by a slight velocity increase (feature 2, cf. Section 4.5.2 for a thorough discussion of the impact of seismic events on dv/v). We do not identify any correlation between the seismic velocity and the TADR in Figure 4.5 or any of the following figures.

Similarly to Figure 4.5, we show a selection of dv/v results, climatological, and

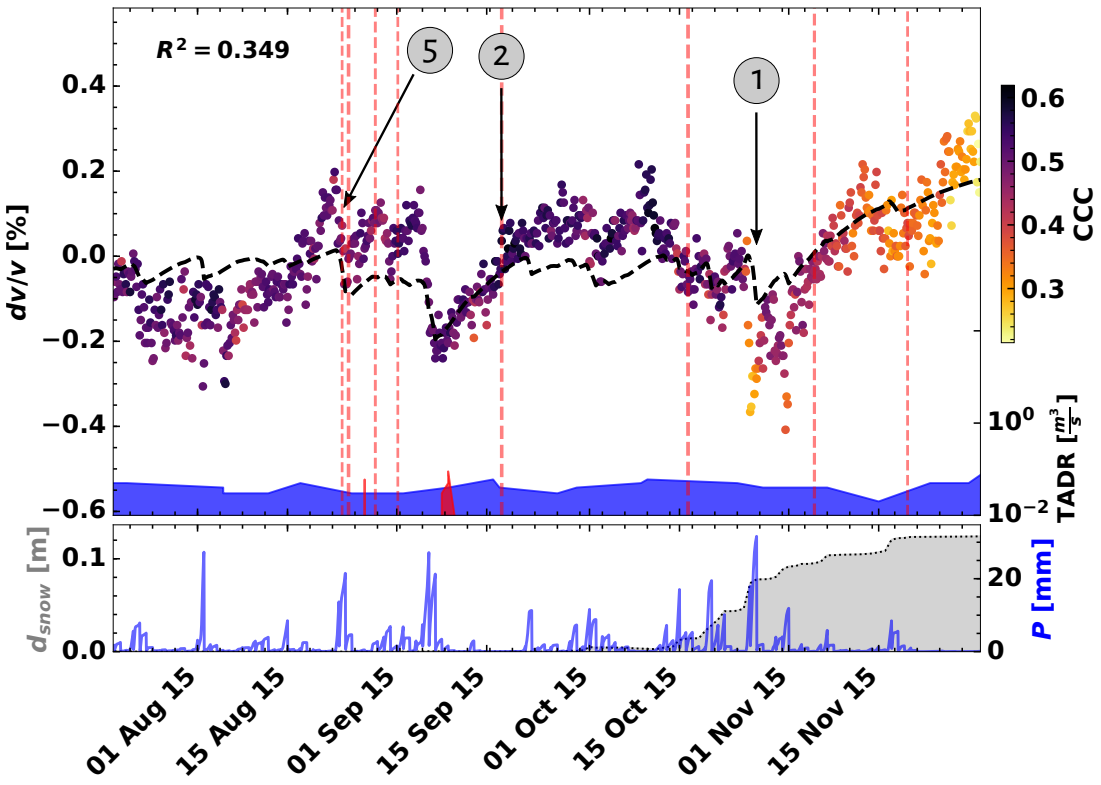

Figure 4.5: Velocity change for the station group CKD (see Figure 4.4) created from auto- and self-correlations between all components for 4-8 Hz. We show dv/v estimates as circles with colour scaling dependent upon the cumulative correlation coefficient (CCC) (see text body for details). Each point represents a time window of four hours, at two hours intervals. Red dashed lines mark the origin times of regional earthquakes with magnitudes≥4.8. The dv/v model is given by the black dashed line, the corresponding coefficient of determination (R^2) is shown in the upper left corner of the large tile. The time-averaged lava discharge rate (TADR) for Klyuchevskoy and Bezymianny are plotted logarithmically at the bottom of the plot in red and blue, respectively (Coppola et al., 2021). In the small tile below, we show values for snow depth d_{snow} (grey) and hourly precipitation P (blue) averaged over the region. Both values are given in water-equivalent. Note that, particularly for these high frequencies, dv/v shows strong responses to changes in precipitation and snow load. Our dv/v model (see Section 4.5.1) is able to reproduce these changes on a first order. Features 1, 2, and 5 marked with arrows are discussed in the text body.

volcanological data from a set of groups and time windows in Figure 4.6, but for 2-4 Hz. As before, we note velocity reductions at times with high precipitation (e.g., Figure 4.6 (d) feature 3). In Figures 4.6 (b), (c), and (d), we find that the velocity reductions over the respective periods coincide with a decrease in snow load, whereas, in Figure 4.6 (a), both snow load and velocity show an increasing trend. While these weather-driven effects are less obvious on inter-station correlations, they are nonetheless visible (see Figures B.27-B.44). In Figure 4.6 (c), we see a low correlation coefficient at the beginning of the time window, which coincides with the change in noise source dominance reflected by a shift from cluster 1 to 0. Consequently, we attribute it to an effect introduced by a change in wavefield properties. On 30 January 2016, the Magnitude 7.2 Zhupanov earthquake struck Kamchatka south of the network. Simultaneously, a sharp velocity decrease occurred at almost all station groups and frequencies (see Figure 4.6 (a) feature 4). We show a more extensive selection of dv/v results for various time windows, frequencies, and regions in Figures B.9-B.44, including results from cross-correlations (i.e., inter-station). In the following section, we elaborate on the hydrological, meteorological, seismic, and volcanic forcing that causes velocity changes and discuss the impact of each respective mechanism on the different study sites.

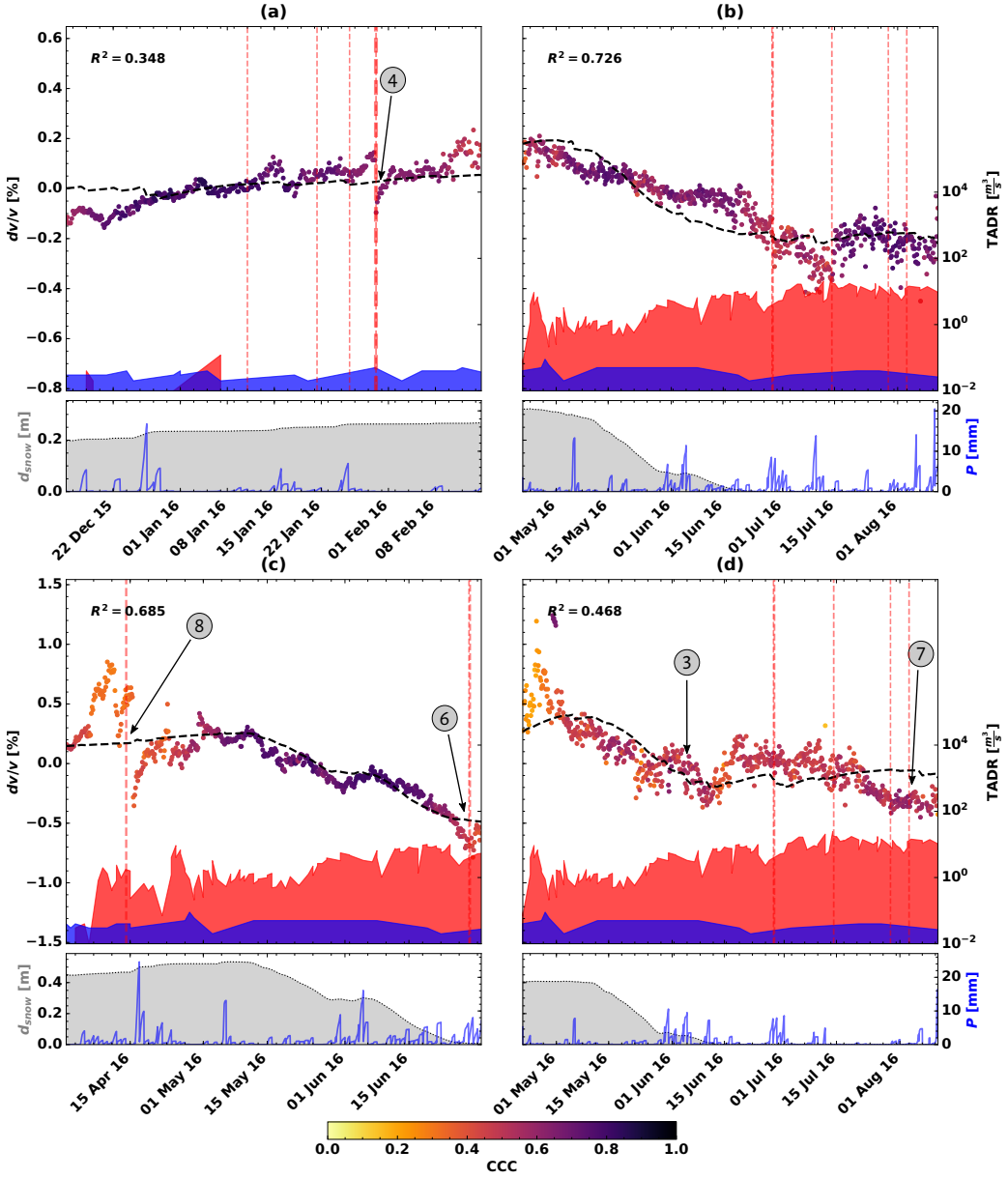

Figure 4.6: Velocity change estimates for different station groups and time intervals for 2-4 Hz. Refer to Figure 4.5 for an explanation of the plot's details. **(a)** Region KVG_vic, time window from 2015/12/15 to 2016/02/15. Bold dashed line marks the 2016/01/30 M7.2 Zhupanov earthquake. **(b)** Region CKD, time window from 2016/04/22 to 2016/09/01. **(c)** Region KVG, time window from 2016/04/01 to 2016/07/01. **(d)** Region Shiveluch, time window from 2016/04/22 to 2016/09/01. Locations of the stations belonging to each of the regions can be found in Figure 4.4 (b).

4.5 Discussion of Physical Mechanisms Causing Velocity Changes

After demonstrating how velocity changes can be computed from data with challenging noise conditions and noting that the dv/v variations exhibit strong correlations to weather data, we discuss physical mechanisms related to meteorological events, seismic events, and volcanic events that induce or could induce the observed dv/v variations and, in particular, have a closer look at velocity changes that do not coincide with precipitation or changes in the snow cover. The impact on dv/v of these mechanisms has been reported by other studies before. Observing them with our method gives confidence that the dv/v time series resulting from TSPII are sufficiently robust to contribute to environmental and volcanological monitoring.

Since we focus on velocity changes obtained from frequencies > 2 Hz and examine earlier parts in the coda, we mainly interpret velocity changes down to about 350 m (Obermann, Planès, Larose, Sens-Schönfelder, & Campillo, 2013; Obermann et al., 2016), assuming a surface wave velocity of 1 $\frac{\text{km}}{\text{s}}$ (Green et al., 2020). Surface waves of the lowest analysed frequency of 0.5 Hz are sensitive to velocity changes down to about 1300 m.

4.5.1 Climatic and Meteorological Variations on Kamchatka

In Section 4.4, we already denoted a clear anti-correlation between precipitation and dv/v. Such an anti-correlation has been observed since the dawn of PII and was explained by an increased pore pressure resulting in a reduction of the shear wave velocity v_S (e.g., Andajani et al., 2020; Donaldson et al., 2019; Feng et al., 2021; Q. Y. Wang et al., 2017). As we examine high frequencies, we are particularly sensitive to changes in the shallow subsurface (Obermann, Planès, Larose, Sens-Schönfelder, & Campillo, 2013), which contains the vadose zone that is constantly subject to

groundwater recharge and drainage cycles resulting in the observed velocity drop and recovery patterns.

However, in our case and for other observations in temperate and cold environments, this mechanism can only explain precipitation in the form of rain. In large parts of the year (i.e., approximately between October and May), temperatures are below freezing. Consequently, precipitation occurs as snowfall, leading to the accumulation of a compacting snow layer. This added layer would alter the scattering properties of the medium in addition to the induced shear wave velocity change and, consequently, introduce a decorrelation (Guillemot et al., 2021; Obermann, Planès, Larose, & Campillo, 2013) as observed after periods of heavy snowfall (e.g., Figure 4.5 feature 1).

Guillemot et al. (2021) observed velocity drops, which they attributed to the build-up of a low-density and low-rigidity snow layer. In contrast to them, we see clear signs of a positive long-term correlation of overall snow load with dv/v (c.f. Hotovec-Ellis et al., 2014; Q. Y. Wang et al., 2017). In our case, the relationship appears remarkably linear aside from previously discussed immediate effects of snowfall. We explain the relationship by invoking a loading mechanism, i.e., an increased surface loading due to the snow mass (Heki, 2001; Silver et al., 2007) that results in a pore space reduction and closure of cracks leading to compaction of the snow and soil layers. In addition, the snow and ground frost might act as a seal that blocks groundwater recharge. Conversely, during spring, the seismic velocity decreases rapidly due to a decrease in load and groundwater recharge from meltwater and an associated opening of cracks (Gassenmeier et al., 2015; Guillemot et al., 2021). While most studies find that the velocity increases with increasing snow load, Taira and Brenguier (2016) observed a velocity decrease, which they explain by an increase in pore fluid diffusion.

Modelling dv/v

We use snow load and precipitation to create a simple model for the evolution of the seismic velocity at the various sites. In our model, dv/v depends bilinearly on the two environmental parameters. We express dv/v as:

$$\frac{dv}{v}_{syn} = aP * f(\tau) + bd_{snow} + \gamma \tag{4.1}$$

where P is the precipitation in m (water equivalent), d_{snow} is the snow thickness in m (water equivalent), and a, b, and γ are constants that we determine for each of the four octave frequency bands between 0.5-8 Hz and each station group. Akin to Sens-Schönfelder and Wegler (2006) and Hillers et al. (2014), we define a filter function $f(\tau)$ that we convolve (denoted as $*$) with the precipitation to model the drainage after each precipitation event. We define $f(\tau)$ in agreement with Darcy's law as a decaying exponential function that varies between 1 and 0:

$$f(\tau) = \begin{cases} 0 & \forall \tau \in (-\infty, 0) \\ \exp^{-\tau/\lambda} & \forall \tau \in [0, \infty) \end{cases} \tag{4.2}$$

where τ is the lag time (i.e., the time that has passed since the precipitation event) and λ is the decay.

To invert for a, b, γ, and λ, we employ a least-squares inversion that optimises a cost function to minimise the misfit between dv/v_{syn} and dv/v. For a and b, we jointly invert for all time windows using data from one station group and each octave frequency band. For the offset γ, we perform a separate inversion for each time window. We determine λ to be optimal for the whole dataset at λ=10 days. As expected, the magnitudes of a and b are higher for 2-8 Hz than for lower frequencies indicating that precipitation and snow load have a higher impact on the velocity of shallower layers. We do not identify clear trends in a and b for the different station groups (see Figure B.8).

We show dv/v_{syn} as a black dashed line in Figures 4.5 and 4.6. Additionally, we provide the coefficient of determination R^2 for each time window as an objective measure to evaluate the fit of our model. R^2 reaches a value of 1 for a perfect fit, $R^2 = 0$ implies that the model has the same fit as the mean of the data points, and values below 0 have a fit worse than the mean. We achieve the highest R^2 values for times dominated by strong precipitation and changes in snow load (e.g., Figure 4.6 (a), (b), and (c), whereas, for dv/v curves that are strongly affected by mechanisms that our model does not take into account (e.g., earthquake damage, Figure 4.6), we obtain lower R^2 values.

Despite its simplicity, our model reproduces first-order trends of the dataset reliably. For lower frequencies between 0.5 and 2 Hz, it generally performs worse with R^2 values around 0 than for the higher frequencies, probably due to higher scatter in the dv/v data points in those low-frequency velocity change estimates (see Figures B.9-B.44). In addition, estimates from lower frequencies are not affected much by environmental mechanisms. Instead, lower frequencies sample deeper parts of the medium (Obermann, Planès, Larose, Sens-Schönfelder, & Campillo, 2013) whose velocity is not as strongly influenced by meteorological events (Donaldson et al., 2019). During times with relatively constant snow load, the model underestimates the velocity increase leading to lower R^2 values (see Figures 4.6 (a) and B.9-B.44) potentially because we do not model snow compaction.

We could increase the fit of our model by adding the influence of non-environmental effects such as ground shaking, employing separate models for rain and snowfall, adding the influence of snow compaction, utilising a more complex model for snow layer thawing that accounts for the sudden availability of melt water, or taking thermal stress into account (Hillers et al., 2015). However, the model accuracy is limited by (1) the limited spatial resolution of satellite weather data (Tang et al., 2020) as ground measurements are unavailable to us and (2) the fact that we compare lin-

ear stacks of environmental data with non-linear stacks of dv/v measurements. The latter factor becomes especially important when the temperature is close to freezing or thawing so that freezing, snowfall, rain, and thawing could occur out of phase at stations belonging to one group of stations.

4.5.2 Impact of the 2016/01/30 Zhupanov Earthquake

Due to the subduction of the Pacific Plate below Kamchatka (Yogodzinski et al., 2001), the region is regularly shaken by large earthquakes, which are generally known to induce velocity changes (e.g., Brenguier, Campillo, et al., 2008). In our results (Figures 4.5, 4.6, and S10-S45), we show the origin times of regional earthquakes with magnitudes larger than 4.8. For most of these events, the impact on dv/v remains either unclear due to coincident events of precipitation (e.g., Figure 4.5 - feature 5 or feature 6 in Figure 4.6 (c)) or vanishes below the noise level (feature 7 in Figure 4.6 (d)). The seismic event marked as feature 8 in Figure 4.6 (c) illustrates the importance of examining all potential parameters that might influence dv/v. Shortly, though not immediately, after the earthquake, we measure an abrupt velocity drop of almost 1 % that, on first look, seems to be associated to the earthquake. However, the velocity decrease has a higher temporal correlation to the precipitation event occurring about 12 hours after the earthquake. Due to the high temporal resolution of the dv/v estimates, we can observe a few unaffected values after the earthquake and a rather sudden decrease coincident with the onset of a strong precipitation event. Therefore, we consider it the likelier cause for the observed velocity drop.

The largest seismic event during our study period is the M7.2 Zhupanov earthquake that struck on 30 January 2016 in the South of the peninsula about 250 km from Klyuchevskoy with a hypocentral depth of 177 km (see Figure 4.7). The earthquake-induced sudden velocity drops range between 0.1 and 0.5 % across our network (Figure 4.6(a) feature 4 and Figures B.15-B.17). We determined the peak

ground velocity (PGV) from the horizontal components of all active stations and show the result in Figure 4.7 (a). As expected, we find a higher PGV in the CKD due to low shear wave velocities and its location closer to the epicentre (i.e., in the South). We then computed the ratio of the PGV and observed velocity drop, which we define as the difference between the average of the five data points (i.e., 12 h) prior to and after the event's origin time, respectively (see Figure 4.7 (b)). Most notably, station groups KVG and Shiveluch exhibit remarkably high $\frac{dv/v}{PGV}$ ratios, indicating a high sensitivity to the co-seismic shaking. These two station groups correspond to the stations located high up on the volcanic edifices of the Klyuchevskoy/Bezymianny massif and Shiveluch, respectively. ERidge, combining stations on the mountain range in the East, on the other hand, shows the lowest $\frac{dv/v}{PGV}$ ratios.

Previous studies have observed dv/v drops in volcanic areas that exceed these in neighbouring areas by two or three times (Brenguier et al., 2014; Lesage et al., 2014). Lesage et al. (2014) observed a marked velocity drop at Volcán de Colima induced by the M7.4 Tecomán earthquake that struck about 140 km from the volcano. Regarding the magnitude and epicentral distance of the earthquake, their case is very similar to the one we observe in Kamchatka. They invoke material softening due to the pronounced non-linear elastic response of rocks with high porosity and pore space saturation - such as unconsolidated volcanic material (Johnson & Jia, 2005; Van Den Abeele, 2002). Brenguier et al. (2014) found that the M9.0 Tohoku-Oki earthquake induced higher velocity changes in active volcanic regions and ascribed this observation to the presence of pressurised fluids in the pore space amplifying the non-linear response even under increased confining pressure at depth.

For Kamchatka, tomography revealed high $\frac{v_P}{v_S}$ ratios in shallow regions below the KVG, indicating a high water content in sediments of the CKD and in the volcanic edifices (Green et al., 2020; Ivanov et al., 2016; Koulakov et al., 2017, 2021). Also, the presence of hydrothermal reservoirs is well documented (e.g., Kiryukhin et al., 2012;

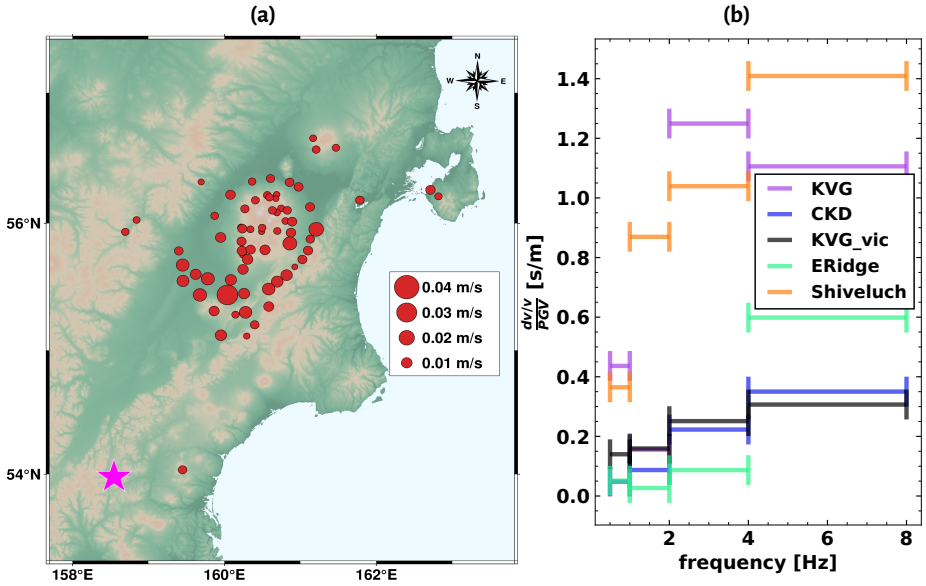

Figure 4.7: **(a)** Horizontal PGVs recorded during the M7.2 Zhupanov earthquake. The circles mark stations active on the day of the event, with their diameters scaling with the PGV. We plot the epicentre of the Zhupanov earthquake as a star. **(b)** Corresponding $\frac{(dv/v)}{PGV}$ ratio for the different groups of stations and the examined frequency bands. The volcanic regions (Shiveluch and KVG) exhibit particularly high ratios.

Taran, 2009), for which a higher sensitivity to ground shaking was observed (e.g., Caudron et al., 2022; Chaves & Schwartz, 2016; Taira & Brenguier, 2016). However, Shiveluch is not equally well studied and only few images exists that, contrary to the implication of the higher $\frac{dv/v}{PGV}$ ratio at the highest frequencies, show a high $\frac{v_P}{v_S}$ zone that is slightly deeper than the one under the KVG (Koulakov et al., 2020; Koulakov, 2021). This could either be an indication that additional seismic data around Shiveluch are required to improve our understanding of the crustal structure below Shiveluch or simply be within the uncertainty of our data - particularly around Shiveluch, where the station coverage is lower.

Generally, the non-linear stress-strain behaviour of rocks appears to depend on material inhomogeneities, such as pores, cracks, or matrix/clast distribution that lead to the formation of force chains and a concentration of stress at "stability bridges" in the material (Sens-Schönfelder et al., 2019) . Volcanic rocks are highly heterogeneous (Schaefer et al., 2015), therefore, we expect a significant contribution of non-linear elasticity to the observed dv/v response. However, based on this discussion, we suspect that both elastic non-linearity and the presence of fluids in the pore space contribute to the pronounced velocity reduction at the KVG and Shiveluch. We expect that the magnitude of the contribution of each of these factors depends on the pore space saturation (or pressurisation) at the time of shaking. In practice, that could mean that volcanoes with higher pressurisation are more susceptible to ground shaking (as proposed by Brenguier et al., 2014). In the present case, we neither observe nor expect significant differences in pressurisation between Shiveluch, Klyuchevskoy, and Bezymianny because they are fed by the same magma system (e.g., Koulakov, 2021) and had recent eruptions (i.e., $<$ 10 yrs before the data collection).

4.5.3 Influence of Volcanic Activity

A previous study by Coppola et al. (2021) has revealed a complex relationship between the major volcanoes of the KVG and a potential modulation by tectonic triggers. At Klyuchevskoy and Bezymianny, a period of unrest commenced in 2016, accompanied by eruptive activity (Journeau et al., 2022; Mania et al., 2019, 2021). For Bezymianny Volcano, Mania et al. (2019) found signs of an extrusion onset in early 2016, which is why we focus on stations in Bezymianny's vicinity. Unfortunately, stations D0.BZM, D0.BZW, X9.B07, X9.B08, X9.SV8, and X9.SV9 on the volcanic edifice failed in late 2015 and early 2016 leading to a lower spatial sensitivity, but permanent station D0.BZG near the summit was fortunately operational throughout this episode and delivers stable dv/v estimates.

Satellite synthetic aperture RADAR (SAR) offset tracking reveals the first evidence of a starting plug extrusion at Bezymianny between January and April 2016 (see Figure 4.9, and Mania et al., 2019). With an intermittent uplift but almost continuously increasing uplift rate, the average crater offset reached about 1.5 meters on 16 February 2016. With 4 hours, the dv/v time series presented in Figure 4.8 affords a significantly higher time resolution than the SAR data provided in Figure 4.9, which has a maximum resolution of 11 days. From the dv/v time series, we estimate a gradual velocity increase of about 0.3 % at D0.BZG initiating around 6-7 February, which we interpret as an expression of deeper medium changes associated with the surface deformation estimated by pixel offset. In conjunction with the velocity increase at BZG, we find a decorrelation (i.e., a decreasing CCC) at several stations surrounding Bezymianny (see Figure 4.8). The velocity increase at BZG exceeds the effects of snow compaction and damage recovery observed at all the other stations and is significant with respect to the short-term fluctuations.

Many studies linked volcanic inflation to dv/v decreases rather than increases (e.g., Brenguier et al., 2011, 2016; De Plaen et al., 2016, 2019; Machacca-Puma et

al., 2019; Takano et al., 2017). However, local velocity increases could occur if a shallow magma, gas, or hydrothermal reservoir, as it may exist beneath Bezymianny (Ivanov et al., 2016; Koulakov et al., 2017, 2021), inflates and, thereby, causes local compaction through increased pressure (Caudron et al., 2021, 2022; Donaldson et al., 2019; Donaldson et al., 2017; Hotovec-Ellis et al., 2015; A. S. Yates et al., 2019). Our hypothesis is further supported by a recently published study by Berezhnev et al. (2023), who found increasing velocities at Bezymianny immediately before its 2017 eruption. They modelled the mechanical deformation associated with the observed velocity changes and concluded that an inflating shallow reservoir is the most likely cause for the changing velocity.

A combination of localised velocity increases and decreases in the vicinity of Bezymianny, as expected to arise from a shallow pressure source (Donaldson et al., 2017), would also lead to decreasing correlation. As with any inhomogeneous velocity change, these decreases and increases would cause the shapes of the correlation functions (CFs) to alter significantly, resulting in a decorrelation. Alternatively, the observed decorrelation could have resulted from other modulations of the scattering properties of the subsurface due to incipient deformation of the volcanic edifice (Obermann, Planès, Larose, & Campillo, 2013).

The closely spaced occurrences of the Zhupanov earthquake, the detected velocity increase at BZG, and the proposed initiation of Bezymianny's eruptive cycle (Mania et al., 2019) are noteworthy. It raises the question of whether Bezymianny's 2016/2017 eruption was tectonically triggered as reported in some rare cases (D. P. Hill et al., 2002; Kennedy, 2017; Seropian et al., 2021; Walter & Amelung, 2007; Watt et al., 2009). However, based on the currently available data, we would consider such conclusions speculative.

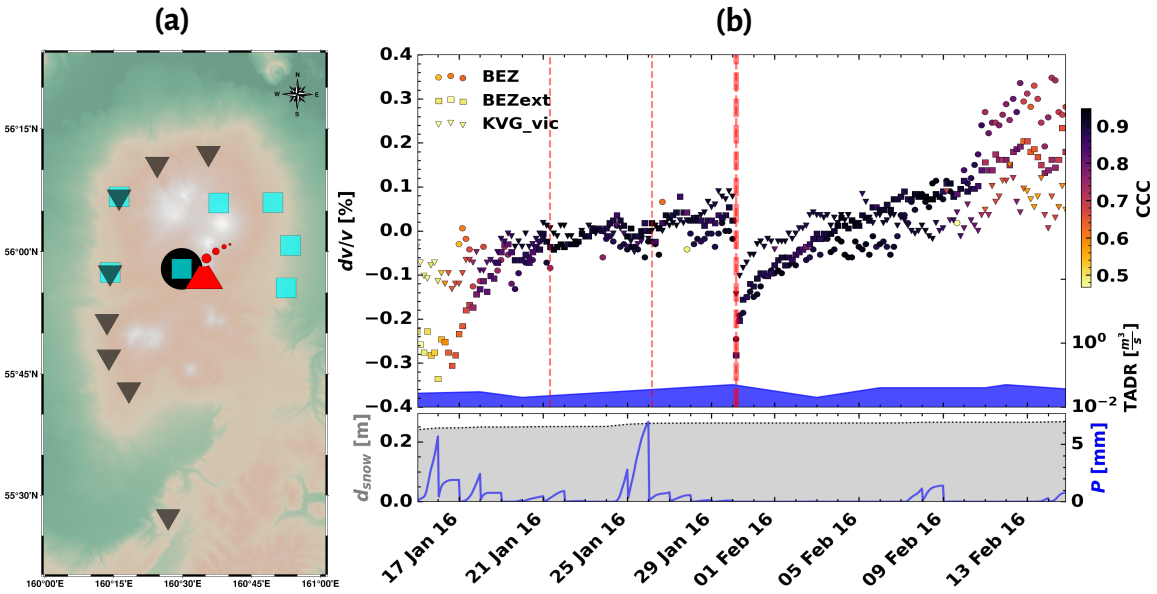

Figure 4.8: **(a)** Definition of the station groupings used in (b). **(b)** Evolution of the seismic velocity as computed from auto and self-correlations between 2016/01/15 and 2016/02/15 close to Bezymianny Volcano at 2-4 Hz. We show dv/v estimates as coloured symbols (matched with symbols in (a)) with colour scaling dependent upon the CCC. Each point represents a time window of two hours. Red vertical dashed lines mark the origin times of regional earthquakes with a magnitude≥4.8. The bold dashed line marks the 2016/01/30 M7.2 Zhupanov earthquake. The time-averaged lava discharge rate (TADR) of Bezymianny is plotted logarithmically in blue. In the lower panel, we show precipitation and snow load data in water equivalent averaged over all locations of the station group KVG_vic. Towards the end of the time window, we measure an especially strong increase of the seismic velocity at station D0.BZG (circles). Simultaneously, we see a decorrelation at all shown groups.

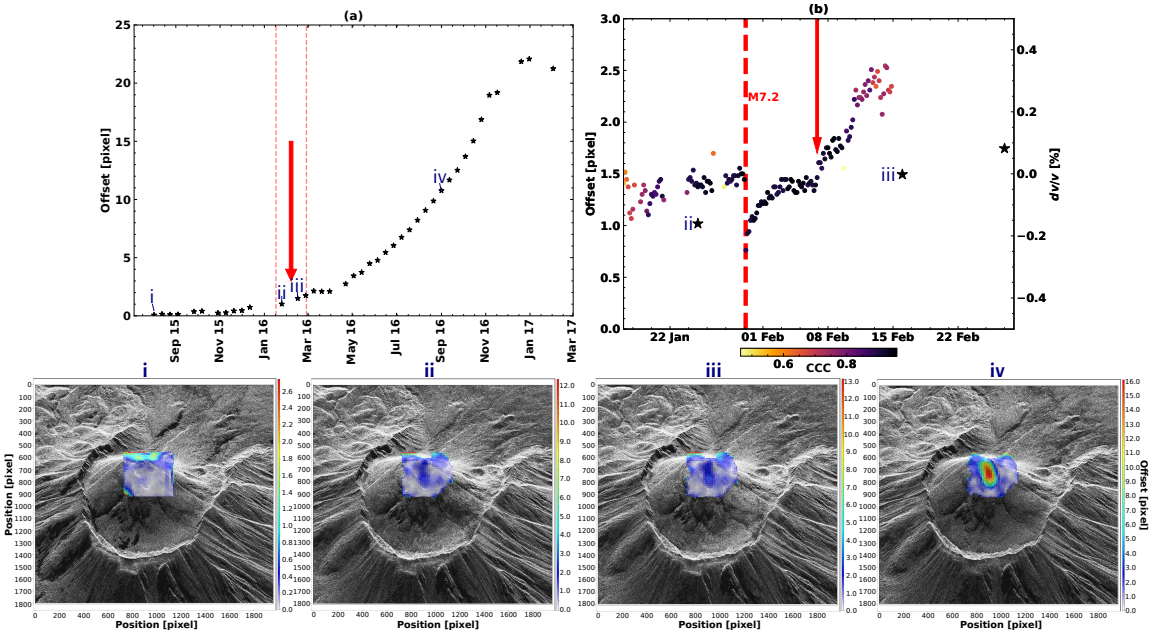

Figure 4.9: **(a)** Pixel offset values obtained from a reanalysis of the SAR dataset by Mania et al. (2019) (plotted as stars). The shown values are means over a 16x16 pixel area around Bezymmiany's summit. On average, one pixel covers an area of about 1 m^2. **(b)** A zoom on (a) as marked by the red dashed lines. We superimposed dv/v between 2 and 4 Hz at D0.BZG with the points' colour scale depending upon the CCC. The red dashed line labelled "M7.2" marks the origin time of the M7.2 Zhupanov earthquake. In (a) and (b), the red arrow marks the initiation of the observed velocity increase in the evening of 6 February 2016 (UTC). In the bottom row, we show the SAR images with a colour-scaled pixel offset overlay for the four different times, i-iv, marked in (a) and (b).

4.6 Conclusions

4.6.1 Time-Segmented Passive Image Interferometry for Fluctuant Noise Fields

For data from the Klyuchevskoy Volcanic Group (KVG), established preprocessing strategies and passive image interferometry (PII) algorithms were not sufficient to produce stable velocity change estimates for high frequencies ($>\sim 1\,\mathrm{Hz}$) and fine temporal resolutions ($<\sim$1 week) as needed to understand the effect of several forcing mechanisms operating at these and lower time scales. In this chapter, we demonstrate that PII is feasible even in the presence of pronounced, long-lasting fluctuations of the noise wavefield if one applies the time-segmented passive image interferometry (TSPII) technique, as proposed here. We utilise a hierarchical clustering algorithm to find time windows with temporarily stationary noise fields suitable for separate PII surveys. Subsequently, we spatially average the results to increase the temporal resolution even further.

In its current form, TSPII is best suited for settings where the noise field has several distinct "modes", e.g., spatially stable noise sources, which stay active or inactive over extended periods. Therefore, it is particularly well-suited for volcanic environments with long-lasting phases of tremor activity. In cases with sporadic, rapid shifts, approaches based on filters are more likely to be successful.

4.6.2 Evolution of the Seismic Velocity at the Klyuchevskoy Volcano Group

After applying TSPII and spatial averaging, we present velocity change observations for Kamchatka from five different regions for five time segments and various frequency bands. When analysing the velocity changes, we find dominant forcing from

environmental factors. We analyse dv/v time series computed from high-frequency data ($> 2\,\mathrm{Hz}$), which exhibits a lower noise level and a higher resolution than the time series from lower frequencies ($< 1\,\mathrm{Hz}$). High frequencies are particularly sensitive to pore pressure changes in the shallow subsurface. The pore pressure, in turn, is strongly impacted by precipitation leading to immediate short-term velocity decreases following precipitation events. In contrast, increasing snow depth causes a velocity increase. These findings again emphasise the value of PII in monitoring the vadose zone, which is a vital component for groundwater recharge and drainage cycles. Monitoring groundwater levels is especially critical in regions with little precipitation or strongly pronounced dry seasons. To these ends, PII provides a low-cost, non-invasive method that probes the vicinity of the station rather than only a single spot as a well would. We present a simple model that relates snow load and precipitation to the seismic velocity reproducing first-order variations in dv/v.

In addition to environmental events, we find impacts of tectonic events - first and foremost, the M7.2 Zhupanov earthquake, which leads to high-amplitude damage-induced velocity drops across the network with subsequent recovery. The amplitude of said velocity drop is not solely dependent on the strength of the ground shaking, which we quantify by computing the peak ground velocity. Instead, we find that volcanic regions (i.e., the KVG and Shiveluch) are more sensitive to ground shaking and experience more pronounced velocity drops. For Kamchatka, we explain this unusually high dv/v response with the non-classical non-linear behaviour of the volcanic rock, possibly amplified by the high fluid contents in the pore space.

Lastly, we see a marked velocity increase accompanied by a decorrelation of the noise correlation functions at Bezymianny Volcano commencing 6-7 February 2016, shortly after the Zhupanov earthquake. The velocity increase occurs together with a first uplift marking the beginning of the 2016/2017 eruption cycle (Coppola et al., 2021; Mania et al., 2019, 2021). We argue that the inflation of a shallow gas,

magma, or hydrothermal reservoir could cause localised velocity increases and decreases. This inhomogeneous velocity change combined with the deformation of the volcanic edifice would lead to the observed apparent homogeneous velocity change close to the deformation and a net-zero velocity change in the far-field, concurrently inducing the decorrelation at all locations. Our study, once again, demonstrates that passive image interferometry is a valuable tool for monitoring volcanic deformation, possibly in near real-time and with a denser temporal sampling than, for example, satellite-based techniques could resolve.

4.7 Open Research

The KISS dataset (N. Shapiro et al., 2015, doi:10.14470/K47560642124) is openly available via the GFZ Data Services. Access to the data recorded by the D0 seismic network is restricted but can be obtained via the GFZ Data Services. The ERA5 climate data (Hersbach et al., 2020, doi:10.24381/cds.e2161bac) are available upon registration at https://cds.climate.copernicus.eu/cdsapp#!/dataset/10.24381/cds.e2161bac?tab=overview. The TADR datasets are provided as supplementary material to Coppola et al. (2021). All TerraSAR-X data are available through the German Aerospace Centre (DLR). The origin times of the seismic events plotted in Sections 4.4 and 4.5 can be queried via the USGS FDSN web service. The seismic data download and the computation of correlations and dv/v were executed using SeisMIC 0.1.28 (Makus & Sens-Schönfelder, 2022, doi:105880/GFZ.2.4.2022.002), available under the EUPL license agreement at https://github.com/PeterMakus/SeisMIC. TheSequencer algorithm (Baron & Ménard, 2021) that we used to sort the similarity matrices of the stations can be executed online at http://sequencer.org, its source code can be downloaded at https://github.com/dalya/Sequencer. TheSequencer is licensed under the MIT license agreement. All maps were plotted using PyGMT

(Uieda et al., 2021). For Figures 4.1(a), 4.4, and 4.7(a), we used the SRTM15+ digital elevation model (DEM) by Tozer et al. (2019). For Figures 4.1(b) and 4.8(a), we obtained the SRTMGL1 DEM from (Kobrick & Crippen, 2017).

CHAPTER 5

Long-Term Monitoring of the Spatiotemporal Evolution of the Seismic Velocity:

An Application to the Mount St. Helens Region

While Chapter 4 revolves around the analysis of a fairly short (i.e., one-year-long) seismic dataset from a temporary experiment of a large spatial extent, in this chapter[1], we will discuss a seismic velocity change (dv/v) time series from 25 years of

[1]This chapter has been published as Makus, P., Denolle, M. A., Sens-Schönfelder, C., Köpfli, M., & Tilmann, F. (2024). Analyzing Volcanic, Tectonic, and Environmental Influences on the Seismic Velocity from 25 Years of Data at Mount St. Helens. *Seismological Research Letters*, *95*(5), 2674–2688. https://doi.org/10.1785/0220240088 The version reprinted in this thesis is a modification of the author accepted manuscript. Compared to the original version, the introduction was modified. In the interest of conciseness, descriptions of procedures already described in Chapter 3 were condensed or replaced by references to said chapter. In addition, minor changes in the mathematical notation and text body were introduced. To ensure consistency across the thesis, I adapted the orthography to comply with the British/Canadian standard.

ambient seismic noise recorded at Mount St. Helens (MSH).

At MSH, the availability of seismic stations changes frequently due to station failure and the installation of new stations. It is, therefore, difficult to combine relative measurements that do not span the same time and space. Here, we tackle this challenge by developing a spatial imaging algorithm to normalise all ∼1,400 dv/v time series onto one spatial grid. Thereby, we obtain time-dependent velocity change maps of the MSH region, which we analyse with the help of auxiliary observations, such as ground position (i.e., global navigation satellite system (GNSS)), weather data, environmental observations, and regional seismicity.

Like in Kamchatka, we find evidence for a breadth of dynamics in dv/v caused by volcanic, tectonic, and environmental forcing. With the initiation of MSH's 2004-2008 volcanic crisis, dv/v exhibits a significant increase, which we link to the deflation of the volcanic plumbing system, also observed on GNSS data. Between 2013 and 2018, when seismicity levels were elevated, we observe lower velocities at depth. This phase is followed by an episode of relative quiescence, accompanied by significant dv/v increases close to the St. Helens Seismic Zone (SHZ). We suggest a reinflation of the magmatic plumbing system after MSH's 2004-2008 eruption, lasting until about 2017. Afterwards, the magmatic activity in the subsurface reduces, thereby decreasing pressure and increasing the seismic velocity. Fluctuating groundwater levels may dominate the seasonal cycles in the dv/v time series. A contrasting seasonal response between the high-elevation edifice and foothill valleys may indicate that surface freezing inhibits subsurface groundwater infiltration at higher altitudes.

5.0.1 Mount St. Helens

MSH is an explosively erupting andesitic volcano in southern Washington, United States. Its devastating 1980 eruption, accompanied by the dramatic gravitational failure of its northern flank, caused almost 1 billion US$ in damage (Hunt & Mac-

Cready, 1980) and claimed 57 casualties. In 2004-2008, a new volcanic activity started at MSH. Even though the eruption was less dramatic than in 1980, it was particularly well-instrumented and studied (e.g., Sherrod et al., 2008).

Unlike earthquakes, volcanic eruptions tend to exhibit precursory activity that can be investigated via geophysical and geochemical data and analysis. Precursors may, for example, be observed by remote sensing data due to ground deformation (e.g., Reath et al., 2016), gravity changes (e.g., Rymer & Brown, 1989), and seismicity associated with the uprising magma or gas (Einarsson, 2018). However, every volcano shows a unique behaviour, and each of the discussed precursors varies in presence, strength, and warning time before the eruption. For example, while some volcanoes exhibit significantly elevated seismicity before eruptions (Chouet & Matoza, 2013; Power et al., 1994) others may be quasi-aseismic (Lu et al., 2000; Scandone et al., 2007). Additionally, the eruption style and warning time may also vary at a single volcano, such as MSH (Malone et al., 1983; Sherrod et al., 2008).

As discussed in Chapter 2.1, there are opportunities to reduce warning times and uncertainties while improving our understanding of the volcanic system and dynamics with system-level science to evaluate spatial and temporal changes (e.g., Roman & Cashman, 2018). Motivated by this goal, scientists conducted many studies attempting to constrain the dynamics and structural complexity of MSH, employing a multitude of geophysical methodologies such as gravity measurements (Battaglia et al., 2018), electric resistivity surveys (Bedrosian et al., 2018), probing the ground's heat flow (Grady et al., 1982), pixel offset monitoring (Salzer et al., 2016), Interferometric Synthetic Aperture Radar (INSAR) (Welch & Schmidt, 2017), or by analysing magnetotelluric data (G. J. Hill et al., 2009). Probably, the most widely used are seismic methods, as the volcanic edifice and its surroundings are well-instrumented, and instrumentation is improving constantly. Seismologists have, for example, studied the medium's scattering and attenuation (De Siena et al., 2014; Gabrielli et al.,

2020), the local velocity structure using local earthquake, teleseismic, or ambient noise tomography (e.g., Crosbie et al., 2019; Ulberg et al., 2020; Y. Wang et al., 2017). Numerous publications that focus on seismic source properties and local earthquakes preceding the eruptions (e.g., Lehto et al., 2010), during the eruption (e.g., Moran et al., 2008; Sabra et al., 2006; Thelen et al., 2011; Zhang et al., 2022), and in intereruptive periods (e.g., Glasgow et al., 2018; Hansen & Schmandt, 2015) complement these structural studies.

Hotovec-Ellis et al. (2014) and Hotovec-Ellis et al. (2015) used local source coda wave interferometry (CWI) to analyse the temporal modifications in MSH's local velocity structure. They find velocity changes associated with seasonal weather variations, volcanic explosions during the 2004-2008 eruption, and damage following the 2001 Nisqually earthquake.

Here, we apply passive image interferometry (PII) to the considerable amount of continuous seismic data recorded at MSH to shed light on the velocity changes and their temporal and spatial evolution at MSH over the past 25 years, building on the pioneering work of Hotovec-Ellis et al. (2014) and Hotovec-Ellis et al. (2015). We will discuss challenges that arise from the heterogeneous nature of the data and present solutions and workarounds. To analyse the evolution of the seismic velocity in space, we apply an inversion algorithm that models the spatial sensitivity of coda waves and generates maps of dv/v based on station-pair-wise measurements. Lastly, we will discuss mechanisms impacting dv/v at MSH and show that a multitude of complex mechanisms of environmental, MSH, and volcanic nature affect the seismic velocity. This work focuses on the structural dynamics at MSH as interpreted from changes in seismic velocities. A companion paper, (Köpfli et al., 2024), complements this study by exploring aseismic properties (attenuation).

5.1 Data and Processing

5.1.1 Seismic Data

The analysis of ambient seismic noise requires continuous waveform recordings. At MSH, continuous data has been collected since 1998, and data are continuously updated. For this study, we obtain data from stations that were active for at least three years during our study period from 1998 to 2023 (see Figure 5.1), resulting in a diverse collection of seismic instruments, including broadband, short-period seismometers with a combination of digital and analogue telemetry (cf. Table C.1 and Figure C.1 for detailed station availability).

The long-standing seismic network at MSH is remote and subject to weather and volcanic hazards. Because data stability is critical for ambient noise monitoring, we developed conservative quality control and extensive pre-processing workflows to mitigate instrumental issues. For instance, the MSH seismic network includes "analogue stations" that are radio-telemetered seismometers with data digitised at the Pacific Northwest Seismic Network (PNSN) data centre. These stations are prone to recording issues, such as data gaps, empty recordings, abnormal amplitudes, and clock errors. Some stations record single vertical channels (EHZ), while others record three components. In our quality control, we discard a daily raw recording if (a) the maximum range of the data amplitudes is less than 500 counts using the values provided by IRIS' Mustang service (Casey et al., 2018) or (b) the root mean square amplitude (A_{rms}) exceeds a threshold of $A_{rms}(t_0) > 300\tilde{A}_{rms}(t)$, where $\tilde{A}_{rms}(t)$ is the median root mean square amplitude of all available data for the given channel. We plot the amount of remaining data in Figure C.1 in the supporting information.

Following this initial quality control, we process our data using SeisMIC (Makus & Sens-Schönfelder, 2024). SeisMIC further identifies data gaps and interpolates between them if they are exactly one data sample long. For longer gaps, SeisMIC

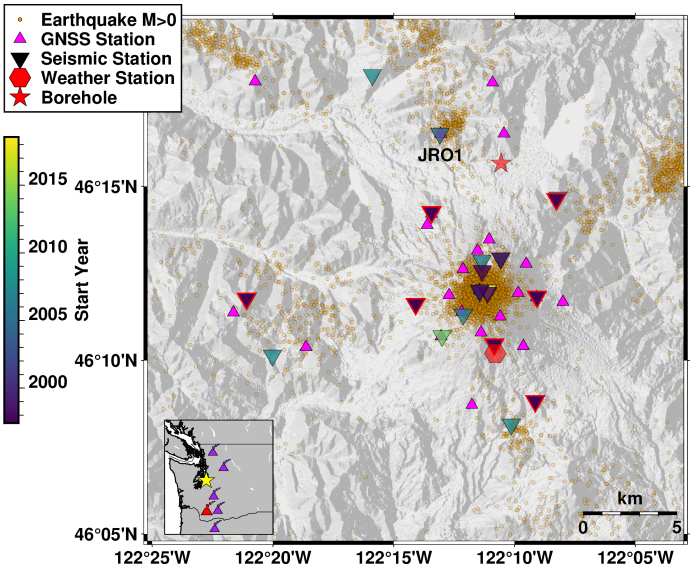

Figure 5.1: Locations of the seismic stations, GNSS sites, the weather station, and the borehole, from which we obtain data for this study. Seismic stations are inverted triangles coloured by the time of their first continuous recording. Seismic stations with red outlines are used to create the plot in Figure 5.3. For all other plots, we used data from all stations. The weather station corresponds to the Swift Creek (1012) SNOTEL station, for which we show temperature and snow load data in Figure 5.6. The seismicity shown in this plot occurred between 1998 and 2023. In the map inset in the lower left corner, we depict the locations of MSH and other active Cascade volcanoes in red and purple, respectively. The epicentre of the M6.8 2001 Nisqually earthquake is plotted as a yellow star.

mutes data chunks shorter than two minutes and tapers the ends of the available data segments with a 20-second-long cosine taper. We choose standard processing techniques for ambient seismic field monitoring (Bensen et al., 2007): We apply an anti-alias filter with a low-pass frequency of 2.25 Hz, decimate the data to 5 Hz, detrend, taper, remove the instrumental response from the daily data, and band-pass filter the data between 0.01 and 2.5 Hz. Then, we slice the data into one-hour-long windows, detrend, and taper the windows' ends by 3 %. The data are then filtered in three one-octave-wide frequency bands: 0.25-0.5 Hz, 0.5-1 Hz, and 1-2 Hz, resulting in three different datasets. Subsequently, we apply one-bit normalisation in the time domain. We obtain three groups of correlation functions (CFs): auto-correlations (single channel pairs), self-correlations (single station, multi-channel pairs), and cross-correlations (multi-station, multi-channel pairs). For self- and cross-correlations, we whiten the amplitude spectrum of the data (Bensen et al., 2007) in the Fourier domain. Finally, we average the resulting CFs over five days to reduce the amount of data and smooth the stacked CFs with a 60-day-wide moving Hanning taper, thereby weighing the contributions of particular 5-day stacks.

Visual inspection of the CFs reveals artefacts in the auto-correlations of the single-component analogue stations (see Figure C.2). To avoid biases in the final velocity change estimate, we disregard auto-correlations from stations with analogue telemetry.

We use the mean of all CFs for each channel pair as reference CF (i.e., the state at which $dv/v = 0$). The stacked CFs, therefore, span different periods and are not valid references across the network. We then estimate velocity change time series using the stretching method first proposed by Sens-Schönfelder and Wegler (2006). The algorithm is described in detail in Chapter 3.1.2. We set the increment in our similarity matrix (eq. 3.5) to $\kappa_n - \kappa_{n-1}$=0.006 %. Because cross-correlation functions are two-sided, we evaluate the stretch for up to 3 % for the coda of both sides of the

CF. We apply the algorithm only for a part of the coda of the CFs starting at four times the lowcut period of the three bands T_0 and ending at $50T_0$ after the theoretical arrival, assuming a Rayleigh wave velocity of 2.5 km/s (Y. Wang et al., 2017). We find that using such a long coda window improves the stability of the dv/v estimate. After executing this step for all data, we obtain one dv/v time series per frequency band for each auto-, self-, and cross-correlation, totalling about 1,400 dv/v time series. Their overall stacks are taken as the reference for dv/v and, because these time series of dv/v start and end at different times, their relative mean is arbitrary. We show examples of the resulting CFs and dv/v time series in Figure 5.2.

Sudden phase shifts and coherence drops in the cross-correlation may indicate a clock advance that sites with analogue telemetry may be subject to. We detected one such event on 17 October 2013 (see Figure C.3).

5.1.2 Auxiliary Data

We obtain snow load and temperature data from the US Department of Agriculture's Natural Resources Conservation Service. These data were recorded at Swift Creek by a weather station that includes a SNOTEL sensor at 1353 m.a.s.l., about 300 m above the base of the edifice (see Figure 5.1 for the location of the weather station), which is probably a lower bound estimate as the edifice peaks at 2549 m. To compute the water supply rate, we obtain rainfall and modelled snowmelt data from the ERA5 reanalysis satellite data set (Hersbach et al., 2020).

Additionally, we collect earthquake hypocentres determined by the PNSN and the United States Geological Survey (USGS).

To analyse surface deformation and ground movements, we obtained cleaned and detrended displacement time series for the GNSS stations in the vicinity of MSH from the USGS (Murray & Svarc, 2017), see Figure 5.1 for locations.

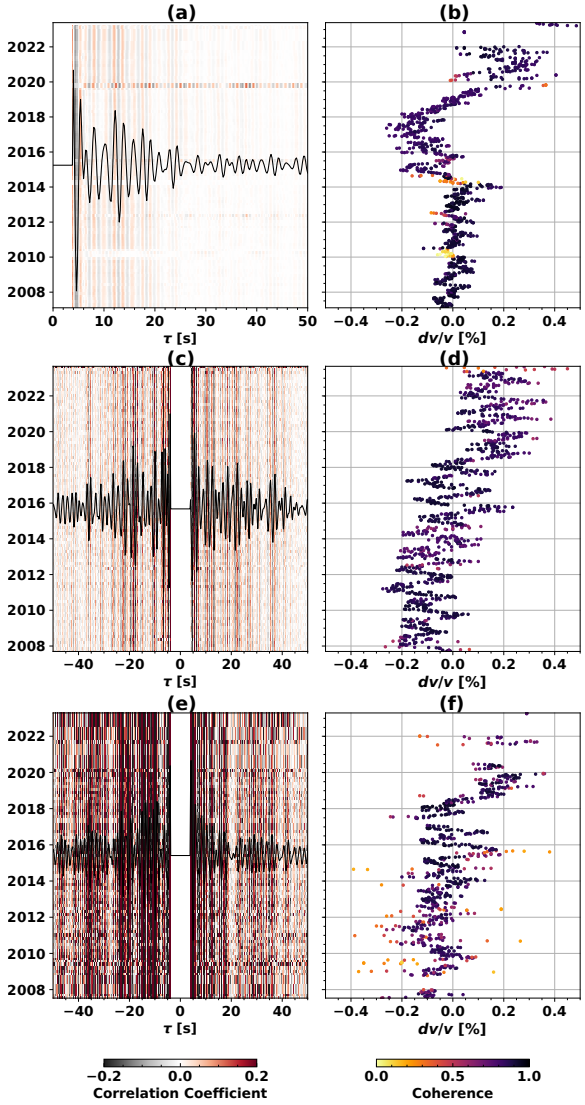

Figure 5.2: Exemplary CFs from channel combinations and their corresponding 0.5-1 Hz dv/v estimates. **(a)** & **(b)**: Auto-correlation at CC.VALT.BHN. **(c)** & **(d)**: Cross-correlation PB.B201.EH1-PB.B201.EHZ, **(e)** & **(f)**: Cross-correlation CC.STD.BHE-PB.B203.EH1. Data for up to 4 s is muted for visualisation. We show the mean of all CFs superimposed on the heatmap. We stack the CFs in the heatmap so that each corresponds to 60 days of data. The features observed in the dv/v estimates are consistent with those seen in the spatial inversion and the station stacks shown later.

5.2 Reconciling and Locating Velocity Changes

Direct inspection of the dv/v time series calculated using the steps described above has several challenges: 1. Their sheer number makes it difficult to keep an overview and condense them into interpretable results. 2. More importantly, since most of the dv/v curves describe different periods, they are not directly comparable. This is due to the nature of the reference CFs. Mathematically, we can describe the relation between the absolute velocity change and the reference velocity v_{ref} as follows (see appendix A for a more thorough discussion):

$$\frac{dv}{v_{ref}} = \frac{v(t) - v_{ref}}{v_{ref}} \tag{5.1}$$

where, in our case, we define the reference:

$$v_{ref} = \frac{1}{N} \sum_{t=1}^{N} v(t_n) \tag{5.2}$$

Note that t_1 corresponds to the starting date of the seismic stations shown in Figure 5.1 and N to the length of the time series, both differ for many of the dv/v series. Therefore, the different dv/v times series will be offset against each other. We correct for this offset during the spatial inversion as described in section 5.2.2. Note that the difference in v_{ref} does not only lead to an offset but also to a different scaling. However, these scaling errors are negligible (e.g., about 0.01 %, if dv/v=1 %).

5.2.1 Locating Velocity Changes in Space

This study uses a linear-least-squares inversion as proposed by Obermann, Planès, Larose, and Campillo (2013) to obtain a spatial dv/v grid from a large number of velocity change time series. Using this algorithm, we receive a prediction for dv/v as a function of space and time. As the problem is ill-posed and underdetermined (i.e., the number of grid points is usually higher than the number of CFs), it requires

damping. In the supporting information (section C.4), we describe the algorithm in detail and the damping parameters that we choose to compensate for the ill-posed nature of the problem.

5.2.2 Compensating for Clock Shifts and Constant Offsets in the dv/v Time Series Estimates

We correct for the non-conform references and instrumental clock shifts by leveraging the dv/v predictions from the spatial inversion. In the spatial inversion, we set the reference, $\frac{dv}{v}(\mathbf{x}, t_1) = 0$, where t_1 is the start time of the spatial inversion. First, we offset the $\frac{dv}{v}$ time series available at t_1 so that $\frac{dv}{v}(t_1) = 0$. We then proceed by inverting for each time step. Whenever a new time series becomes available (e.g., at $t = t_n$), we predict the velocity change at each "new" observation at t_n by solving the spatial forward problem (eq. C.3) and offset the corresponding time series by the obtained value. Here, we consider a times series available when the coherence of the following 5 points satisfies a minimum average value of $CC(t_n) \geq 0.5$.

A second example is when the PNSN digitisers were restarted in October 2011, and all analogue stations were advanced by 0.25 s (see section C.1). This reset in the digitiser at the PNSN created a different clock time for the "analogue stations" and those with on-site digital telemetry. As we already compensate for changes in the reference using the approach described above, we opt to compute two dv/v time series - one before the clock advance and one after - for each of these CFs and feed them into the spatial inversion as separate dv/v time series.

5.3 Results

In the following, we will show how the seismic velocity at MSH varies spatially and temporally. First, we discuss long-term trends and changes. Thereafter, we will

examine repeating seasonal signals.

5.3.1 Long-term dv/v Trends

To build the longest time series of our study, we use cross-correlation data from the seven stations active between 1998 and 2023: UW.EDM, UW.FL2, UW.HSR, UW.JUN, UW.SOS, UW.STD, and UW.SHW. To obtain the final network averaged dv/v time series, we average the similarity matrices resulting from the stretching algorithm and, subsequently, pick a new velocity change corresponding to the best-fitting stretch and calculate the cumulative correlation coefficient (CCC) as the average of the cross-correlation coefficients in all contributing similarity matrices along the best-fit curve (for details, see Illien et al., 2023; Makus, Sens-Schönfelder, et al., 2023, or Chapter 4). The resulting dv/v time series and the vertical ground movement recorded at GNSS station JRO1, the only station recording at the time of the eruption, are plotted in Figure 5.3. We also show dv/v and vertical motion for which the seasonal components were suppressed by applying a two-year Gaussian smoothing.

Following the 2001 M6.8 Nisqually earthquake, which struck the Puget Sound region on 28 February 2001, dv/v shows a drop in all investigated frequency bands albeit somewhat subtle between 0.25 and 0.5 Hz (between 0.05 % for 0.25-0.5 Hz and 0.2 % for 1-2 Hz, see Figure 5.3). The drop marks the lowest level of seismic velocity in the record.

Coinciding with the first explosions of MSH's 2004-2008 eruption, a vertical downward movement of about 20 mm is measured at the JR01 GNSS station, whereas dv/v exhibits a rapid increase of 0.1 % and 0.2 % for frequencies between 0.5 and 1.0 Hz and 1.0-2.0 Hz, respectively. For 0.25-0.5 Hz, dv/v increases temporally by about 0.2 % for around eight months. Afterward, it remains slightly elevated ($\sim$0.05 %). Following its low level during the eruption, the GNSS signal shows an upward motion that lasts until about 2013. Thereafter, the GNSS long-term trend remains stable.

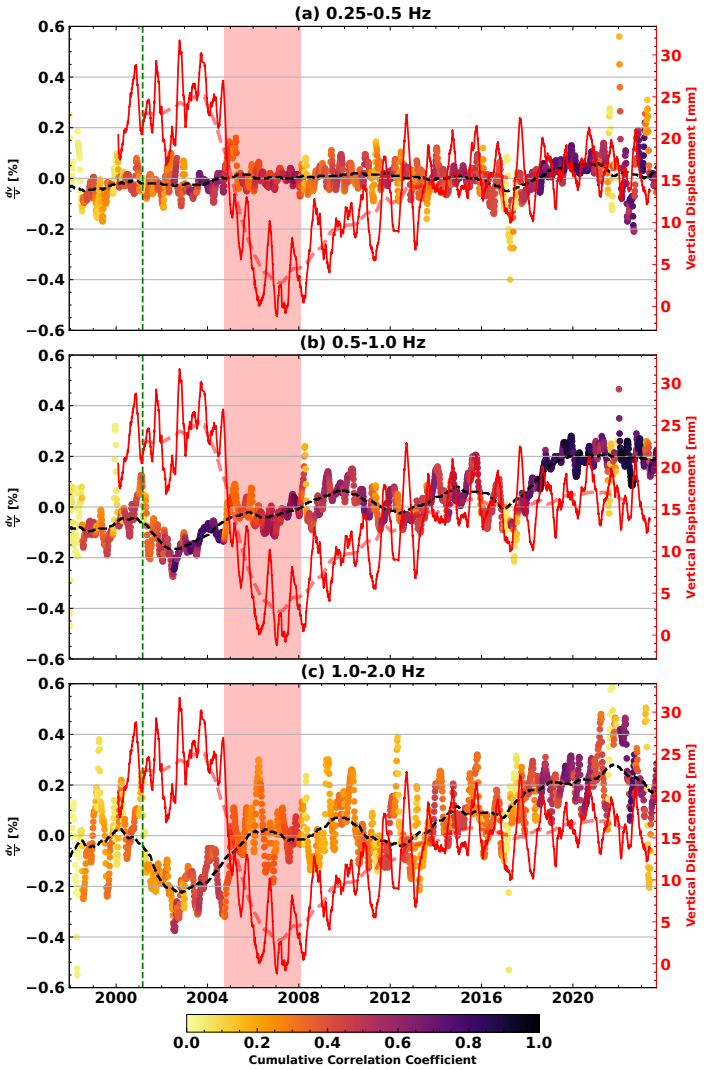

Figure 5.3: Weighted average of the dv/v time series available for the whole study period for the frequency bands 0.25-0.5 Hz **(a)**, 0.5-1 Hz **(b)**, and 1-2 Hz **(c)**. dv/v was computed with data from stations UW.EDM, UW.FL2, UW.HSR, UW.JUN, UW.SOS, and UW.SHW (marked by red outlines in Figure 5.1). The colour scales with the CCC. The dashed line shows the low-pass filtered dv/v time series. The dashed vertical green line indicates the 2001 M6.8 Nisqually earthquake known to perturb dv/v (Hotovec-Ellis et al., 2014). The salmon-shaded period marks MSH's 2004-2008 eruption. The solid (dashed) red line shows the (low-pass-filtered) vertical ground motion as recorded by GNSS station JRO1.

We do not observe any significant trends in dv/v corresponding to this GNSS trend. From 2017 to 2020, the seismic velocity increased notably by about 0.2 %, which is particularly clear between 0.5 and 1.0 Hz though seen on all frequency bands, including the noisier low-frequency band between 0.25 and 0.5 Hz.

Using the spatial imaging algorithm, we compute one time-dependent dv/v map for each of the investigated frequency bands with a grid spacing of 1 km and a sampling interval of 5 days. The time-dependent maps are available as GIF files in the electronic supplement. To avoid drastic changes in spatial resolution over the investigated time, we exclude times before 2007 when there were significantly fewer seismic stations available at MSH. To emphasise the long-term change in the seismic velocity, we plot the accumulated velocity change between 31 May 2007 and 01 June 2023 for all three examined frequency bands in Figure 5.4. For the lowest frequency band, 0.25-0.5 Hz, the spatial resolution is too low to constrain velocity changes in space. Therefore, we do not show maps for this frequency range.

We observe seismic velocity changes dominated by increases around the northern flank of the volcano. For 0.5-1.0 Hz, the velocity increases are highest north of the volcano along the St. Helens Seismic Zone (SHZ). We find a second velocity peak to the east of the volcano. For 1.0 to 2.0 Hz, the dv/v increase focuses mainly on the SHZ. In addition, we find a dv/v minimum to the south of the volcano. However, this minimum still shows a significant increase of about 0.5 %.

Temporally, a prominent velocity increase is observed in the period between 2017 and 2020 (as seen in Figures 5.3 and 5.5). Before this increase occurs, we observe a moderate decrease starting in late 2017 that exceeds the amplitude of the usual seasonal oscillations. While for 0.5-1.0 Hz the strong velocity increase is entirely focused on the period of late 2017 to 2020, the other two frequency bands show some additional jumps. For 0.25-0.5 Hz, the seismic velocities across are depressed by 0.1 % between 2014 and 2017, compared to the previous five years. For 1-2 Hz,

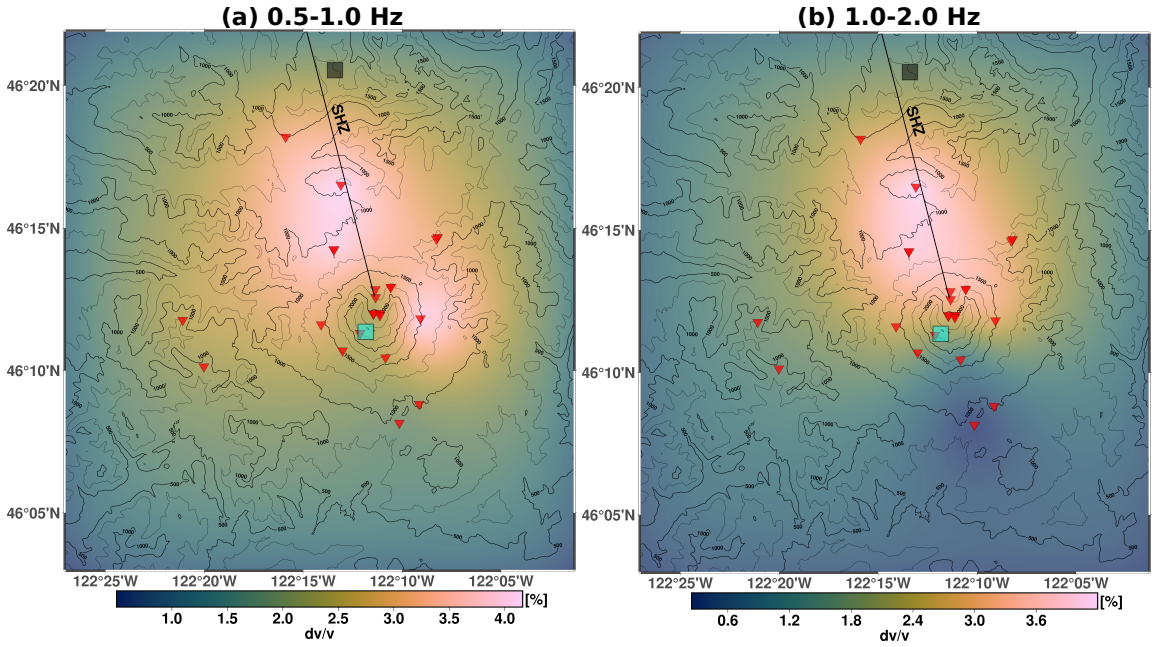

Figure 5.4: Total accumulated velocity change between 31 May 2007 and 01 June 2023 superimposed onto the regional topography. Total accumulated velocity change obtained from ambient noise between **(a)** 0.5 and 1.0 Hz, **(b)** 1.0 and 2.0 Hz from all available seismic data. The red inverted triangles mark the locations of seismic stations from which we used data for this inversion. The black line corresponds to the St. Helens Seismic Zone (SHZ). The black and cyan boxes correspond to the locations from which we extracted time series in Figures 5.6 and 5.5. Please note that we use different colour scales for the two frequency bands.

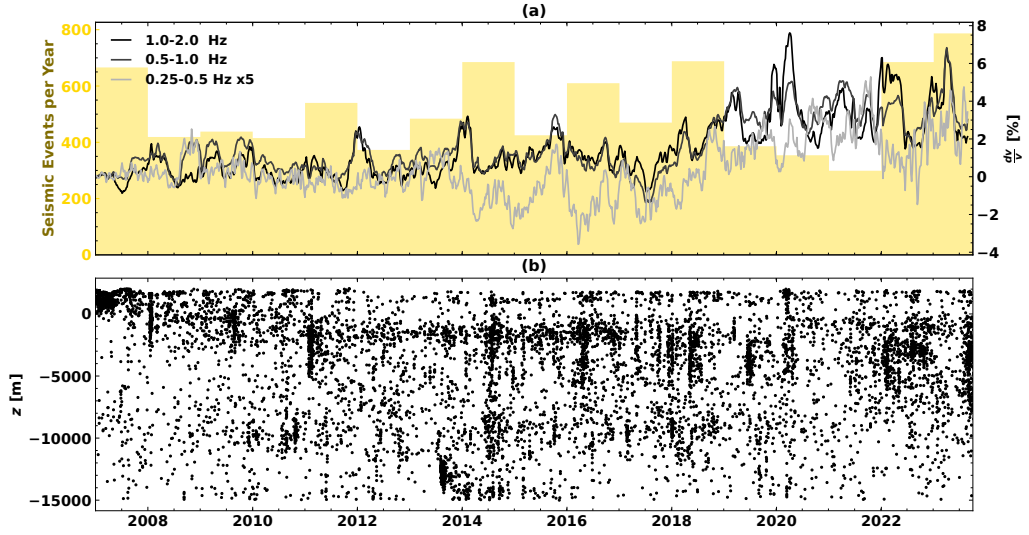

Figure 5.5: Seismic velocity changes set in the context of seismicity at MSH. In **(a)** yearly rate of seismic events with $M > -1$ and hypocentres above 15 km depth below sea level. Seismic velocity changes extracted from the spatial inversion at MSH's summit (cyan box in Figure 5.4) for all investigated frequency bands and all seismic stations. For 0.25-0.5 Hz, the curve is five-fold exaggerated. **(b)** Depth distribution of seismic events with M>-1.

the velocity change rate reaches its maximum in an increase between 2017-2020 (see Figure 5.5).

5.3.2 Seasonal Variations in the Seismic Velocity

After showing long-term variations in the seismic velocity, we now focus on seasonal variability. In many cases, such variability is driven by environmental factors, which, in turn, are strongly affected by the seasons. Therefore, we show dv/v in direct comparison to environmental parameters. Here, we choose to show dv/v together with the snow load on the south flank of MSH and the water level of Spirit Lake, which we assume to be a proxy for groundwater level and pore space saturation.

Although the water level is also controlled by a drainage tunnel (Grant et al., 2017), we confirm this assumption by comparing the lake water level to groundwater well levels available after 2020. Here, we only examine seasonal trends. In Figure C.16, we show the full-length time series.

To examine the seasonal cycles in dv/v, we extract median seasonal cycles from our velocity change estimates and the vertical GNSS movements. To this end, we process the time series as follows. First, we apply a highpass filter with a four-year corner period to the dv/v and vertical motion time series recorded at the seismic channel combinations and GNSS stations, respectively. Then, we extract the curve for each calendar year, remove their means, and calculate a median over all years to generate station- and channel-combination-specific time series. From these time series, we extract the total median. We provide the individual annual functions for each GNSS and seismic channel combination in Figures C.18 and C.17, respectively. We show the median seasonal evolutions in Figure 5.6(a). The vertical ground motion displays a simple sinusoidal movement that peaks in early September and exhibits an annual low in April.

For the medians extracted from the channel combinations, dv/v differs in behaviour depending on the frequency band. For 0.5-2 Hz, dv/v has two annual peaks. The first peak in March occurs between the highest snow load and the lowest temperature, while the second peak coincides with the highest ground displacement (i.e., September). The velocity change obtained from the lowest frequency band, 0.25-0.5 Hz, only exhibits one clear peak in September, while its shape does not follow the ground displacement curve during the rest of the year, where dv/v decreases rapidly after the September peak to reach a low in January, followed by a much more gradual increase, in contrast to the sinusoidal GNSS displacement time series.

To investigate spatial heterogeneities in seasonal behaviour, we compute the median annual velocity change for each grid point in the time-dependent dv/v maps.

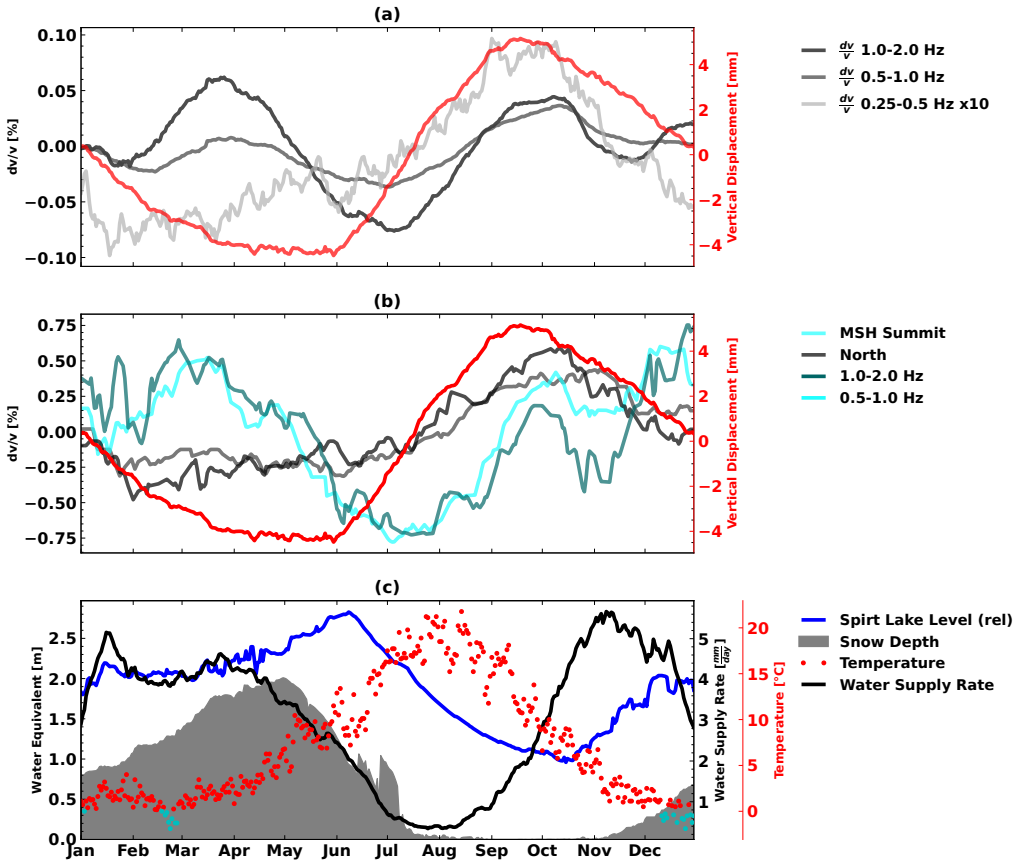

Figure 5.6: Annual median velocity changes and median vertical ground motion (red). **(a)** Annual median dv/v curve for the study region extracted from CFs between all components and stations. **(b)** Annual median dv/v curve extracted from two grid points with diverging behaviours in the time-dependent dv/v maps (using data from all stations). These grid points are marked in Figure 5.4 as black (North) and cyan boxes (MSH summit). On both panels, we indicate the frequency band by varying the curves' luminance. **(c)** The annual median snow load extracted from the SNOTEL station and the annual median of Spirit Lake's relative level are both shown in meter water equivalent. The black line represents the smoothed annual mean water supply rate (i.e., the sum of modelled snowmelt and rainfall per hour). We plot the annual median temperature at the base of MSH as red dot markers. We emphasise temperatures below freezing by plotting them in cyan instead of red.

We find two predominant patterns, for which we plotted exemplary curves in Figure 5.6 (b). North of the edifice, we find a single and broad peak in the annual dv/v around September, and the annual minimum is located in winter, January through March, for all frequency bands. On the volcanic edifice and for higher frequencies between 0.5 and 2 Hz, the dv/v have a different pattern: They peak in April and October, whereas the summer is characterised by lower velocities.

Figure 5.6 (c) provides relevant environmental time series to set the context to the geophysical measurements (GNSS and seismic). We show the annual median changes in snow load, temperature, and lake levels at Spirit Lake. In addition, we show the annual mean water supply rate smoothed using a 30-day-wide boxcar function. We find an approximately anticorrelating pattern between snow load and vertical ground motion. Furthermore, we observe a peak in dv/v at MSH's summit, occurring between the snow load maximum and the temperature minimum. When the seismic velocity in the north decreases the strongest, the water supply rate peaks.

5.4 Discussion

5.4.1 Spatial Resolution

To evaluate the capabilities of the imaging and the distortions introduced into the velocity change maps by the station geometry and the chosen damping parameters, we apply the spatial inversion to various synthetic velocity change models. In addition, we compute the resolution parameter as defined in Tarantola and Valette (1982). We provide the results in the supporting Figures C.12-C.15. We find that the inversion can recover large-scale velocity change patterns. Outside the seismic network boundaries, the resolution is severely limited, and no shapes can be recovered. In the centre of the grid around MSH's summit, the test suggests that obtained dv/v amplitudes might be somewhat exaggerated. The inversion results are generally

strongly smoothed, probably due to the large sensitivity kernels that we obtain when using values from the late coda of the CFs. We denote that the results are particularly smooth between 0.25 and 0.5 Hz and, often, fail to recover the models' shapes. Therefore, we opted not to interpret spatial variations in dv/v from 0.25-0.5 Hz.

The three frequency bands investigated in this study are sensitive to different depth ranges. Assuming a wavefield dominated by surface waves, the maximum depth resolution is about 2/3 of the central wavelength (Obermann, Planès, Larose, Sens-Schönfelder, & Campillo, 2013; Yin et al., 2014). For a Rayleigh wave velocity of 2.5 $\frac{km}{s}$ (Y. Wang et al., 2017), this would correspond to about 6.6, 3.3, and 1.6 km for results obtained from 0.25-0.5, 0.5-1.0, and 1.0-2.0 Hz, respectively.

5.4.2 Long-term Velocity Changes over 25 Years

Using the long-term dv/v time series shown in Figure 5.3, we can make some initial assessments about the long-term evolution of the seismic velocity at MSH. From this dataset, we can also infer how MSH's 2004-2008 eruption impacted the seismic velocity, although seasonal variations have a strong imprint on the evolution of dv/v during the eruption, and the seismic signature of the eruption is the most pronounced in 2004-2005 (Köpfli et al., 2024).

Probably the easiest to interpret is the seismic velocity drop in late February 2001 coinciding with the M6.8 Nisqually earthquake. Such velocity drops during large earthquakes have been associated with nonlinear elastic damage to the dynamic ground shaking and were observed by a multitude of studies (e.g., Brenguier, Campillo, et al., 2008; Olivier et al., 2015; Wegler et al., 2009). Our observation of this coseismic velocity change agrees with findings by Hotovec-Ellis et al. (2014), who used CWI of repeating earthquakes and found an elevated drop at higher frequencies (1-10 Hz) at UW.SHW and UW.HSR. From the larger velocity drop at higher frequencies, we infer a larger damage in the shallow subsurface, which is due

to larger ground acceleration and a higher damage susceptibility of the unconfined near-surface (e.g., Sheng et al., 2021). Usually, long datasets are well suited to study the postseismic damage recovery phase, in which the seismic velocity returns to its previous state following a logarithmic healing law typical of slow dynamics (Sens-Schönfelder et al., 2019; Snieder et al., 2017). While we see signs of a recovery process following the Nisqually earthquake, particularly in the dv/v curve obtained from 0.5-1.0 Hz between 2002 and 2004, its later part is obscured by effects likely linked to MSH's eruption.

The arguably most notable event during this time series is MSH's 2004-2008 volcanic crisis, which caused various structural changes in the subsurface, impacting the seismic velocity (Hotovec-Ellis et al., 2015). The 1-month-long drop in the dv/v reported by (Hotovec-Ellis et al., 2015) is absent in our dataset, which could be due to our post-processing smoothing (30 days), our choice of the frequency band, or an effect of the different spatial sensitivities of the two methods. The vertical GNSS motions indicate a sudden deflation (compression) of $\sim$20 mm, which would explain the increase in velocity that we see at the lowest frequencies ($\sim$+0.15 %).

While deflation continues at a lower rate until 2007, re-inflation occurs until 2013 to return to the 2000 levels (+15 mm, Figure 5.3). We infer an unplugging followed by the depressurisation of the volcanic plumbing system caused by the phreatic explosions in late 2004. This depressurisation likely caused the closure of cracks and pore space, leading to the observed subsidence accompanied by the velocity increase driven by the acoustoelastic effect (e.g., Silver et al., 2007). Similar observations were made, for example, at Piton de la Fournaise (Brenguier, Shapiro, et al., 2008; Rivet et al., 2014; Sens-Schönfelder, Pomponi, & Peltier, 2014) and Mt. Etna (De Plaen et al., 2019).

While yielding a higher resolution in times with many similar seismic signals, CWI cannot be employed when seismic sources are too dissimilar, which is why, in

contrast to PII, the technique does not allow a direct comparison of seismic velocities during the eruption to post- and pre-eruptive seismic velocities. Therefore, our observation of the seismic velocity increase coincident with the initiation of the eruption is original.

5.4.3 Evolution in dv/v post 2004

In Figure 5.4, we show the total dv/v change between 2007 and 2023. The resulting pattern appears to be a strong velocity change from the northern flank of the volcanic edifice and the SHZ. For depths below 3 km, the main velocity change is under the volcanic edifice (see Figure 5.4 (a). The SHZ is a strongly scattering, seismically active zone with a high $\frac{v_P}{v_S}$-ratio at depth linked to MSH's magmatic plumbing system (Bedrosian et al., 2018; Crosbie et al., 2019; Ulberg et al., 2020; Waite & Moran, 2009). While the frequency bands employed here are too high to be sensitive to changes in the plumbing system located mostly below 6 km depth (Ulberg et al., 2020), pressure changes within the plumbing system can induce crack opening and closing in the surrounding areas and, thereby, alter the seismic velocity and the scattering properties of the medium in a larger volume (Donaldson et al., 2017). A dv/v increase east of MSH appears more clearly on results from 0.5-1.0 Hz than for 1-2 Hz. This is in agreement with an eastwards extension of MSH's magma reservoir at depth (De Siena et al., 2014; G. J. Hill et al., 2009; Waite & Moran, 2009).

The bulk of the observed dv/v increase occurs in the time range of 2017-2020. There are no significant changes in vertical displacement (Figure 5.3), neither are there notable spikes in seismic activity. However, Battaglia et al. (2018) interpreted additional dense materials below MSH from a gravity survey limited from 2010 to 2016, and they further interpreted this mass addition to be caused by a magma reservoir recharge. Ground inflation between 2008 and 2012 preceded this mass addition (see Figure 5.3). From the 2017-2020 velocity increase, we infer a slowing

or ending of the recharging process, leading to a decreased pressure at depth. While the seismic activity between 2013 and 2018 was somewhat elevated with 560 events per year (with $M > -1$), indicating increased fluid movement at depth, it decreased to $\sim$ 350 events per year between late 2018 and early 2022. We conclude that the increased fluid movement and pressure changes from 2013 to 2018 led to a decreased seismic velocity at depth (i.e., only seen between 0.25 and 0.5 Hz or down to 6 km depth). This period was then followed by decreased seismic activity and increased seismic velocity (see Figure 5.5, late 2017-2020). The observed dv/v increase is comparable with that at the initiation of the 2004 eruption (see Figure 3), for which magma ascent rates of 0.005–0.015 m/s were calculated (Rutherford, 2008; Thornber et al., 2008). We suggest that the cumulative magma removal and, thus, pressure decrease in the magmatic conduit was of the same order of magnitude as at the beginning of the eruption. We also note that the 2017-2020 increase is expressed more strongly in lower frequencies and, hence, larger depths than the increase at the initiation of the 2004 eruption, which is compatible with our hypothesis that the 2017-2020 increase was caused by an alteration of the magma supply at depth.

5.4.4 Seasonal Velocity Changes

At MSH, the seismic velocity variations are strongly seasonal and, similar to findings by Hotovec-Ellis et al. (2014), we observe two distinct peaks, one in spring and one in autumn (see Figure 5.6). Spatial imaging provides insights into the locations of the perturbations (see Figures C.19 and C.20) The spring peak focuses on the MSH edifice (i.e., occurring at higher altitudes), and the autumn peak occurs across the whole study region but is more pronounced in the MSH edifice base.

Changes in seismic velocities are often modelled as a superposition of effects (Clements & Denolle, 2023; Donaldson et al., 2019). Dilational strains in the non-linear elastic regime can soften subsurface materials (Ostrovsky & Johnson, 2001).

Shallow seismic velocities are known to vary due to poroelastic effects of rainfall loads, rainwater diffusion, groundwater level variations (Barajas et al., 2021; Clements & Denolle, 2018; Mao et al., 2022; Tsai, 2011), changes in snow load (Caudron et al., 2022; Q. Y. Wang et al., 2017), thermoelastic stresses (Colombero et al., 2018; Fokker et al., 2024; Gassenmeier et al., 2016), and ground freezing and thawing (Gassenmeier et al., 2015; James et al., 2017; Lindner et al., 2021; Steinmann et al., 2021).

The vertical GNSS motion at MSH seems to mainly indicate the elastic effect of the snow load with a single cycle (Figure 5.6). Downward motions possibly indicate compression and closure of pores and would correspond to an increase in dv/v. Upward motions likely indicate a dilation and expansion of pores and would correspond to a decrease in dv/v (e.g., Dong et al., 2002; Heki, 2001). Because the dv/v time series do not anticorrelate with vertical motion, we discuss possible alternative explanations.

Generally, the northern part of MSH, and likely the base of MSH, does not exhibit any positive peak in the winter. It has rather the signature of the low-frequency dv/v with a single peak in autumn. Snow loading and unloading do not seem to have a significant impact on the seismic velocity. While the snow load at MSH's edifice is most likely higher than at the Swift Creek SNOTEL station (1353 m a.s.l.), where the measurements were taken, a significant snow mass still accumulates in all parts of the study area with an average altitude of about 1100 m a.s.l.. Autumn is characterised by the driest period of the year (low rainfall) and the lowest lake level. The observed positive dv/v peak may correspond to 1) lower pore pressure or 2) a 70 or 80-day phase-shifted thermoelastic effects (Clements & Denolle, 2023), but likely has contributions from both effects. Following this peak, dv/v decreases probably due to heavy rainfalls (i.e., pore water refill) and decreasing temperatures in the late autumn/early winter. The lack of clear negative dv/v after the temperature trough may indicate some contribution of ground freezing and snow load, although the

constantly high water supply rate implies that, even in winter, rainfall and melting events remain common.

At the MSH edifice, we expect larger contributions of ground freezing and elastic loading effects of the snow cover due to the higher altitudes. In contrast to the northern part of the study region, on the edifice, dv/v increases in early winter, indicating that precipitation occurs as snow rather than rainfall. The elastic loading effect of the snow load leads to a closing of cracks and pores. The response of the seismic velocity is quasi-instantaneous (e.g., Li et al., 2021). Another factor positively contributing to increasing the velocity is ground freezing (Gassenmeier et al., 2015; Steinmann et al., 2021). Snow cover and low temperatures remain until late spring, likely inhibiting the infiltration of surface water and thus leading to further increases in dv/v. To explain the secondary peak in early autumn, we invoke similar mechanisms as for the northern part, i.e., the decrease of groundwater level and soil moisture combined with thermoelastic effects.

Interpreting why the increased snow load in winter and early spring has no measurable impact on the deeper velocity and the velocity structure north of the volcanic edifice is more challenging. One potential factor could be a lower stress sensitivity at depth to load changes at the surface (Heki, 2003). It could also indicate that the true perturbation of velocity, or stresses, is only in the shallowest layers (Obermann, Planès, Larose, Sens-Schönfelder, & Campillo, 2013; Yuan et al., 2021), though we would need to invoke a vertical heterogeneity in stress perturbation.

5.5 Conclusions

In this study, we estimate changes in the seismic velocity from ambient seismic noise using 25 years of continuous seismic data from MSH and surroundings. Usually, only data from seismic stations continuously available during the whole study period can

be used for passive image interferometry studies since dv/v estimates from different periods are offset by unknown amounts, posing a severe limitation on long-term dv/v estimations from seismic networks. At MSH, we overcome this limitation by employing a spatial imaging approach (Obermann, Planès, Larose, & Campillo, 2013) to estimate the velocity at newly installed station combinations iteratively. We demonstrate the effectiveness of this approach for data between 2007 and 2023, thereby creating time-dependent velocity change maps. In addition, we show a network-averaged dv/v time series for the whole study period from 1998 to 2023.

The various dv/v time series exhibit effects from volcanic and tectonic interactions with the subsurface. Following the 2001 M6.8 Nisqually earthquake, the velocity drops in all investigated frequency bands. We attribute this velocity drop to a nonlinear damage reaction to the ground shaking. With the initiation of MSH's 2004-2008 volcanic crisis, the seismic velocity exhibits a sudden jump by up to 0.2 %, while GNSS measurements imply deflation. Therefore, we infer a depressurisation of the volcanic plumbing system, causing cracks and pore space to close, which, in turn, caused a velocity increase.

Following the eruption, we find dynamics dominated by additional velocity increases. We analyse the spatial distribution of these dynamics and observe that velocity increases in shallow layers focus on the St. Helens Seismic Zone (SHZ), an area in which other studies have placed MSH's plumbing system. We deem the following interpretation of the complex dynamics the likeliest: An acceleration of the deep recharging process between 2013 and 2017, expressed by a surge in volcano-tectonic activity, led to a decreased seismic velocity at depths below 3 km. This recharging process is not only inferred from seismic observations but also from GNSS and gravity data. After this period, dv/v shows drastic increases accompanied by a slight decrease in seismic activity, indicating a slowing or ending of the recharging process and its associated deformation at depth.

Finally, we analyse seasonal cycles in the seismic velocity. Snow loading and ground freezing appear to have limited impacts on the seismic velocity in areas other than on the volcanic edifice. In these regions, we find that dv/v's seasonal cycles can be largely explained by modulations in thermoelastic stress and pore space saturation. On the edifice, we have to invoke additional mechanisms to produce a satisfactory explanation. Here, the freezing temperatures (accompanied by snow) inhibit a pore water refill for most of the year. Additionally, we find evidence for contributions of the snow mass due to elastic loading and ground freezing in the winter. In the late summer, all areas show velocity increases due to reduced moisture by evaporation combined with little water influx and increased thermoelastic stress.

Compared to event-based CWI, PII offers quasi-homogeneous temporal and spatial sampling with the caveat of sampling mostly the shallow structure. During periods of high and consistent seismic activity, CWI offers a higher temporal resolution. However, when the sources' signals become too dissimilar, for instance, when comparing seismic sources before and after MSH's eruption, a direct comparison is no longer possible (see Hotovec-Ellis et al., 2015). Therefore, and because of different spatial sensitivities, both techniques can make unique observations and should be viewed as complementary rather than redundant.

Data and Resources

The waveform data used in this study are collected by the PNSN (University of Washington, 1963, 10.7914/SN/UW) and the Cascades Volcano Observatory (Cascades Volcano Observatory/USGS, 2001, 10.7914/SN/CC). The facilities of EarthScope Consortium were used for access to waveforms, related metadata, and/or derived products used in this study. These services are funded through the Seismological Facility for the Advancement of Geoscience (SAGE) Award of the National Sci-

ence Foundation under Cooperative Agreement EAR-1724509. The ERA5 climate data (Hersbach et al., 2020) are available upon registration at https://cds.climate.copernicus.eu/cdsapp#!/dataset/10.24381/cds.e2161bac?tab=overview. The origin times of the seismic events can be queried via the USGS FDSN web service. The detrended NA2014 GNSS solutions (Murray & Svarc, 2017) can be downloaded from the USGS homepage. The seismic data download, the computation of correlations, velocity change estimates, and spatial imaging were executed using SeisMIC 0.5.22 (Makus & Sens-Schönfelder, 2024). All maps were plotted using PyGMT (Uieda et al., 2021). For the map plots, we obtained the SRTMGL1 digital elevation model (Kobrick & Crippen, 2017). For all other plotting tasks, we used Matplotlib (Hunter, 2007). The full-stack software to reproduce this analysis is available at https://github.com/Denolle-Lab/Mt-St-Helens. With this manuscript, we provide a supplementary document containing supporting information, figures, and tables. Additionally, we provide two animated GIF images showing the temporal evolution of dv/v for 0.5-1.0 Hz and 1.0-2.0 Hz.

CHAPTER 6

Conclusion and Outlook

This thesis explored seismological means to detect time-dependent medium changes in and around volcanoes. More specifically, we applied the method of passive image interferometry (PII) to volcanic environments while setting the results into context to volcanic, tectonic, and environmental data to gain insight into the dynamics at active volcanoes and evaluate strengths and weaknesses of PII at this task. A significant part of the thesis revolved around developing tools and methods to achieve these goals. In this chapter, I summarise the findings and contributions of each chapter. Afterwards, I will indicate directions for potential further research and ways to complement the presented studies.

Active volcanoes pose a significant risk to society that can be mitigated by monitoring and improving the understanding of their dynamics. All monitoring techniques currently employed by volcano observatories focus on secondary effects caused by uprising magma prior to volcanic eruptions (e.g., measuring ground deformation or

monitoring seismic events) rather than directly measuring changes in the volcanic plumbing system. In this thesis, I exploit recent advances in ambient noise seismology that allow interrogating changes in the subsurface and, thereby, within the volcanic plumbing system (see Chapter 1 for details).

The ubiquitous ambient seismic noise is a composite yet deterministic signal produced by environmental, tectonic, and anthropogenic processes. By correlating its energy, we can retrieve an approximation of the subsurface Green's function. Repeating this process over time allows us to quantify changes in the seismic propagation velocity (dv/v) - a tool called passive image interferometry (PII). The seismic velocity is coupled to the shear modulus, which describes the material's rigidity. Therefore, PII can be used to monitor many physical processes that deform a material - among these are also volcanic processes. Chapter 2 describes the theoretical background in detail.

Chapter 3 discusses the methodology of PII in greater detail and introduces a software tool, SeisMIC, for end-to-end processing from continuous seismic noise data to dv/v estimates. After describing the employed algorithms, we show some use cases, API examples, and benchmarks. We remark that SeisMIC is currently the only publicly available software solution to map dv/v in space. To this end, we implemented the algorithm proposed by Obermann, Planès, Larose, and Campillo (2013). Furthermore, we highlight its ease of use, flexibility, and high computational efficiency compared to other existing solutions. At the moment, the software's main drawback is that the user is limited to computing dv/v using only one of the possible methods, the stretching method (as described in Sens-Schönfelder & Wegler, 2006, and Chapter 3). With the software, we proposed new ways of standardising correlation functions and their storage. SeisMIC is being employed by an increasing number of users and research groups and, looking forward, will obviously require further updates and support to be future-proof and further establish itself in the

community.

Relying on this new tool, chapters 4 and 5 present studies on data recorded at field sites dominated by active volcanism. In Chapter 4, we investigated the influences on the seismic velocity using a large-N array at the Klyuchevskoy Volcanic Group (KVG) in Kamchatka, Russia, consisting of more than 100 seismic stations with only one year recording time. This dataset violates a crucial assumption taken in Green's function estimation via noise interferometry: Throughout time, tremors from different volcanoes dominate the wavefield. It can, thus, not be assumed to be stationary. We showed a machine learning-assisted approach to circumvent this issue and obtained temporally finely resolved dv/v estimates. Using these, we found that the seismic velocity changes are strongly dependent on the geological conditions at the corresponding station site. $\sim$10 months before an eruption at Bezymianny volcano, its surrounding stations register a dv/v increase coinciding with surface deformation of the volcanic edifice.

In this thesis' third study, Chapter 5, we analysed data collected at Mount St. Helens (MSH) in Washington, United States of America. The seismic network at MSH has been in operation for a remarkably long period and has recorded continuous seismic waveform data since 1998. However, various equipment changes and upgrades have been performed over time, requiring us to compensate for in the PII algorithm. We address the problem using a spatial inversion, quantifying the changing spatial sensitivity of Rayleigh waves with the addition and removal of further stations. In the final velocity change estimate, we observed a drop with the initiation of MSH's 2004-2008 eruption, from which we inferred an unplugging, causing a sudden pressure decrease in the volcanic conduit. After 2017, dv/v increased above MSH's plumbing system. This seismic velocity change, a decreased seismic event rate, the end of the surface reinflation, and a temporal gravity anomaly (Battaglia et al., 2018) indicate a slowing of the magma recharging processes at depth.

6.1 Validity of the Underlying Assumptions in Passive Image Interferometry

As outlined in Chapter 4, PII grounds on several assumptions concerning the medium and, more importantly, the temporal and spatial distribution of the ambient seismic noise sources. Firstly, the correlation function (CF) will only be identical to the medium's Green's function if the noise sources are distributed homogeneously in the far field (Aki, 1957; Campillo & Paul, 2003). For PII, an actual Green's function is strictly not required. Instead, one can investigate changes in a partial Green's function, which might overrepresent parts of the medium illuminated more strongly by unevenly distributed noise sources. However, this noise field should remain stable (Hadziioannou et al., 2009).

The fluctuating noise field violates this assumption for the dataset presented in Chapter 4. In the case of Kamchatka, strong volcanic tremors cause the non-stationarity of the noise field, which may generally cause an issue at several volcanoes. While we demonstrate that one can circumvent this issue by identifying similar partial Green's functions using a clustering algorithm, it somewhat limits the applicability for volcano monitoring. Firstly, monitoring requires an automation of the method. However, automating clustering and subsequent PII monitoring poses an additional hurdle. Secondly, the dv/v time series created from different clusters are not directly comparable. Hence, velocity changes may remain undetected if they coincide with the transition between clusters. However, the cluster transition could be used as a monitoring criterion itself as it indicates changing dynamics within the volcanic conduit (see A. Yates et al., 2023).

In conclusion, while non-homogeneous and non-stationary noise fields might pose an additional challenge, they do not prevent employing PII as an additional criterion in volcano monitoring.

6.2 Unravelling the Physics Behind Changes in the Seismic Velocity

In chapters 4 and 5, we found that multiple processes impact the seismic velocity and the medium's scattering properties. However, the physical laws governing some of these mechanisms remain elusive. To unravel the forcing on the seismic velocity, a deeper understanding of its components is required. Below, I attempt to provide a short review of the different mechanisms that contribute significantly to dv/v observations in field data and, in my opinion, would benefit from further investigation.

Still, microscopically damage and healing processes, for example, remain elusive, and no physical models link observations and theory. Currently, various empirical models to explain the damage-healing hysteresis have been proposed (e.g., Berjamin et al., 2017; Lyakhovsky et al., 1997; Niu et al., 2024; Sens-Schönfelder et al., 2019) and it seems that the nonlinear non-classical effect originates from effects at the grain boundaries (Darling et al., 2004). Having physical models available would not only help to illuminate the processes responsible for dv/v variations in geophysical field surveys but also be a great stride for non-destructive testing, where CWI is commonly applied (e.g. Diewald et al., 2022; Grabke et al., 2021; Legland et al., 2017; Xue et al., 2022).

In contrast to the nonlinear non-classical elasticity, the stress-dependent change of wave propagation velocities, also known as the acoustoelastic effect (see, e.g., Pao, 1987), is better understood. This effect results in a wave speed increase with increasing stress. Acoustoelasticity is a material constant determining the change of a material's compliance under stress (Abiza et al., 2012). This relationship is an extension of Hooke's law, linking stress and strain (see, e.g., Shearer, 2019), and consists of a linear and a nonlinear component (Johnson & Rasolofosaon, 1996), sometimes referred to as the classical linear and nonlinear elasticity. Physically,

the effect is interpreted as the closing of preexisting (micro)pores and cracks in the medium. Many studies invoke this effect to explain velocity changes coinciding with pressure changes in volcanic plumbing systems (e.g., Donaldson et al., 2017, and chapters 4 and 5).

Variations in pore space saturation and content are the final factors significantly impacting dv/v in field studies. The pore saturation impacts the seismic velocity due to the pore pressure-induced change in effective stress. Fokker et al. (2021) quantified the relationship between dv/v and the pore pressure based on the induced stresses and the medium-dependent pore pressure diffusion. Recently, Fokker et al. (2023) extended their method into a theory applicable to 4D problems (i.e., a 3D space extended into the time domain). Also, the pores' content can influence the medium's wave speed and scattering properties. For example, in Chapter 5, we observed a dv/v increase during times of ground freezing. Effectively, this is due to the ground's overall increased stiffness (i.e., shear modulus, see Chapter 2) due to frozen pore waters. Simultaneously, the scattering properties of the medium will be affected when the properties of the pore space are changing. For PII investigations, this signifies a coherence change at those times (Thery et al., 2020). Further development of models that quantify the expected frequency (i.e., depth) dependent changes in the coherence upon changing the pore space content and saturation could yield an additional tool to investigate changes in ground moisture or, for the case of volcano monitoring, hydrothermal fluids.

To deepen the understanding of the outlined mechanisms, it would be necessary to evaluate them separately in controlled laboratory environments. Ultimately, by linking theory, laboratory-scale, and field data, the scientific community will benefit by being able to unravel the various influences in complex composite dv/v time series like the ones presented in chapters 4 and 5 of this thesis.

6.3 Towards Automated Volcanic Eruption Forecasting with Seismic Velocity Changes

In this thesis, we demonstrated that passive image interferometry (PII) can detect changes in the subsurface caused by volcanic processes. In contrast to volcano monitoring techniques employing tiltmeters, GNSS, or INSAR, which measure surface deformation, seismic velocity changes can detect structural changes in the subsurface that do not necessarily cause surface effects. PII can also be used for aseismic processes. In addition, PII exploits the energy of the ubiquitous ambient seismic noise and does not require any active shots or passive seismicity, making it ideal for continuous monitoring systems. However, it is crucial to emphasise that the presented studies and almost all studies in the literature were performed on historical data after an eruption occurred. To the best of my knowledge, there is currently only one example of real-time PII monitoring at an active volcano executed at Piton de La Fournaise (La Reúnion) between 2006 and 2007 (for details, see Duputel et al., 2009). In future work, I would encourage more real-time ambient noise monitoring studies at active volcanoes to demonstrate their feasibility and usefulness. Combining dv/v with established proxies, such as Real-time Seismic-Amplitude Measurement (RSAM) or ground deformation, will decrease the uncertainty of eruption forecasting and early warning. This thesis paves the way towards real-time monitoring, as outlined below.

In Chapter 3, we developed a tool easily adaptable to real-time monitoring applications. Its high computational efficiency will allow for computations of seismic velocity changes orders of magnitude faster than real-time, even for the very largest datasets, for example, recorded by fibre optics systems (i.e., distributed acoustic sensing). Its flexibility makes it easy for individual volcano observatories to introduce custom pre- and post-processing steps that may be required depending on the

local instrumentation, data quality, and properties of the regional ambient field (as was necessary for chapters 4 and 5).

In Chapter 4, we showed that seismic velocity changes preceded an eruption at Bezymianny volcano. Simultaneously, we demonstrated that, when combined with a clustering approach, PII can also be employed for non-stationary wave fields. This is of importance since non-stationary wavefields are particularly prevalent at active volcanoes due to volcanic tremors.

Chapter 5 focuses on seismic velocity changes at Mount St. Helens (MSH). We found a seismic velocity drop due to a pressure decrease in the volcanic conduit. We also observed a seismic velocity increase, from which we inferred a decreasing magma supply rate at depth. In addition, we showed that even with constantly changing instrumentation PII can to some extent be normalised to yield a continuous velocity change time series.

Another lesson learned from chapters 4 and 5 is that data from different volcanoes might require vastly different processing strategies. Also, different volcanoes might exhibit contrasting dynamics in terms of changes in seismic velocity. Before rolling out an automated real-time monitoring system, one should tune the required parameters by processing historical data recorded at the location of interest, as facilitated by SeisMIC's adaptable processing schemes.

Declaration

Hiermit versichere ich, dass ich die vorliegende Dissertation ohne unzulässige Hilfe Dritter und ohne Benutzung anderer als der angegebenen Literatur angefertigt wurde. Die Stellen der Arbeit, die anderen Werken wörtlich oder inhaltlich entnommen sind, wurden durch entsprechende Angaben der Quellen kenntlich gemacht. Diese Arbeit hat in gleicher oder ähnlicher Form noch keiner Prüfungsbehörde vorgelegen. Die deutsche Kurzfassung wurde mit Hilfe einer Übersetzungssoftware erstellt. Die grammatikalische Korrektheit und Rechtschreibung dieser Arbeit wurde von einer automatisierten Software unterstützt von einer künstlichen Intelligenz (KI) überprüft. Diese Dissertation enhält keinerlei KI-generierte Inhalte.

I hereby declare that except where specific reference is made to the work of others, the contents of this dissertation are original and have not been submitted in whole or in part for consideration for any other degree or qualification in this or any other university. This dissertation is my own work and contains nothing which is the outcome of work done in collaboration with others except as declared and specified in

the text. I created the German Abstract with the help of translation software. The thesis' grammar and orthographic soundness were verified using artificial intelligence (AI) accelerated software. This thesis does not contain any AI-generated content.

Peter Makus

Potsdam, 2024

Bibliography

Abiza, Z., Destrade, M., & Ogden, R. W. (2012). Large acoustoelastic effect. *Wave Motion*, *49*(2), 364–374. https://doi.org/10.1016/j.wavemoti.2011.12.002

Aizawa, K., Kanda, W., Ogawa, Y., Iguchi, M., Yokoo, A., Yakiwara, H., & Sugano, T. (2011). Temporal changes in electrical resistivity at Sakurajima volcano from continuous magnetotelluric observations. *Journal of Volcanology and Geothermal Research*, *199*(1), 165–175. https://doi.org/10.1016/j.jvolgeores.2010.11.003

Aki, K. (1957). Space and time spectra of stationary stochastic waves, with special reference to microtremors. *Bulletin of the Earthquake Research Institute*, *35*, 415–456.

Albaric, J., Kühn, D., Ohrnberger, M., Langet, N., Harris, D., Polom, U., Lecomte, I., & Hillers, G. (2021). Seismic Monitoring of Permafrost in Svalbard, Arctic Norway. *Seismological Research Letters*, *92*(5), 2891–2904. https://doi.org/10.1785/0220200470

Andajani, R. D., Tsuji, T., Snieder, R., & Ikeda, T. (2020). Spatial and temporal influence of rainfall on crustal pore pressure based on seismic velocity monitoring. *Earth, Planets and Space*, *72*(1), 177. https://doi.org/10.1186/s40623-020-01311-1

Ardhuin, F., Gualtieri, L., & Stutzmann, E. (2019, April). Physics of Ambient Noise Generation by Ocean Waves. In N. Nakata, L. Gualtieri, & A. Fichtner (Eds.), *Seismic Ambient Noise* (pp. 69–108). Cambridge University Press. https://doi.org/10.1017/9781108264808

Arrowsmith, S. J., Trugman, D. T., MacCarthy, J., Bergen, K. J., Lumley, D., & Magnani, M. B. (2022). Big Data Seismology. *Reviews of Geophysics*, *60*(2), e2021RG000769. https://doi.org/10.1029/2021RG000769

Asnar, M., Sens-Schönfelder, C., Bonnelye, A., & Dresen, G. (2023, February). *Non-classical, non-linear elasticity in rocks: Experiments in a triaxial cell with pore pressure control* (tech. rep. No. EGU23-8050). Copernicus Meetings. https://doi.org/10.5194/egusphere-egu23-8050

Barajas, A., Poli, P., D'Agostino, N., Margerin, L., & Campillo, M. (2021). Separation of Poroelastic and Elastic Processes of an Aquifer From Tectonic Phenomena Using Geodetic, Seismic, and Meteorological Data in the Pollino Region, Italy. *Geochemistry, Geophysics, Geosystems*, *22*(11), e2021GC009742. https://doi.org/10.1029/2021GC009742

Barbe, K., Pintelon, R., & Schoukens, J. (2010). Welch Method Revisited: Nonparametric Power Spectrum Estimation Via Circular Overlap. *IEEE Transactions on Signal Processing*, *58*(2), 553–565. https://doi.org/10.1109/TSP.2009.2031724

Barker, M., Chue Hong, N. P., Katz, D. S., Lamprecht, A.-L., Martinez-Ortiz, C., Psomopoulos, F., Harrow, J., Castro, L. J., Gruenpeter, M., Martinez, P. A., &

Honeyman, T. (2022). Introducing the FAIR Principles for research software. *Scientific Data*, *9*(1), 622. https://doi.org/10.1038/s41597-022-01710-x

Baron, D., & Ménard, B. (2021). Extracting the Main Trend in a Data Set: The Sequencer Algorithm. *The Astrophysical Journal*, *916*(2), 91. https://doi.org/10.3847/1538-4357/abfc4d

Battaglia, M., Lisowski, M., Dzurisin, D., Poland, M. P., Schilling, S., Diefenbach, A., & Wynn, J. (2018). Mass Addition at Mount St. Helens, Washington, Inferred From Repeated Gravity Surveys. *Journal of Geophysical Research: Solid Earth*, *123*(2), 1856–1874. https://doi.org/10.1002/2017JB014990

Battaglia, M., Gottsmann, J., Carbone, D., & Fernández, J. (2008). 4D volcano gravimetry. *GEOPHYSICS*, *73*(6), WA3–WA18. https://doi.org/10.1190/1.2977792

Bedrosian, P. A., Peacock, J. R., Bowles-Martinez, E., Schultz, A., & Hill, G. J. (2018). Crustal inheritance and a top-down control on arc magmatism at Mount St Helens. *Nature Geoscience*, *11*(11), 865–870. https://doi.org/10.1038/s41561-018-0217-2

Belousov, A., Voight, B., Belousova, M., & Muravyev, Y. (2000). Tsunamis generated by subaquatic volcanic explosions: Unique data from 1996 Eruption in Karymskoye Lake, Kamchatka, Russia. *Pure and Applied Geophysics*, *157*(6-8), 1135–1143. https://doi.org/10.1007/s000240050021

Bensen, G. D., Ritzwoller, M. H., Barmin, M. P., Levshin, A. L., Lin, F., Moschetti, M. P., Shapiro, N. M., & Yang, Y. (2007). Processing seismic ambient noise data to obtain reliable broad-band surface wave dispersion measurements. *Geophysical Journal International*, *169*(3), 1239–1260. https://doi.org/10.1111/j.1365-246X.2007.03374.x

Berezhnev, Y., Belovezhets, N., Shapiro, N., & Koulakov, I. (2023). Temporal changes of seismic velocities below Bezymianny volcano prior to its explosive eruption

on 20.12.2017. *Journal of Volcanology and Geothermal Research*, *433*, 107735. https://doi.org/10.1016/j.jvolgeores.2022.107735

Berjamin, H., Favrie, N., Lombard, B., & Chiavassa, G. (2017). Nonlinear waves in solids with slow dynamics: An internal-variable model. *Proceedings of the Royal Society A: Mathematical, Physical and Engineering Sciences*, *473*(2201), 20170024. https://doi.org/10.1098/rspa.2017.0024

Beyreuther, M., Barsch, R., Krischer, L., Megies, T., Behr, Y., & Wassermann, J. (2010). ObsPy: A Python Toolbox for Seismology. *Seismological Research Letters*, *81*(3), 530–533. https://doi.org/10.1785/gssrl.81.3.530

Biggs, J., & Pritchard, M. E. (2017). Global Volcano Monitoring: What Does It Mean When Volcanoes Deform? *Elements*, *13*(1), 17–22. https://doi.org/10.2113/gselements.13.1.17

Brenguier, F., Campillo, M., Hadziioannou, C., Shapiro, N. M., Nadeau, R. M., & Larose, E. (2008). Postseismic Relaxation Along the San Andreas Fault at Parkfield from Continuous Seismological Observations. *Science*, *321*(5895), 1478–1481. https://doi.org/10.1126/science.1160943

Brenguier, F., Campillo, M., Takeda, T., Aoki, Y., Shapiro, N. M., Briand, X., Emoto, K., & Miyake, H. (2014). Mapping pressurized volcanic fluids from induced crustal seismic velocity drops. *Science*, *345*(6192), 80–82. https://doi.org/10.1126/science.1254073

Brenguier, F., Clarke, D., Aoki, Y., Shapiro, N. M., Campillo, M., & Ferrazzini, V. (2011). Monitoring volcanoes using seismic noise correlations. *Comptes Rendus - Geoscience*, *343*(8-9), 633–638. https://doi.org/10.1016/j.crte.2010.12.010

Brenguier, F., Rivet, D., Obermann, A., Nakata, N., Boué, P., Lecocq, T., Campillo, M., & Shapiro, N. (2016). 4-D noise-based seismology at volcanoes: Ongoing

efforts and perspectives. *Journal of Volcanology and Geothermal Research*, *321*, 182–195. https://doi.org/10.1016/j.jvolgeores.2016.04.036

Brenguier, F., Shapiro, N. M., Campillo, M., Ferrazzini, V., Duputel, Z., Coutant, O., & Nercessian, A. (2008). Towards forecasting volcanic eruptions using seismic noise. *Nature Geoscience*, *1*(2), 126–130. https://doi.org/10.1038/ngeo104

Budi-Santoso, A., Lesage, P., Dwiyono, S., Sumarti, S., Subandriyo, Surono, Jousset, P., & Metaxian, J. P. (2013). Analysis of the seismic activity associated with the 2010 eruption of Merapi Volcano, Java. *Journal of Volcanology and Geothermal Research*, *261*(November 2010), 153–170. https://doi.org/10.1016/j.jvolgeores.2013.03.024

Bürgmann, R., Kogan, M. G., Steblov, G. M., Hilley, G., Levin, V. E., & Apel, E. (2005). Interseismic coupling and asperity distribution along the Kamchatka subduction zone. *Journal of Geophysical Research: Solid Earth*, *110*(7), 1–17. https://doi.org/10.1029/2005JB003648

Campillo, M., & Paul, A. (2003). Long-Range Correlations in the Diffuse Seismic Coda. *Science*, *299*(5606), 547–549. https://doi.org/10.1126/science.1078551

Cascades Volcano Observatory/USGS. (2001). Cascade chain volcano monitoring. https://doi.org/10.7914/SN/CC

Casey, R., Templeton, M. E., Sharer, G., Keyson, L., Weertman, B. R., & Ahern, T. (2018). Assuring the Quality of IRIS Data with MUSTANG. *Seismological Research Letters*, *89*(2A), 630–639. https://doi.org/10.1785/0220170191

Cassidy, M., Manga, M., Cashman, K., & Bachmann, O. (2018). Controls on explosive-effusive volcanic eruption styles. *Nature Communications*, *9*(1), 2839. https://doi.org/10.1038/s41467-018-05293-3

Caudron, C., Aoki, Y., Lecocq, T., De Plaen, R., Soubestre, J., Mordret, A., Seydoux, L., & Terakawa, T. (2022). Hidden pressurized fluids prior to the 2014 phreatic

eruption at Mt Ontake. *Nature Communications*, *13*(1), 6145. https://doi.org/10.1038/s41467-022-32252-w

Caudron, C., Girona, T., Jolly, A., Christenson, B., Savage, M. K., Carniel, R., Lecocq, T., Kennedy, B., Lokmer, I., Yates, A., Hamling, I., Park, I., Kilgour, G., & Mazot, A. (2021). A quest for unrest in multiparameter observations at Whakaari/White Island volcano, New Zealand 2007–2018. *Earth, Planets and Space*, *73*(1), 195. https://doi.org/10.1186/s40623-021-01506-0

Caudron, C., Girona, T., Taisne, B., Suparjan, Gunawan, H., Kristianto, & Kasbani. (2019). Change in seismic attenuation as a long-term precursor of gas-driven eruptions. *Geology*, *47*(7), 632–636. https://doi.org/10.1130/G46107.1

Chaves, E. J., & Schwartz, S. Y. (2016). Monitoring transient changes within overpressured regions of subduction zones using ambient seismic noise. *Science Advances*, *2*(1), 1–7. https://doi.org/10.1126/sciadv.1501289

Chester, D. K., Degg, M., Duncan, A. M., & Guest, J. E. (2000). The increasing exposure of cities to the effects of volcanic eruptions: A global survey. *Global Environmental Change Part B: Environmental Hazards*, *2*(3), 89–103. https://doi.org/10.3763/ehaz.2000.0214

Chouet, B. A. (1996). Long-period volcano seismicity: Its source and use in eruption forecasting. *Nature*, *380*(6572), 309–316. https://doi.org/10.1038/380309a0

Chouet, B. A., & Matoza, R. S. (2013). A multi-decadal view of seismic methods for detecting precursors of magma movement and eruption. *Journal of Volcanology and Geothermal Research*, *252*, 108–175. https://doi.org/10.1016/j.jvolgeores.2012.11.013

Clements, T., & Denolle, M. A. (2023). The Seismic Signature of California's Earthquakes, Droughts, and Floods. *Journal of Geophysical Research: Solid Earth*, *128*(1), e2022JB025553. https://doi.org/10.1029/2022JB025553

Clements, T., & Denolle, M. A. (2018). Tracking Groundwater Levels Using the Ambient Seismic Field. *Geophysical Research Letters*, *45*(13), 6459–6465. https://doi.org/10.1029/2018GL077706

Clements, T., & Denolle, M. A. (2021). SeisNoise.jl: Ambient Seismic Noise Cross Correlation on the CPU and GPU in Julia. *Seismological Research Letters*, *92*(1), 517–527. https://doi.org/10.1785/0220200192

Collette, A., Kluyver, T., Caswell, T. A., Tocknell, J., Kieffer, J., Scopatz, A., Dale, D., Chen, Jelenak, A., payno, juliagarriga, VINCENT, T., Sciarelli, P., Valls, V., Kofoed Pedersen, U., jakirkham, Raspaud, M., Parsons, A., Abbasi, H., ... Hole, L. (2020). H5py/h5py: 3.1.0. *Zenodo*. https://doi.org/10.5281/zenodo.4250762

ADS Bibcode: 2020zndo...4250762C.

Colombero, C., Baillet, L., Comina, C., Jongmans, D., Larose, E., Valentin, J., & Vinciguerra, S. (2018). Integration of ambient seismic noise monitoring, displacement and meteorological measurements to infer the temperature-controlled long-term evolution of a complex prone-to-fall cliff. *Geophysical Journal International*, *213*(3), 1876–1897. https://doi.org/10.1093/gji/ggy090

Coppola, D., Marco, L., Massimetti, F., Hainzl, S., Shevchenko, A. V., Mania, R., M, N., Shapiro, & Walter, T. R. (2021). Thermal remote sensing reveals communication between volcanoes of the Klyuchevskoy Volcanic Group. *Scientific Reports*, *11*(1), 1–16. https://doi.org/10.1038/s41598-021-92542-z

Crosbie, K. J., Abers, G. A., Mann, M. E., Janiszewski, H. A., Creager, K. C., Ulberg, C. W., & Moran, S. C. (2019). Shear Velocity Structure From Ambient Noise and Teleseismic Surface Wave Tomography in the Cascades Around Mount St. Helens. *Journal of Geophysical Research: Solid Earth*, *124*(8), 8358–8375. https://doi.org/10.1029/2019JB017836

Dalcin, L., & Fang, Y.-L. L. (2021). Mpi4py: Status Update After 12 Years of Development. *Computing in Science & Engineering*, *23*(4), 47–54. https://doi.org/10.1109/MCSE.2021.3083216

Darling, T. W., TenCate, J. A., Brown, D. W., Clausen, B., & Vogel, S. C. (2004). Neutron diffraction study of the contribution of grain contacts to nonlinear stress-strain behavior. *Geophysical Research Letters*, *31*(16). https://doi.org/10.1029/2004GL020463

De Fazio, T. L., Aki, K., & Alba, J. (1973). Solid earth tide and observed change in the in situ seismic velocity. *Journal of Geophysical Research (1896-1977)*, *78*(8), 1319–1322. https://doi.org/10.1029/JB078i008p01319

De Plaen, R. S., Cannata, A., Cannavo', F., Caudron, C., Lecocq, T., & Francis, O. (2019). Temporal changes of seismic velocity caused by volcanic activity at Mt. Etna revealed by the autocorrelation of ambient seismic noise. *Frontiers in Earth Science*, *6*(January), 1–11. https://doi.org/10.3389/feart.2018.00251

De Plaen, R. S., Lecocq, T., Caudron, C., Ferrazzini, V., & Francis, O. (2016). Single-station monitoring of volcanoes using seismic ambient noise. *Geophysical Research Letters*, *43*(16), 8511–8518. https://doi.org/10.1002/2016GL070078

De Siena, L., Thomas, C., Waite, G. P., Moran, S. C., & Klemme, S. (2014). Attenuation and scattering tomography of the deep plumbing system of Mount St. Helens. *Journal of Geophysical Research: Solid Earth*, *119*(11), 8223–8238. https://doi.org/10.1002/2014JB011372

Diewald, F., Epple, N., Kraenkel, T., Gehlen, C., & Niederleithinger, E. (2022). Impact of External Mechanical Loads on Coda Waves in Concrete. *Materials*, *15*(16), 5482. https://doi.org/10.3390/ma15165482

Donaldson, C., Winder, T., Caudron, C., & White, R. S. (2019). Crustal seismic velocity responds to a magmatic intrusion and seasonal loading in Iceland's

Northern Volcanic Zone. *Science Advances*, *5*(11), eaax6642. https://doi.org/10.1126/sciadv.aax6642

Donaldson, C., Caudron, C., Green, R. G., Thelen, W. A., & White, R. S. (2017). Relative seismic velocity variations correlate with deformation at Kīlauea volcano. *Science Advances*, *3*(6), 1–12. https://doi.org/10.1126/sciadv.1700219

Dong, D., Fang, P., Bock, Y., Cheng, M. K., & Miyazaki, S. (2002). Anatomy of apparent seasonal variations from GPS-derived site position time series. *Journal of Geophysical Research: Solid Earth*, *107*(B4), ETG 9-1-ETG 9–16. https://doi.org/10.1029/2001JB000573

Dorendorf, F., Wiechert, U., & Wörner, G. (2000). Hydrated sub-are mantle: A source for the Kluchevskoy volcano, Kamchatka/Russia. *Earth and Planetary Science Letters*, *175*(1-2), 69–86. https://doi.org/10.1016/s0012-821x(99)00288-5

Droznin, D. V., Shapiro, N. M., Droznina, S. Y., Senyukov, S. L., Chebrov, V. N., & Gordeev, E. I. (2015). Detecting and locating volcanic tremors on the Klyuchevskoy group of volcanoes (Kamchatka) based on correlations of continuous seismic records. *Geophysical Journal International*, *203*(2), 1001–1010. https://doi.org/10.1093/gji/ggv342

Duputel, Z., Ferrazzini, V., Brenguier, F., Shapiro, N., Campillo, M., & Nercessian, A. (2009). Real time monitoring of relative velocity changes using ambient seismic noise at the Piton de la Fournaise volcano (La Réunion) from January 2006 to June 2007. *Journal of Volcanology and Geothermal Research*, *184*(1), 164–173. https://doi.org/10.1016/j.jvolgeores.2008.11.024

Einarsson, P. (2018). Short-Term Seismic Precursors to Icelandic Eruptions 1973–2014. *Frontiers in Earth Science*, *6*.

Eisler, J. D. (1967). Investigation of a method for determining stress accumulation at depth. *Bulletin of the Seismological Society of America*, *57*(5), 891–911. https://doi.org/10.1785/BSSA0570050891

Fedotov, S. A., Zharinov, N. A., & Gontovaya, L. I. (2010). The magmatic system of the Klyuchevskaya group of volcanoes inferred from data on its eruptions, earthquakes, deformation, and deep structure. *Journal of Volcanology and Seismology*, *4*(1), 1–33. https://doi.org/10.1134/S074204631001001X

Feng, K.-F., Huang, H.-H., Hsu, Y.-J., & Wu, Y.-M. (2021). Controls on Seasonal Variations of Crustal Seismic Velocity in Taiwan Using Single-Station Cross-Component Analysis of Ambient Noise Interferometry. *Journal of Geophysical Research: Solid Earth*, *126*(11), e2021JB022650. https://doi.org/10.1029/2021JB022650

Fichtner, A., & Tsai, V. C. (2019, April). Theoretical Foundations of Noise Interferometry. In *Seismic Ambient Noise* (pp. 109–143). Cambridge University Press. https://doi.org/10.1017/9781108264808.006

Fokker, E., Ruigrok, E., Hawkins, R., & Trampert, J. (2021). Physics-Based Relationship for Pore Pressure and Vertical Stress Monitoring Using Seismic Velocity Variations. *Remote Sensing*, *13*(14), 2684. https://doi.org/10.3390/rs13142684

Fokker, E., Ruigrok, E., Hawkins, R., & Trampert, J. (2023). 4D Physics-Based Pore Pressure Monitoring Using Passive Image Interferometry. *Geophysical Research Letters*, *50*(5), e2022GL101254. https://doi.org/10.1029/2022GL101254

Fokker, E., Ruigrok, E., & Trampert, J. (2024). On the temperature sensitivity of near-surface seismic wave speeds: Application to the Groningen region, the Netherlands. *Geophysical Journal International*, *237*(2), 1129–1141. https://doi.org/10.1093/gji/ggae102

Fontaine, F. R., Roult, G., Michon, L., Barruol, G., & Muro, A. D. (2014). The 2007 eruptions and caldera collapse of the Piton de la Fournaise volcano (La Réunion Island) from tilt analysis at a single very broadband seismic station.

Geophysical Research Letters, *41*(8), 2803–2811. https://doi.org/10.1002/2014GL059691

Fournier, T. J., Pritchard, M. E., & Riddick, S. N. (2010). Duration, magnitude, and frequency of subaerial volcano deformation events: New results from Latin America using InSAR and a global synthesis. *Geochemistry, Geophysics, Geosystems*, *11*(1). https://doi.org/10.1029/2009GC002558

Gabrielli, S., De Siena, L., Napolitano, F., & Del Pezzo, E. (2020). Understanding seismic path biases and magmatic activity at Mount St Helens volcano before its 2004 eruption. *Geophysical Journal International*, *222*(1), 169–188. https://doi.org/10.1093/gji/ggaa154

Gassenmeier, M., Sens-Schönfelder, C., Delatre, M., & Korn, M. (2015). Monitoring of environmental influences on seismic velocity at the geological storage site for CO2 in Ketzin (Germany) with ambient seismic noise. *Geophysical Journal International*, *200*(1), 524–533. https://doi.org/10.1093/gji/ggu413

Gassenmeier, M., Sens-Schönfelder, C., Eulenfeld, T., Bartsch, M., Victor, P., Tilmann, F., & Korn, M. (2016). Field observations of seismic velocity changes caused by shaking-induced damage and healing due to mesoscopic nonlinearity. *Geophysical Journal International*, *204*(3), 1490–1502. https://doi.org/10.1093/gji/ggv529

Girina, O. A., Manevich, A. G., Melnikov, D. V., Nuzhdaev, A. A., & Petrova, E. G. (2019). The 2016 Eruptions in Kamchatka and on the North Kuril Islands: The Hazard to Aviation. *Journal of Volcanology and Seismology*, *13*(3), 157–171. https://doi.org/10.1134/S0742046319030047

Glasgow, M. E., Schmandt, B., & Hansen, S. M. (2018). Upper crustal low-frequency seismicity at Mount St. Helens detected with a dense geophone array. *Journal of Volcanology and Geothermal Research*, *358*, 329–341. https://doi.org/10.1016/j.jvolgeores.2018.06.006

Gómez-García, C., Brenguier, F., Boué, P., Shapiro, N. M., Droznin, D. V., Droznina, S. Y., Senyukov, S. L., & Gordeev, E. I. (2018). Retrieving robust noise-based seismic velocity changes from sparse data sets: Synthetic tests and application to Klyuchevskoy volcanic group (Kamchatka). *Geophysical Journal International*, 1218–1236. https://doi.org/10.1093/gji/ggy190

Grabke, S., Clauß, F., Bletzinger, K.-U., Ahrens, M. A., Mark, P., & Wüchner, R. (2021). Damage Detection at a Reinforced Concrete Specimen with Coda Wave Interferometry. *Materials*, *14*(17), 5013. https://doi.org/10.3390/ma14175013

Grady, T., Brown, R. L., Adams, E., & Sato, A. (1982). An evaluation of heat flow and its geological implications on Mt. St. Helens. *Geophysical Research Letters*, *9*(4), 377–379. https://doi.org/10.1029/GL009i004p00377

Grant, G. E., Major, J. J., & Lewis, S. L. (2017). *The geologic, geomorphic, and hydrologic context underlying options for long-term management of the Spirit Lake outlet near Mount St. Helens, Washington.* U.S. Department of Agriculture, Forest Service, Pacific Northwest Research Station. https://doi.org/10.2737/PNW-GTR-954

Greco, F., Currenti, G., D'Agostino, G., Germak, A., Napoli, R., Pistorio, A., & Del Negro, C. (2012). Combining relative and absolute gravity measurements to enhance volcano monitoring. *Bulletin of Volcanology*, *74*(7), 1745–1756. https://doi.org/10.1007/s00445-012-0630-0

Green, R. G., Sens-Schönfelder, C., Shapiro, N., Koulakov, I., Tilmann, F., Dreiling, J., Luehr, B., Jakovlev, A., Abkadyrov, I., Droznin, D., & Gordeev, E. (2020). Magmatic and Sedimentary Structure beneath the Klyuchevskoy Volcanic Group, Kamchatka, From Ambient Noise Tomography. *Journal of Geophysical Research: Solid Earth*, *125*(3). https://doi.org/10.1029/2019JB018900

Guillemot, A., Helmstetter, A., Larose, É., Baillet, L., Garambois, S., Mayoraz, R., & Delaloye, R. (2020). Seismic monitoring in the Gugla rock glacier (Switzerland): Ambient noise correlation, microseismicity and modelling. *Geophysical Journal International*, *221*(3), 1719–1735. https://doi.org/10.1093/gji/ggaa097

Guillemot, A., Van Herwijnen, A., Larose, E., Mayer, S., & Baillet, L. (2021). Effect of snowfall on changes in relative seismic velocity measured by ambient noise correlation. *Cryosphere*, *15*(12), 5805–5817. https://doi.org/10.5194/tc-15-5805-2021

Hadziioannou, C., Larose, E., Baig, A., Roux, P., & Campillo, M. (2011). Improving temporal resolution in ambient noise monitoring of seismic wave speed. *Journal of Geophysical Research: Solid Earth*, *116*(7), 1–10. https://doi.org/10.1029/2011JB008200

Hadziioannou, C., Larose, E., Coutant, O., Roux, P., & Campillo, M. (2009). Stability of monitoring weak changes in multiply scattering media with ambient noise correlation: Laboratory experiments. *The Journal of the Acoustical Society of America*, *125*(6), 3688–3695. https://doi.org/10.1121/1.3125345

Hansen, S. M., & Schmandt, B. (2015). Automated detection and location of microseismicity at Mount St. Helens with a large-N geophone array. *Geophysical Research Letters*, *42*(18), 7390–7397. https://doi.org/10.1002/2015GL064848

Harris, C. R., Millman, K. J., van der Walt, S. J., Gommers, R., Virtanen, P., Cournapeau, D., Wieser, E., Taylor, J., Berg, S., Smith, N. J., Kern, R., Picus, M., Hoyer, S., van Kerkwijk, M. H., Brett, M., Haldane, A., del Río, J. F., Wiebe, M., Peterson, P., ... Oliphant, T. E. (2020). Array programming with NumPy. *Nature*, *585*(7825), 357–362. https://doi.org/10.1038/s41586-020-2649-2

Heki, K. (2001). Seasonal Modulation of Interseismic Strain Buildup in Northeastern Japan Driven by Snow Loads. *Science*, *293*(5527), 89–92. https://doi.org/10.1126/science.1061056

Heki, K. (2003). Snow load and seasonal variation of earthquake occurrence in Japan. *Earth and Planetary Science Letters*, *207*(1), 159–164. https://doi.org/10.1016/S0012-821X(02)01148-2

Hersbach, H., Bell, B., Berrisford, P., Hirahara, S., Horányi, A., Muñoz-Sabater, J., Nicolas, J., Peubey, C., Radu, R., Schepers, D., Simmons, A., Soci, C., Abdalla, S., Abellan, X., Balsamo, G., Bechtold, P., Biavati, G., Bidlot, J., Bonavita, M., ... Thépaut, J. N. (2020). The ERA5 global reanalysis. *Quarterly Journal of the Royal Meteorological Society*, *146*(730), 1999–2049. https://doi.org/10.1002/qj.3803

Hill, D. P., Pollitz, F., & Newhall, C. (2002). Earthquake-Volcano Interactions. New measurements, statistical analyses, and models support can trigger subsequent long distance times scales. *Physics Today*, 41–47.

Hill, G. J., Caldwell, T. G., Heise, W., Chertkoff, D. G., Bibby, H. M., Burgess, M. K., Cull, J. P., & Cas, R. A. F. (2009). Distribution of melt beneath Mount St Helens and Mount Adams inferred from magnetotelluric data. *Nature Geoscience*, *2*(11), 785–789. https://doi.org/10.1038/ngeo661

Hillers, G., Ben-Zion, Y., Campillo, M., & Zigone, D. (2015). Seasonal variations of seismic velocities in the San Jacinto fault area observed with ambient seismic noise. *Geophysical Journal International*, *202*(2), 920–932. https://doi.org/10.1093/gji/ggv151

Hillers, G., Campillo, M., & Ma, K. F. (2014). Seismic velocity variations at TCDP are controlled by MJO driven precipitation pattern and high fluid discharge properties. *Earth and Planetary Science Letters*, *391*, 121–127. https://doi.org/10.1016/j.epsl.2014.01.040

Hobiger, M., Wegler, U., Shiomi, K., & Nakahara, H. (2012). Coseismic and postseismic elastic wave velocity variations caused by the 2008 Iwate-Miyagi Nairiku earthquake, Japan. *Journal of Geophysical Research: Solid Earth*, *117*(B9). https://doi.org/10.1029/2012JB009402

Hobiger, M., Wegler, U., Shiomi, K., & Nakahara, H. (2014). Single-station cross-correlation analysis of ambient seismic noise: Application to stations in the surroundings of the 2008 Iwate-Miyagi Nairiku earthquake. *Geophysical Journal International*, *198*(1), 90–109. https://doi.org/10.1093/gji/ggu115

Hotovec-Ellis, A. J., Gomberg, J., Vidale, J. E., & Creager, K. C. (2014). A continuous record of intereruption velocity change at Mount St. Helens from coda wave interferometry. *Journal of Geophysical Research: Solid Earth*, *119*(3), 2199–2214. https://doi.org/10.1002/2013JB010742

Hotovec-Ellis, A. J., Vidale, J. E., Gomberg, J., Thelen, W., & Moran, S. C. (2015). Changes in seismic velocity during the first 14 months of the 2004-2008 eruption of Mount St. Helens, Washington. *Journal of Geophysical Research: Solid Earth*, *120*(9), 6226–6240. https://doi.org/10.1002/2015JB012101

Hunt, C. E., & MacCready, J. S. (1980). *The Short-term Economic Consequences of the Mount St. Helens Volcanic Eruptions in May and June, 1980* (tech. rep.). Washington State, Department of Commerce and Economic Development, Research Division.

Hunter, J. D. (2007). Matplotlib: A 2D Graphics Environment. *Computing in Science & Engineering*, *9*(03), 90–95. https://doi.org/10.1109/MCSE.2007.55

Illien, L., Sens-Schönfelder, C., & Ke, K.-Y. (2023). Resolving minute temporal seismic velocity changes induced by earthquake damage: The more stations, the merrier? *Geophysical Journal International*, *234*(1), 124–135. https://doi.org/10.1093/gji/ggad038

Ivanov, A. I., Koulakov, I. Y., West, M., Jakovlev, A. V., Gordeev, E. I., Senyukov, S., & Chebrov, V. N. (2016). Magma source beneath the Bezymianny volcano and its interconnection with Klyuchevskoy inferred from local earthquake seismic tomography. *Journal of Volcanology and Geothermal Research*, *323*, 62–71. https://doi.org/10.1016/j.jvolgeores.2016.04.010

Jack, I. (2017). 4D seismic — Past, present, and future. *The Leading Edge*, *36*(5), 386–392. https://doi.org/10.1190/tle36050386.1

James, S. R., Knox, H. A., Abbott, R. E., & Screaton, E. J. (2017). Improved moving window cross-spectral analysis for resolving large temporal seismic velocity changes in permafrost. *Geophysical Research Letters*, *44*(9), 4018–4026. https://doi.org/10.1002/2016GL072468

Jenkins, S. F., Wilson, _., Magill, C., Miller, V., Stewart, C., Blong, R., Marzocchi, W., Boulton, M., Bonadonna, C., & Costa, A. (2015, July). In S. C. Loughlin, S. Sparks, S. K. Brown, S. F. Jenkins, & C. Vye-Brown (Eds.), *Global Volcanic Hazards and Risk* (1st ed., pp. 173–222). Cambridge University Press. https://doi.org/10.1017/CBO9781316276273

Jiang, C., & Denolle, M. A. (2020). Noisepy: A new high-performance python tool for ambient-noise seismology. *Seismological Research Letters*, *91*(3), 1853–1866. https://doi.org/10.1785/0220190364

Johnson, P. A., & Rasolofosaon, P. N. J. (1996). Nonlinear elasticity and stress-induced anisotropy in rock. *Journal of Geophysical Research: Solid Earth*, *101*(B2), 3113–3124. https://doi.org/10.1029/95JB02880

Johnson, P. A., & Jia, X. (2005). Nonlinear dynamics, granular media and dynamic earthquake triggering. *Nature*, *437*(7060), 871–874. https://doi.org/10.1038/nature04015

Journeau, C., Shapiro, N. M., Seydoux, L., Soubestre, J., Koulakov, I. Y., Jakovlev, A. V., Abkadyrov, I., Gordeev, E. I., Chebrov, D. V., Droznin, D. V., Sens-

Schönfelder, C., Luehr, B. G., Tong, F., Farge, G., & Jaupart, C. (2022). Seismic tremor reveals active trans-crustal magmatic system beneath Kamchatka volcanoes. *Science Advances*, *8*(5), 1–12. https://doi.org/10.1126/sciadv.abj1571

Kayzar, T. M., Nelson, B. K., Bachmann, O., Bauer, A. M., & Izbekov, P. E. (2014). Deciphering petrogenic processes using Pb isotope ratios from time-series samples at Bezymianny and Klyuchevskoy volcanoes, Central Kamchatka Depression. *Contributions to Mineralogy and Petrology*, *168*(4), 1–28. https://doi.org/10.1007/s00410-014-1067-6

Kennedy, B. (2017). What effects do earthquakes have on volcanoes? *Geology*, *45*(8), 765–766. https://doi.org/10.1130/focus0820172.1

Kiryukhin, A. V., Rychkova, T. V., & Dubrovskaya, I. K. (2012). Formation of the hydrothermal system in Geysers Valley (Kronotsky Nature Reserve, Kamchatka) and triggers of the Giant Landslide. *Applied Geochemistry*, *27*(9), 1753–1766. https://doi.org/10.1016/j.apgeochem.2012.02.011

Kobrick, M., & Crippen, R. (2017). Srtmgl1: Nasa shuttle radar topography mission global 1 arc second v003.

Köpfli, M., Denolle, M. A., Thelen, W. A., Makus, P., & Malone, S. D. (2024). Examining 22 Years of Ambient Seismic Wavefield at Mount St. Helens. *Seismological Research Letters*. https://doi.org/10.1785/0220240079

Koranne, S. (2011). Hierarchical Data Format 5 : HDF5. In S. Koranne (Ed.), *Handbook of Open Source Tools* (pp. 191–200). Springer US.

Koulakov, I., Abkadyrov, I., Al Arifi, N., Deev, E., Droznina, S., Gordeev, E. I., Jakovlev, A., El Khrepy, S., Kulakov, R. I., Kugaenko, Y., Novgorodova, A., Senyukov, S., Shapiro, N., Stupina, T., & West, M. (2017). Three different types of plumbing system beneath the neighboring active volcanoes of Tolbachik, Bezymianny, and Klyuchevskoy in Kamchatka. *Journal of Geophys-*

ical Research: Solid Earth, *122*(5), 3852–3874. https://doi.org/10.1002/2017JB014082

Koulakov, I., Gordeev, E. I., Dobretsov, N. L., Vernikovsky, V. A., Senyukov, S., Jakovlev, A., & Jaxybulatov, K. (2013). Rapid changes in magma storage beneath the Klyuchevskoy group of volcanoes inferred from time-dependent seismic tomography. *Journal of Volcanology and Geothermal Research*, *263*, 75–91. https://doi.org/10.1016/j.jvolgeores.2012.10.014

Koulakov, I., Plechov, P., Mania, R., Walter, T. R., Smirnov, S. Z., Abkadyrov, I., Jakovlev, A., Davydova, V., Senyukov, S., Bushenkova, N., Novgorodova, A., Stupina, T., & Droznina, S. Y. (2021). Anatomy of the Bezymianny volcano merely before an explosive eruption on 20.12.2017. *Scientific Reports*, *11*(1), 1–12. https://doi.org/10.1038/s41598-021-81498-9

Koulakov, I., Shapiro, N. M., Sens-Schönfelder, C., Luehr, B. G., Gordeev, E. I., Jakovlev, A., Abkadyrov, I., Chebrov, D. V., Bushenkova, N., Droznina, S. Y., Senyukov, S. L., Novgorodova, A., & Stupina, T. (2020). Mantle and Crustal Sources of Magmatic Activity of Klyuchevskoy and Surrounding Volcanoes in Kamchatka Inferred From Earthquake Tomography. *Journal of Geophysical Research: Solid Earth*, *125*(10), e2020JB020097. https://doi.org/10.1029/2020JB020097

Koulakov, I. (2021). Seismic Tomography of Kamchatkan Volcanoes. *Russian Geology and Geophysics*, *1815*, 1–38. https://doi.org/10.2113/rgg20214380

La Spina, G., Arzilli, F., Burton, M. R., Polacci, M., & Clarke, A. B. (2022). Role of volatiles in highly explosive basaltic eruptions. *Communications Earth & Environment*, *3*(1), 1–13. https://doi.org/10.1038/s43247-022-00479-6

Lecocq, T., Caudron, C., & Brenguier, F. (2014). MSNoise, a Python Package for Monitoring Seismic Velocity Changes Using Ambient Seismic Noise. *Seismological Research Letters*, *85*(3), 715–726. https://doi.org/10.1785/0220130073

Lecocq, T., Hicks, S. P., Van Noten, K., van Wijk, K., Koelemeijer, P., De Plaen, R. S. M., Massin, F., Hillers, G., Anthony, R. E., Apoloner, M.-T., Arroyo-Solórzano, M., Assink, J. D., Büyükakpınar, P., Cannata, A., Cannavo, F., Carrasco, S., Caudron, C., Chaves, E. J., Cornwell, D. G., … Xiao, H. (2020). Global quieting of high-frequency seismic noise due to COVID-19 pandemic lockdown measures. *Science*, *369*(6509), 1338–1343. https://doi.org/10.1126/science.abd2438

Lecocq, T., Longuevergne, L., Pedersen, H. A., Brenguier, F., & Stammler, K. (2017). Monitoring ground water storage at mesoscale using seismic noise: 30 years of continuous observation and thermo-elastic and hydrological modeling. *Scientific Reports*, *7*(1). https://doi.org/10.1038/s41598-017-14468-9

Legland, J.-B., Zhang, Y., Abraham, O., Durand, O., & Tournat, V. (2017). Evaluation of crack status in a meter-size concrete structure using the ultrasonic nonlinear coda wave interferometry. *The Journal of the Acoustical Society of America*, *142*(4), 2233–2241. https://doi.org/10.1121/1.5007832

Lehto, H. L., Roman, D. C., & Moran, S. C. (2010). Temporal changes in stress preceding the 2004–2008 eruption of Mount St. Helens, Washington. *Journal of Volcanology and Geothermal Research*, *198*(1), 129–142. https://doi.org/10.1016/j.jvolgeores.2010.08.015

Lesage, P., Reyes-Dávila, G., & Arámbula-Mendoza, R. (2014). Large tectonic earthquakes induce sharp temporary decreases in seismic velocity in Volcán de Colima, Mexico. *Journal of Geophysical Research: Solid Earth*, *119*(5), 4360–4376. https://doi.org/10.1002/2013JB010884

Li, J., Song, X., Yang, Y., Li, M., Li, J., & Li, Y. (2021). Strong Seasonal Variations of Seismic Velocity in Eastern Margin of Tibetan Plateau and Sichuan Basin From Ambient Noise Interferometry. *Journal of Geophysical Research: Solid Earth*, *126*(11), e2021JB022600. https://doi.org/10.1029/2021JB022600

Lindner, F., Wassermann, J., & Igel, H. (2021). Seasonal Freeze-Thaw Cycles and Permafrost Degradation on Mt. Zugspitze (German/Austrian Alps) Revealed by Single-Station Seismic Monitoring. *Geophysical Research Letters*, *48*(18), 1–11. https://doi.org/10.1029/2021GL094659

Lu, Z., Wicks, C., Dzurisin, D., Thatcher, W., Freymueller, J. T., McNutt, S. R., & Mann, D. (2000). Aseismic inflation of Westdahl Volcano, Alaska, revealed by satellite radar interferometry. *Geophysical Research Letters*, *27*(11), 1567–1570. https://doi.org/10.1029/1999GL011283

Lyakhovsky, V., Ben-Zion, Y., & Agnon, A. (1997). Distributed damage, faulting, and friction. *Journal of Geophysical Research: Solid Earth*, *102*(B12), 27635–27649. https://doi.org/10.1029/97JB01896

Machacca-Puma, R., Lesage, P., Larose, E., Lacroix, P., & Anccasi-Figueroa, R. M. (2019). Detection of pre-eruptive seismic velocity variations at an andesitic volcano using ambient noise correlation on 3-component stations: Ubinas volcano, Peru, 2014. *Journal of Volcanology and Geothermal Research*, *381*, 83–100. https://doi.org/10.1016/j.jvolgeores.2019.05.014

Makus, P., Denolle, M., Sens-Schönfelder, C., Köpfli, M., & Tilmann, F. (2023). The Complex Relationship between Seismic Velocity and Volcanic, Tectonic, and Environmental Forcings Illustrated by 23 Years of Data at Mt. St. Helens. *EGU23*. https://doi.org/10.5194/egusphere-egu23-6757

Makus, P., Denolle, M. A., Sens-Schönfelder, C., Köpfli, M., & Tilmann, F. (2024). Analyzing Volcanic, Tectonic, and Environmental Influences on the Seismic Velocity from 25 Years of Data at Mount St. Helens. *Seismological Research Letters*, *95*(5), 2674–2688. https://doi.org/10.1785/0220240088

Makus, P., & Sens-Schönfelder, C. (2022). Seismological Monitoring using Interferometric Concepts (SeisMIC). https://doi.org/10.5880/GFZ.2.4.2022.002

Makus, P., & Sens-Schönfelder, C. (2024). SeisMIC - an Open Source Python Toolset to Compute Velocity Changes from Ambient Seismic Noise. *Seismica*, *3*(1). https://doi.org/10.26443/seismica.v3i1.1099

Makus, P., Sens-Schönfelder, C., Illien, L., Walter, T. R., Yates, A., & Tilmann, F. (2023). Deciphering the Whisper of Volcanoes: Monitoring Velocity Changes at Kamchatka's Klyuchevskoy Group With Fluctuating Noise Fields. *Journal of Geophysical Research: Solid Earth*, *128*(4), e2022JB025738. https://doi.org/10.1029/2022JB025738

Malone, S. D., Boyko, C., & Weaver, C. S. (1983). Seismic Precursors to the Mount St. Helens Eruptions in 1981 and 1982. *Science*, *221*(4618), 1376–1378. https://doi.org/10.1126/science.221.4618.1376

Mania, R., Cesca, S., Walter, T. R., Koulakov, I., & Senyukov, S. L. (2021). Inflating Shallow Plumbing System of Bezymianny Volcano, Kamchatka, Studied by InSAR and Seismicity Data Prior to the 20 December 2017 Eruption. *Frontiers in Earth Science*, *9*(December), 1–17. https://doi.org/10.3389/feart.2021.765668

Mania, R., Walter, T. R., Belousova, M., Belousov, A., & Senyukov, S. L. (2019). Deformations and morphology changes associated with the 2016-2017 eruption sequence at Bezymianny volcano, Kamchatka. *Remote Sensing*, *11*(11). https://doi.org/10.3390/rs11111278

Mao, S., Lecointre, A., van der Hilst, R. D., & Campillo, M. (2022). Space-time monitoring of groundwater fluctuations with passive seismic interferometry. *Nature Communications*, *13*(1), 4643. https://doi.org/10.1038/s41467-022-32194-3

Mao, S., Mordret, A., Campillo, M., Fang, H., & van der Hilst, R. D. (2020). On the measurement of seismic traveltime changes in the time–frequency domain with

wavelet cross-spectrum analysis. *Geophysical Journal International*, *221*(1), 550–568. https://doi.org/10.1093/gji/ggz495

Margerin, L., Planès, T., Mayor, J., & Calvet, M. (2016). Sensitivity kernels for coda-wave interferometry and scattering tomography: Theory and numerical evaluation in two-dimensional anisotropically scattering media. *Geophysical Journal International*, *204*(1), 650–666. https://doi.org/10.1093/gji/ggv470

Massonnet, D., Briole, P., & Arnaud, A. (1995). Deflation of Mount Etna monitored by spaceborne radar interferometry. *Nature*, *375*(6532), 567–570. https://doi.org/10.1038/375567a0

Mayor, J., Margerin, L., & Calvet, M. (2014). Sensitivity of coda waves to spatial variations of absorption and scattering: Radiative transfer theory and 2-D examples. *Geophysical Journal International*, *197*(2), 1117–1137. https://doi.org/10.1093/gji/ggu046

McNamara, D. E., & Boaz, R. E. (2019, April). Visualization of the Seismic Ambient Noise Spectrum. In N. Nakata, L. Gualtieri, & A. Fichtner (Eds.), *Seismic Ambient Noise* (pp. 1–29). Cambridge University Press. https://doi.org/10.1017/9781108264808

McNutt, S. R., & Roman, D. C. (2015, January). Chapter 59 - Volcanic Seismicity. In H. Sigurdsson (Ed.), *The Encyclopedia of Volcanoes (Second Edition)* (pp. 1011–1034). Academic Press. https://doi.org/10.1016/B978-0-12-385938-9.00059-6

Minato, S., Tsuji, T., Ohmi, S., & Matsuoka, T. (2012). Monitoring seismic velocity change caused by the 2011 Tohoku-oki earthquake using ambient noise records. *Geophysical Research Letters*, *39*(9). https://doi.org/10.1029/2012GL051405

Moran, S. C., Malone, S. D., Qamar, A. I., Thelen, W. A., Wright, A. K., & Caplan-Auerbach, J. (2008). Seismicity associated with renewed dome building at

Mount St. Helens, 2004-2005. In *A volcano Rekindled: The Renewed Eruption of Mount St. Helens, 2004-2006* (pp. 27–60). U.S. Geological Survey. https://doi.org/10.3133/pp17502

Moreau, L., Stehly, L., Boué, P., Lu, Y., Larose, E., & Campillo, M. (2017). Improving ambient noise correlation functions with an SVD-based Wiener filter. *Geophysical Journal International*, *211*(1), 418–426. https://doi.org/10.1093/GJI/GGX306

Müllner, D. (2013). Fastcluster: Fast hierarchical, agglomerative clustering routines for R and Python. *Journal of Statistical Software*, *53*(9), 1–18. https://doi.org/10.18637/jss.v053.i09

Murray, J. R., & Svarc, J. (2017). Global Positioning System Data Collection, Processing, and Analysis Conducted by the U.S. Geological Survey Earthquake Hazards Program. *Seismological Research Letters*, *88*(3), 916–925. https://doi.org/10.1785/0220160204

Nakata, N., Gualtieri, L., & Fichtner, A. (Eds.). (2019, April). *Seismic Ambient Noise*. Cambridge University Press. https://doi.org/10.1017/9781108264808

Nanni, U., Pauze, T., Goulet, L., Köhler, A., Bouchayer, C., & Schuler, T. (2023). Study of the structural and dynamic changes of a surging glacier using seismic observations. *IUGG*.

Nicolson, H., Curtis, A., Baptie, B., & Galetti, E. (2012). Seismic interferometry and ambient noise tomography in the British Isles. *Proceedings of the Geologists' Association*, *123*(1), 74–86. https://doi.org/10.1016/j.pgeola.2011.04.002

Niu, Z., Gabriel, A.-A., Seelinger, L., & Igel, H. (2024). Modeling and Quantifying Parameter Uncertainty of Co-Seismic Non-Classical Nonlinearity in Rocks. *Journal of Geophysical Research: Solid Earth*, *129*(1), e2023JB027149. https://doi.org/10.1029/2023JB027149

Oakley, D. O. S., Forsythe, B., Gu, X., Nyblade, A. A., & Brantley, S. L. (2021). Seismic Ambient Noise Analyses Reveal Changing Temperature and Water Signals to 10s of Meters Depth in the Critical Zone. *Journal of Geophysical Research: Earth Surface*, *126*(2), e2020JF005823. https://doi.org/10.1029/2020JF005823

Obermann, A., Planès, T., Larose, E., & Campillo, M. (2013). Imaging preeruptive and coeruptive structural and mechanical changes of a volcano with ambient seismic noise. *Journal of Geophysical Research: Solid Earth*, *118*(12), 6285–6294. https://doi.org/10.1002/2013JB010399

Obermann, A., Planés, T., Hadziioannou, C., & Campillo, M. (2016). Lapse-time-dependent coda-wave depth sensitivity to local velocity perturbations in 3-D heterogeneous elastic media. *Geophysical Journal International*, *207*(1), 59–66. https://doi.org/10.1093/gji/ggw264

Obermann, A., Planès, T., Larose, E., Sens-Schönfelder, C., & Campillo, M. (2013). Depth sensitivity of seismic coda waves to velocity perturbations in an elastic heterogeneous medium. *Geophysical Journal International*, *194*(1), 372–382. https://doi.org/10.1093/gji/ggt043

O'Connell, R. J., & Budiansky, B. (1974). Seismic velocities in dry and saturated cracked solids. *Journal of Geophysical Research (1896-1977)*, *79*(35), 5412–5426. https://doi.org/10.1029/JB079i035p05412

Olivier, G., Brenguier, F., Campillo, M., Roux, P., Shapiro, N. M., & Lynch, R. (2015). Investigation of coseismic and postseismic processes using in situ measurements of seismic velocity variations in an underground mine. *Geophysical Research Letters*, *42*(21), 9261–9269. https://doi.org/10.1002/2015GL065975

Ostrovsky, L. A., & Johnson, P. A. (2001). Dynamic nonlinear elasticity in geomaterials. *La Rivista del Nuovo Cimento*, *24*(7), 1–46. https://doi.org/10.1007/BF03548898

Ozerov, A. Y., Ariskin, A. A., Kyle, P., Bogoyavlenskaya, G. E., & Karpenko, S. F. (1997). Petrological-geochemical model for genetic relationships between basaltic and andesitic magmatism of Klyuchevskoi and Bezymyannyi volcanoes, Kamchatka. *Petrology*, *5*(6), 550–569.

Paasschens, J. C. J. (1997). Solution of the time-dependent Boltzmann equation. *Physical Review E*, *56*(1), 1135–1141. https://doi.org/10.1103/PhysRevE.56.1135

Pacheco, C., & Snieder, R. (2005). Time-lapse travel time change of multiply scattered acoustic waves. *The Journal of the Acoustical Society of America*, *118*(3), 1300–1310. https://doi.org/10.1121/1.2000827

Pao, Y.-H. (1987). Theory of Acoustoelasticity and Acoustoplasticity. In J. D. Achenbach & Y. Rajapakse (Eds.), *Solid mechanics research for quantitative nondestructive evaluation* (pp. 257–273). Springer Netherlands. https://doi.org/10.1007/978-94-009-3523-5_16

Peltier, A., Ferrazzini, V., Staudacher, T., & Bachèlery, P. (2005). Imaging the dynamics of dyke propagation prior to the 2000-2003 flank eruptions at Piton de la Fournaise, Reunion Island. *Geophysical Research Letters*, *32*(22), 1–5. https://doi.org/10.1029/2005GL023720

Petersen, G. N. (2010). A short meteorological overview of the Eyjafjallajökull eruption 14 April–23 May 2010. *Weather*, *65*(8), 203–207. https://doi.org/10.1002/wea.634

Piccinini, D., Giunchi, C., Olivieri, M., Frattini, F., Di Giovanni, M., Prodi, G., & Chiarabba, C. (2020). COVID-19 lockdown and its latency in Northern Italy: Seismic evidence and socio-economic interpretation. *Scientific Reports*, *10*(1), 16487. https://doi.org/10.1038/s41598-020-73102-3

Poupinet, G., Ellsworth, W. L., & Frechet, J. (1984). Monitoring velocity variations in the crust using earthquake doublets: An application to the Calaveras Fault,

California. *Journal of Geophysical Research: Solid Earth*, *89*(B7), 5719–5731. https://doi.org/10.1029/JB089iB07p05719

Power, J. A., Lahr, J. C., Page, R. A., Chouet, B. A., Stephens, C. D., Harlow, D. H., Murray, T. L., & Davies, J. N. (1994). Seismic evolution of the 1989–1990 eruption sequence of Redoubt Volcano, Alaska. *Journal of Volcanology and Geothermal Research*, *62*(1), 69–94. https://doi.org/10.1016/0377-0273(94)90029-9

Quinteros, J., Strollo, A., Evans, P. L., Hanka, W., Heinloo, A., Hemmleb, S., Hillmann, L., Jaeckel, K.-H., Kind, R., Saul, J., Zieke, T., & Tilmann, F. (2021). The GEOFON Program in 2020. *Seismological Research Letters*, *92*(3), 1610–1622. https://doi.org/10.1785/0220200415

Ratdomopurbo, A., & Poupinet, G. (1995). Monitoring a temporal change of seismic velocity in a volcano: Application to the 1992 eruption of Mt. Merapi (Indonesia). *Geophysical Research Letters*, *22*(7), 775–778. https://doi.org/10.1029/95GL00302

Reath, K. A., Ramsey, M. S., Dehn, J., & Webley, P. W. (2016). Predicting eruptions from precursory activity using remote sensing data hybridization. *Journal of Volcanology and Geothermal Research*, *321*, 18–30. https://doi.org/10.1016/j.jvolgeores.2016.04.027

Richter, T., Sens-Schönfelder, C., Kind, R., & Asch, G. (2014). Comprehensive observation and modeling of earthquake and temperature-related seismic velocity changes in northern Chile with passive image interferometry. *Journal of Geophysical Research: Solid Earth*, *119*(6), 4747–4765. https://doi.org/10.1002/2013JB010695

Rivet, D., Brenguier, F., Clarke, D., Shapiro, N. M., & Peltier, A. (2014). Long-term dynamics of Piton de la Fournaise volcano from 13 years of seismic velocity change measurements and GPS observations. *Journal of Geophysi-*

cal Research: Solid Earth, *119*(10), 7654–7666. https://doi.org/10.1002/2014JB011307

Roman, D. C., & Cashman, K. V. (2018). Top–Down Precursory Volcanic Seismicity: Implications for 'Stealth' Magma Ascent and Long-Term Eruption Forecasting. *Frontiers in Earth Science*, *6*.

Rutherford, M. J. (2008). Magma Ascent Rates. *Reviews in Mineralogy and Geochemistry*, *69*(1), 241–271. https://doi.org/10.2138/rmg.2008.69.7

Rymer, H., & Brown, G. (1989). Gravity changes as a precursor to volcanic eruption at Poás volcano, Costa Rica. *Nature*, *342*(6252), 902–905. https://doi.org/10.1038/342902a0

Sabra, K. G., Roux, P., Gerstoft, P., Kuperman, W. A., & Fehler, M. C. (2006). Extracting coherent coda arrivals from cross-correlations of long period seismic waves during the Mount St. Helens 2004 eruption. *Geophysical Research Letters*, *33*(6). https://doi.org/10.1029/2005GL025563

Salzer, J. T., Thelen, W. A., James, M. R., Walter, T. R., Moran, S., & Denlinger, R. (2016). Volcano dome dynamics at Mount St. Helens: Deformation and intermittent subsidence monitored by seismicity and camera imagery pixel offsets. *Journal of Geophysical Research: Solid Earth*, *121*(11), 7882–7902. https://doi.org/10.1002/2016JB013045

Scandone, R., Cashman, K. V., & Malone, S. D. (2007). Magma supply, magma ascent and the style of volcanic eruptions. *Earth and Planetary Science Letters*, *253*(3), 513–529. https://doi.org/10.1016/j.epsl.2006.11.016

Scarpa, R., & Gasparini, P. (1996). A Review of Volcano Geophysics and Volcano-Monitoring Methods. In R. Scarpa & R. I. Tilling (Eds.), *Monitoring and Mitigation of Volcano Hazards* (pp. 3–22). Springer. https://doi.org/10.1007/978-3-642-80087-0_1

Schaefer, L. N., Kendrick, J. E., Oommen, T., Lavallée, Y., & Chigna, G. (2015). Geomechanical rock properties of a basaltic volcano. *Frontiers in Earth Science*, *3*(June), 1–15. https://doi.org/10.3389/feart.2015.00029

Schaff, D. P., & Beroza, G. C. (2004). Coseismic and postseismic velocity changes measured by repeating earthquakes. *Journal of Geophysical Research: Solid Earth*, *109*(B10). https://doi.org/10.1029/2004JB003011

Schimmel, M., Stutzmann, E., & Gallart, J. (2011). Using instantaneous phase coherence for signal extraction from ambient noise data at a local to a global scale. *Geophysical Journal International*, *184*(1), 494–506. https://doi.org/10.1111/j.1365-246X.2010.04861.x

Schippkus, S., Hadziioannou, C., & Safarkhani, M. (2023). Continuous isolated noise sources induce repeating waves in the coda of ambient noise correlations. *Seismica*, *2*(2). https://doi.org/10.26443/seismica.v2i2.499

Segall, P. (2013). Volcano deformation and eruption forecasting. *Geological Society, London, Special Publications*, *380*(1), 85–106. https://doi.org/10.1144/SP380.4

Sens-Schönfelder, C., & Wegler, U. (2006). Passive image interferemetry and seasonal variations of seismic velocities at Merapi Volcano, Indonesia. *Geophysical Research Letters*, *33*(21), 1–5. https://doi.org/10.1029/2006GL027797

Sens-Schönfelder, C., & Brenguier, F. (2019, April). Noise-Based Monitoring. In N. Nakata, L. Gualtieri, & A. Fichtner (Eds.), *Seismic Ambient Noise* (pp. 267–301). Cambridge University Press. https://doi.org/10.1017/9781108264808.011

Sens-Schönfelder, C., & Eulenfeld, T. (2019). Probing the in situ Elastic Nonlinearity of Rocks with Earth Tides and Seismic Noise. *Physical Review Letters*, *122*(13), 138501. https://doi.org/10.1103/PhysRevLett.122.138501

Sens-Schönfelder, C., Flores-Estrella, H., Gassenmeier, M., Korn, M., Köllner, F., Milkereit, C., Niederleithinger, E., Parolai, S., Pilz, M., Pomponi, E., Schuck, A., Thiemann, K., & Völkel, J. (2014). MIIC: Monitoring and Imaging Based on Interferometric Concepts. In M. Weber & U. Münch (Eds.), *Tomography of the Earth's Crust: From Geophysical Sounding to Real-Time Monitoring: GEOTECHNOLOGIEN Science Report No. 21* (pp. 43–61). Springer International Publishing.

Sens-Schönfelder, C., & Larose, E. (2010). Lunar noise correlation, imaging and monitoring. *Earthquake Science*, *23*(5), 519–530. https://doi.org/10.1007/s11589-010-0750-6

Sens-Schönfelder, C., Pomponi, E., & Peltier, A. (2014). Dynamics of Piton de la Fournaise volcano observed by passive image interferometry with multiple references. *Journal of Volcanology and Geothermal Research*, *276*, 32–45. https://doi.org/10.1016/j.jvolgeores.2014.02.012

Sens-Schönfelder, C., Snieder, R., & Li, X. (2019). A model for nonlinear elasticity in rocks based on friction of internal interfaces and contact aging. *Geophysical Journal International*, *216*(1), 319–331. https://doi.org/10.1093/gji/ggy414

Seropian, G., Kennedy, B. M., Walter, T. R., Ichihara, M., & Jolly, A. D. (2021). A review framework of how earthquakes trigger volcanic eruptions. *Nature Communications*, *12*(1), 1–13. https://doi.org/10.1038/s41467-021-21166-8

Seydoux, L., Balestriero, R., Poli, P., de Hoop, M., Campillo, M., & Baraniuk, R. (2020). Clustering earthquake signals and background noises in continuous seismic data with unsupervised deep learning. *Nature Communications*, *11*(1). https://doi.org/10.1038/s41467-020-17841-x

Shapiro, N., Sens-Schönfelder, C., Lühr, B., Weber, M., Abkadyrov, I., Gordeev, E., Koulakov, I., Jakovlev, A., Kugaenko, Y., & Saltykov, V. (2017). Under-

standing Kamchatka's Extraordinary Volcano Cluster. *Eos*. https://doi.org/10.1029/2017EO071351

Shapiro, N., Sens-Schönfelder, C., Lühr, B., Weber, M., Abkadyrov, I., Gordeev, E., Koulakov, I., Jakovlev, A., Kugaenko, Y., & Saltykov, V. (2015). Klyuchevskoy volcanic group experiment (kiss). https://doi.org/10.14470/K47560642124

Shearer, P. M. (2019, May). *Introduction to Seismology*. Cambridge University Press. https://doi.org/10.1017/9781316877111

Sheng, Y., Ellsworth, W. L., Lellouch, A., & Beroza, G. C. (2021). Depth Constraints on Coseismic Velocity Changes From Frequency-Dependent Measurements of Repeating Earthquake Waveforms. *Journal of Geophysical Research: Solid Earth*, *126*(2), 1–12. https://doi.org/10.1029/2020JB020421

Sherrod, D. R., Scott, W. E., & Stauffer, P. H. (2008). *A Volcano Rekindled; The Renewed Eruption of Mount St. Helens, 2004-2006*.

Silver, P. G., Daley, T. M., Niu, F., & Majer, E. L. (2007). Active Source Monitoring of Cross-Well Seismic Travel Time for Stress-Induced Changes. *Bulletin of the Seismological Society of America*, *97*(1B), 281–293. https://doi.org/10.1785/0120060120

Simpson, J., van Wijk, K., Adam, L., & Esteban, L. (2023). Temperature-Induced Nonlinear Elastic Behavior in Berea Sandstone Explained by a Modified Sheared Contacts Model. *Journal of Geophysical Research: Solid Earth*, *128*(1), e2022JB025452. https://doi.org/10.1029/2022JB025452

Singh, J., Curtis, A., Zhao, Y., Cartwright-Taylor, A., & Main, I. (2019). Coda Wave Interferometry for Accurate Simultaneous Monitoring of Velocity and Acoustic Source Locations in Experimental Rock Physics. *Journal of Geophysical Research: Solid Earth*, *124*(6), 5629–5655. https://doi.org/10.1029/2019JB017577

Snieder, R., Sens-Schönfelder, C., & Wu, R. (2017). The time dependence of rock healing as a universal relaxation process, a tutorial. *Geophysical Journal International*, *208*(1), 1–9. https://doi.org/10.1093/gji/ggw377

Snieder, R., Singh, J., Curtis, A., Zhao, Y., Cartwright-Taylor, A., & Main, I. (2019). Coda Wave Interferometry for Accurate Simultaneous Monitoring of Velocity and Acoustic Source Locations in Experimental Rock Physics. *Journal of Geophysical Research: Solid Earth*, *124*(6), 5629–5655. https://doi.org/10.1029/2019JB017577

Soubestre, J., Seydoux, L., Shapiro, N. M., de Rosny, J., Droznin, D. V., Droznina, S. Y., Senyukov, S. L., & Gordeev, E. I. (2019). Depth Migration of Seismovolcanic Tremor Sources Below the Klyuchevskoy Volcanic Group (Kamchatka) Determined From a Network-Based Analysis. *Geophysical Research Letters*, *46*(14), 8018–8030. https://doi.org/10.1029/2019GL083465

Soubestre, J., Chouet, B., & Dawson, P. (2021). Sources of Volcanic Tremor Associated With the Summit Caldera Collapse During the 2018 East Rift Eruption of Kı¯lauea Volcano, Hawaii. *Journal of Geophysical Research: Solid Earth*, 1–33. https://doi.org/10.1029/2020jb021572

Sparks, R. S. J. (2003). Forecasting volcanic eruptions. *Earth and Planetary Science Letters*, *210*(1), 1–15. https://doi.org/10.1016/S0012-821X(03)00124-9

Sparks, R. S. J., Biggs, J., & Neuberg, J. W. (2012). Monitoring Volcanoes. *Science*, *335*(6074), 1310–1311. https://doi.org/10.1126/science.1219485

Steinmann, R., Hadziioannou, C., & Larose, E. (2021). Effect of centimetric freezing of the near subsurface on Rayleigh and Love wave velocity in ambient seismic noise correlations. *Geophysical Journal International*, *224*(1), 626–636. https://doi.org/10.1093/gji/ggaa406

Steinmann, R., Seydoux, L., Journeau, C., Shapiro, N. M., & Campillo, M. (2023, June). Machine learning analysis of seismograms reveals a continuous plumb-

ing system evolution beneath the Klyuchevskoy volcano in Kamchatka, Russia. https://doi.org/10.22541/essoar.168614505.54607219/v1

Steinmann, R., Seydoux, L., Beaucé, É., & Campillo, M. (2022). Hierarchical Exploration of Continuous Seismograms With Unsupervised Learning. *Journal of Geophysical Research: Solid Earth*, *127*(1), 1–21. https://doi.org/10.1029/2021JB022455

Steinmann, R., Seydoux, L., & Campillo, M. (2022). AI-Based Unmixing of Medium and Source Signatures From Seismograms: Ground Freezing Patterns. *Geophysical Research Letters*, *49*(15), e2022GL098854. https://doi.org/10.1029/2022GL098854

Strollo, A., Cambaz, D., Clinton, J., Danecek, P., Evangelidis, C. P., Marmureanu, A., Ottemöller, L., Pedersen, H., Sleeman, R., Stammler, K., Armbruster, D., Bienkowski, J., Boukouras, K., Evans, P. L., Fares, M., Neagoe, C., Heimers, S., Heinloo, A., Hoffmann, M., … Triantafyllis, N. (2021). EIDA: The European Integrated Data Archive and Service Infrastructure within ORFEUS. *Seismological Research Letters*, *92*(3), 1788–1795. https://doi.org/10.1785/0220200413

Taira, T., & Brenguier, F. (2016). Response of hydrothermal system to stress transients at Lassen Volcanic Center, California, inferred from seismic interferometry with ambient noise 4. Seismology. *Earth, Planets and Space*, *68*(1). https://doi.org/10.1186/s40623-016-0538-6

Takano, T., Nishimura, T., & Nakahara, H. (2017). Seismic velocity changes concentrated at the shallow structure as inferred from correlation analyses of ambient noise during volcano deformation at Izu-Oshima, Japan. *Journal of Geophysical Research: Solid Earth*, *122*(8), 6721–6736. https://doi.org/10.1002/2017JB014340

Tang, G., Clark, M. P., Papalexiou, S. M., Ma, Z., & Hong, Y. (2020). Have satellite precipitation products improved over last two decades? A comprehensive comparison of GPM IMERG with nine satellite and reanalysis datasets. *Remote Sensing of Environment*, *240*(September 2019), 111697. https://doi.org/10.1016/j.rse.2020.111697

Taran, Y. A. (2009). Geochemistry of volcanic and hydrothermal fluids and volatile budget of the Kamchatka-Kuril subduction zone. *Geochimica et Cosmochimica Acta*, *73*(4), 1067–1094. https://doi.org/10.1016/j.gca.2008.11.020

Tarantola, A., & Valette, B. (1982). Generalized nonlinear inverse problems solved using the least squares criterion. *Reviews of Geophysics*, *20*(2), 219–232. https://doi.org/10.1029/RG020i002p00219

Thelen, W., Malone, S., & West, M. (2011). Multiplets: Their behavior and utility at dacitic and andesitic volcanic centers. *Journal of Geophysical Research: Solid Earth*, *116*(B8). https://doi.org/10.1029/2010JB007924

Thery, R., Guillemot, A., Abraham, O., & Larose, E. (2020). Tracking fluids in multiple scattering and highly porous materials: Toward applications in non-destructive testing and seismic monitoring. *Ultrasonics*, *102*, 106019. https://doi.org/10.1016/j.ultras.2019.106019

Thornber, C., Pallister, J., Lowers, H., Rowe, M., Mandeville, C., & Meeker, G. (2008). Chemistry, mineralogy, and petrology of amphibole in Mount St. Helens 2004-2006 dacite. *US Geological Survey Professional Paper*, *1750*, 727–754.

Tilling, R. I. (2008). The critical role of volcano monitoring in risk reduction. *Advances in Geosciences*, *14*, 3–11. https://doi.org/10.5194/adgeo-14-3-2008

Titzschkau, T., Savage, M., & Hurst, T. (2010). Changes in attenuation related to eruptions of Mt. Ruapehu Volcano, New Zealand. *Journal of Volcanology and*

Geothermal Research, *190*(1), 168–178. https://doi.org/10.1016/j.jvolgeores.2009.07.012

Tozer, B., Sandwell, D. T., Smith, W. H., Olson, C., Beale, J., & Wessel, P. (2019). Global bathymetry and topography at 15 arc sec: Srtm15+. *Earth and Space Science*, *6*(10), 1847–1864. https://doi.org/10.1029/2019EA000658

Tsai, V. C. (2011). A model for seasonal changes in GPS positions and seismic wave speeds due to thermoelastic and hydrologic variations. *Journal of Geophysical Research: Solid Earth*, *116*(B4). https://doi.org/10.1029/2010JB008156

Uieda, L., Tian, D., Leong, W. J., Toney, L., Schlitzer, W., Grund, M., Newton, D., Ziebarth, M., Jones, M., & Wessel, P. (2021). Pygmt: A python interface for the generic mapping tools.

Ulberg, C. W., Creager, K. C., Moran, S. C., Abers, G. A., Thelen, W. A., Levander, A., Kiser, E., Schmandt, B., Hansen, S. M., & Crosson, R. S. (2020). Local Source Vp and Vs Tomography in the Mount St. Helens Region With the iMUSH Broadband Array. *Geochemistry, Geophysics, Geosystems*, *21*(3), e2019GC008888. https://doi.org/10.1029/2019GC008888

University of Leipzig. (2001). SXNET Saxon Seismic Network. https://doi.org/10.7914/SN/SX

University of Washington. (1963). Pacific northwest seismic network - university of washington. https://doi.org/10.7914/SN/UW

Utada, H. (2003). Interpretation of time changes in the apparent resistivity observed prior to the 1986 eruption of Izu–Oshima volcano, Japan. *Journal of Volcanology and Geothermal Research*, *126*(1), 97–107. https://doi.org/10.1016/S0377-0273(03)00119-7

Van Den Abeele, K. E.-A. (2002). Influence of water saturation on the nonlinear elastic mesoscopic response in Earth materials and the implications to the

mechanism of nonlinearity. *Journal of Geophysical Research*, *107*(B6), 1–11. https://doi.org/10.1029/2001jb000368

Viens, L., Jiang, C., & Denolle, M. A. (2022). Imaging the Kanto Basin seismic basement with earthquake and noise autocorrelation functions. *Geophysical Journal International*, *230*(2), 1080–1091. https://doi.org/10.1093/gji/ggac101

Viens, L., & Van Houtte, C. (2020). Denoising ambient seismic field correlation functions with convolutional autoencoders. *Geophysical Journal International*, *220*(3), 1521–1535. https://doi.org/10.1093/gji/ggz509

Virtanen, P., Gommers, R., Oliphant, T. E., Haberland, M., Reddy, T., Cournapeau, D., Burovski, E., Peterson, P., Weckesser, W., Bright, J., van der Walt, S. J., Brett, M., Wilson, J., Millman, K. J., Mayorov, N., Nelson, A. R. J., Jones, E., Kern, R., Larson, E., ... van Mulbregt, P. (2020). SciPy 1.0: Fundamental algorithms for scientific computing in Python. *Nature Methods*, *17*(3), 261–272. https://doi.org/10.1038/s41592-019-0686-2

Waite, G. P., & Moran, S. C. (2009). VP Structure of Mount St. Helens, Washington, USA, imaged with local earthquake tomography. *Journal of Volcanology and Geothermal Research*, *182*(1), 113–122. https://doi.org/10.1016/j.jvolgeores.2009.02.009

Walter, T. R., & Amelung, F. (2007). Volcanic eruptions following M 9 megathrust earthquakes: Implications of the Sumatra-Andaman volcanoes. *Geology*, *35*(6), 539–542. https://doi.org/10.1130/G23429A.1

Wang, B., Yang, W., Wang, W., Yang, J., Li, X., & Ye, B. (2020). Diurnal and Semidiurnal P- and S-Wave Velocity Changes Measured Using an Airgun Source. *Journal of Geophysical Research: Solid Earth*, *125*(1), e2019JB018218. https://doi.org/10.1029/2019JB018218

Wang, Q. Y., Brenguier, F., Campillo, M., Lecointre, A., Takeda, T., & Aoki, Y. (2017). Seasonal Crustal Seismic Velocity Changes Throughout Japan. *Journal of Geophysical Research: Solid Earth*, *122*(10), 7987–8002. https://doi.org/10.1002/2017JB014307

Wang, Y., Lin, F.-C., Schmandt, B., & Farrell, J. (2017). Ambient noise tomography across Mount St. Helens using a dense seismic array. *Journal of Geophysical Research: Solid Earth*, *122*(6), 4492–4508. https://doi.org/10.1002/2016JB013769

Ward, J. H. J. (1963). Hierarchical Grouping to Optimize an Objective Function. *Journal of the American Statistical Association*, *58*(301), 236–244.

Watt, S. F., Pyle, D. M., & Mather, T. A. (2009). The influence of great earthquakes on volcanic eruption rate along the Chilean subduction zone. *Earth and Planetary Science Letters*, *277*(3-4), 399–407. https://doi.org/10.1016/j.epsl.2008.11.005

Weaver, R. L. (2005). Information from Seismic Noise. *Science*, *307*(5715), 1568–1569. https://doi.org/10.1126/science.1109834

Weaver, R. L., Hadziioannou, C., Larose, E., & Campillo, M. (2011). On the precision of noise correlation interferometry. *Geophysical Journal International*, *185*(3), 1384–1392. https://doi.org/10.1111/j.1365-246X.2011.05015.x

Wegler, U., Nakahara, H., Sens-Schönfelder, C., Korn, M., & Shiomi, K. (2009). Sudden drop of seismic velocity after the 2004 Mw 6.6 mid-Niigata earthquake, Japan, observed with Passive Image Interferometry B06305. *Journal of Geophysical Research: Solid Earth*, *114*(6), 1–11. https://doi.org/10.1029/2008JB005869

Welch, M. D., & Schmidt, D. A. (2017). Separating volcanic deformation and atmospheric signals at Mount St. Helens using Persistent Scatterer InSAR. *Journal*

of Volcanology and Geothermal Research, *344*, 52–64. https://doi.org/10.1016/j.jvolgeores.2017.05.015

Wilson, G., Wilson, T. M., Deligne, N. I., & Cole, J. W. (2014). Volcanic hazard impacts to critical infrastructure: A review. *Journal of Volcanology and Geothermal Research*, *286*, 148–182. https://doi.org/10.1016/j.jvolgeores.2014.08.030

Woods, A. W. (1995). The dynamics of explosive volcanic eruptions. *Reviews of Geophysics*, *33*(4), 495–530. https://doi.org/10.1029/95RG02096

Wu, C., Tan, X., Li, H., & Sun, G. (2022). An Efficient Ambient Noise Cross-Correlation Algorithm on Heterogeneous CPU-GPU Cluster. *2022 IEEE 13th International Symposium on Parallel Architectures, Algorithms and Programming (PAAP)*, 1–5. https://doi.org/10.1109/PAAP56126.2022.10010612

Xue, Q., Larose, E., Moreau, L., Thery, R., Abraham, O., & Henault, J.-M. (2022). Ultrasonic monitoring of stress and cracks of the 1/3 scale mock-up of nuclear reactor concrete containment structure. *Structural Health Monitoring*, *21*(4), 1474–1482. https://doi.org/10.1177/14759217211034729

Yamamura, K., Sano, O., Utada, H., Takei, Y., Nakao, S., & Fukao, Y. (2003). Long-term observation of in situ seismic velocity and attenuation. *Journal of Geophysical Research: Solid Earth*, *108*(B6). https://doi.org/10.1029/2002JB002005

Yates, A. S., Savage, M. K., Jolly, A. D., Caudron, C., & Hamling, I. J. (2019). Volcanic, Coseismic, and Seasonal Changes Detected at White Island (Whakaari) Volcano, New Zealand, Using Seismic Ambient Noise. *Geophysical Research Letters*, *46*(1), 99–108. https://doi.org/10.1029/2018GL080580

Yates, A., Caudron, C., Lesage, P., Mordret, A., Lecocq, T., & Soubestre, J. (2023). Assessing similarity in continuous seismic cross-correlation functions using hierarchical clustering: Application to Ruapehu and Piton de la Fournaise

volcanoes. *Geophysical Journal International*, *233*(1), 472–489. https://doi.org/10.1093/gji/ggac469

Yin, X., Xia, J., Shen, C., & Xu, H. (2014). Comparative analysis on penetrating depth of high-frequency Rayleigh and Love waves. *Journal of Applied Geophysics*, *111*, 86–94. https://doi.org/10.1016/j.jappgeo.2014.09.022

Yogodzinski, G. M., Lees, J. M., Churikova, T. G., Dorendorf, F., Wöerner, G., & Volynets, O. N. (2001). Geochemical evidence for the melting of subducting oceanic lithosphere at plate edges. *Nature*, *409*(6819), 500–504. https://doi.org/10.1038/35054039

Yuan, C., Bryan, J., & Denolle, M. (2021). Numerical comparison of time-, frequency-A nd wavelet-domain methods for coda wave interferometry. *Geophysical Journal International*, *226*(2), 828–846. https://doi.org/10.1093/gji/ggab140

Zhang, H., Glasgow, M., Schmandt, B., Thelen, W. A., Moran, S. C., & Thomas, A. M. (2022). Revisiting the depth distribution of seismicity before and after the 2004–2008 eruption of Mount St. Helens. *Journal of Volcanology and Geothermal Research*, *430*, 107629. https://doi.org/10.1016/j.jvolgeores.2022.107629

Zimmerman, R. W., & King, M. S. (1986). The effect of the extent of freezing on seismic velocities in unconsolidated permafrost. *GEOPHYSICS*, *51*(6), 1285–1290. https://doi.org/10.1190/1.1442181

APPENDIX A

Supporting Information to Chapter 3

In this supporting information, we elaborate on the approximation of the stretching factor implemented in SeisMIC. We show a short derivation in Section A.1.

In Section A.2, we present selected results of the spatial inversion procedure to illustrate the effect of (1) subdividing the coda to obtain several independent velocity change estimates (hereafter referred to as coda splitting) and (2) adding information from autocorrelations and cross-station correlations to the analysis. To this end, we provide several examples using different station configurations and damping parameters. For a thorough discussion of the algorithm, please refer to Chapter 3. The reader can reproduce and extend the shown results using the `spatial.ipynb` Jupyter notebook provided in the digital supplement.

For the coda splitting, we split the total of the used coda window into three equally long subwindows and obtain one sensitivity kernel for each subwindow. That is when exploiting the coda splitting, we compute separate sensitivity kernels for

lapse times from 14 to 20.66 s, from 20.66 s to 27.33 s, and from 27.33 s to 34 s, whereas without coda splitting, we only obtain one sensitivity kernel representing lag times from 14 s to 34 s. To all forward-modelled dv/v results, we add random noise from a Gaussian distribution with a standard deviation of only 0.05 % dv/v to the predicted velocity changes to render the comparison less dependent on the noise level. Otherwise, the procedure for the spatial inversion remains identical to the one described in Section 3.2.5.

Apart from this supporting document, we provide Jupyter notebooks, computing scripts, and the main program, SeisMIC 0.5.3, as a digital supplement. For SeisMIC, however, we strongly encourage the reader to obtain the code's latest version, for example, from GitHub. For details about where to retrieve these additional supplements, please refer to the *data and code availability* section in Chapter 3.

A.1 Derivation of the Stretching

A problem with the commonly used definition of a velocity change dv/v is that it is neither additive nor reversible, i.e. $dv/v_{A\to B} \neq -dv/v_{B\to A}$ because the reference velocity of the two measurements may be different and the commonly used equation $dv/v = -dt/t$ is an approximation for small dv/v. Even though the error is small, we can reduce it further with a different definition of the velocity change. This definition is especially useful for smoothing, averaging, or otherwise manipulating velocity change time series as, in contrast to the common definition, it ensures linearity (see below).

Assuming infinite frequency (i.e., ray theory), the travel time $t(\mathbf{x})$ of a wave travelling from point $\mathbf{x}_1$ to $\mathbf{x}_2$ through any medium is given by:

$$t(\mathbf{x}) = \int_{\mathbf{x}_1}^{\mathbf{x}_2} \frac{1}{v(\mathbf{x})} d\mathbf{x} \tag{A.1}$$

where $v(\mathbf{x})$ is the velocity at point $\mathbf{x}$. If we assume a medium with a homogeneous

velocity, i.e., $v(\mathbf{x}) = v$, equation A.1 simplifies to:

$$t = \frac{\Delta x}{v} \tag{A.2}$$

where $\Delta x = ||\mathbf{x_1} - \mathbf{x_2}||$ is the Euclidean distance which remains constant throughout. In interferometry, we examine the case where the velocity $v(t)$ is variable with time. To quantify the change in velocity, we compare the velocity of a reference state $\tilde{v} = \Delta x/\tilde{t}$ with the velocity $v' = \Delta x/t'$ in a perturbed state. Due to the constant Δx, we obtain from equation A.2:

$$\frac{\tilde{t}}{t'} = \frac{v'}{\tilde{v}} = \xi \tag{A.3}$$

defining the stretching factor ξ.

We seek a transformation

$$\mathcal{S}(\kappa) : \tilde{t} \mapsto t' = \frac{1}{\xi}\tilde{t}$$

that maps the original travel times $\tilde{t}$ of the seismic waves through the unperturbed medium to the travel times t' through the perturbed medium. This transformation shall have the following property:

$$\mathcal{S}(\kappa_1)\mathcal{S}(\kappa_2) = \mathcal{S}(\kappa_1 + \kappa_2)$$

to ensure that stretching is additive and reversible. We choose

$$\xi = e^{\kappa}$$

to calculate the stretching factor. We satisfy the above requirement for any combination of reference and perturbed states since $e^{\kappa_1} * e^{\kappa_2} = e^{\kappa_1+\kappa_2}$. In SeisMIC, we implement $\xi = e^{\kappa}$ to guarantee the linearity in the processing. To interpret measurements in the usual way as fractional velocity change, we use the approximation

$$\frac{dv}{v} = \frac{v' - \tilde{v}}{\tilde{v}} = \xi - 1 \approx \kappa$$

.

Utilising $\xi = 1 + \frac{dv}{v}$ for processing introduces nonlinearities and a dependency on the reference state. We note that this effect is not limited to measurements of the velocity change with the stretching method. Any manipulation of $\frac{dv}{v}$ is affected and can be improved by working with $\kappa = \ln(v'/\tilde{v})$.

A.2 Additional Results of the Synthetic Spatial Imaging

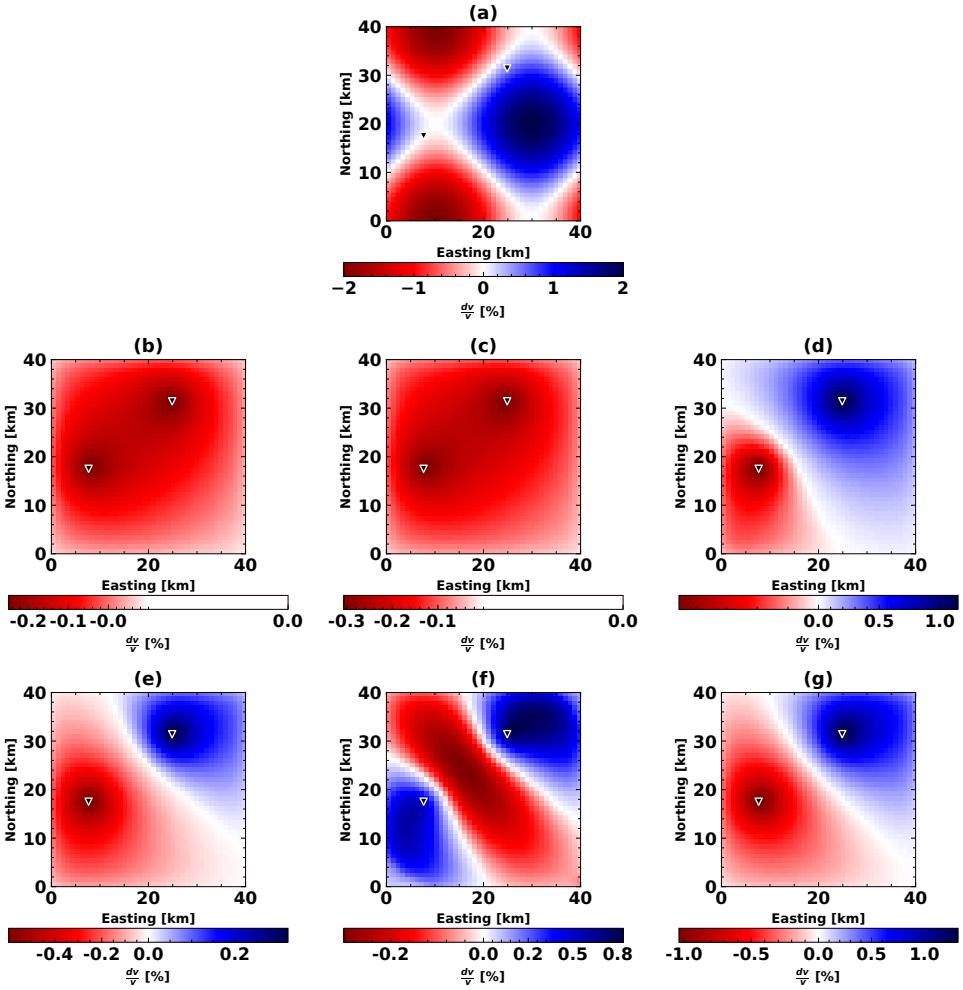

Figure A.1: Examples of the spatial inversion using data from two stations, a model variance $\sigma_m = 0.5\ \frac{\text{km}}{\text{km}^2}$, and a correlation length $\lambda = 2$ km. **(a)** The synthetic velocity model and station configuration used. **(b)** Result of the spatial inversion using only cross-correlations and a single lapse time window. **(c)** Result of the spatial inversion using only cross-correlations and three lapse time windows. **(d)** Result of the spatial inversion using only auto-correlations and a single lapse time window. **(e)** Result of the spatial inversion using only auto-correlations and three lapse time windows. **(f)** Result of the spatial inversion from cross-correlations and auto correlations using a single lapse time window. **(g)** Result of the spatial inversion from cross-correlations and auto correlations using a single lapse time window.

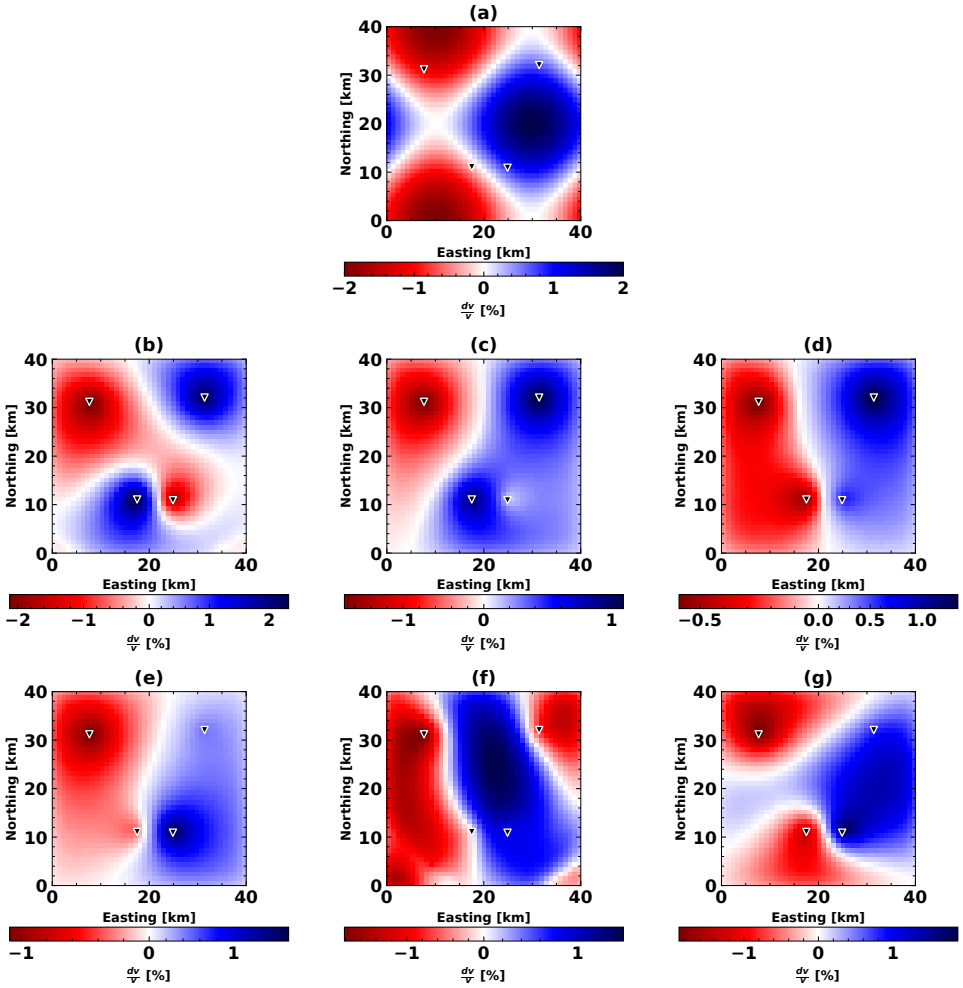

Figure A.2: Examples of the spatial inversion using data from four stations, a model variance $\sigma_m = 0.25\ \frac{\text{km}}{\text{km}^2}$, and a correlation length $\lambda = 2$ km. **(a)** The synthetic velocity model and station configuration used. **(b)** Result of the spatial inversion using only cross-correlations and a single lapse time window. **(c)** Result of the spatial inversion using only cross-correlations and three lapse time windows. **(d)** Result of the spatial inversion using only auto-correlations and a single lapse time window. **(e)** Result of the spatial inversion using only auto-correlations and three lapse time windows. **(f)** Result of the spatial inversion from cross-correlations and auto correlations using a single lapse time window. **(g)** Result of the spatial inversion from cross-correlations and auto correlations using a single lapse time window.

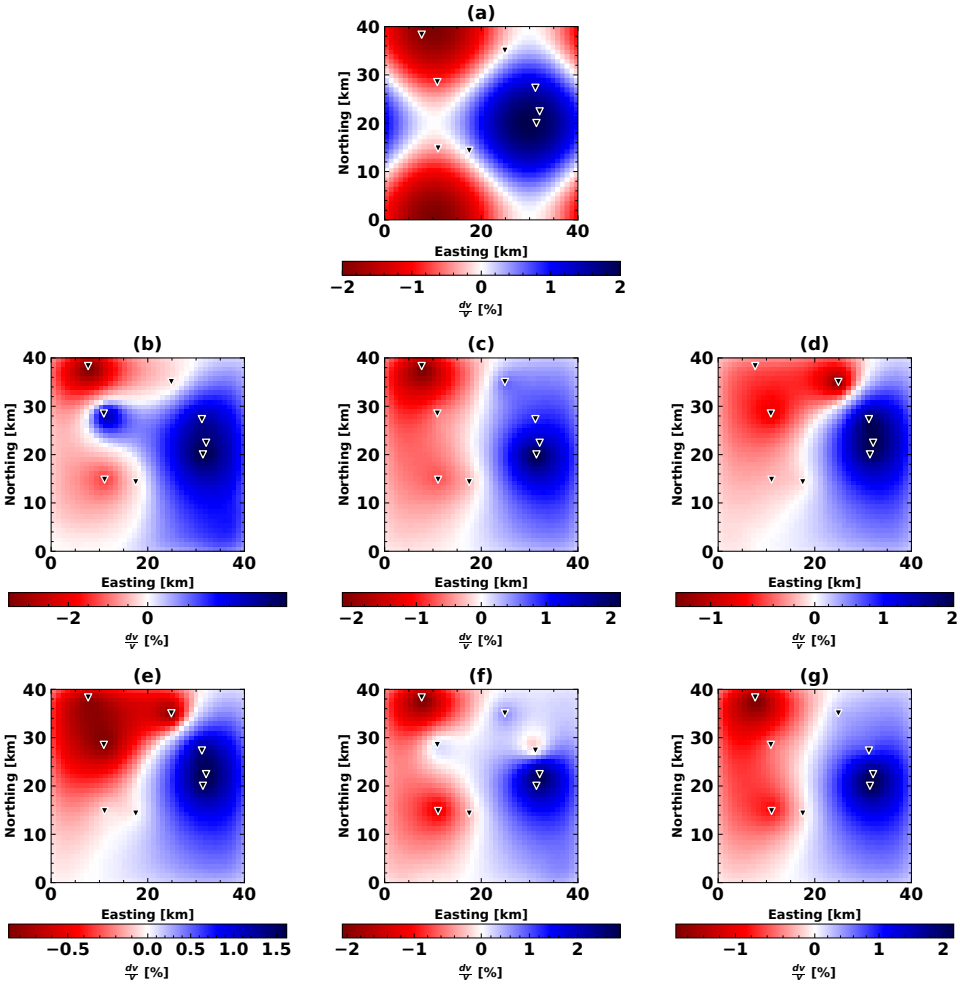

Figure A.3: Examples of the spatial inversion using data from eight stations, a model variance $\sigma_m = 0.05\ \frac{\text{km}}{\text{km}^2}$, and a correlation length $\lambda = 2$ km. **(a)** The synthetic velocity model and station configuration used. **(b)** Result of the spatial inversion using only cross-correlations and a single lapse time window. **(c)** Result of the spatial inversion using only cross-correlations and three lapse time windows. **(d)** Result of the spatial inversion using only auto-correlations and a single lapse time window. **(e)** Result of the spatial inversion using only auto-correlations and three lapse time windows. **(f)** Result of the spatial inversion from cross-correlations and auto correlations using a single lapse time window. **(g)** Result of the spatial inversion from cross-correlations and auto correlations using a single lapse time window.

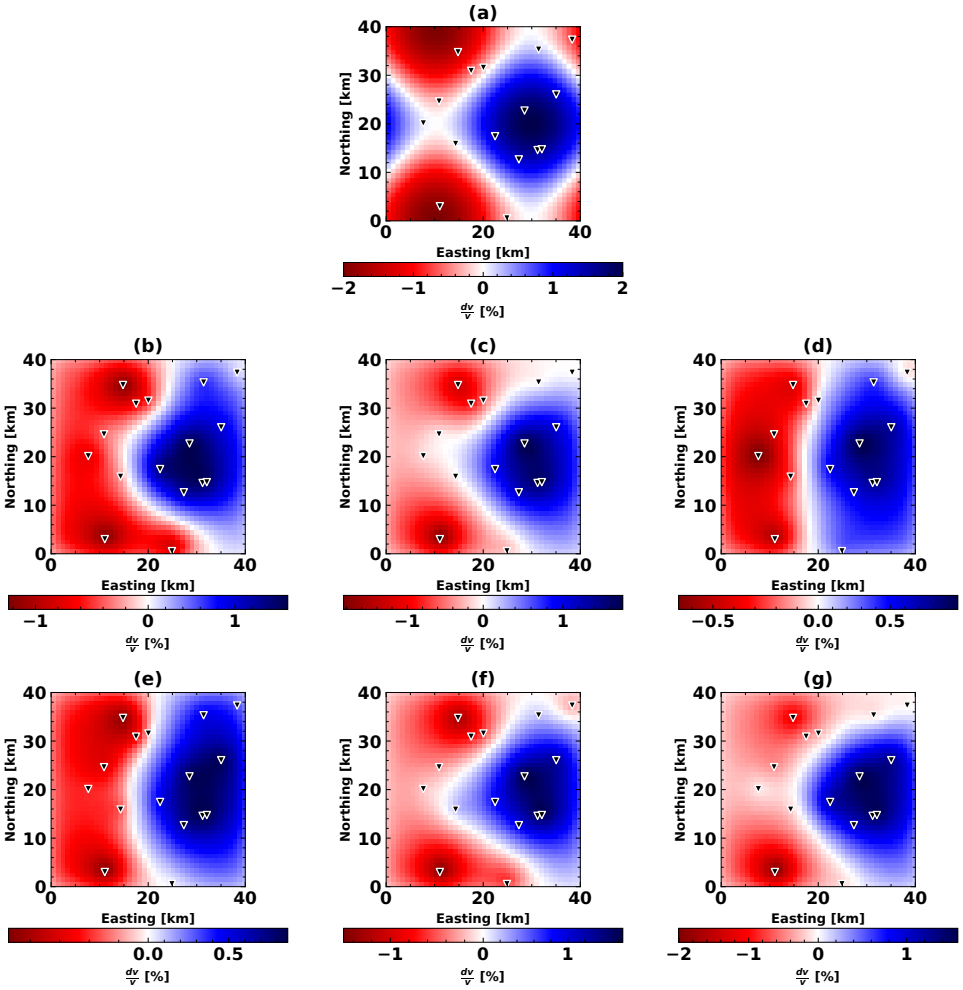

Figure A.4: Examples of the spatial inversion using data from 16 stations, a model variance $\sigma_m = 0.02\ \frac{\text{km}}{\text{km}^2}$, and a correlation length $\lambda = 2$ km. **(a)** The synthetic velocity model and station configuration used. **(b)** Result of the spatial inversion using only cross-correlations and a single lapse time window. **(c)** Result of the spatial inversion using only cross-correlations and three lapse time windows. **(d)** Result of the spatial inversion using only auto-correlations and a single lapse time window. **(e)** Result of the spatial inversion using only auto-correlations and three lapse time windows. **(f)** Result of the spatial inversion from cross-correlations and auto correlations using a single lapse time window. **(g)** Result of the spatial inversion from cross-correlations and auto correlations using a single lapse time window.

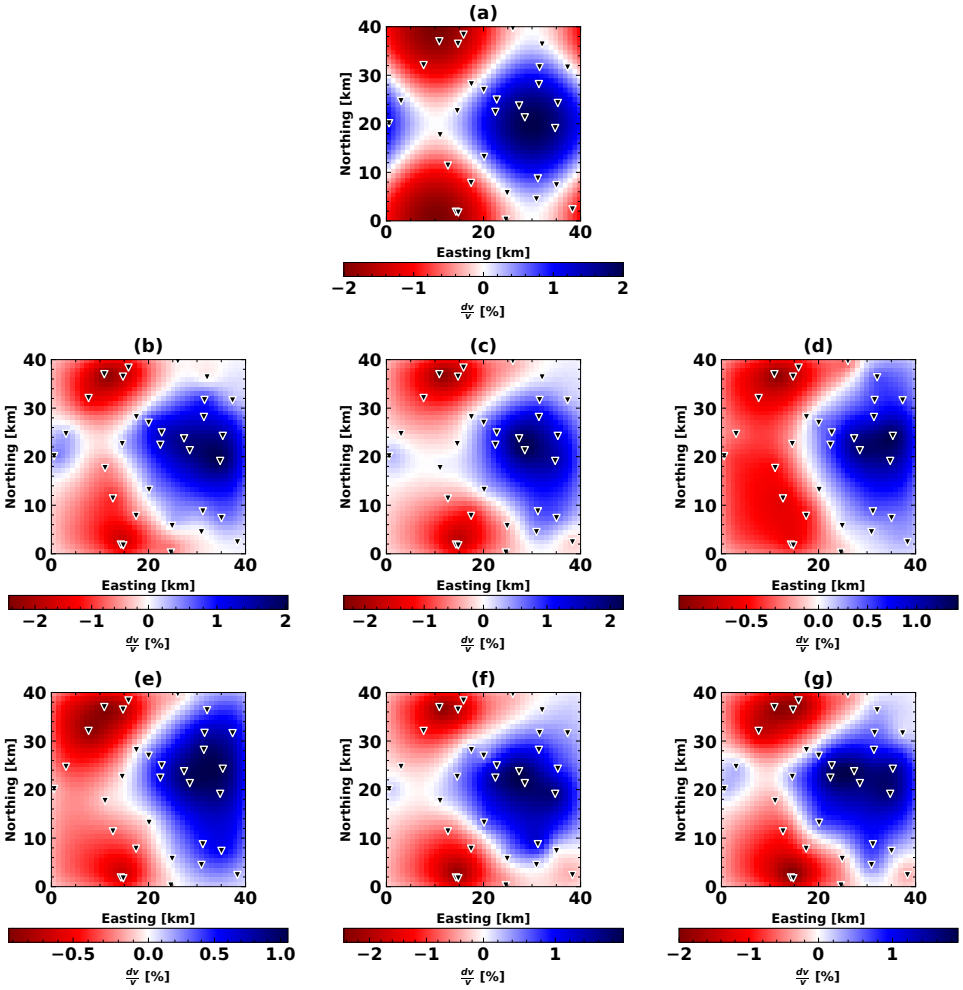

Figure A.5: Examples of the spatial inversion using data from 32 stations a model variance $\sigma_m = 0.05\ \frac{\text{km}}{\text{km}^2}$ and a correlation length $\lambda = 2$ km. **(a)** The synthetic velocity model and station configuration used. **(b)** Result of the spatial inversion using only cross-correlations and a single lapse time window. **(c)** Result of the spatial inversion using only cross-correlations and three lapse time windows. **(d)** Result of the spatial inversion using only auto-correlations and a single lapse time window. **(e)** Result of the spatial inversion using only auto-correlations and three lapse time windows. **(f)** Result of the spatial inversion from cross-correlations and auto correlations using a single lapse time window. **(g)** Result of the spatial inversion from cross-correlations and auto correlations using a single lapse time window.

APPENDIX B

Supporting Information to Chapter 4

Introduction This supporting information includes figures showing the results of the hierarchical clustering algorithm for different frequency bands (Figures B.1 to B.6) and station D0.BZG (Figure B.7). Table S1 provides a quantitative measure of the clusters' dissimilarity, the so-called merging cost, formally, the hypothetical increase of the error sum of squares of the Euclidean distances obtained upon merging the two most similar clusters Ward (1963). Table B.1 shows how the merging cost varies with the frequency band used to compute the correlation functions. We provide the time segments we chose based on the clusters in Table B.2. Figure B.8 shows parameters a and b of the best-fitting dv/v models. In addition, we show relative velocity changes for all station groups computed from auto-, self-, and cross-correlations for one-octave-wide frequency bands between 0.5 and 8 Hz (see Figures B.9 to B.44).

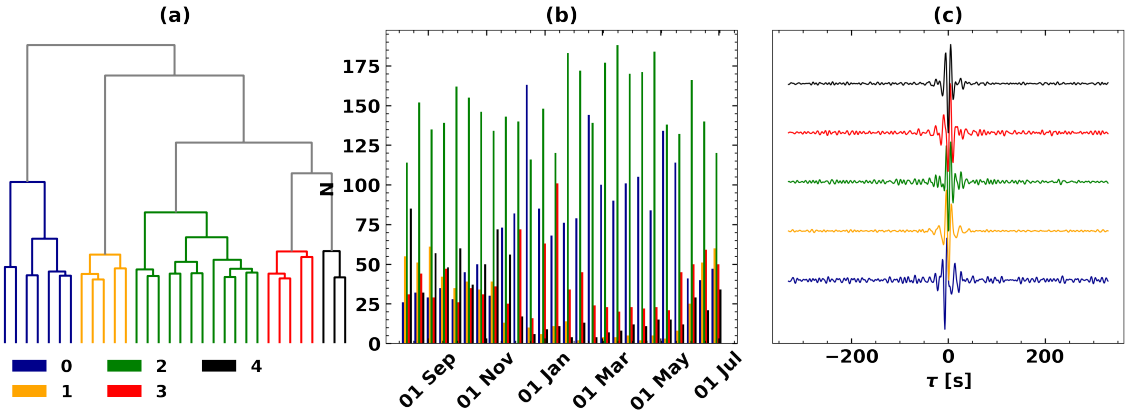

Figure B.1: The output of the hierarchical clustering. As input data, we used one year of self-correlations between station's X9.IR1 (see Figure 4.1 in main publication) east and north component created from waveform data between 0.0625 and 0.125 Hz. Colours are used to identify the different clusters in the three panels. **(a)** A dendrogram that quantifies the similarity between the different clusters. The vertical distance of the branches scales with the merging cost. We show unclustered branches in grey. **(b)** The distribution of the clusters over the whole study period. The bars show the bi-weekly occurrence N of the respective cluster. **(c)** Averages of the CFs belonging to each of the five clusters.

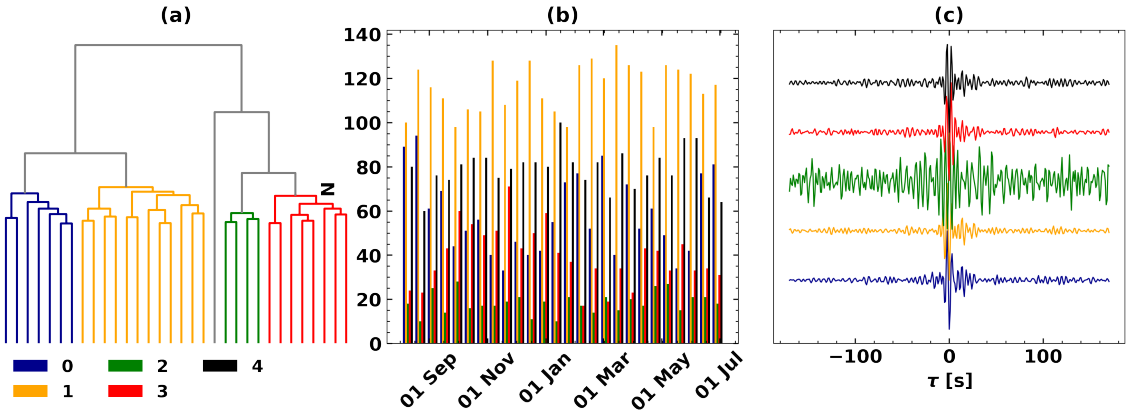

Figure B.2: The result of the hierarchical clustering for station X9.IR1 and the component combination HHE-HHN for frequencies between 0.125 and 0.25 Hz. Colours are used to identify the different clusters in the three panels. **(a)** A dendrogram that quantifies the similarity between the different clusters. The vertical distance of the branches scales with the merging cost. We show unclustered branches in grey. **(b)** The distribution of the clusters over the whole study period. The bars show the bi-weekly occurrence N of the respective cluster. **(c)** Averages of the CFs belonging to each of the five clusters.

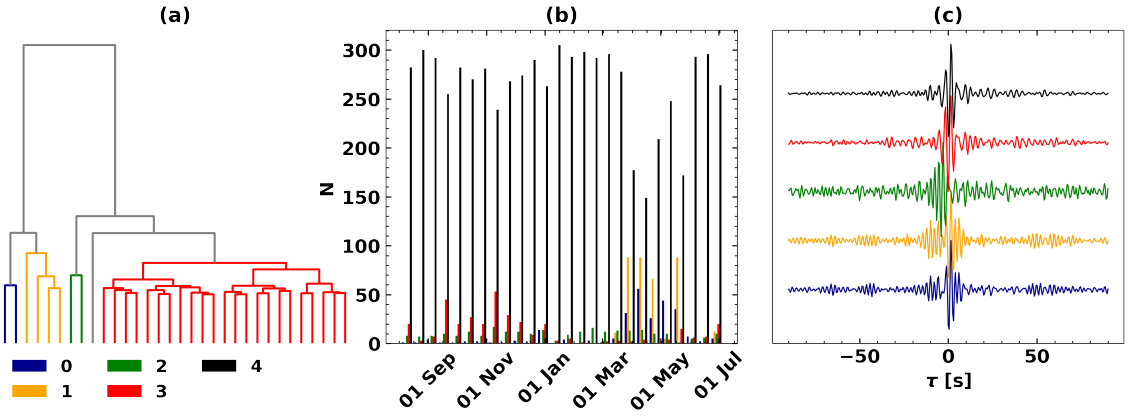

Figure B.3: The result of the hierarchical clustering for station X9.IR1 and the component combination HHE-HHN for frequencies between 0.25 and 0.5 Hz. Colours are used to identify the different clusters in the three panels. **(a)** A dendrogram that quantifies the similarity between the different clusters. The vertical distance of the branches scales with the merging cost. We show unclustered branches in grey. **(b)** The distribution of the clusters over the whole study period. The bars show the bi-weekly occurrence N of the respective cluster. **(c)** Averages of the CFs belonging to each of the five clusters.

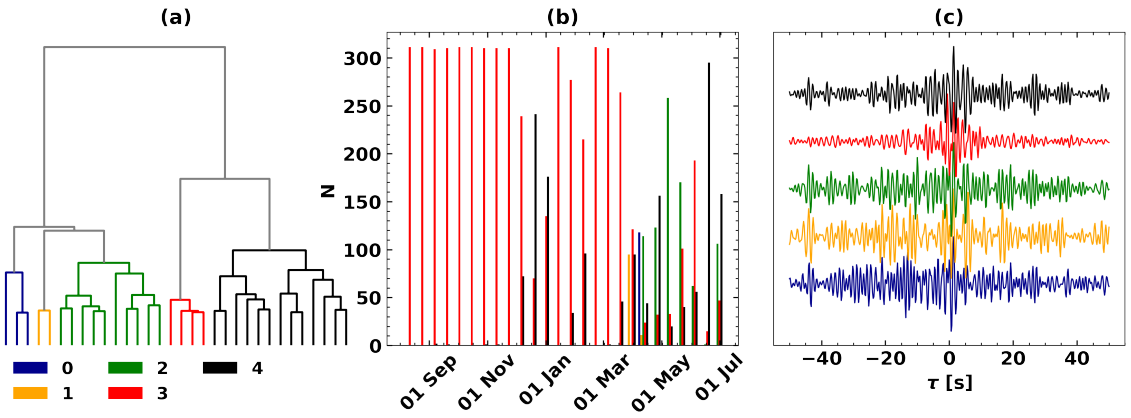

Figure B.4: The result of the hierarchical clustering for station X9.IR1 and the component combination HHE-HHN for frequencies between 0.5 and 1.0 Hz. Colours are used to identify the different clusters in the three panels. **(a)** A dendrogram that quantifies the similarity between the different clusters. The vertical distance of the branches scales with the merging cost. We show unclustered branches in grey. **(b)** The distribution of the clusters over the whole study period. The bars show the bi-weekly occurrence N of the respective cluster. **(c)** Averages of the CFs belonging to each of the five clusters.

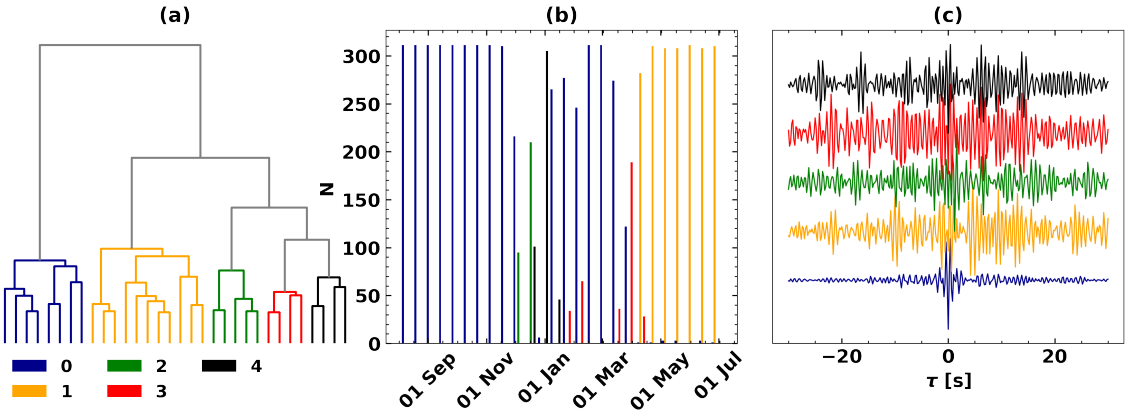

Figure B.5: The result of the hierarchical clustering for station X9.IR1 and the component combination HHE-HHN for frequencies between 1.0 and 2.0 Hz. Colours are used to identify the different clusters in the three panels. **(a)** A dendrogram that quantifies the similarity between the different clusters. The vertical distance of the branches scales with the merging cost. We show unclustered branches in grey. **(b)** The distribution of the clusters over the whole study period. The bars show the bi-weekly occurrence N of the respective cluster. **(c)** Averages of the CFs belonging to each of the five clusters.

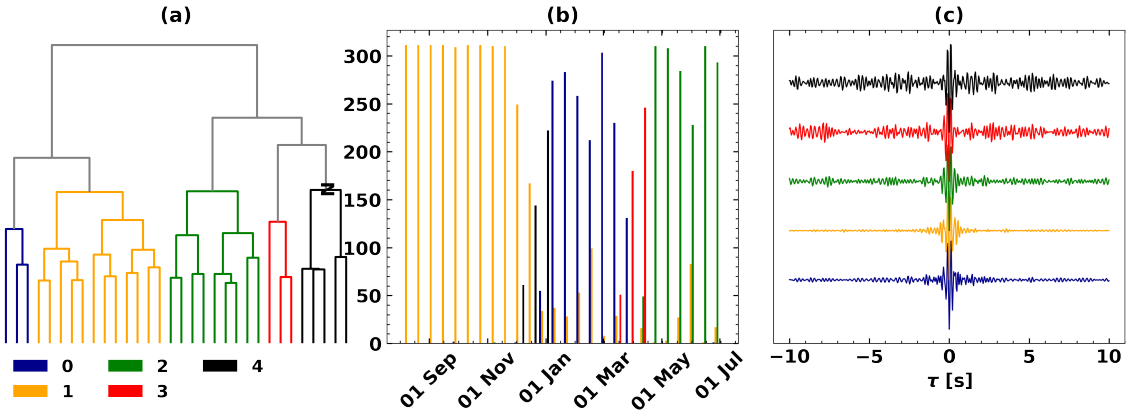

Figure B.6: The result of the hierarchical clustering for station X9.IR1 and the component combination HHE-HHN for frequencies between 4.0 and 8.0 Hz. Colours are used to identify the different clusters in the three panels. **(a)** A dendrogram that quantifies the similarity between the different clusters. The vertical distance of the branches scales with the merging cost. We show unclustered branches in grey. **(b)** The distribution of the clusters over the whole study period. The bars show the bi-weekly occurrence N of the respective cluster. **(c)** Averages of the CFs belonging to each of the five clusters.

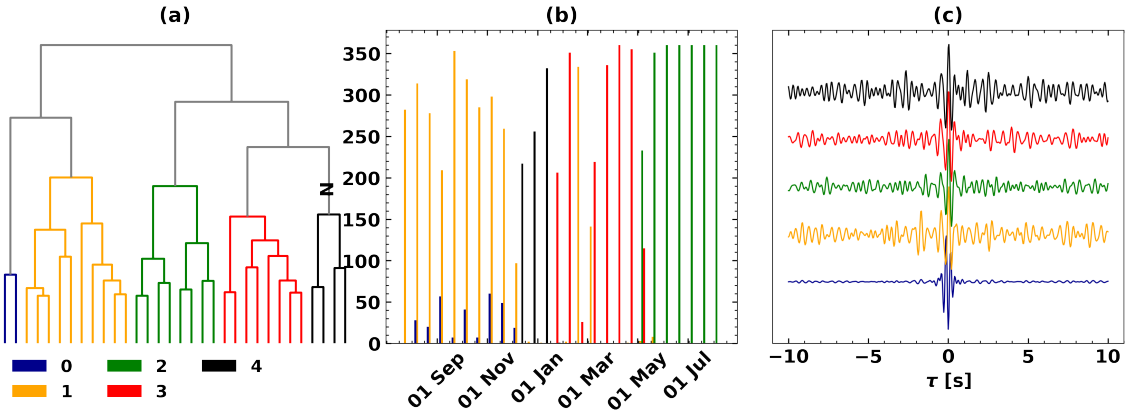

Figure B.7: The result of the hierarchical clustering for station D0.BZG and the component combination HHE-HHN for frequencies between 2.0 and 4.0 Hz. Colours are used to identify the different clusters in the three panels. **(a)** A dendrogram that quantifies the similarity between the different clusters. The vertical distance of the branches scales with the merging cost. We show unclustered branches in grey. **(b)** The distribution of the clusters over the whole study period. The bars show the bi-weekly occurrence N of the respective cluster. **(c)** Averages of the CFs belonging to each of the five clusters.

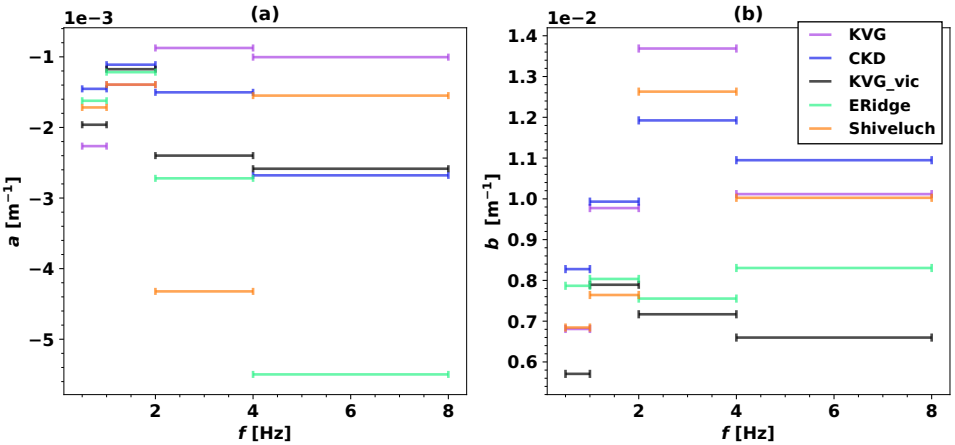

Figure B.8: Values of the modelling parameters a (in panel (a), impact of the precipitation) and b (in panel (b), impact of the snow thickness) as determined by the least-squares inversion from data from auto- and self-correlations. The values are shown for each of the frequency bands and station groups. See Section 4.5.1 and eq. 4.1 for a detailed description of the model.

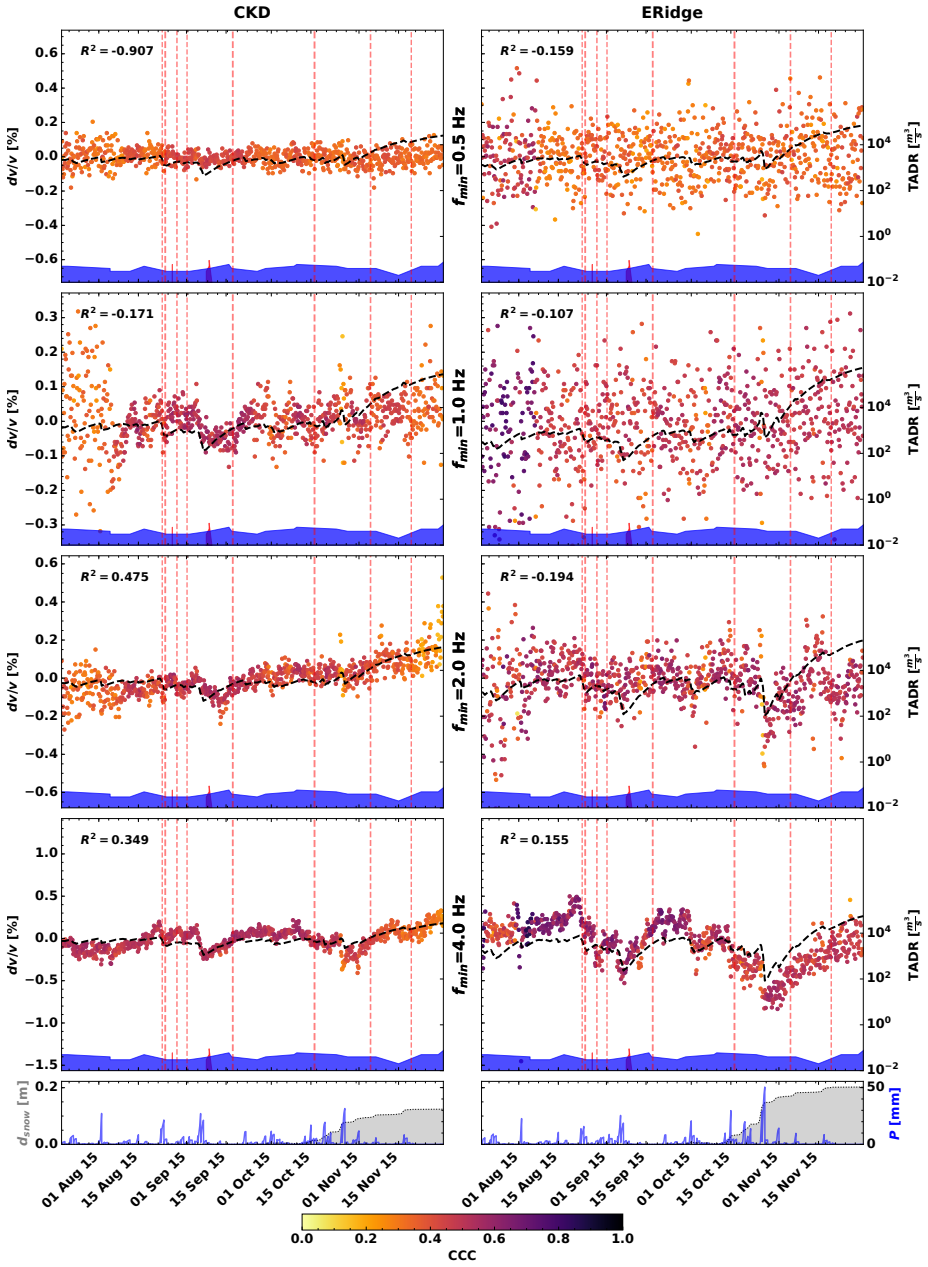

Figure B.9: Velocity change for the station groups CKD and ERidge (see Figure 4.4 for locations) created from auto- and self-correlations between all components for the frequencies between f_{min} and $2f_{min}$ for the time between 2015/07/01 to 2015/12/01. Refer to Figure 8 in the main paper for a detailed explanation of the figure

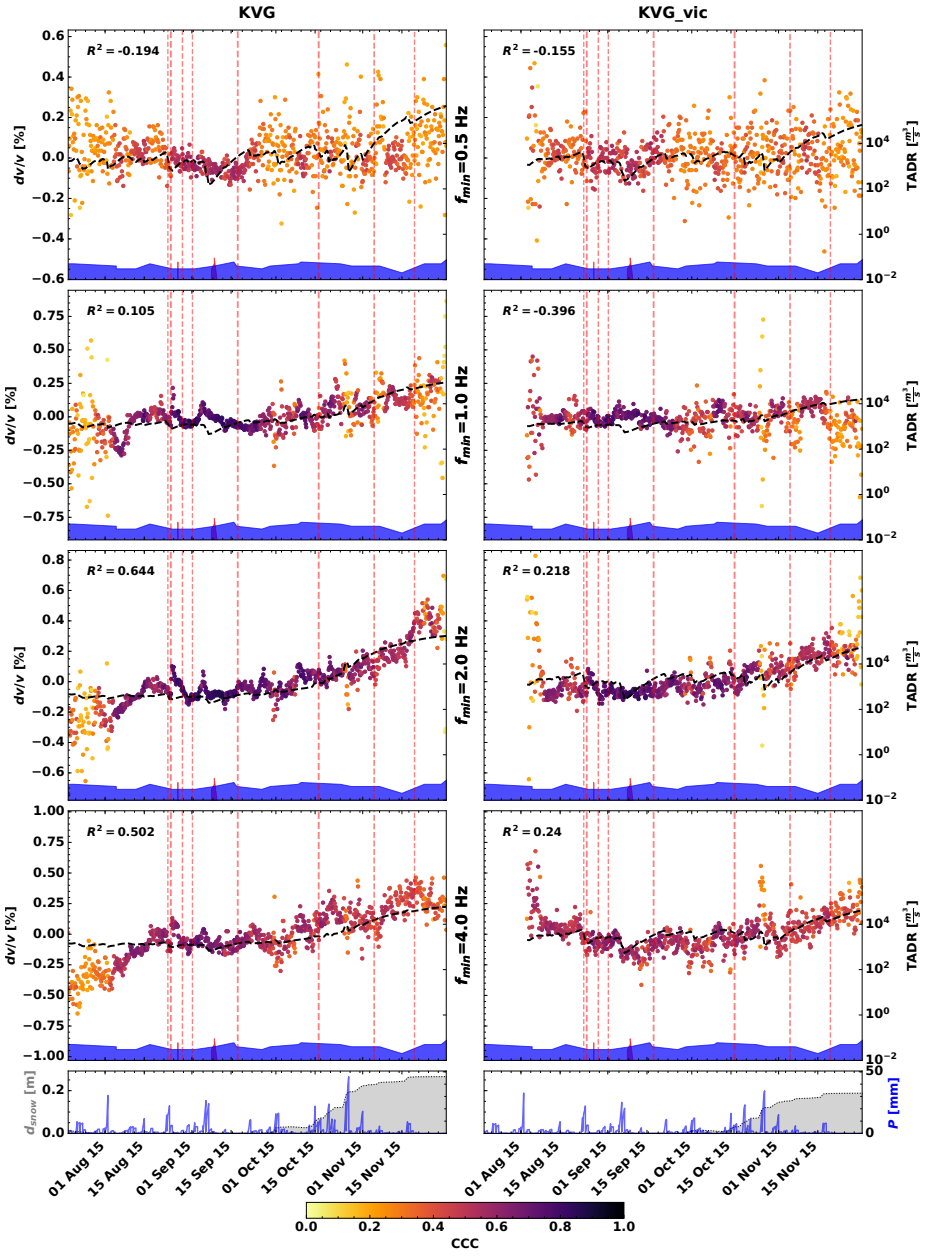

Figure B.10: Velocity change for the station groups KVG and KVG_vic (see Figure 4.4 for locations) created from auto- and self-correlations between all components for the frequencies between f_{min} and $2f_{min}$ for the time between 2015/07/01 to 2015/12/01. Refer to Figure 4.8 for a detailed explanation of the figure.

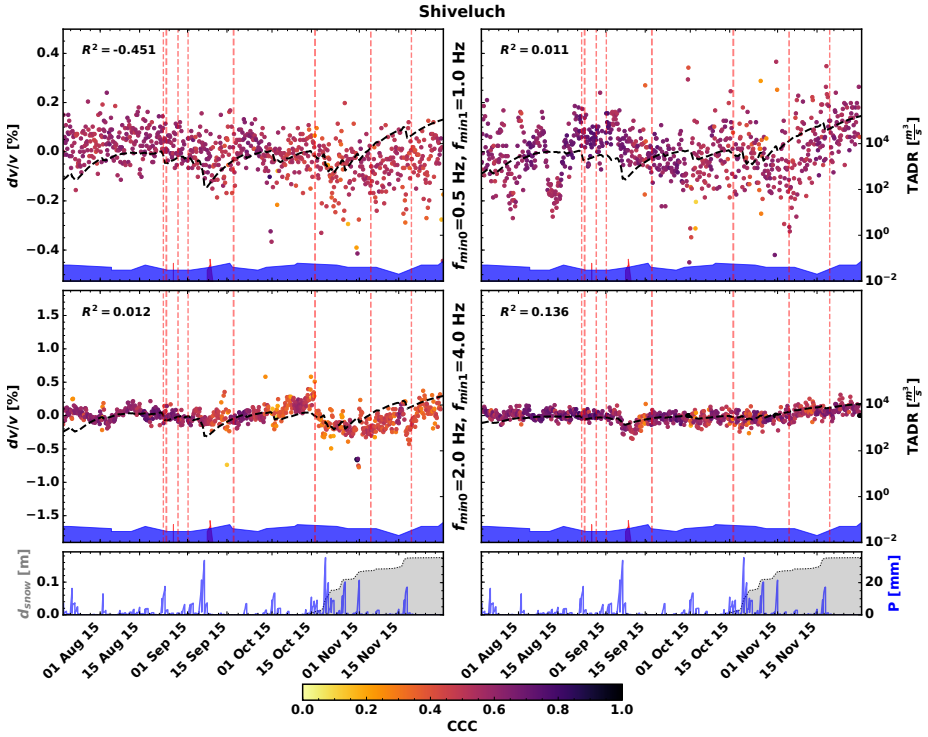

Figure B.11: Velocity change for the station group Shiveluch (see Figure 4.4 for locations) created from auto- and self-correlations between all components for the frequencies between f_{min} and $2f_{min}$ for the time between 2015/07/01 to 2015/12/01. Refer to Figure 4.8 for a detailed explanation of the figure.

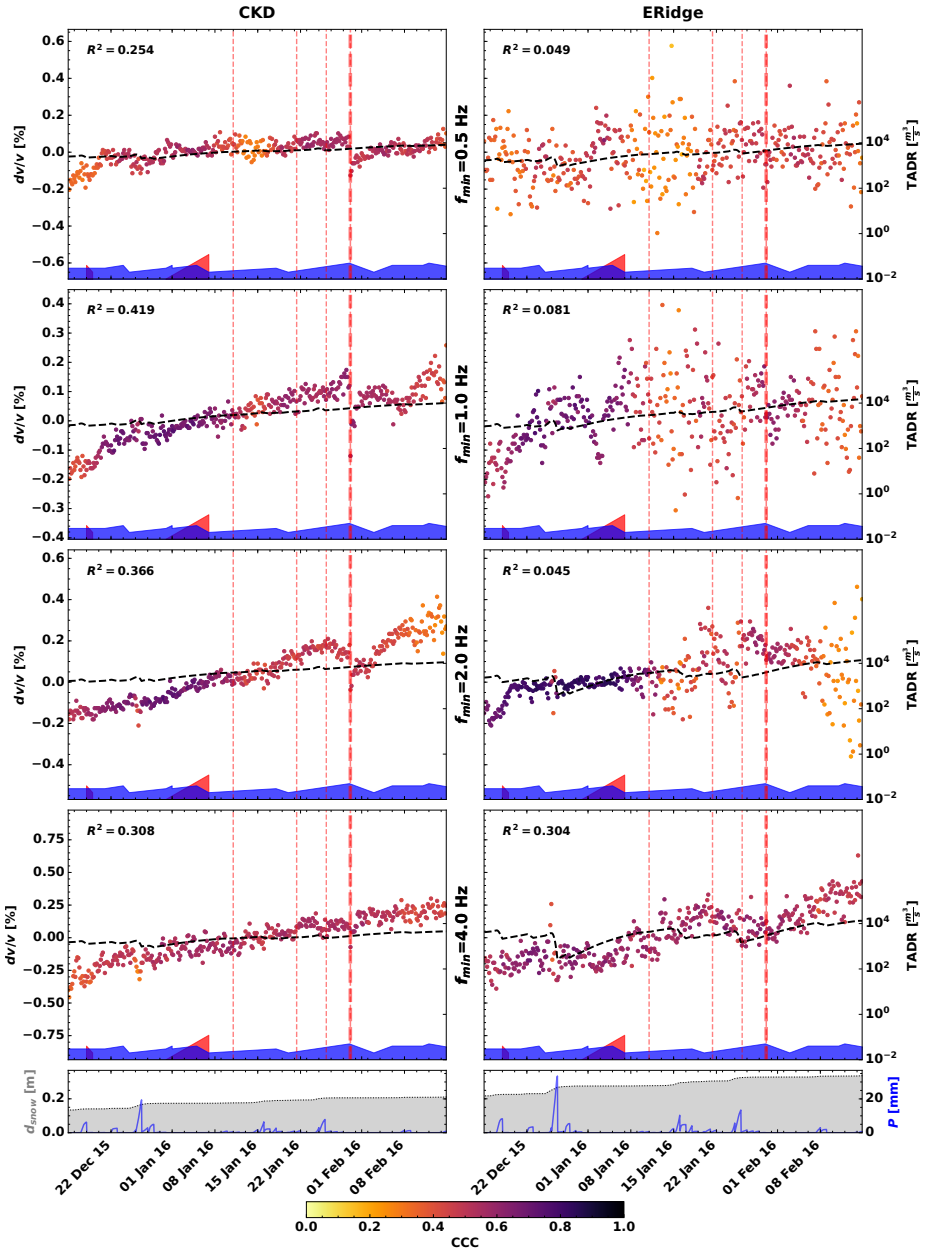

Figure B.12: Velocity change for the station groups CKD and ERidge (see Figure 4.4 for locations) created from auto- and self-correlations between all components for the frequencies between f_{min} and $2f_{min}$ for the time between 2015/12/15 to 2016/02/15. Refer to Figure 4.8 for a detailed explanation of the figure.

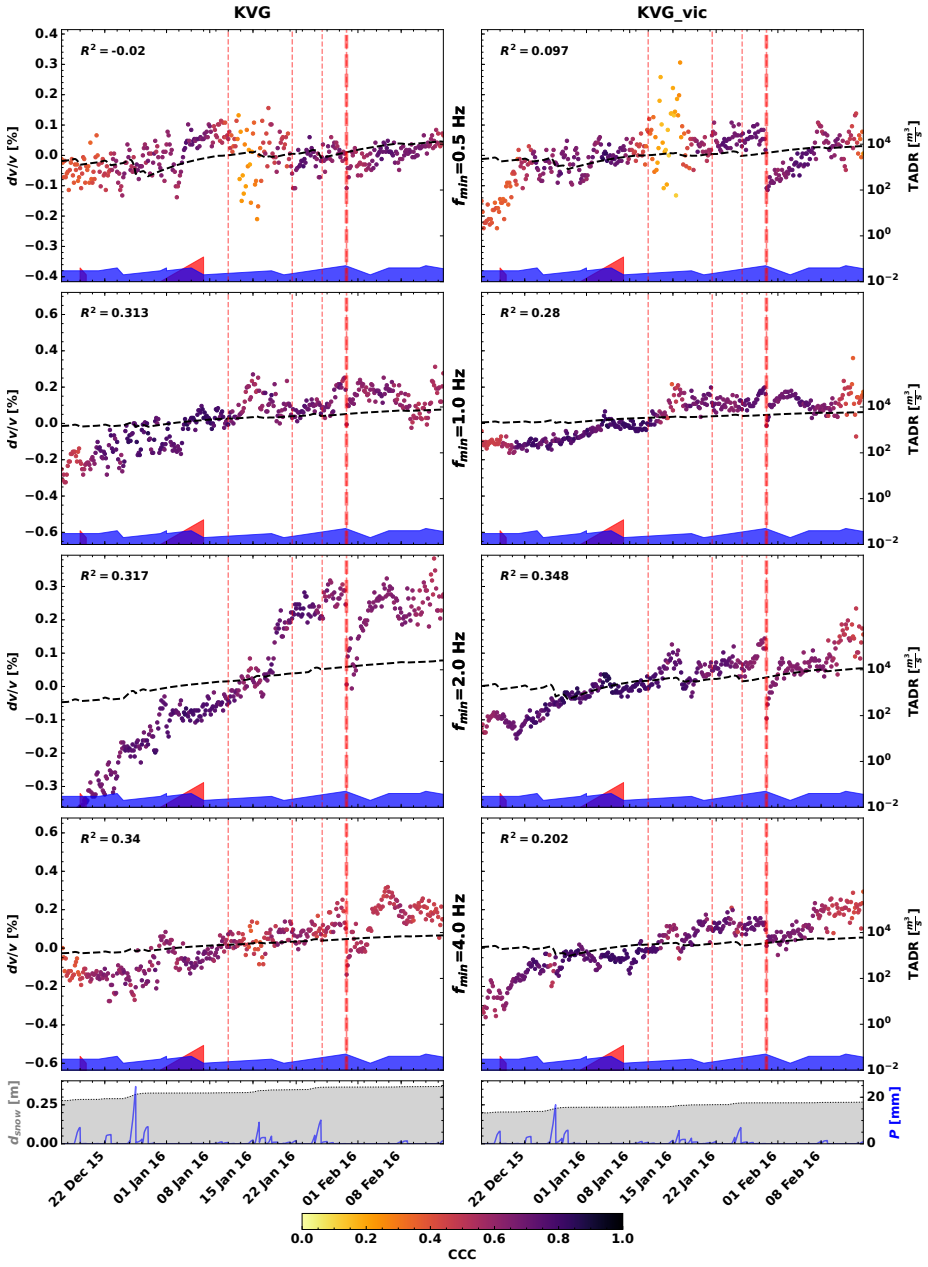

Figure B.13: Velocity change for the station groups KVG and KVG_vic (see Figure 4.4 for locations) created from auto- and self-correlations between all components for the frequencies between f_{min} and $2f_{min}$ for the time between 2015/12/15 to 2016/02/15. Refer to Figure 4.8 for a detailed explanation of the figure.

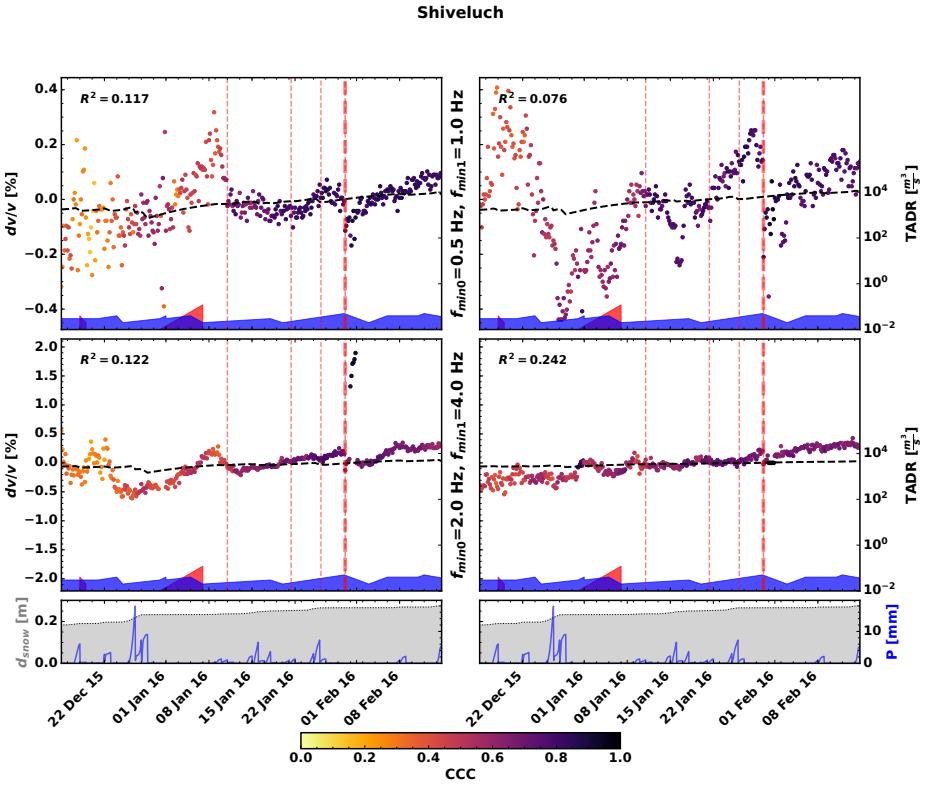

Figure B.14: Velocity change for the station group Shiveluch (see Figure 4.4 for locations) created from auto- and self-correlations between all components for the frequencies between f_{min} and $2f_{min}$ for the time between 2015/12/15 to 2016/02/15. Refer to Figure 4.8 for a detailed explanation of the figure.

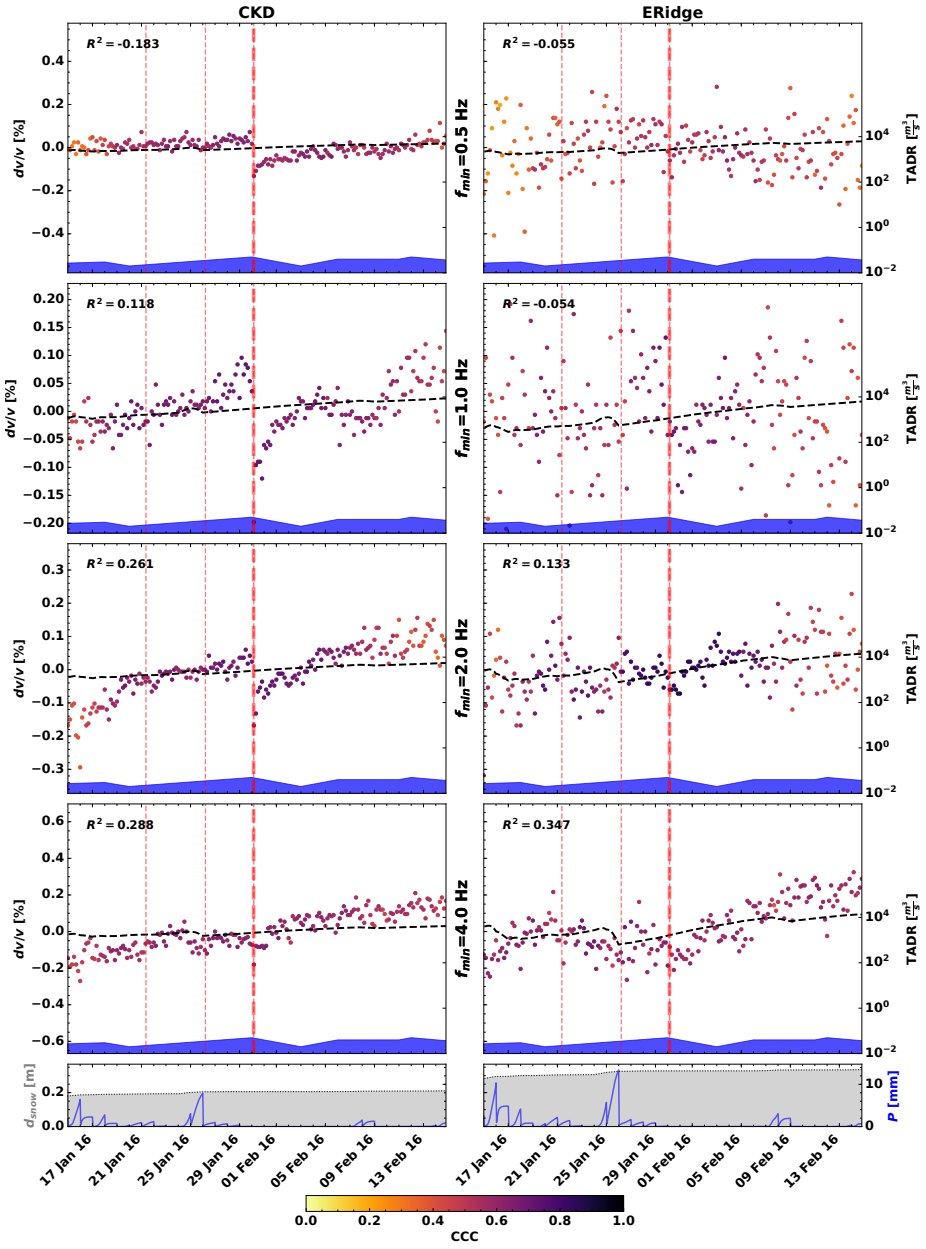

Figure B.15: Velocity change for the station groups CKD and ERidge (see Figure 4.4 for locations) created from auto- and self-correlations between all components for the frequencies between f_{min} and $2f_{min}$ for the time between 2016/01/15 to 2016/02/15. Refer to Figure 4.8 for a detailed explanation of the figure.

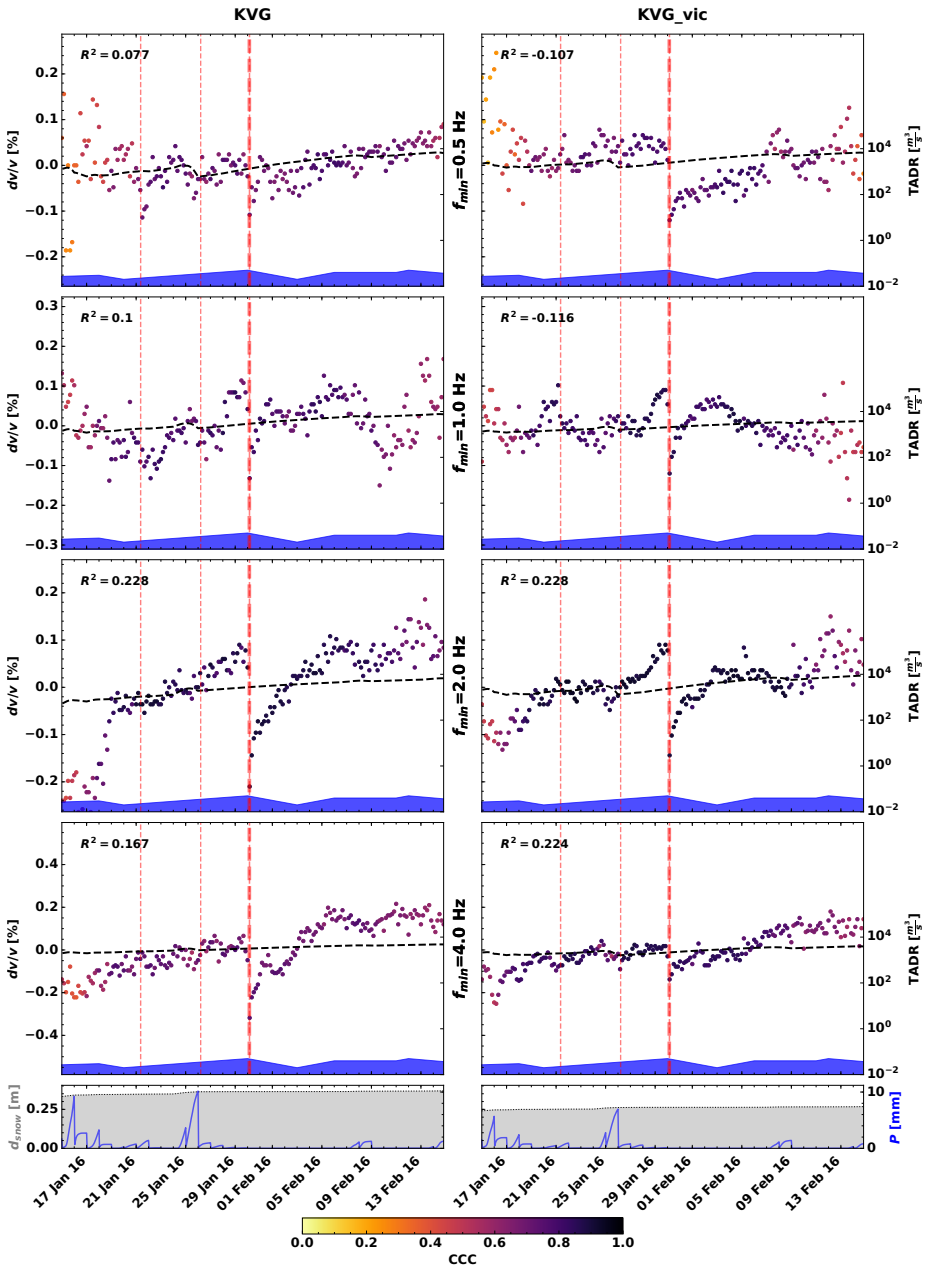

Figure B.16: Velocity change for the station groups KVG and KVG_vic (see Figure 4.4 for locations) created from auto- and self-correlations between all components for the frequencies between f_{min} and $2f_{min}$ for the time between 2016/01/15 to 2016/02/15. Refer to Figure 4.8 for a detailed explanation of the figure.

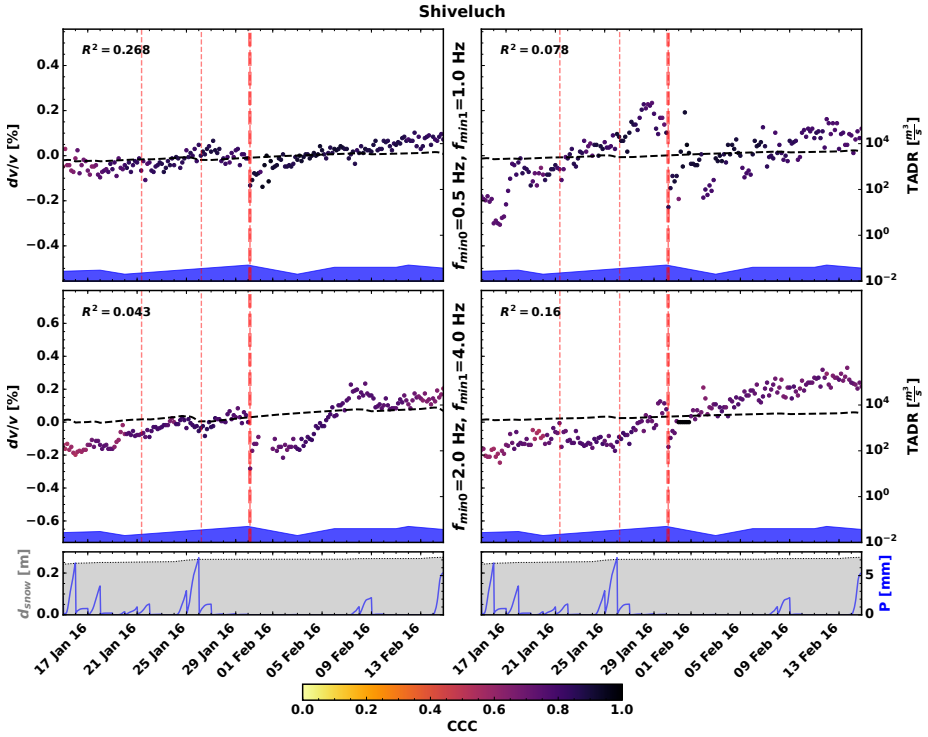

Figure B.17: Velocity change for the station group Shiveluch (see Figure 4.4 for locations) created from auto- and self-correlations between all components for the frequencies between f_{min} and $2f_{min}$ for the time between 2016/01/15 to 2016/02/15. Refer to Figure 4.8 for a detailed explanation of the figure.

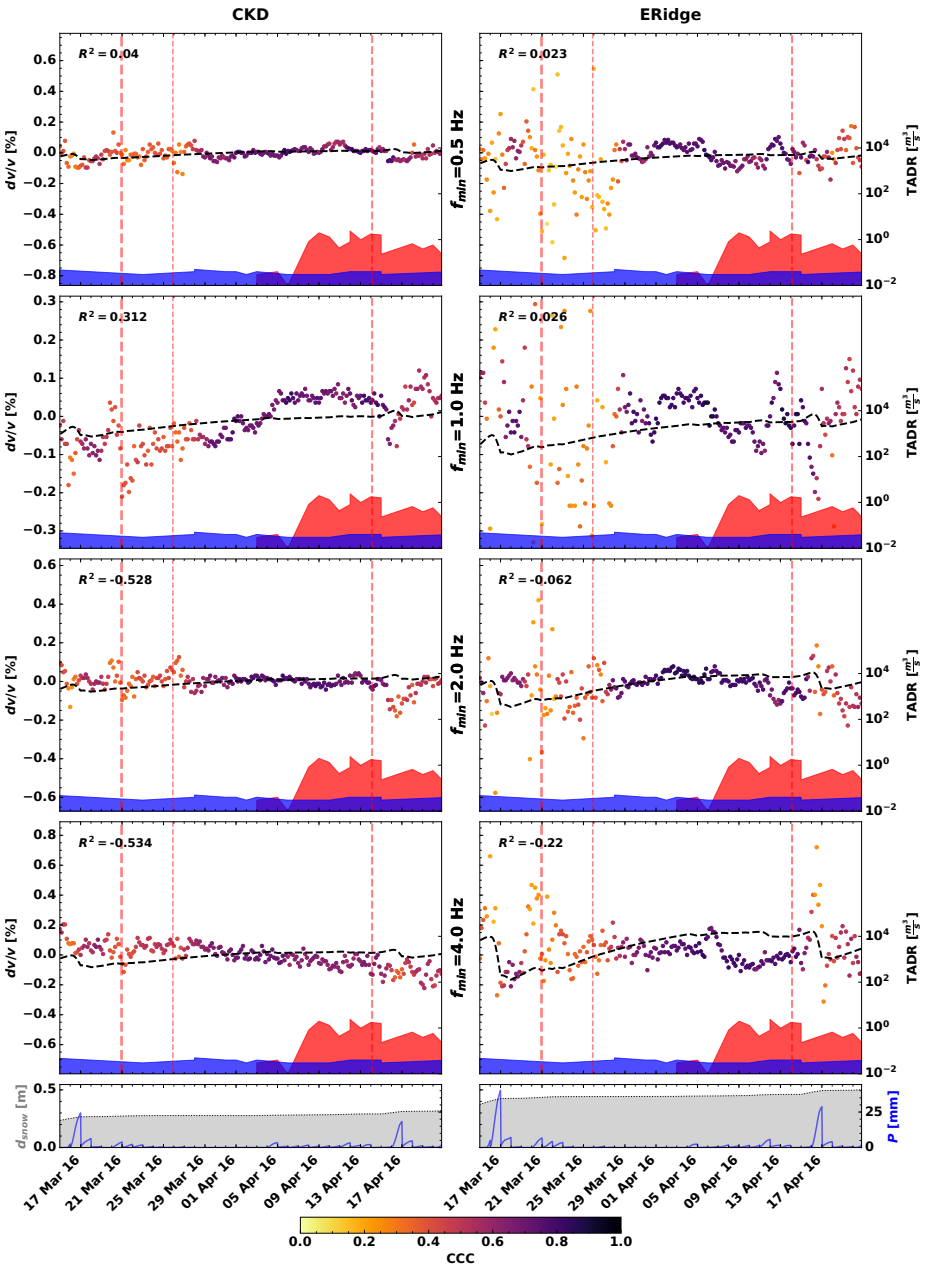

Figure B.18: Velocity change for the station groups CKD and ERidge (see Figure 4.4 for locations) created from auto- and self-correlations between all components for the frequencies between f_{min} and $2f_{min}$ for the time between 2016/03/15 to 2016/04/21. Refer to Figure 4.8 for a detailed explanation of the figure.

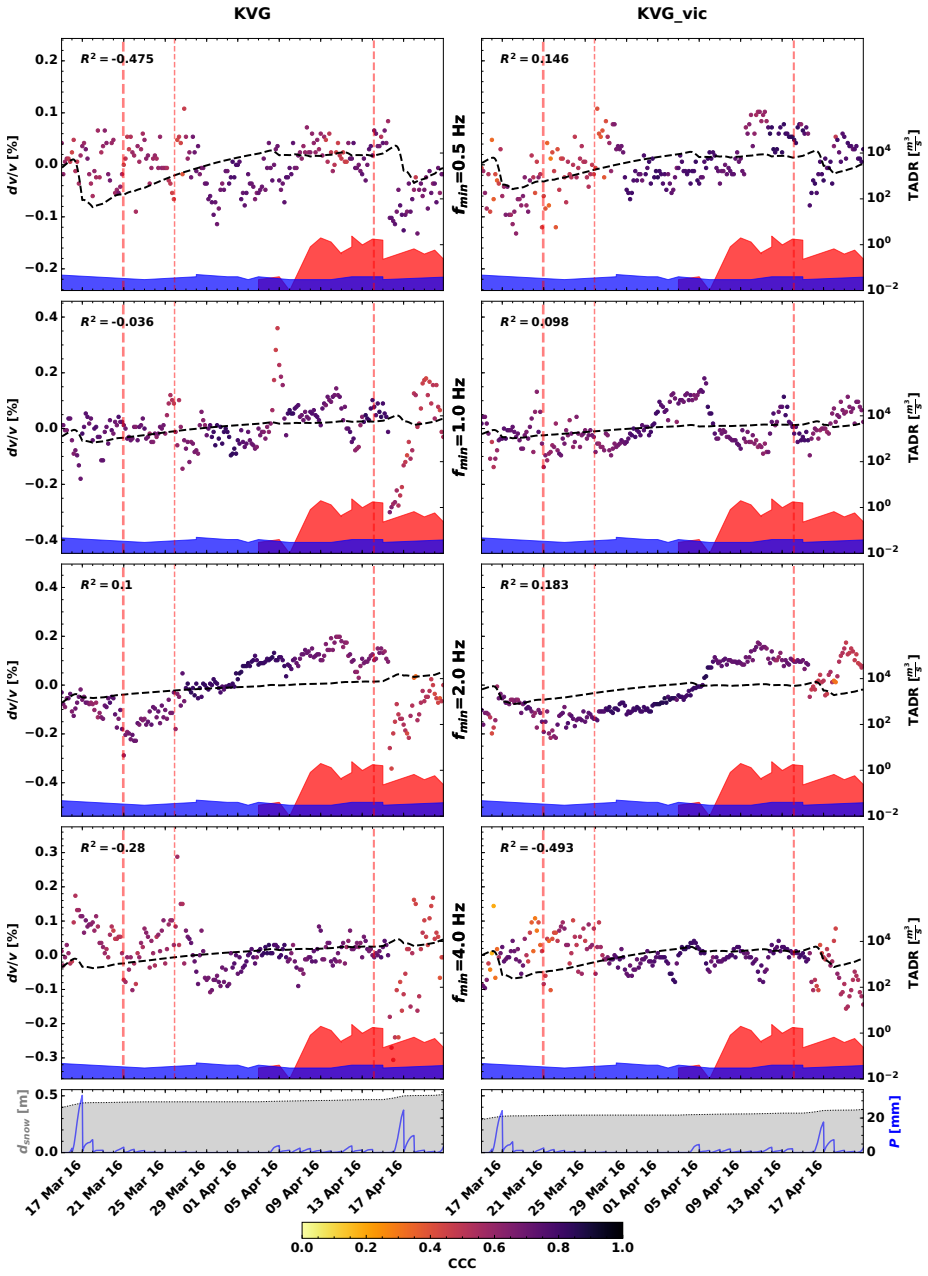

Figure B.19: Velocity change for the station groups KVG and KVG_vic (see Figure 4.4 for locations) created from auto- and self-correlations between all components for the frequencies between f_{min} and $2f_{min}$ for the time between 2016/03/15 to 2016/04/21. Refer to Figure 4.8 for a detailed explanation of the figure.

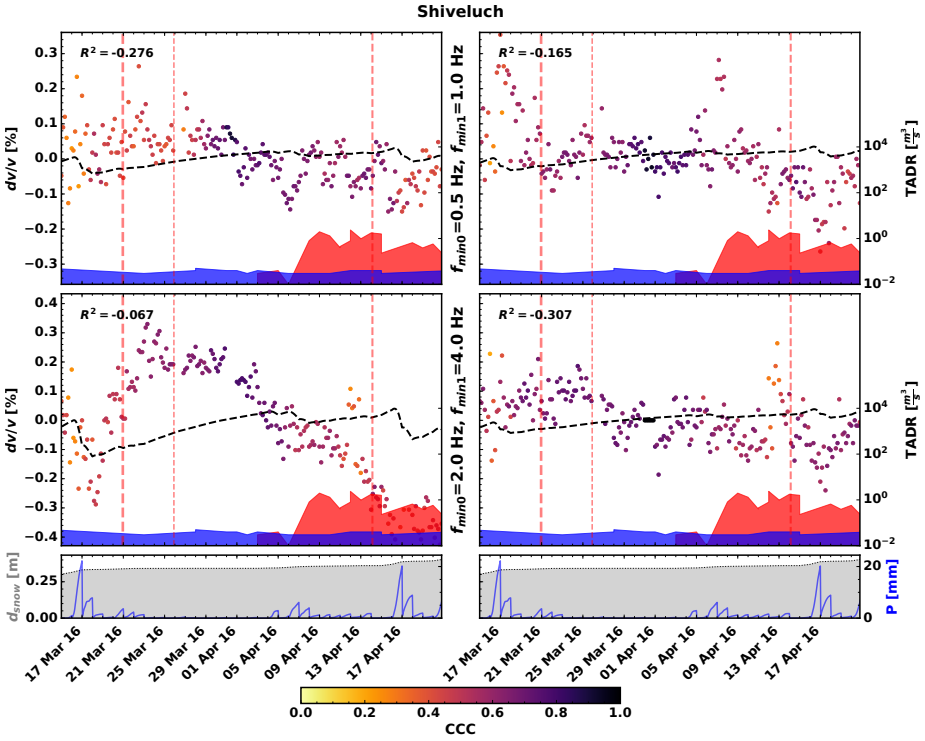

Figure B.20: Velocity change for the station group Shiveluch (see Figure 4.4 for locations) created from auto- and self-correlations between all components for the frequencies between f_{min} and $2f_{min}$ for the time between 2016/03/15 to 2016/04/21. Refer to Figure 4.8 for a detailed explanation of the figure.

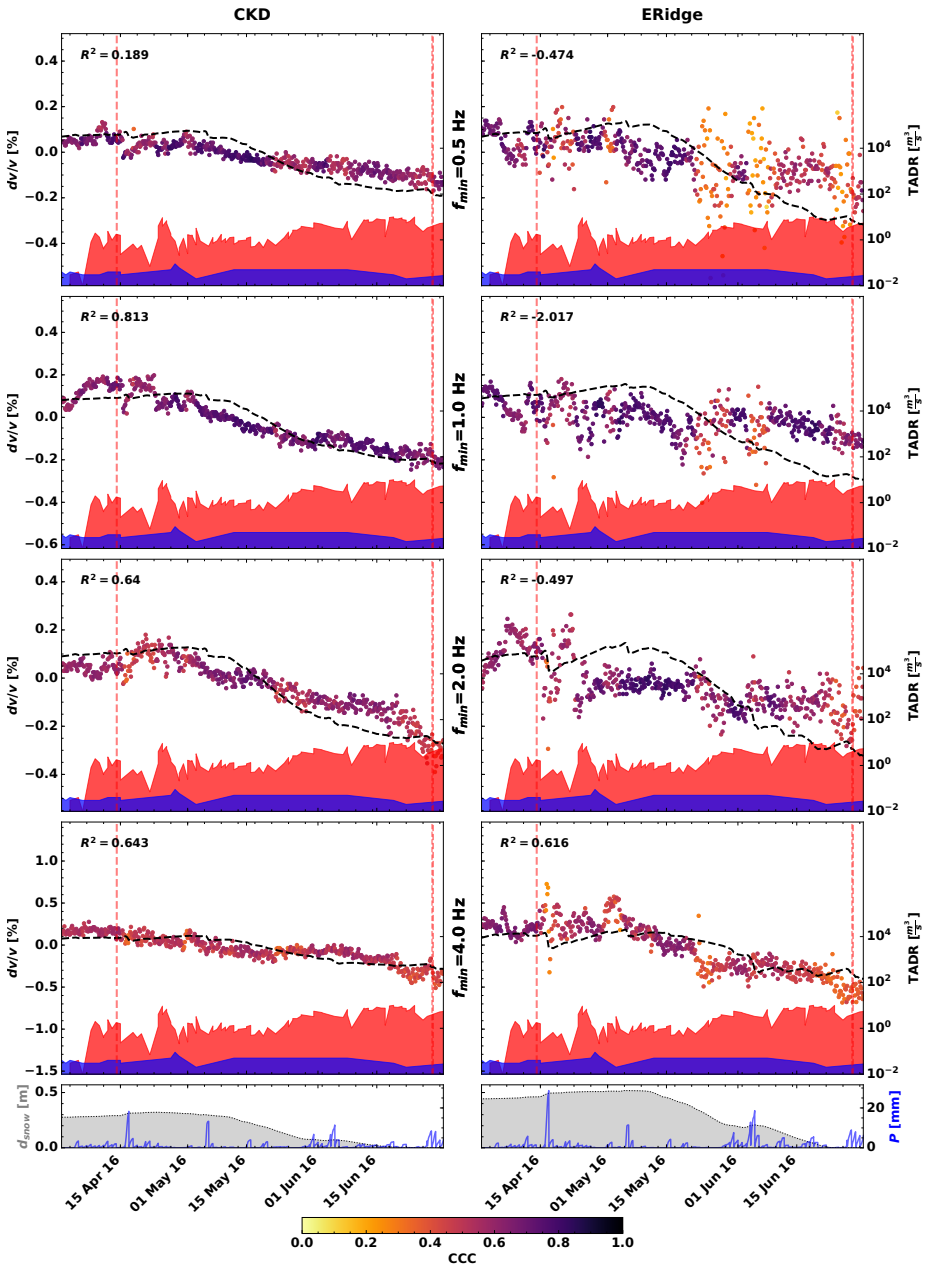

Figure B.21: Velocity change for the station groups CKD and ERidge (see Figure 4.4 for locations) created from auto- and self-correlations between all components for the frequencies between f_{min} and $2f_{min}$ for the time between 2016/04/01 to 2016/07/01. Refer to Figure 4.8 for a detailed explanation of the figure.

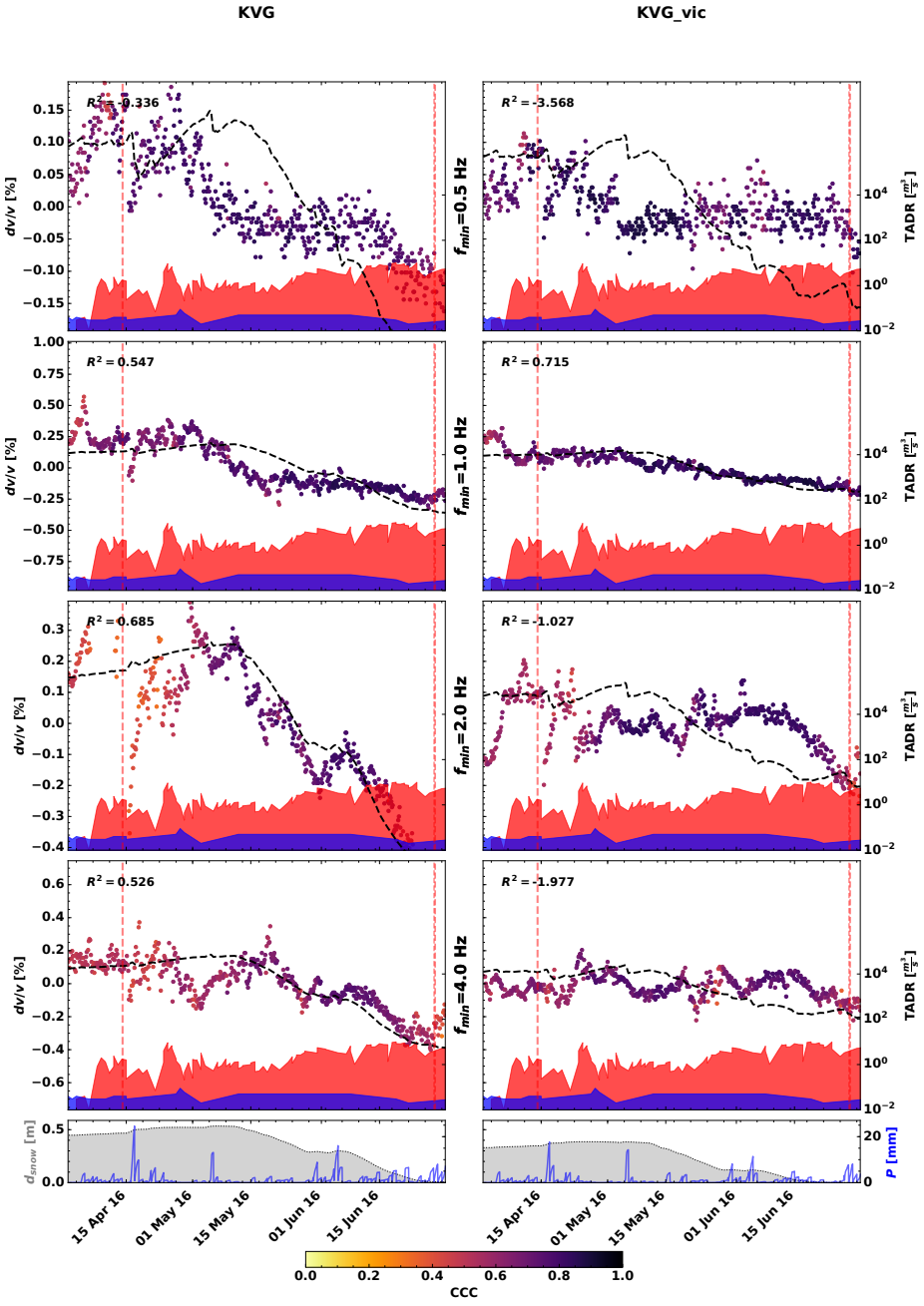

Figure B.22: Velocity change for the station groups KVG and KVG_vic (see Figure 4.4 for locations) created from auto- and self-correlations between all components for the frequencies between f_{min} and $2f_{min}$ for the time between 2016/04/01 to 2016/07/01. Refer to Figure 4.8 for a detailed explanation of the figure.

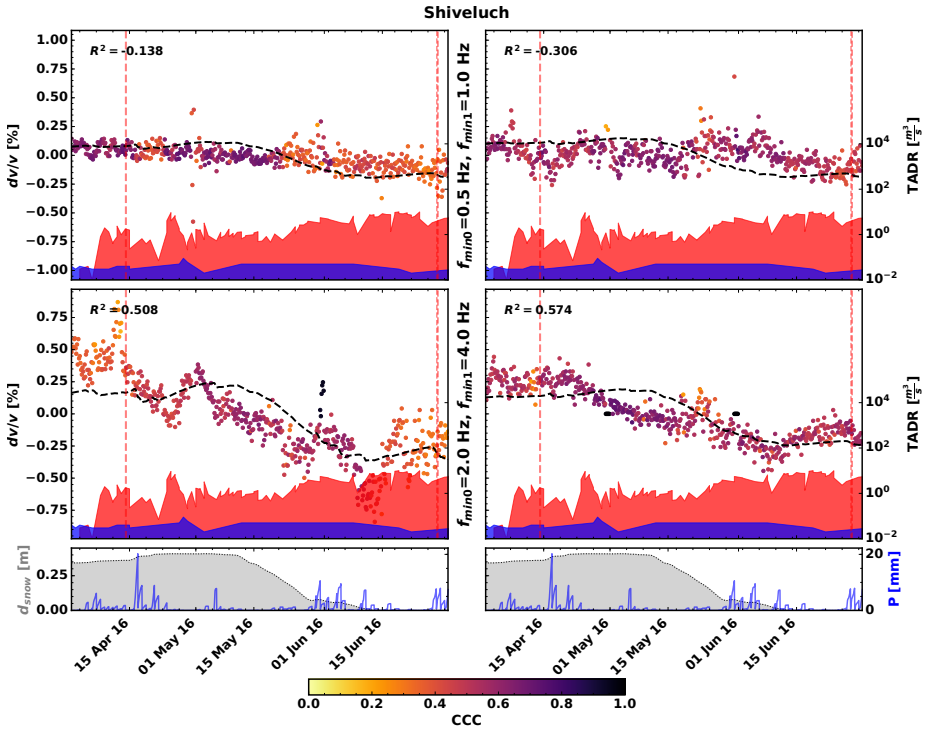

Figure B.23: Velocity change for the station group Shiveluch (see Figure 4.4 for locations) created from auto- and self-correlations between all components for the frequencies between f_{min} and $2f_{min}$ for the time between 2016/04/01 to 2016/07/01. Refer to Figure 4.8 for a detailed explanation of the figure.

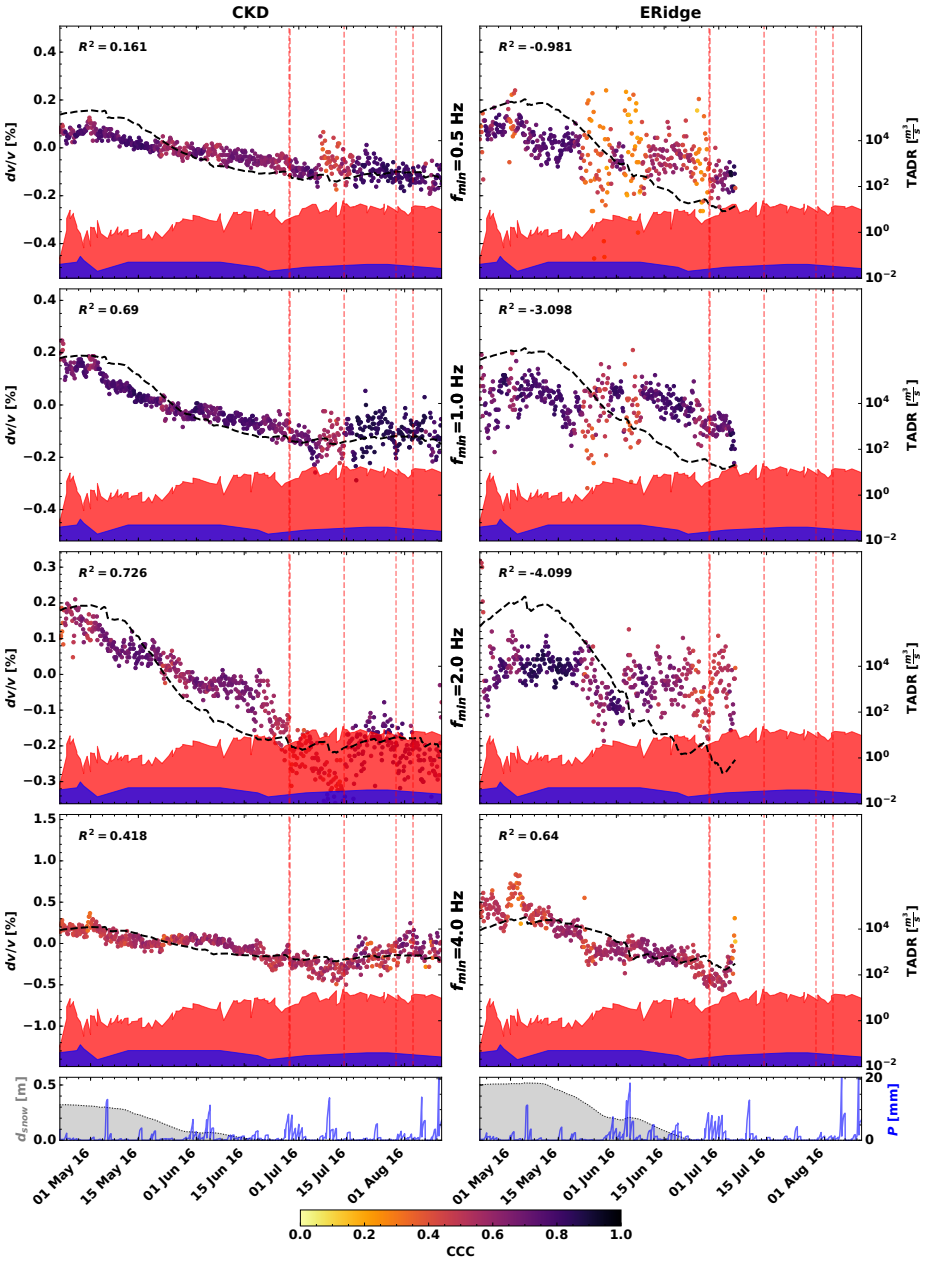

Figure B.24: Velocity change for the station groups CKD and ERidge (see Figure 4.4 for locations) created from auto- and self-correlations between all components for the frequencies between f_{min} and $2f_{min}$ for the time between 2016/04/22 to 2016/09/01. Refer to Figure 4.8 for a detailed explanation of the figure.

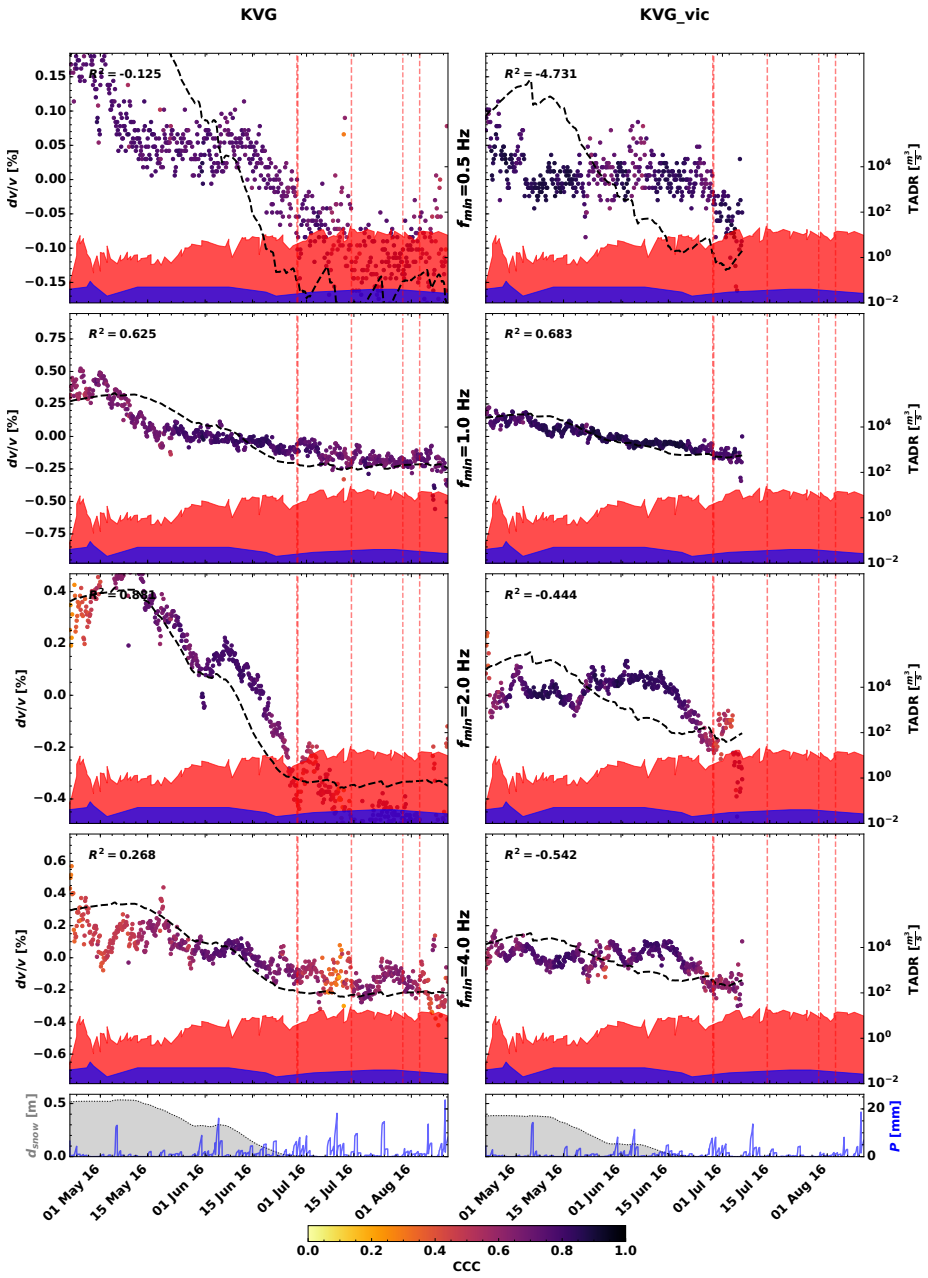

Figure B.25: Velocity change for the station groups KVG and KVG_vic (see Figure 4.4 for locations) created from auto- and self-correlations between all components for the frequencies between f_{min} and $2f_{min}$ for the time between 2016/04/22 to 2016/09/01. Refer to Figure 4.8 for a detailed explanation of the figure.

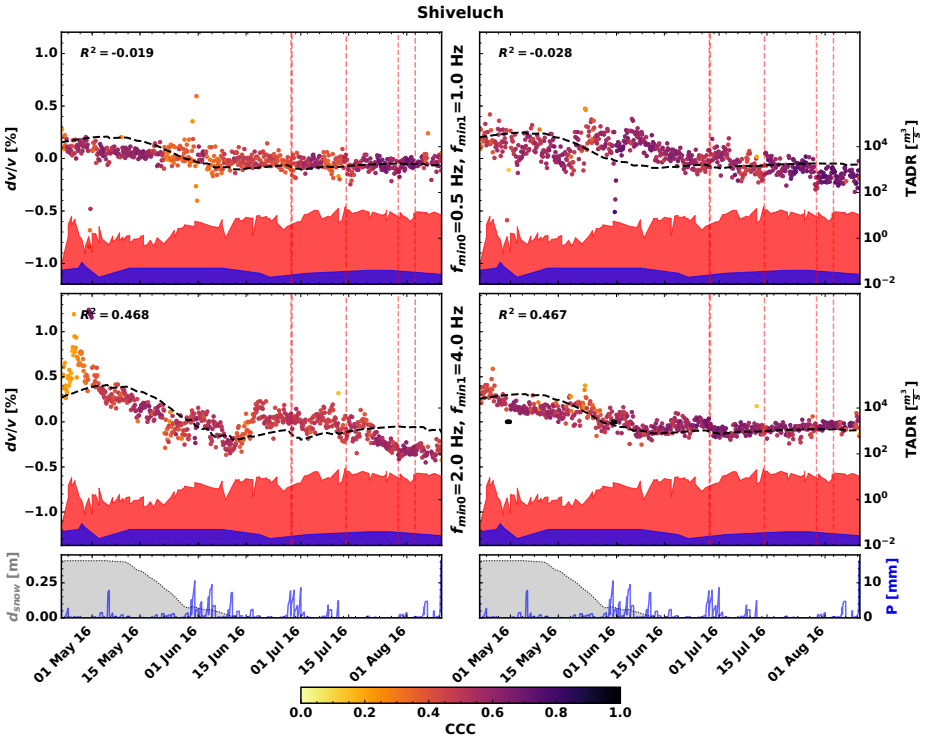

Figure B.26: Velocity change for the station group Shiveluch (see Figure 4.4 for locations) created from auto- and self-correlations between all components for the frequencies between f_{min} and $2f_{min}$ for the time between 2016/04/22 to 2016/09/01. Refer to Figure 4.8 for a detailed explanation of the figure.

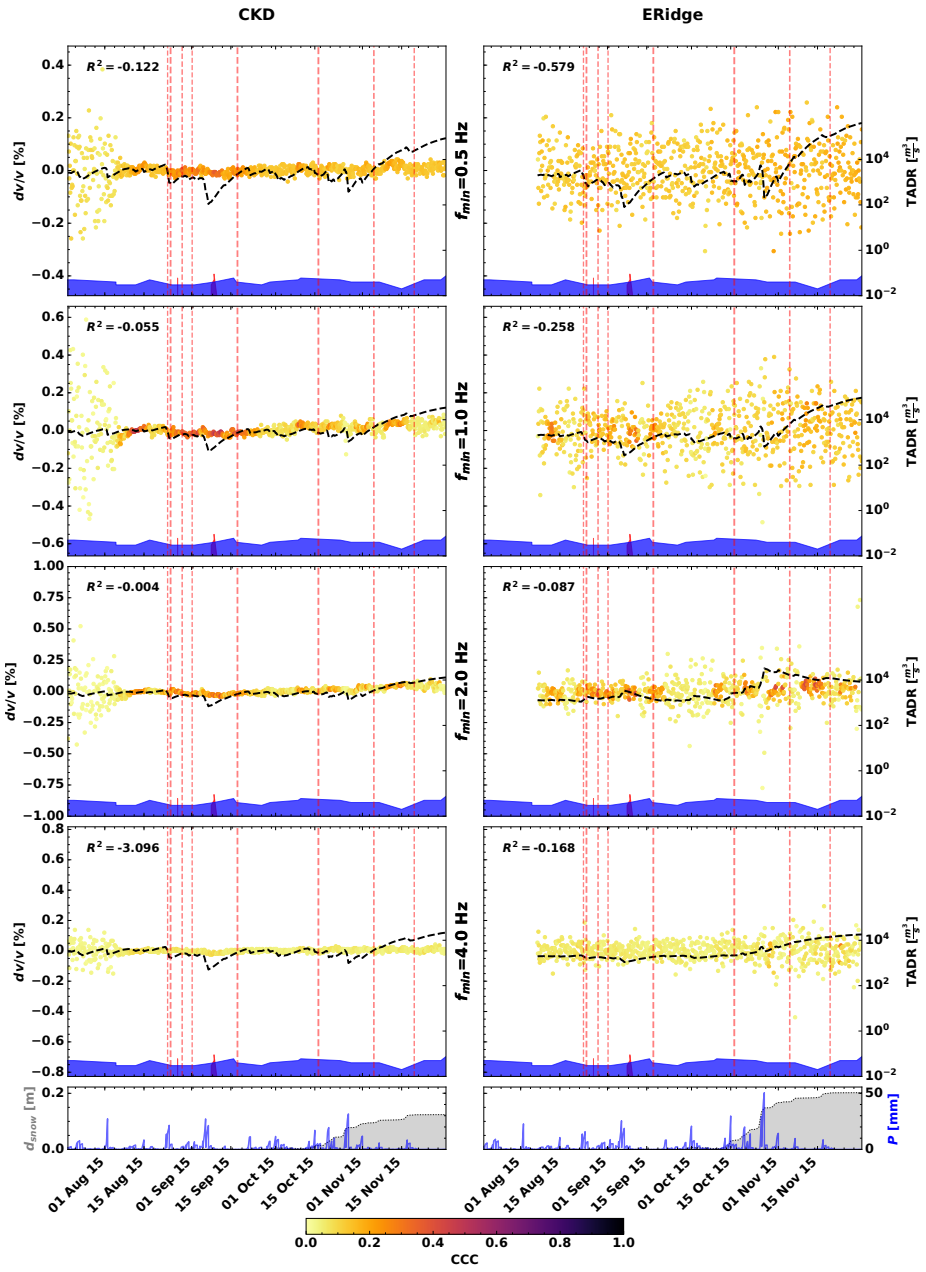

Figure B.27: Velocity change for the station groups CKD and ERidge (see Figure 4.4 for locations) created from cross-correlations (i.e., between stations) between all components for the frequencies between f_{min} and $2f_{min}$ for the time between 2015/07/01 to 2015/12/05. Refer to Figure 4.8 for a detailed explanation of the figure.

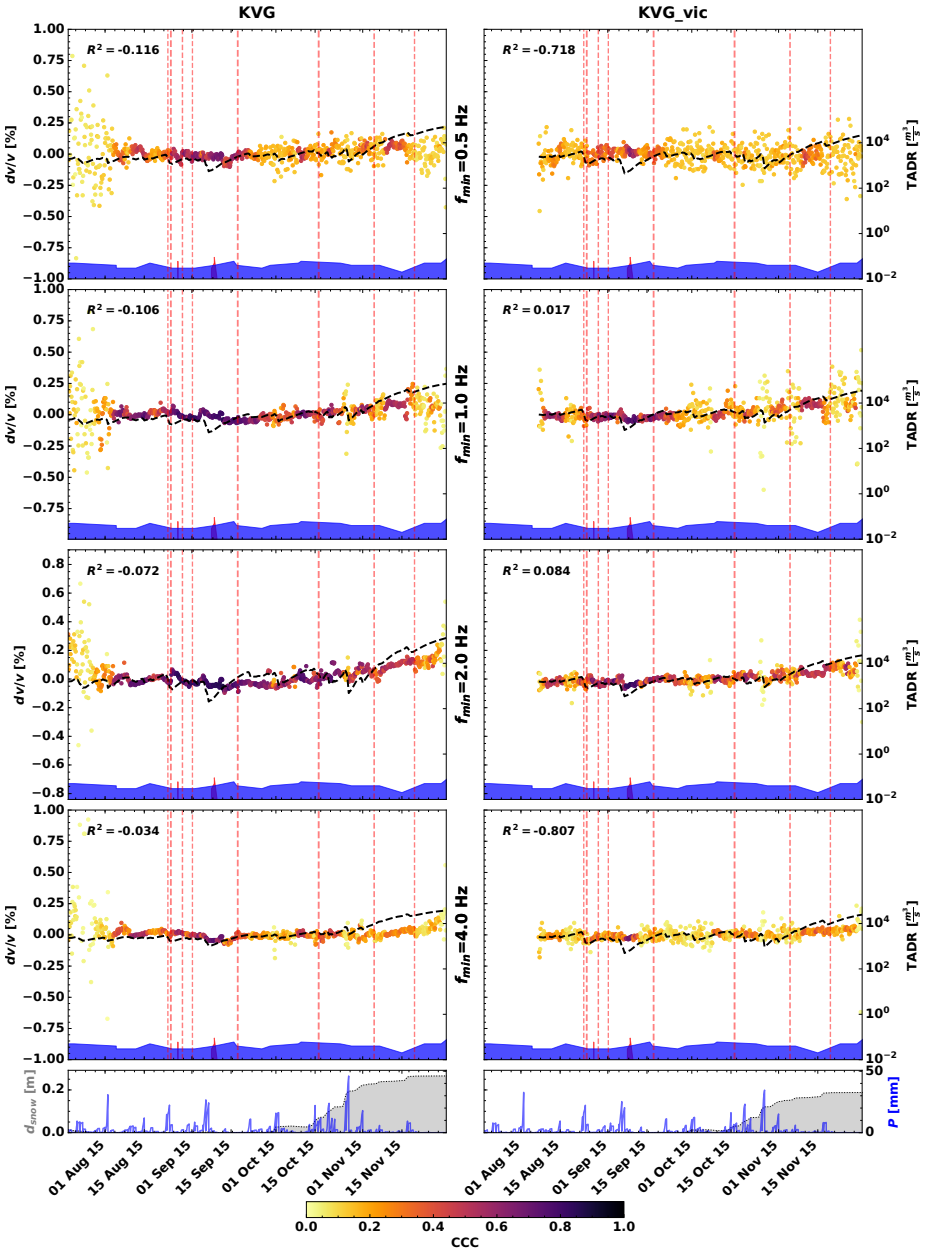

Figure B.28: Velocity change for the station groups KVG and KVG_vic (see Figure 4.4 for locations) created from cross-correlations (i.e., between stations) between all components for the frequencies between f_{min} and $2f_{min}$ for the time between 2015/07/01 to 2015/12/01. Refer to Figure 4.8 for a detailed explanation of the figure.

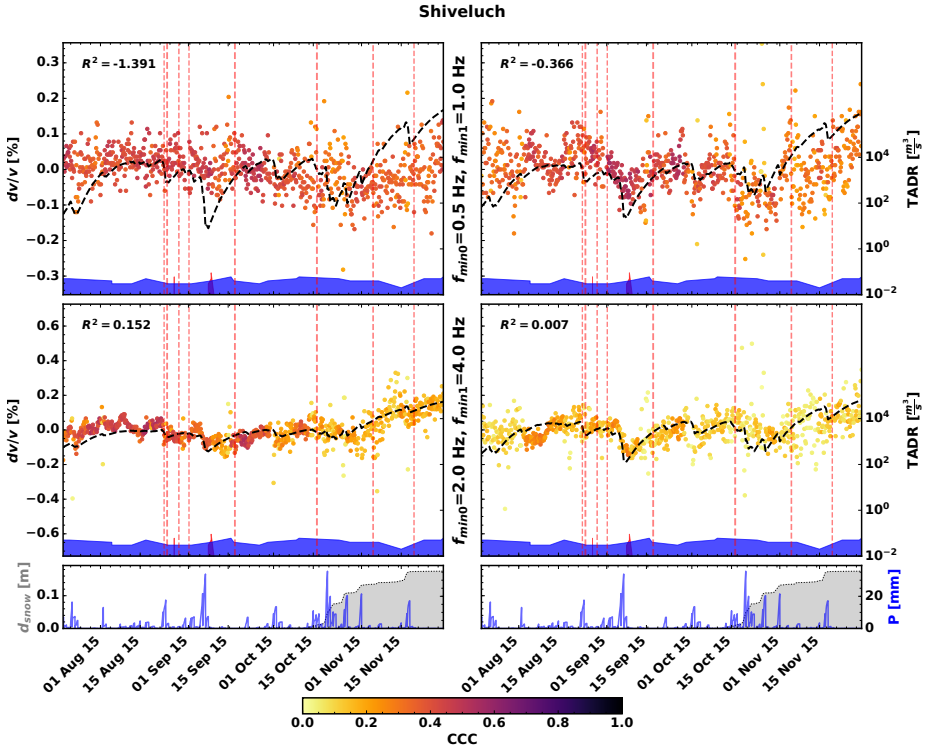

Figure B.29: Velocity change for the station group Shiveluch (see Figure 4.4 for locations) created from cross-correlations (i.e., between stations) between all components for the frequencies between f_{min} and $2f_{min}$ for the time between 2015/07/01 to 2015/12/01. Refer to Figure 4.8 for a detailed explanation of the figure.

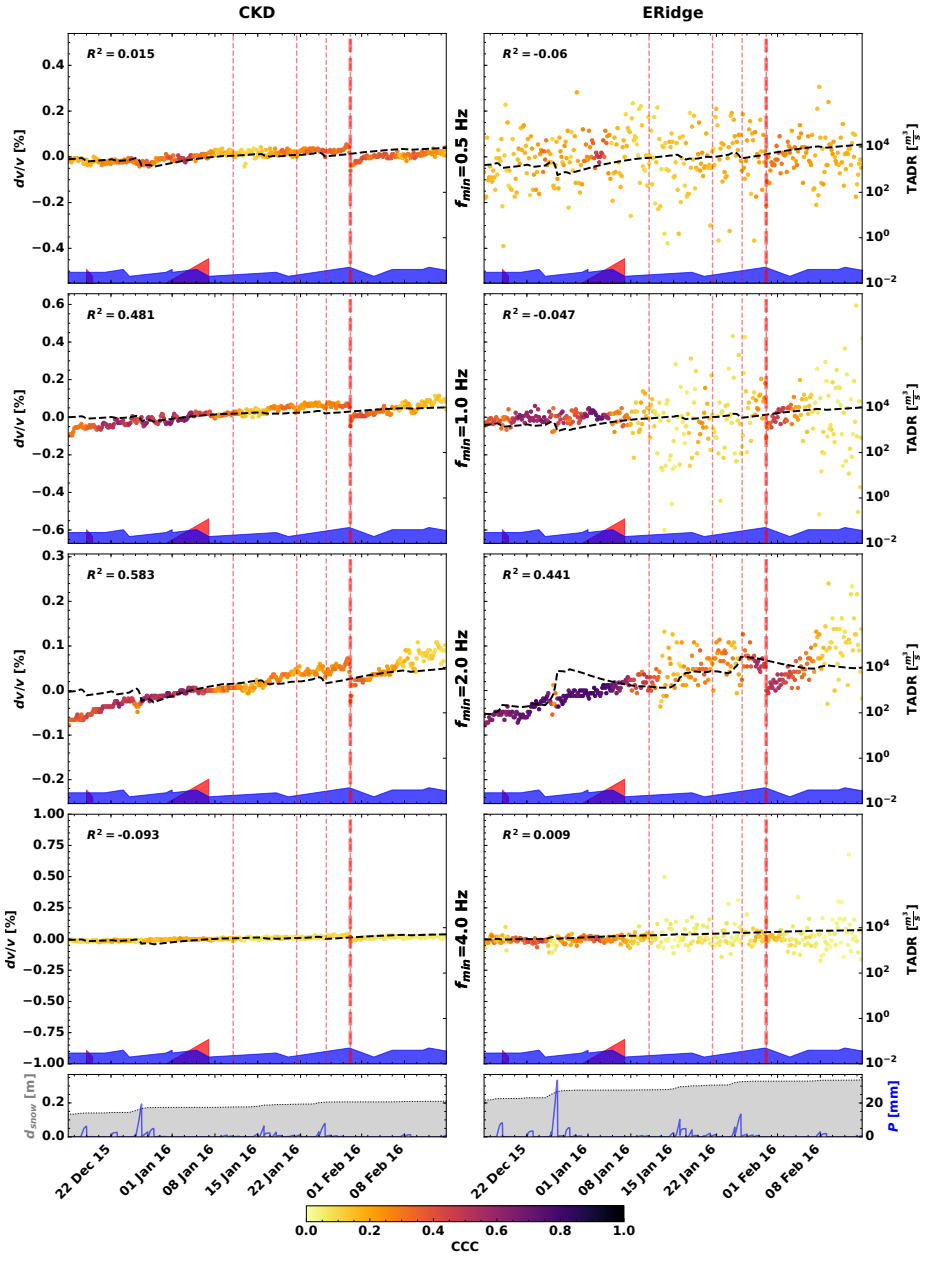

Figure B.30: Velocity change for the station groups CKD and ERidge (see Figure 4.4 for locations) created from cross-correlations (i.e., between stations) between all components for the frequencies between f_{min} and $2f_{min}$ for the time between 2015/12/15 to 2016/02/15. Refer to Figure 4.8 for a detailed explanation of the figure.

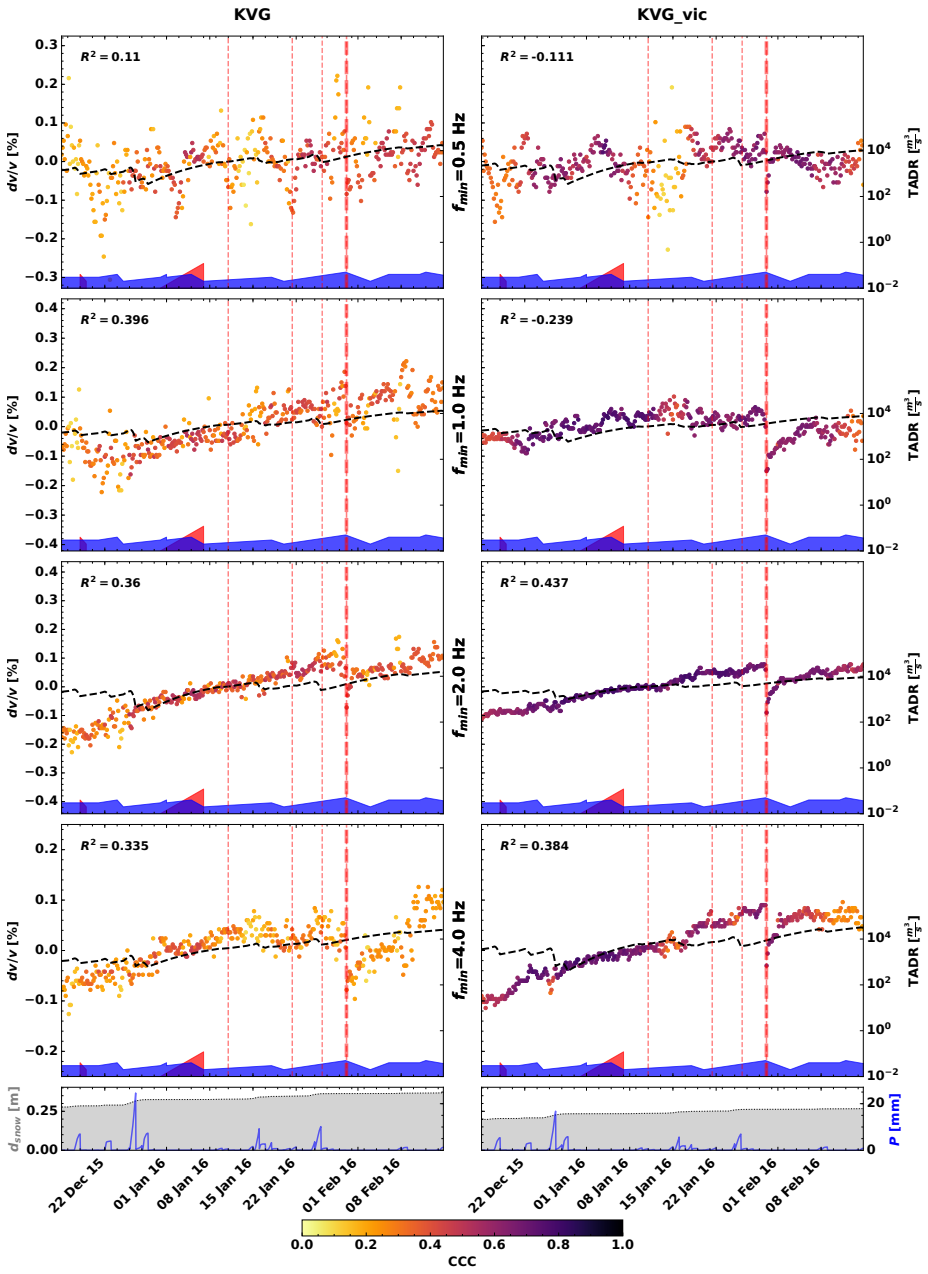

Figure B.31: Velocity change for the station groups KVG and KVG_vic (see Figure 4.4 for locations) created from cross-correlations (i.e., between stations) between all components for the frequencies between f_{min} and $2f_{min}$ for the time between 2015/12/15 to 2016/02/15. Refer to Figure 4.8 for a detailed explanation of the figure.

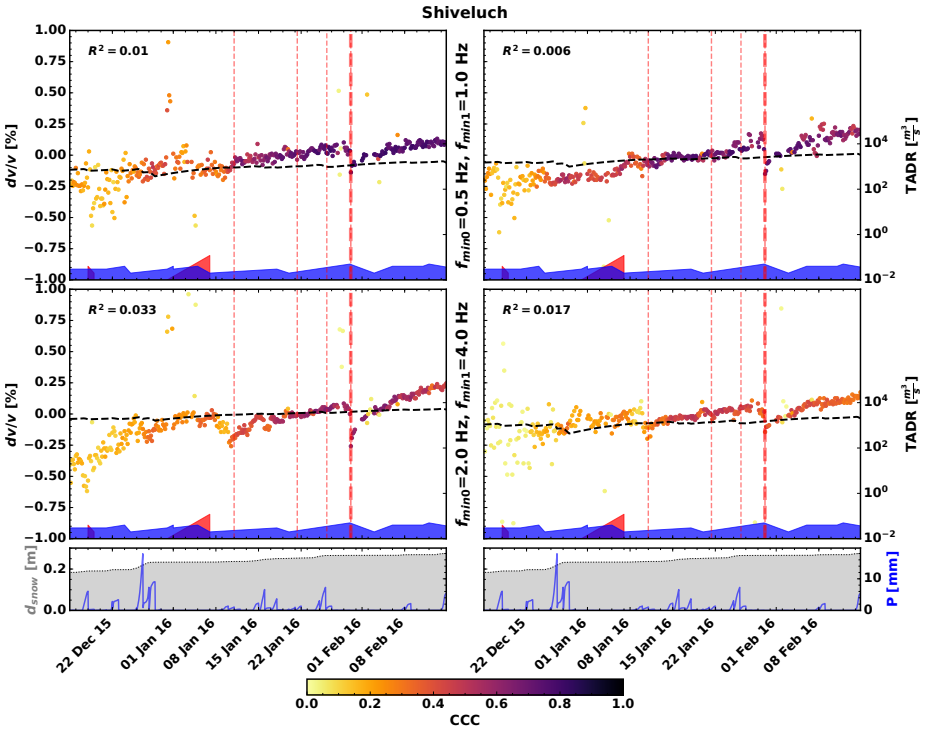

Figure B.32: Velocity change for the station group Shiveluch (see Figure 4.4 for locations) created from cross-correlations (i.e., between stations) between all components for the frequencies between f_{min} and $2f_{min}$ for the time between 2015/12/15 to 2016/02/15. Refer to Figure 4.8 for a detailed explanation of the figure.

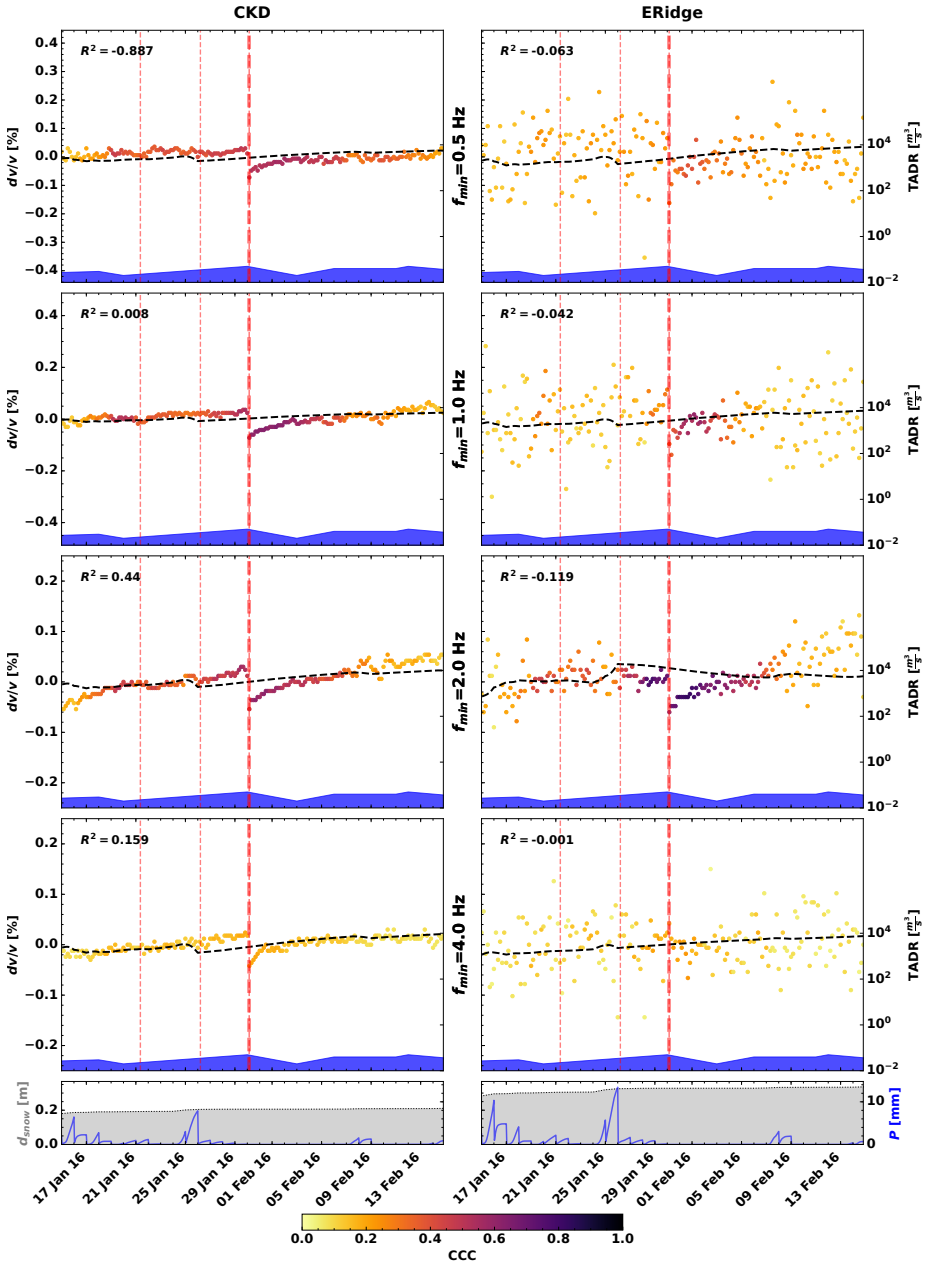

Figure B.33: Velocity change for the station groups CKD and ERidge (see Figure 4.4 for locations) created from cross-correlations (i.e., between stations) between all components for the frequencies between f_{min} and $2f_{min}$ for the time between 2016/01/15 to 2016/02/15. Refer to Figure 4.8 for a detailed explanation of the figure.

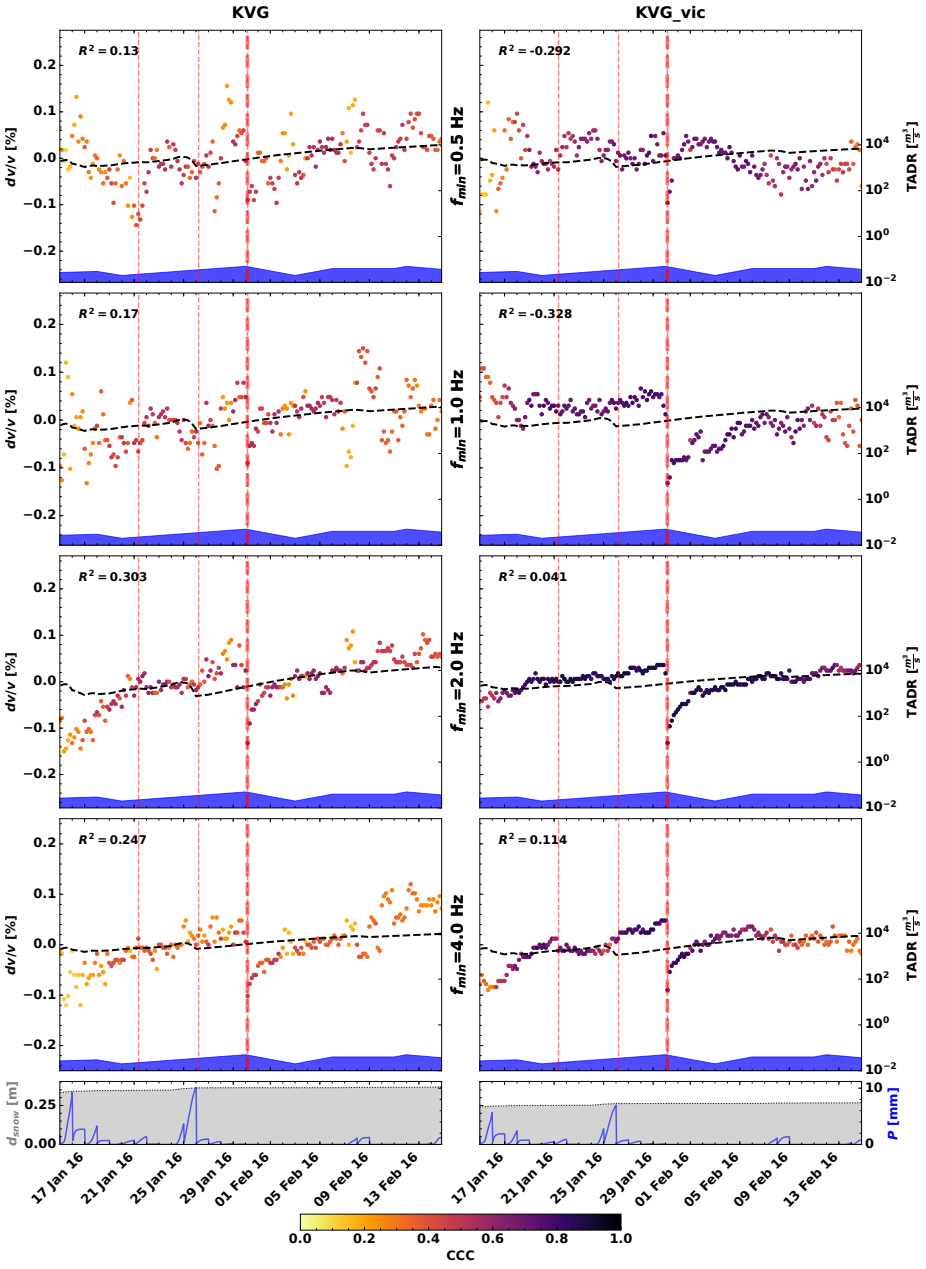

Figure B.34: Velocity change for the station groups KVG and KVG_vic (see Figure 4.4 for locations) created from cross-correlations (i.e., between stations) between all components for the frequencies between f_{min} and $2f_{min}$ for the time between 2016/01/15 to 2016/02/15. Refer to Figure 4.8 for a detailed explanation of the figure.

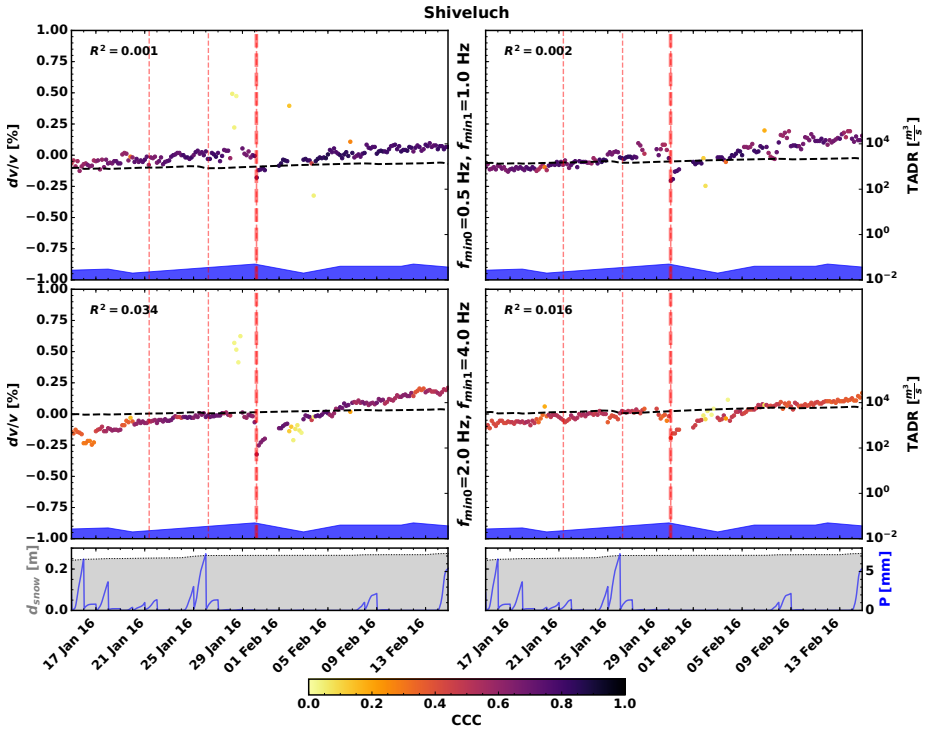

Figure B.35: Velocity change for the station group Shiveluch (see Figure 4.4 for locations) created from cross-correlations (i.e., between stations) between all components for the frequencies between f_{min} and $2f_{min}$ for the time between 2016/01/15 to 2016/02/15. Refer to Figure 4.8 for a detailed explanation of the figure.

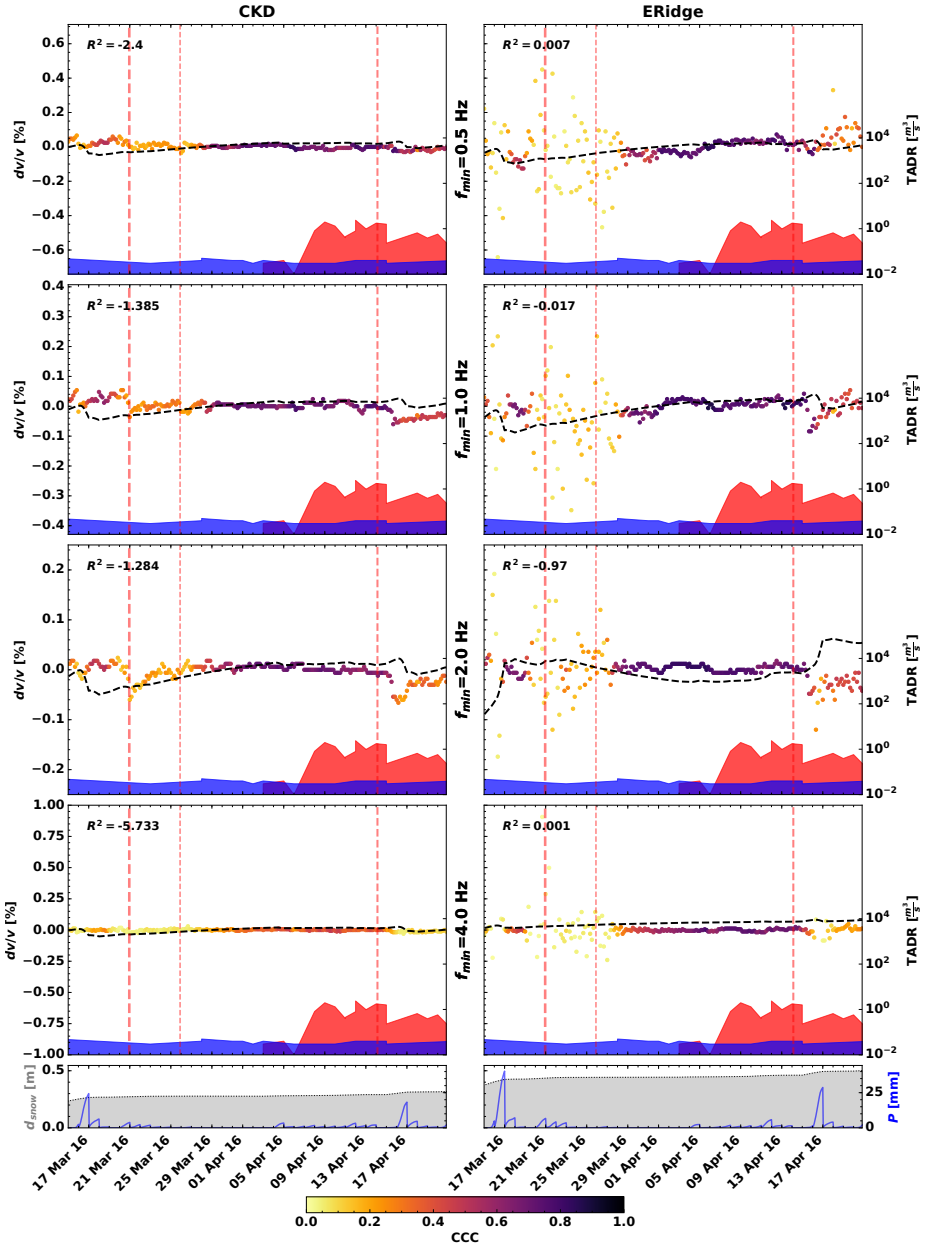

Figure B.36: Velocity change for the station groups CKD and ERidge (see Figure 4.4 for locations) created from cross-correlations (i.e., between stations) between all components for the frequencies between f_{min} and $2f_{min}$ for the time between 2016/03/15 to 2016/04/21. Refer to Figure 4.8 for a detailed explanation of the figure.

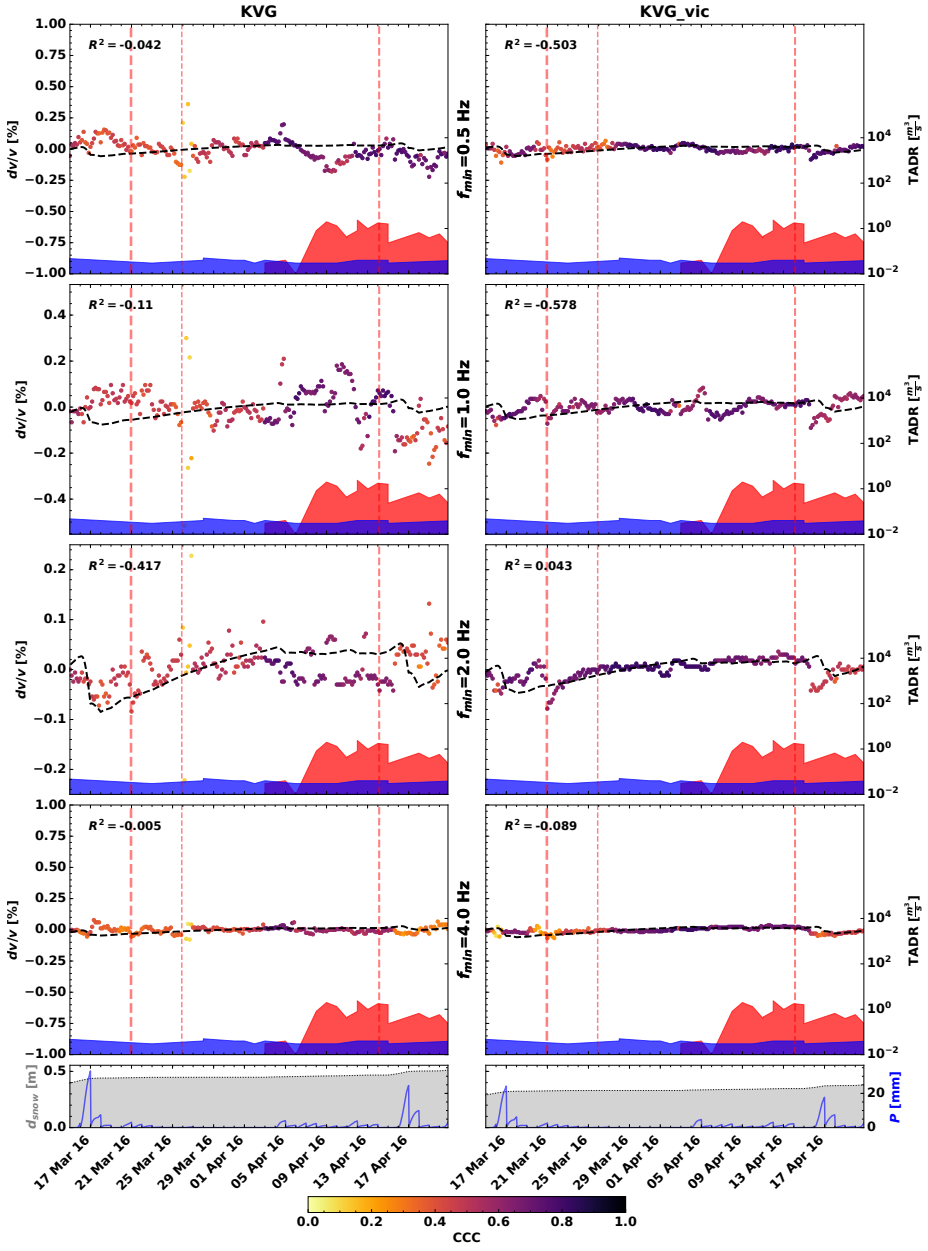

Figure B.37: Velocity change for the station groups KVG and KVG_vic (see Figure 4.4 for locations) created from cross-correlations (i.e., between stations) between all components for the frequencies between f_{min} and $2f_{min}$ for the time between 2016/03/15 to 2016/04/21. Refer to Figure 4.8 for a detailed explanation of the figure.

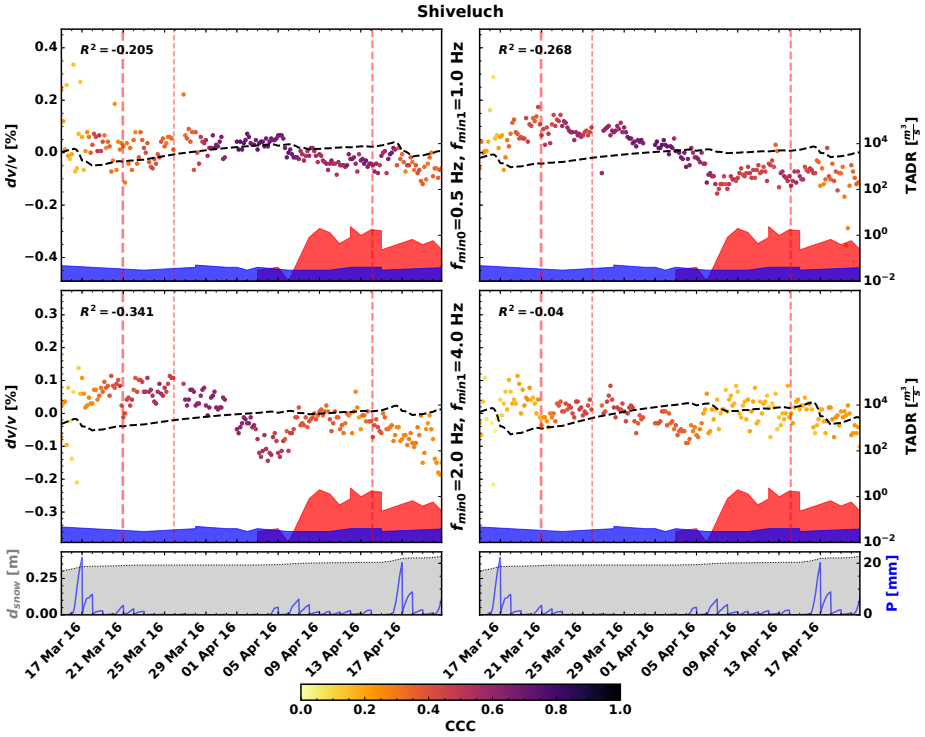

Figure B.38: Velocity change for the station group Shiveluch (see Figure 4.4 for locations) created from cross-correlations (i.e., between stations) between all components for the frequencies between f_{min} and $2f_{min}$ for the time between 2016/03/15 to 2016/04/21. Refer to Figure 4.8 for a detailed explanation of the figure.

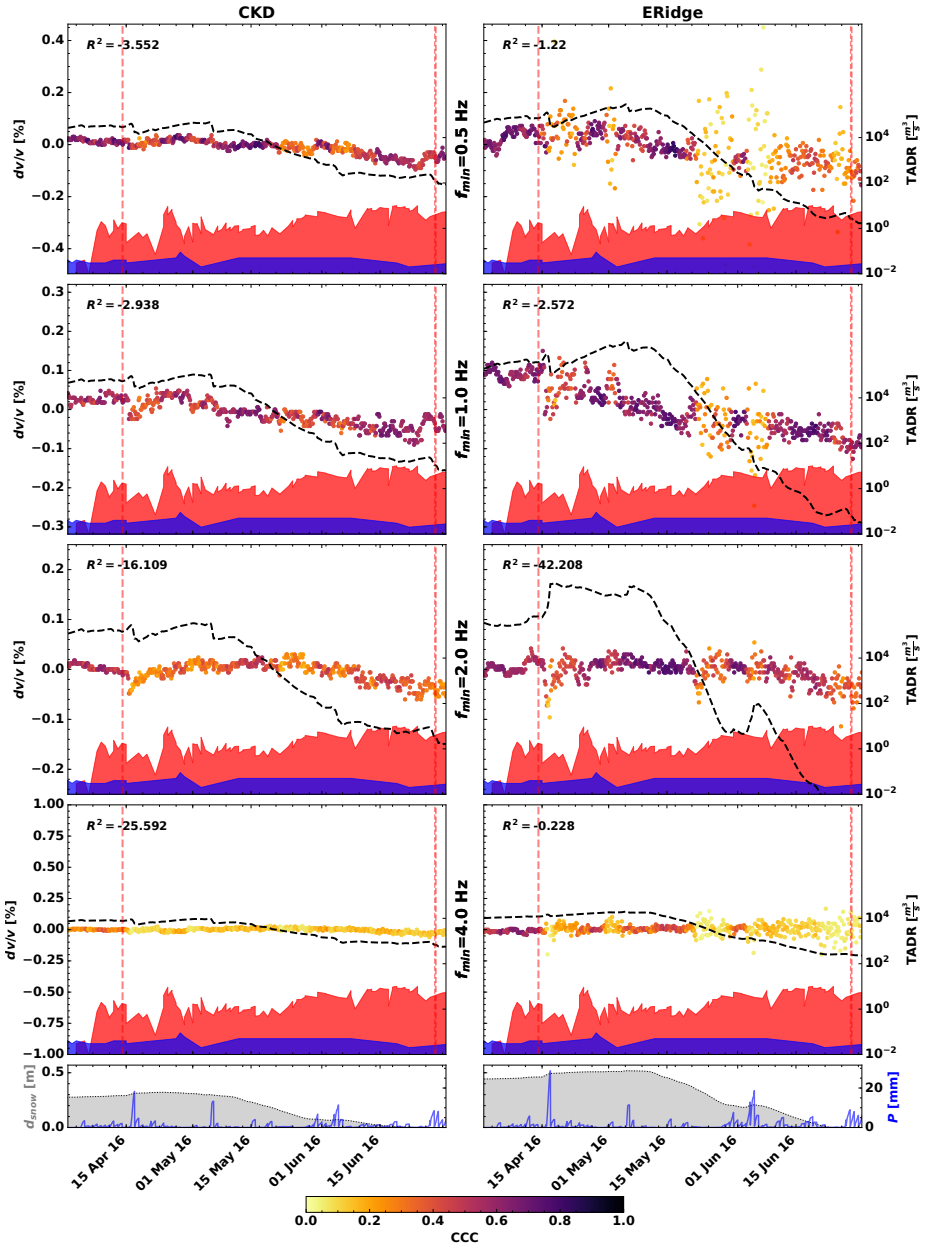

Figure B.39: Velocity change for the station groups CKD and ERidge (see Figure 4.4 for locations) created from cross-correlations (i.e., between stations) between all components for the frequencies between f_{min} and $2f_{min}$ for the time between 2016/04/01 to 2016/07/01. Refer to Figure 4.8 for a detailed explanation of the figure.

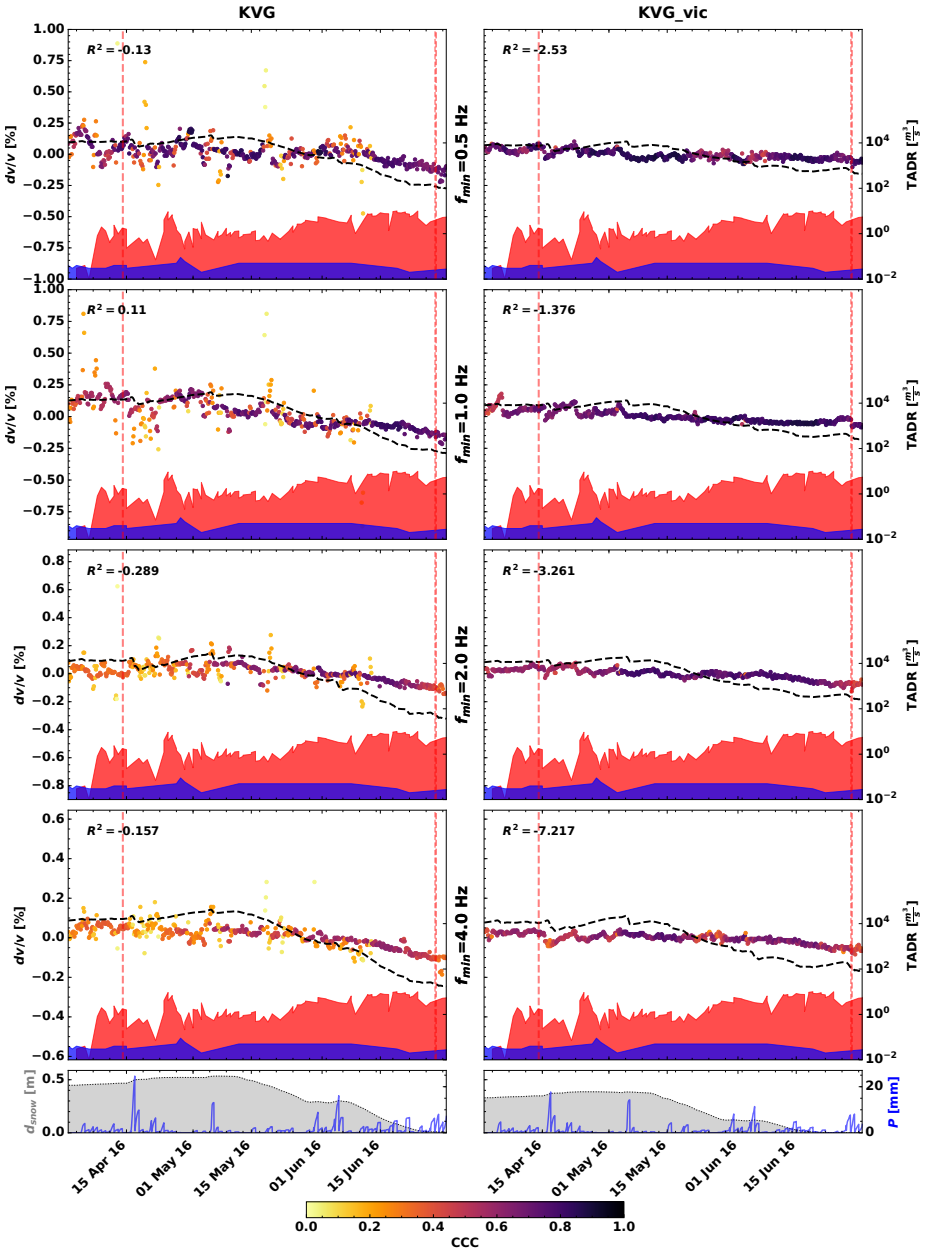

Figure B.40: Velocity change for the station groups KVG and KVG_vic (see Figure 4.4 for locations) created from cross-correlations (i.e., between stations) between all components for the frequencies between f_{min} and $2f_{min}$ for the time between 2016/04/01 to 2016/07/01. Refer to Figure 4.8 for a detailed explanation of the figure.

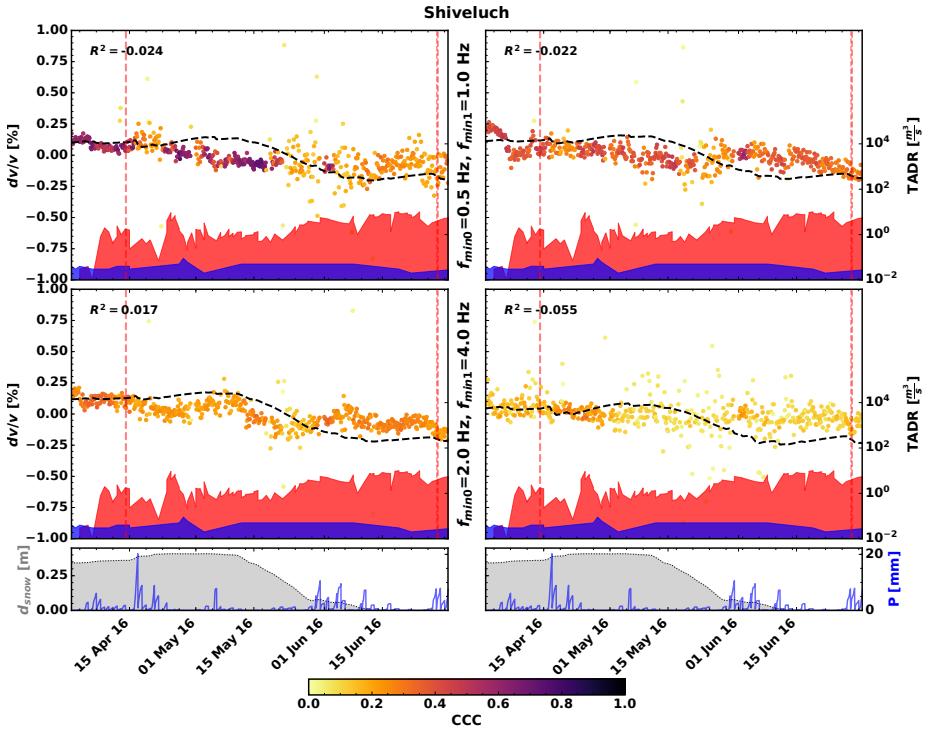

Figure B.41: Velocity change for the station group Shiveluch (see Figure 4.4 for locations) created from cross-correlations (i.e., between stations) between all components for the frequencies between f_{min} and $2f_{min}$ for the time between 2016/04/01 to 2016/07/01. Refer to Figure 4.8 for a detailed explanation of the figure.

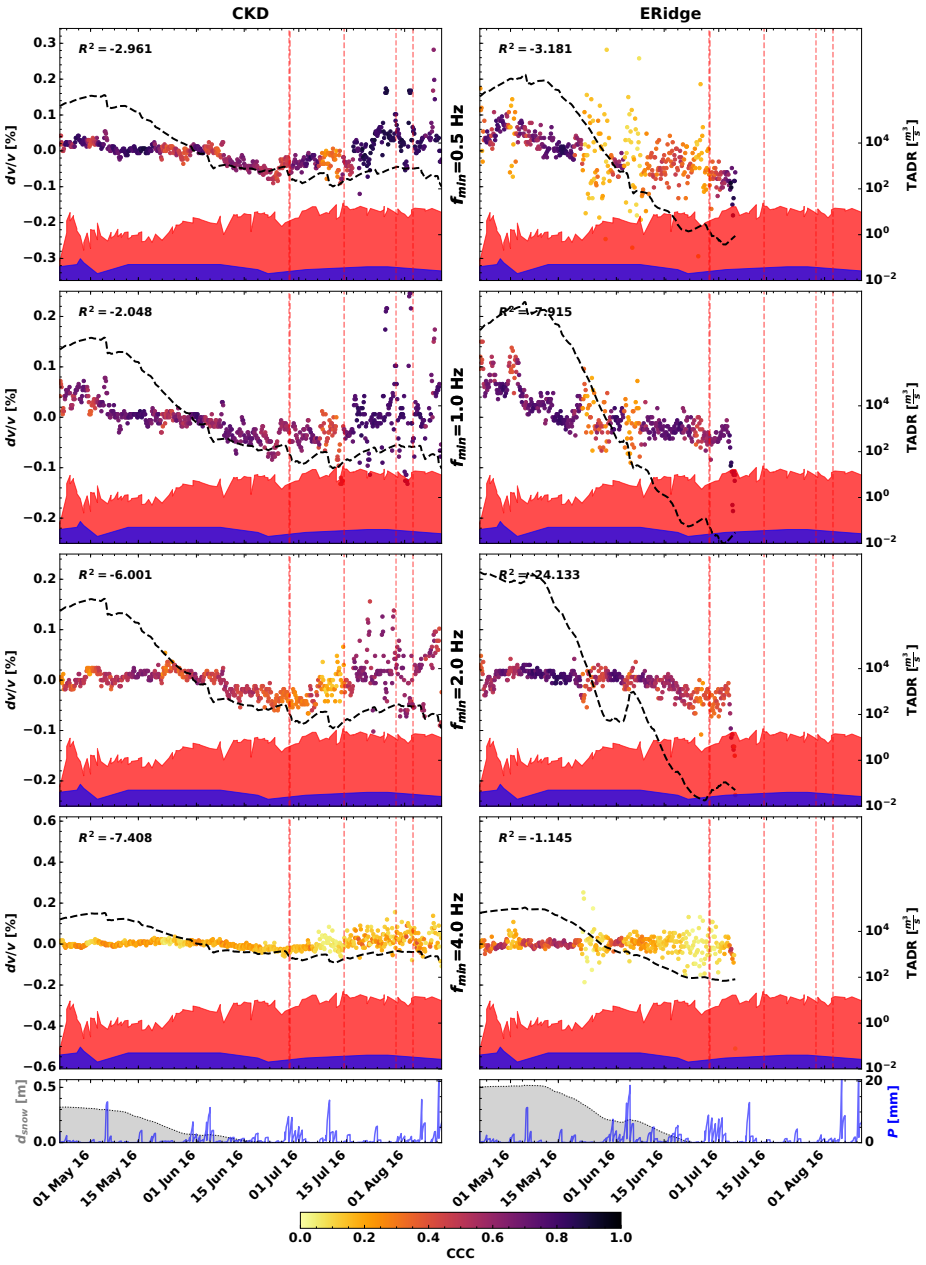

Figure B.42: Velocity change for the station groups CKD and ERidge (see Figure 4.4 for locations) created from cross-correlations (i.e., between stations) between all components for the frequencies between f_{min} and $2f_{min}$ for the time between 2016/04/22 to 2016/09/01. Refer to Figure 4.8 for a detailed explanation of the figure.

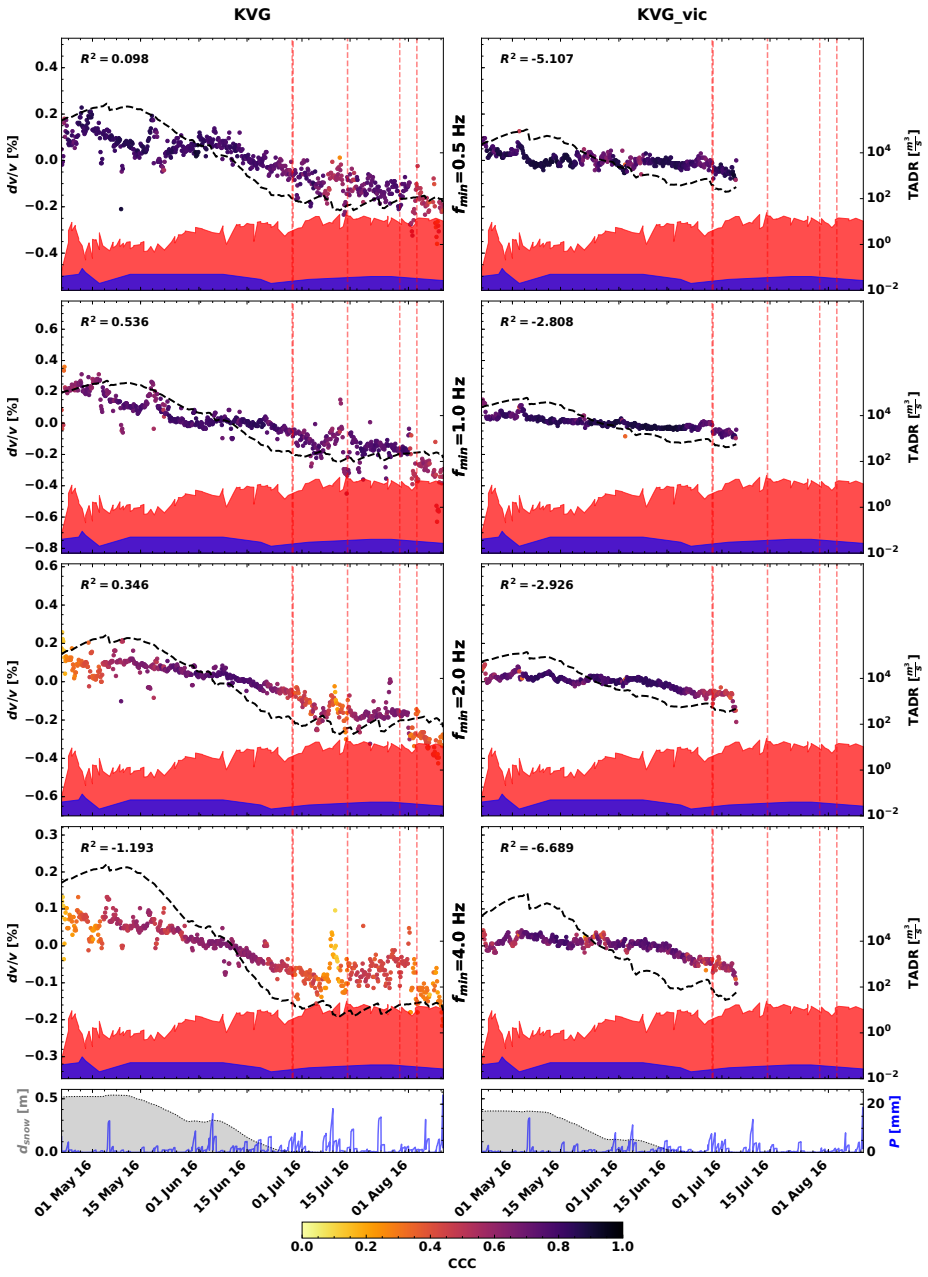

Figure B.43: Velocity change for the station groups KVG and KVG_vic (see Figure 4.4 for locations) created from cross-correlations (i.e., between stations) between all components for the frequencies between f_{min} and $2f_{min}$ for the time between 2016/04/22 to 2016/09/01. Refer to Figure 4.8 for a detailed explanation of the figure.

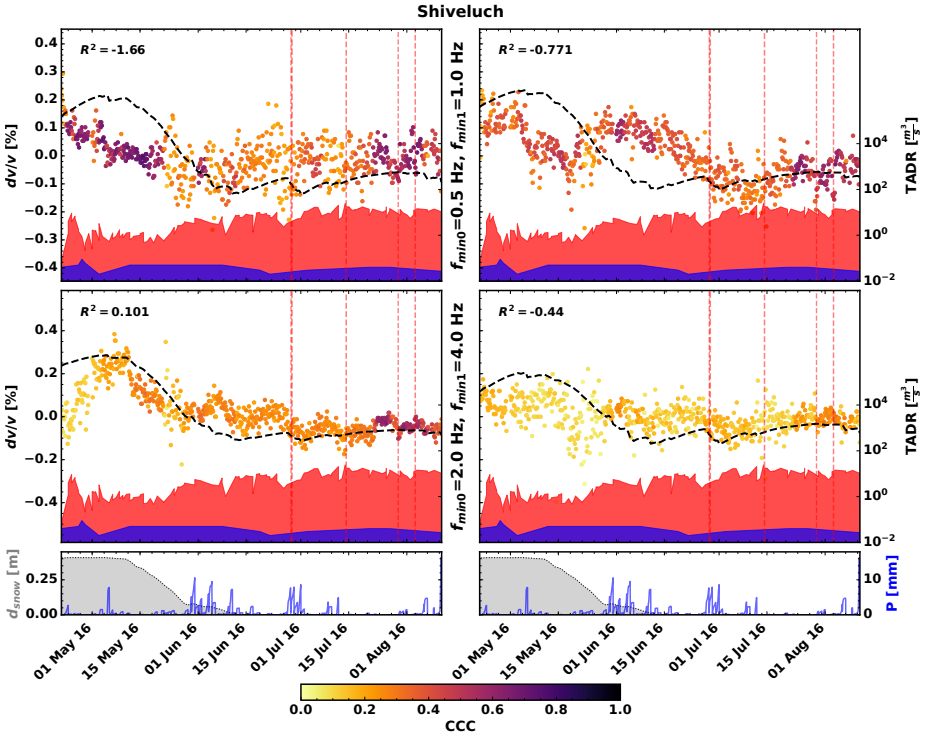

Figure B.44: Velocity change for the station group Shiveluch (see Figure 4.4 for locations) created from cross-correlations (i.e., between stations) between all components for the frequencies between f_{min} and $2f_{min}$ for the time between 2016/04/22 to 2016/09/01. Refer to Figure 4.8 for a detailed explanation of the figure.

Table B.1: Minimum merging cost d_0 of two clusters needed to divide the correlation functions into five separate clusters depending on the used frequency band defined by Ward's linkage algorithm Ward (1963) using an Euclidean distance measure. f_0 and f_1 are the high-pass and low-pass frequencies, respectively, that we used for the bandpass filter in the preprocessing. A lower merging cost corresponds to less pronounced clusters.

f_0(Hz)	f_1(Hz)	d_0
0.0625	0.125	6.0
0.125	0.25	1.55
0.25	0.5	1.9
0.5	1.0	4.0
1.0	2.0	4.6
2.0	4.0	8.9
4.0	8.0	3.2

Table B.2: Chosen time segments for the time-segmented passive image interferometry based on Figure 4.3.

start (yyyy/mm/dd)	end (yyyy/mm/dd)	Figures
2015/07/01	2015/12/01	B.9-B.11, B.27-B.29
2015/12/15	2016/02/15	B.12-B.14, B.30-B.32
2016/01/15	2016/02/15	B.15-B.17, B.33-B.35
2016/03/15	2016/04/21	B.18-B.20, B.36-B.38
2016/04/01	2016/07/01	B.21-B.23, B.39-B.41
2016/04/22	2016/09/01	B.24-B.26, B.42-B.44

APPENDIX C

Supporting Information to Chapter 5

In this supporting information, we provide additional information and data complementing our study.

With the published manuscript, we also provide two animated GIF images showing the evolution of the seismic velocity in the MSH region for 0.5-1.0 and 1.0-2.0 Hz. In the GIFs, dv/v is shown in a 20-day-interval. We also show vertical ground offset at each of the GNSS stations that we plot as upward-pointing triangles. Inverted triangles are seismic stations used in this study. Purple circles are seismic events that occurred in the prior 20 days.

C.1 Data Availability and Data Artefacts

Table C.1: List of seismic stations and data periods used in this study. The question mark in the channel code indicates that the corresponding station is a three-component seismometer. If the end date is replaced by a dash, the station is still active.

Network	Station	Channel	Start Date	End Date
CC	JRO	BH?	2004-10-02	-
CC	NED	EHZ	2004-11-20	2013-05-01
CC	REM	BH?	2018-07-25	-
CC	SEP	EH?	2004-11-05	2018-09-01
CC	SEP	BH?	2019-09-01	-
CC	STD	BH?	2004-10-05	-
CC	SUG	EHZ	2009-08-07	-
CC	SWF2	BH?	2013-08-29	-
CC	SWFL	BH?	2006-10-01	2013-08-28
CC	VALT	BH?	2006-08-01	-
PB	B201	EH?	2007-09-12	-
PB	B202	EH?	2007-07-25	-
PB	B203	EH?	2007-07-18	-
PB	B204	EH?	2007-08-01	-
UW	EDM	EHZ	1998-01-01	-
UW	EDM	HH?	2021-06-01	-
UW	FL2	EHZ	1998-01-01	-
UW	HSR	EHZ	1998-01-01	-
UW	HSR	HH?	2021-06-01	-
UW	JUN	EHZ	1998-01-01	-
UW	REM	BH?	2019-09-01	-
UW	SEP	EH?	2005-09-01	2019-09-01
UW	SHW	EHZ	1998-01-01	-
UW	SHW	HH?	2021-06-01	-
UW	SOS	EHZ	1998-01-01	-
UW	STD	EHZ	1998-01-01	2017-09-14
UW	SUG	EHZ	1998-01-01	2009-08-07
UW	YEL	EHZ	1998-01-01	2007-09-18

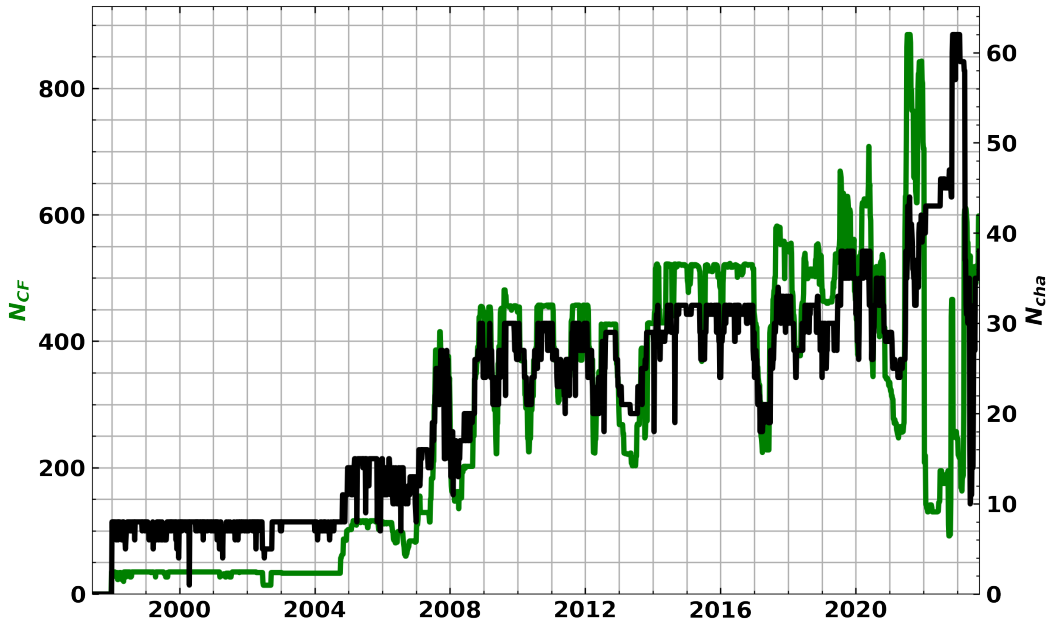

Figure C.1: Availability of seismic data during the study. We plot the number of available channels after quality control as a function of time. In green, we show the number of resulting CFs as a function of time.

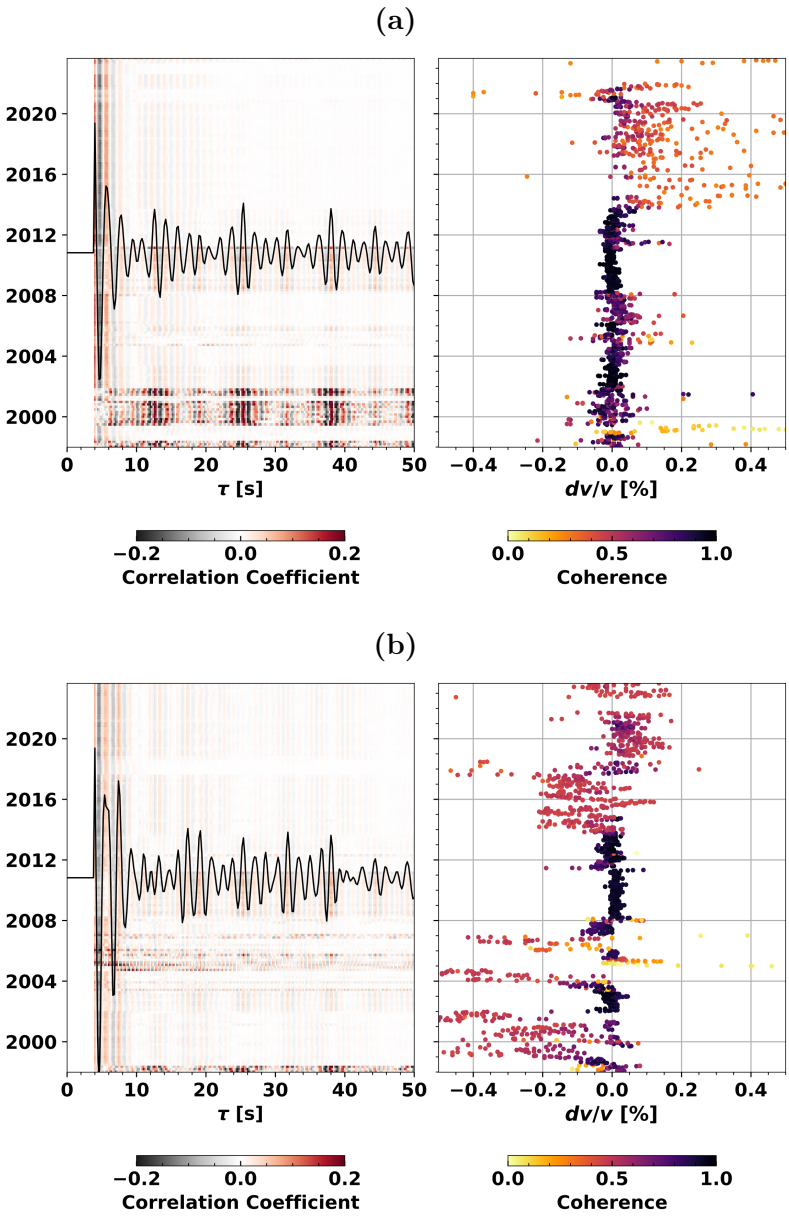

Figure C.2: Examples of artefacts occurring in the autocorrelations of single-component stations with analogue telemetry. The correlations show repeated signals at about 13 seconds for (a). The comb-like pattern suggests an instrumental artefact (Schippkus et al., 2023). We exclude these stations' autocorrelations from the analysis. **(a)** For data from UW.FL2.EHZ. **(b)** For data from UW.SHW.EHZ. These examples are taken from frequencies between 0.5 and 1 Hz. However, artefacts are present on all three frequency bands.

Clock Shifts After a restart of the digitiser unit in October 2013 (PNSN, pers. communication), there is evidence of a clock shift in the analogue telemetered data. We compute the clock shift by estimating the highest coherent shift of continuously computed cross-correlations between an affected and an unaffected station as implemented in SeisMIC (Makus & Sens-Schönfelder, 2024). The result estimates a clock shift of 0.25 s, which was reported back to the PNSN. In this work, we avoid using the data at the time of the clock shift (see Chapter 5). We found no evidence of clock shifts or drifts in our dataset before October 2013.

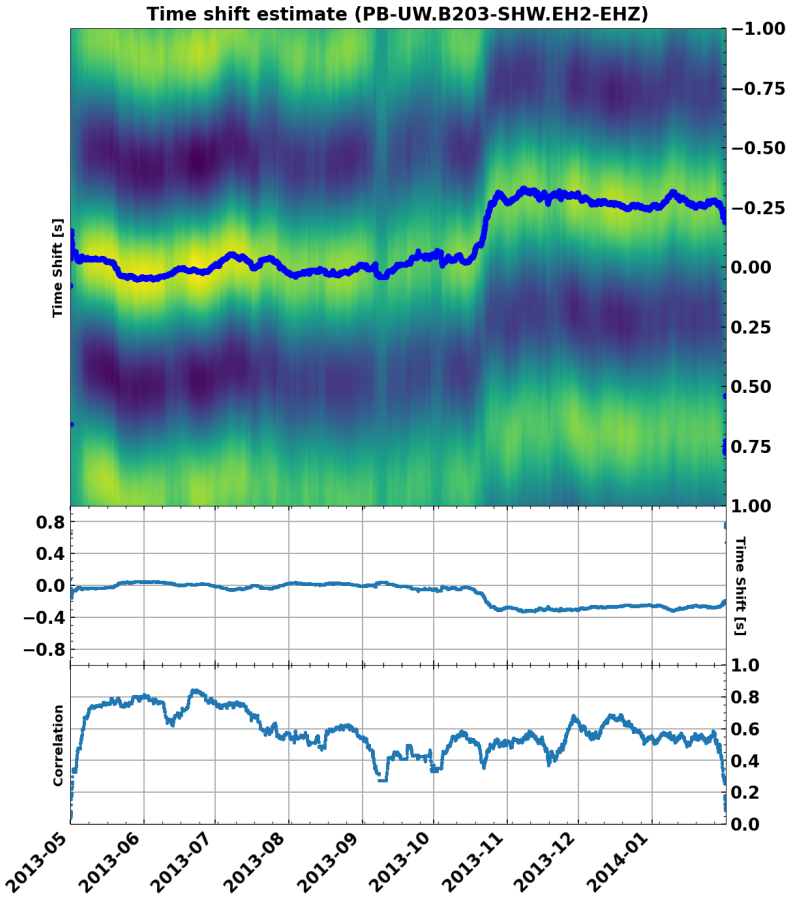

Figure C.3: Digitiser clock shift estimated using SeisMIC (Makus & Sens-Schönfelder, 2024).

C.2 Stability of the Ambient Seismic Field

In Figure 5.2, we show examples of CFs and velocity change estimates from three different channel pairs. Here, we would like to point out that the CFs remain stable over the shown ∼15 years. There are neither strong fluctuations in the shape of the CFs nor the coherence (or correlation coefficient) of the dv/v estimates. The ambient seismic field remains relatively stable over the study period (Figures C.4 and C.5). We show additional examples of time series in Figures C.6-C.8.

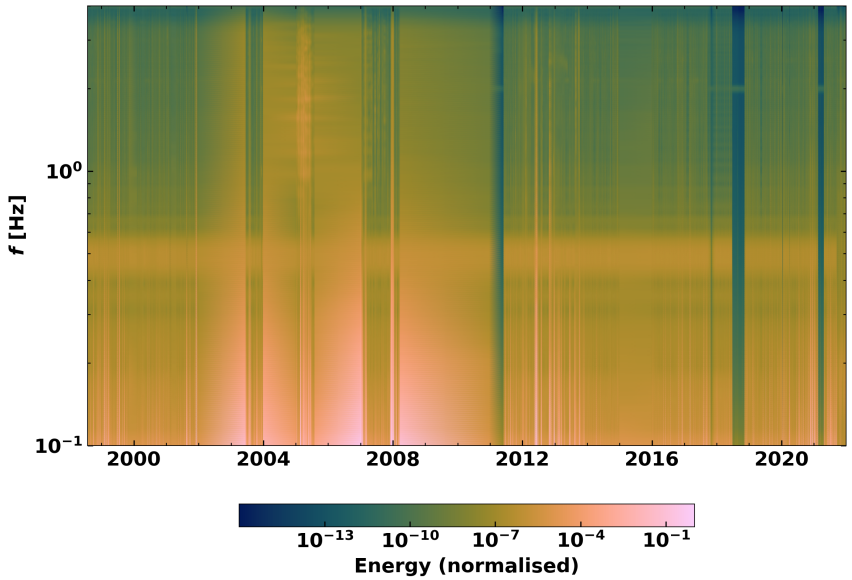

Figure C.4: Spectrogram computed from the raw data recorded by the short-period vertical component of station UW.SHW. The instrumental response was removed. Strong segmentations in the amplification of the spectrum are due to instrumentation failures (e.g., empty recordings). While we find some impacts of the MSH 2004-2008 eruption, overall, the wavefield remains remarkably stable except for a marked seasonal variation. Vertical high-amplitude stripes correspond to periods of seismic unrest.

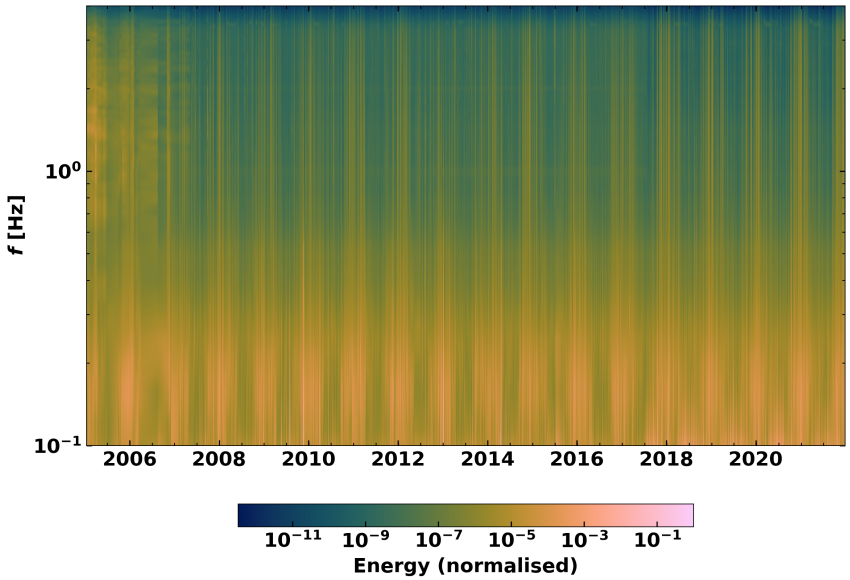

Figure C.5: Spectrogram computed from the raw data recorded by the broadband vertical component of station CC.STD. While we find some impacts of MSH 2004-2008 eruption, overall the wavefield remains remarkably stable except for a marked seasonal variation. Vertical high-amplitude stripes correspond to periods of seismic unrest.

C.3 Examples of Correlation Functions and dv/v Estimates

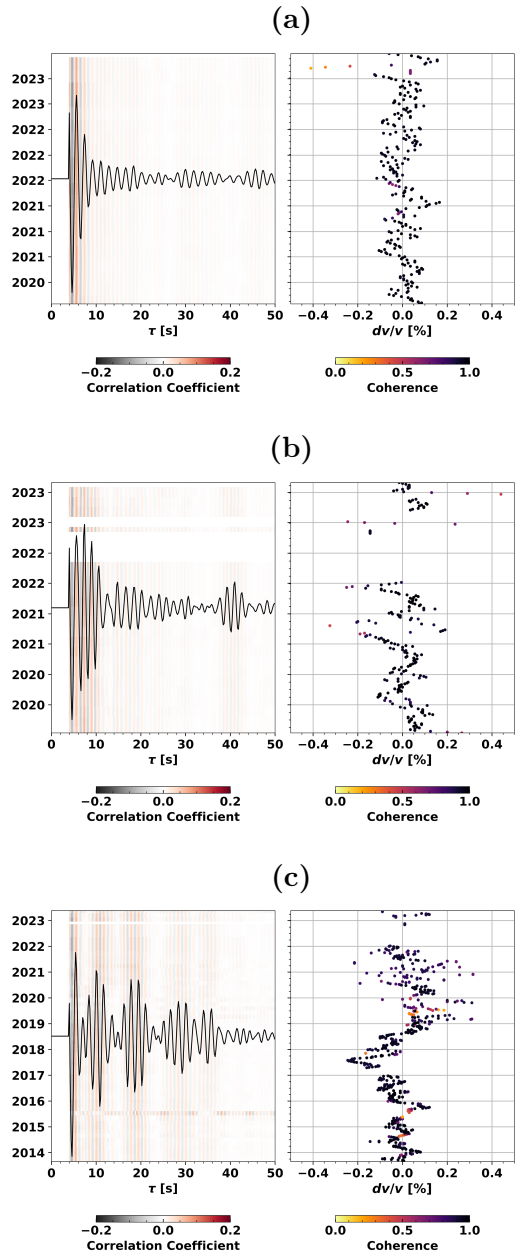

Figure C.6: Examples of autocorrelations and their corresponding dv/v estimates from data between 0.5 and 1 Hz. From CC.JRO.HHE (a), CC.SEP.BHZ (b), and CC.SWF2.BHN (c).

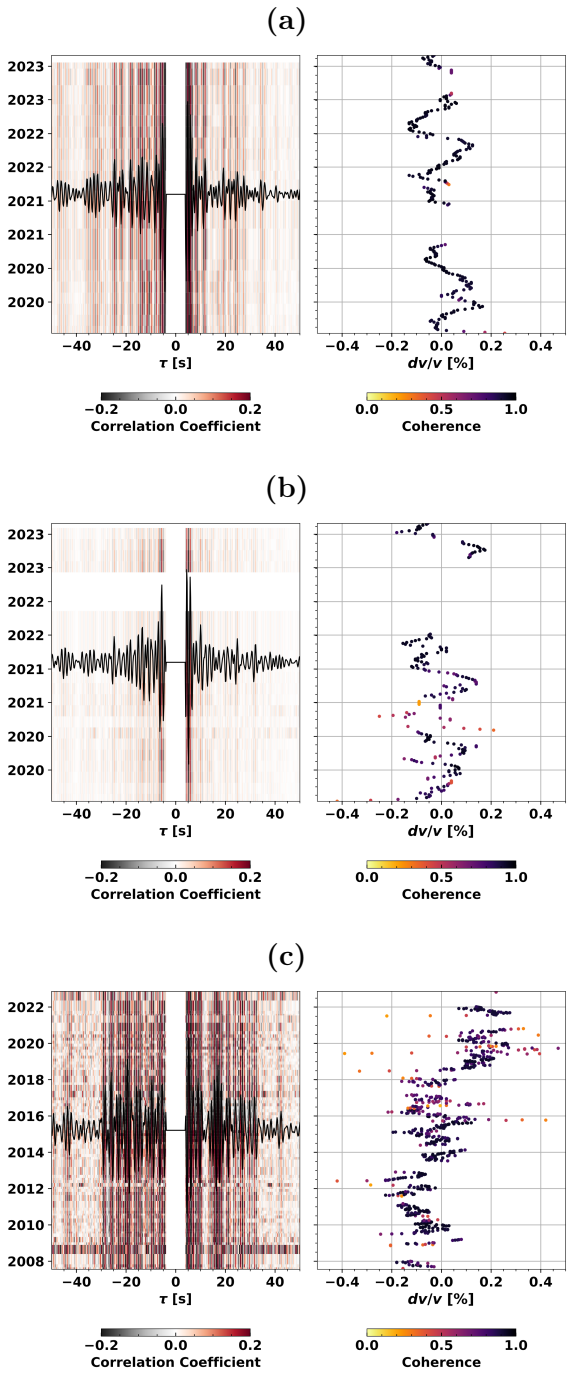

Figure C.7: Examples of self-correlations and their corresponding dv/v estimates from data between 0.5 and 1 Hz. CC.REM.BHE-CC.REM.BHN (a), CC.SEP.BHE-CC.SEP.BHN (b), and PB.B202.EH2-PB.B202.EHZ (c).

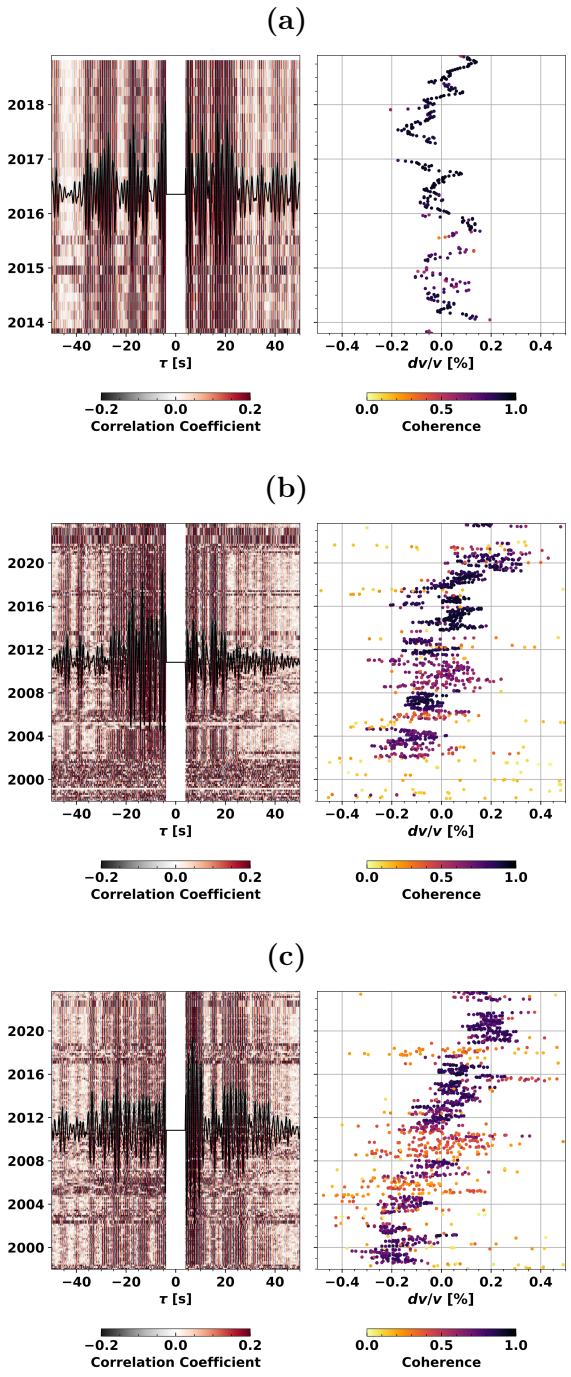

Figure C.8: Examples of cross-correlations and their corresponding dv/v estimates from data between 0.5 and 1 Hz. CC.SUG.EHZ-CC.SWF2.BHN (a), UW.EDM.EHZ-UW.FL2.EHZ (b), and UW.SHW.EHZ-UW.SOS.EHZ (c).

C.4 Spatial Inversion

In this work, we use a linear-least-squares inversion to obtain a dv/v grid from a large number of velocity change time series proposed by Obermann, Planès, Larose, and Campillo (2013).

C.4.1 The Spatial Sensitivities of Ambient Noise Correlations

We assume that surface waves dominate the coda of the cross-correlations. Consequently, the spatial sensitivity is equal to the sensitivity of surface waves propagating between stations (or, for single-station correlations, around). This assumption is reasonable since, for lag times up to about seven times the mean free time t^*, the wavefield is dominated by surface waves (Obermann, Planès, Larose, Sens-Schönfelder, & Campillo, 2013). At MSH, $t^* = \frac{Q_s}{\omega} \approx 37.9$s, based on Gabrielli et al. (2020)'s estimate of the scattering attenuation $Q_s \approx 714$ at 3 Hz. The probability density distribution of a wavefield between two stations (or at a single station with $\mathbf{s_1} = \mathbf{s_2}$) can then be approximated using a sensitivity kernel K as introduced by Pacheco and Snieder (2005):

$$K(\mathbf{s_1}, \mathbf{s_2}, \mathbf{x_0}, \tau) = \frac{\int_0^\tau p(\|\mathbf{s_1} - \mathbf{x_0}\|_2, u) p(\|\mathbf{x_0} - \mathbf{s_2}\|_2, \tau - u) \mathrm{d}u}{p(\|\mathbf{s_1} - \mathbf{s_2}\|_2, \tau)} \tag{C.1}$$

where we estimate the probability density p in 2D space and (lag) time for the station locations $\mathbf{s_1}$ and $\mathbf{s_2}$ and the location of the velocity change $\mathbf{x_0}$. $||\mathbf{x}||_2$ represent the Euclidean norm. In our case, τ is the centre of the lag time window used to estimate dv/v. Employing the solution of the time-dependent Boltzmann equation by Paasschens (1997), p is:

$$p(r, \tau) = \frac{e^{-c\tau/l}}{2\pi r} \delta(c\tau - r) + \frac{(c^2\tau^2 - r^2)^{-\frac{1}{2}}}{2\pi l} e^{(\sqrt{c^2\tau^2 - r^2} - c\tau)/l} \Theta(c\tau - r) \tag{C.2}$$

where p is a model of the spatial probability distribution of a surface wave travelling

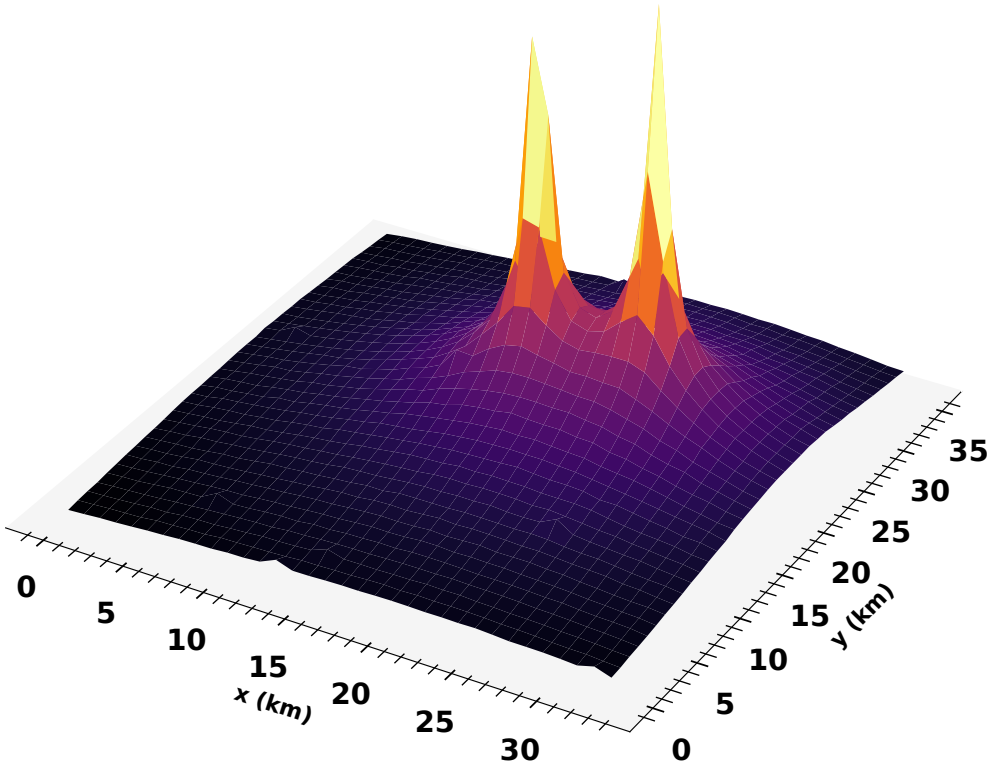

Figure C.9: An example of a probability density kernel describing the spatial sensitivity of surface waves travelling between two stations (co-located with the probability peaks). We estimate the probability at each location using the solution of the Boltzmann equations (Paasschens, 1997) described in the text body. The shown example is for data from the 0.5-1.0 Hz frequency band. The sensitivity kernels for the different frequency bands differ since we modify the lag time τ as a function of the frequency.

between the station locations $\mathbf{s_1}$ and $\mathbf{s_2}$ having visited the location of the velocity change $\mathbf{x_0}$. We show an example of such a kernel extracted from the MSH dataset in Figure C.9. The first term in p corresponds to the impulsive ballistic arrival, whose contribution is almost negligible for larger lag times τ, whereas the second term is the contribution of the emergent and diffusive scattered energy making up the bulk of the coda. From the mean free time and the group velocity $c = 2.5\ \frac{km}{s}$ (Y. Wang et al., 2017), we can compute the mean free path $l = t^*c = 94.75$ km. $\Theta(x)$ is the heaviside function.

With these spatial sensitivity kernels, we can now establish a forward relation between the $(dv/v)_i = \psi_i$ estimated from each station/component combination i and a 2D spatial dv/v grid (Obermann, Planès, Larose, & Campillo, 2013):

$$\psi_i = G_{ij} m_j \tag{C.3}$$

where $G_{ij} = \frac{\Delta s}{\tau} K_{ij}$ is a matrix consisting of the sensitivity Kernels weighted by the pixel area Δs, which is constant on our grid, and the lag time in the coda τ. $\mathbf{m}$ is the flattened grid containing the velocity change of each pixel j.

C.4.2 Damped Least-Squares Inversion

To determine $\mathbf{m}$, we follow the approach of Obermann, Planès, Larose, and Campillo (2013) based on the least-squares method as proposed by Tarantola and Valette (1982):

$$\mathbf{m} = \mathbf{C_m G^t} (\mathbf{G C_m G^t} + \mathbf{C_d})^{-\mathbf{1}} \boldsymbol{\psi} \tag{C.4}$$

where $\mathbf{C_d}$ is a diagonal matrix containing the variance σ_i^2 of each dv/v estimate and $\mathbf{G^t}$ indicates that matrix $\mathbf{G}$ is transposed. $\mathbf{C_m}$ is the model's covariance matrix that must be tuned to stabilise the inversion. We use $\mathbf{C_m}$ in the form proposed by Obermann, Planès, Larose, and Campillo (2013), where $\mathbf{C_m}$ in the shape $i \times j$ is effectively providing smoothing:

$$C_m(i,j) = (\sigma_m \frac{\lambda_0}{\lambda})^2 e^{-\frac{\Delta(i,j)}{\lambda}} \tag{C.5}$$

and is defined by the correlation length λ and the standard deviation of the model σ_m. λ_0 is the cell length (in our case, 1 km) and $\Delta(i,j)$ is the distance between the cells i and j. The degree of smoothing and the model variance are usually chosen to values delivering a compromise between the best fit and the least complex model using an L-curve criterion (see section C.4.3). We estimate the standard deviation of the data $\sigma_{d,i}$ as proposed by Weaver et al. (2011):

$$\sigma_{d,i} = \frac{\sqrt{1-CC_i^2}}{2CC_i} \sqrt{\frac{6\ \sqrt{\frac{\pi}{2}}T}{\omega_c^2(t_2^3 - t_1^3)}} \tag{C.6}$$

Here, CC_i is the correlation coefficient of the optimally stretched CF i, ω_c is the central angular frequency, T is the inverse of the frequency bandwidth, and t_1 and t_2 are the beginning and end of the coda window, respectively.

C.4.3 L-curve

In Figure C.10, we show the absolute normalised residuals against the root mean square value of the resulting model for all three frequencies and the station configuration available in April 2023. We quantify the absolute normalised residual using the definition provided in Obermann, Planès, Larose, and Campillo (2013):

$$res = \sqrt{\frac{1}{N}\sum_{i=1}^{N} \frac{(\psi_i^m - \psi_i^{app})^2}{(\sigma_d^i)^2}} \tag{C.7}$$

where ψ^m and ψ^{app} are the apparent velocity changes measured on the component combinations and the velocity changes obtained for each component combination using the forward equation (eq. C.3), respectively. The data points are computed using logarithmic steps for σ_m between $5 \cdot 10^{-4}$ and 0.128.

Note that we choose values for the prior model standard deviation σ_m and correlation length λ that are compatible for all time steps, also the ones with more sparse station coverage than for the shown time. As we are computing the spatial distribution of velocity changes from different station configurations, we have to find appropriate compromises. Here, we tune the damping parameters so that the areas of largest interest (within the station array and close to MSH) have a resolution of $\sim$1 (see Figure C.11). For all inversions, we choose the smoothing parameters, $\lambda = 2$ km and $\sigma_m = 4 \cdot 10^{-3}$ (marked with a red circle), which yield a good compromise between fit and complexity for all time steps and frequencies.

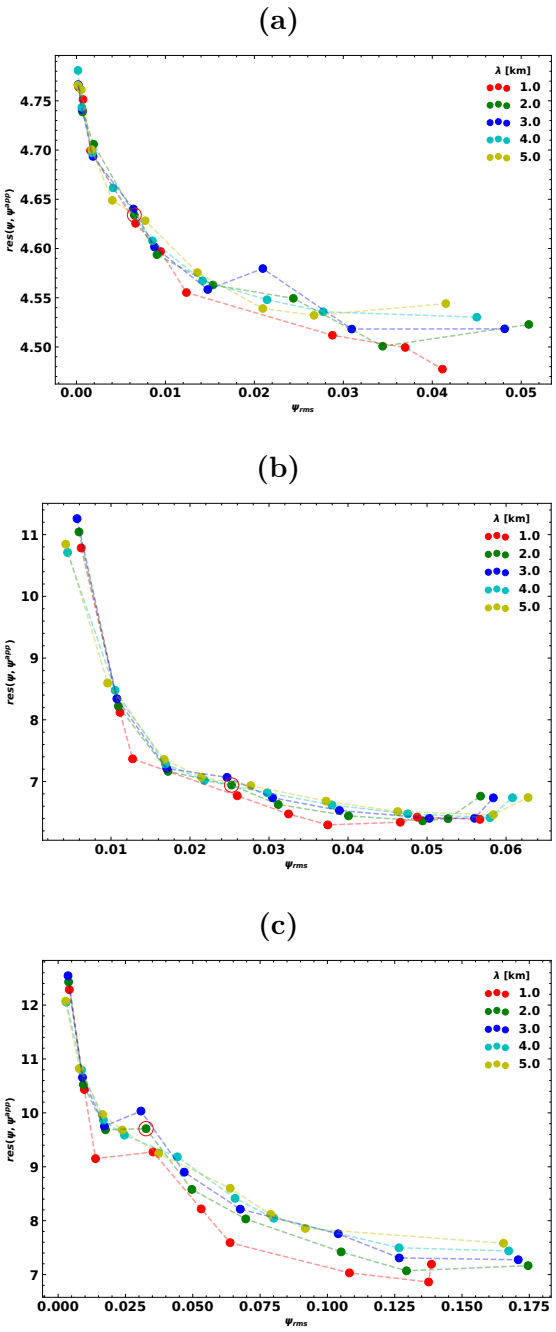

Figure C.10: L-curves plotting the misfit (residual res) as a function of the resulting grid's root mean square value. The values correspond to an inversion of data in April 2023 (comparable to Figure 5.4). (a) For data from 0.25-0.5 Hz. (b) For data from 0.5-1.0 Hz. (c) For data from 1-2 Hz. As a visual aid, we connect the points computed using the same correlation length λ.

C.5 Resolution Tests

To shed light on the impact of the station geometry and the chosen damping parameters on the resulting image, we provide the spatial distribution of the resolution parameter as defined by Tarantola and Valette (1982) in Figure C.11. The resolution matrix $\mathbf{R}$ is given as:

$$\mathbf{R} = \mathbf{C_m G^t} (\mathbf{G C_m G^t} + \mathbf{C_d})^{-1} \mathbf{G} \tag{C.8}$$

Locations, where $\mathbf{R}$ is greater than 1, tend to show exaggerated values, whereas values smaller than 1 indicate that the velocity change is not fully recovered. We also inverted for synthetic velocity models of different shapes to show how potential biases may be introduced. For a discussion of the resolution, please consult Chapter 5.

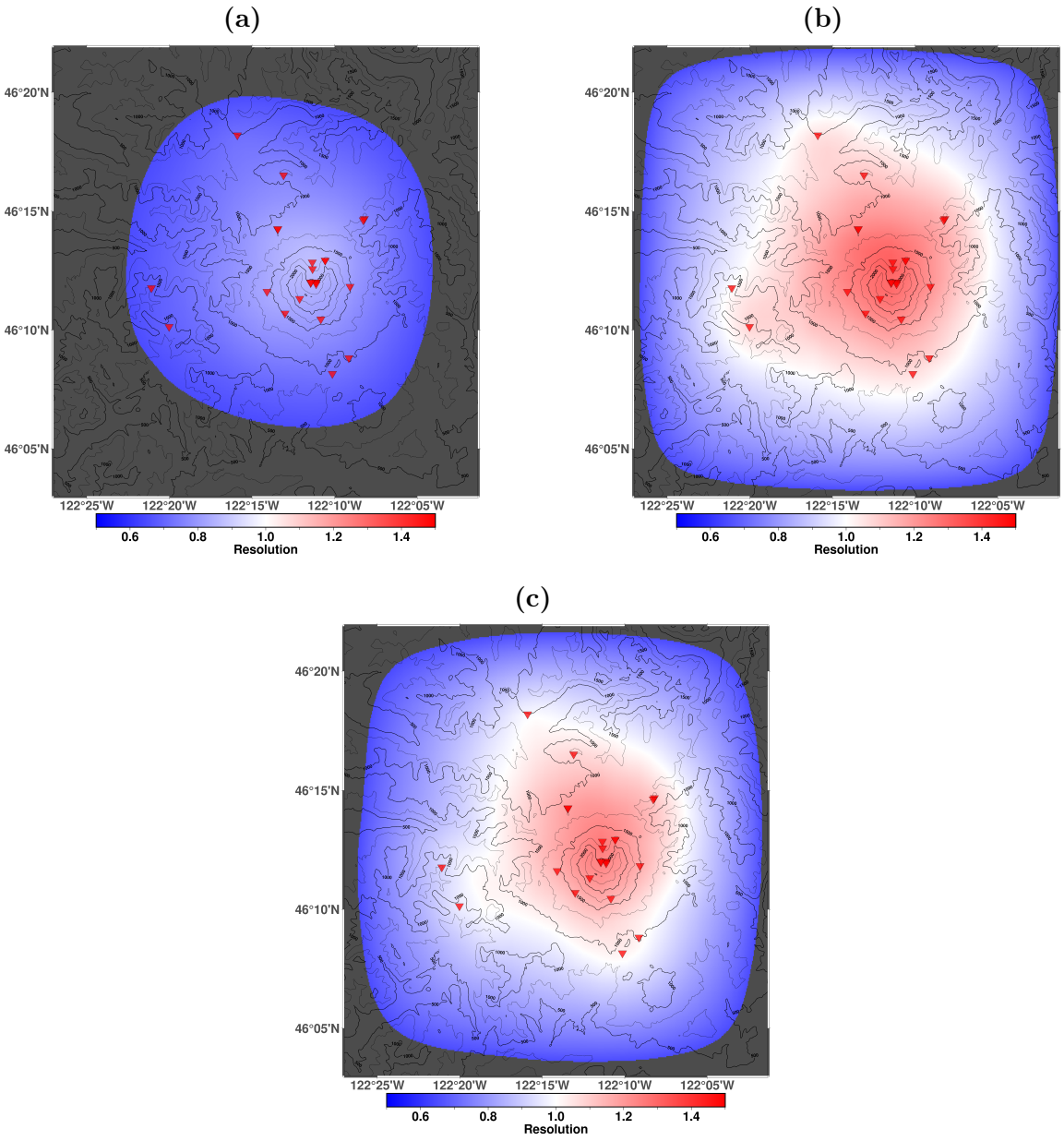

Figure C.11: Resolution parameter for the three frequency bands explored in this study. Red inverse triangles indicate the locations of the seismic stations. Locations where $\mathbf{R} < 0.5$ are greyed out. (a) Obtained from 0.25-0.5 Hz. (b) Obtained from 0.5-1 Hz. (c) Obtained from 1-2 Hz.

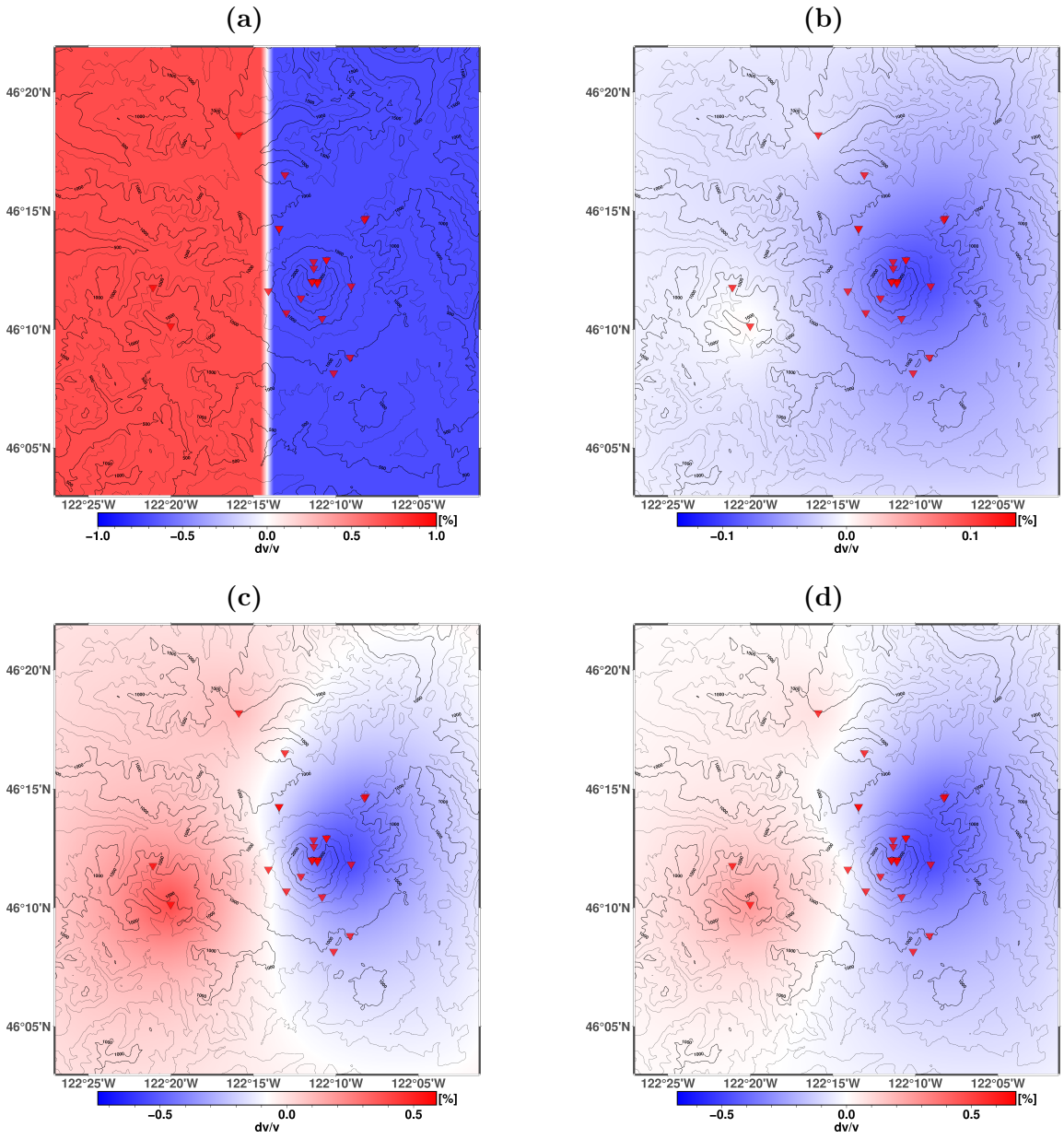

Figure C.12: Recovery of a noise-free synthetic velocity model using the same inversion algorithm, station configuration, and correlation coefficients, and thus σ_d values as in our actual dataset inversion for late 2021 (as Figure 5.4). **(a)** Input velocity model. **(b)** Recovered velocity model using frequencies between 0.25 and 0.5 Hz. **(c)** Recovered velocity model using frequencies between 0.5 and 1 Hz. **(d)** Recovered velocity model using frequencies between 1 and 2 Hz. Red inverse triangles indicate the locations of the seismic stations.

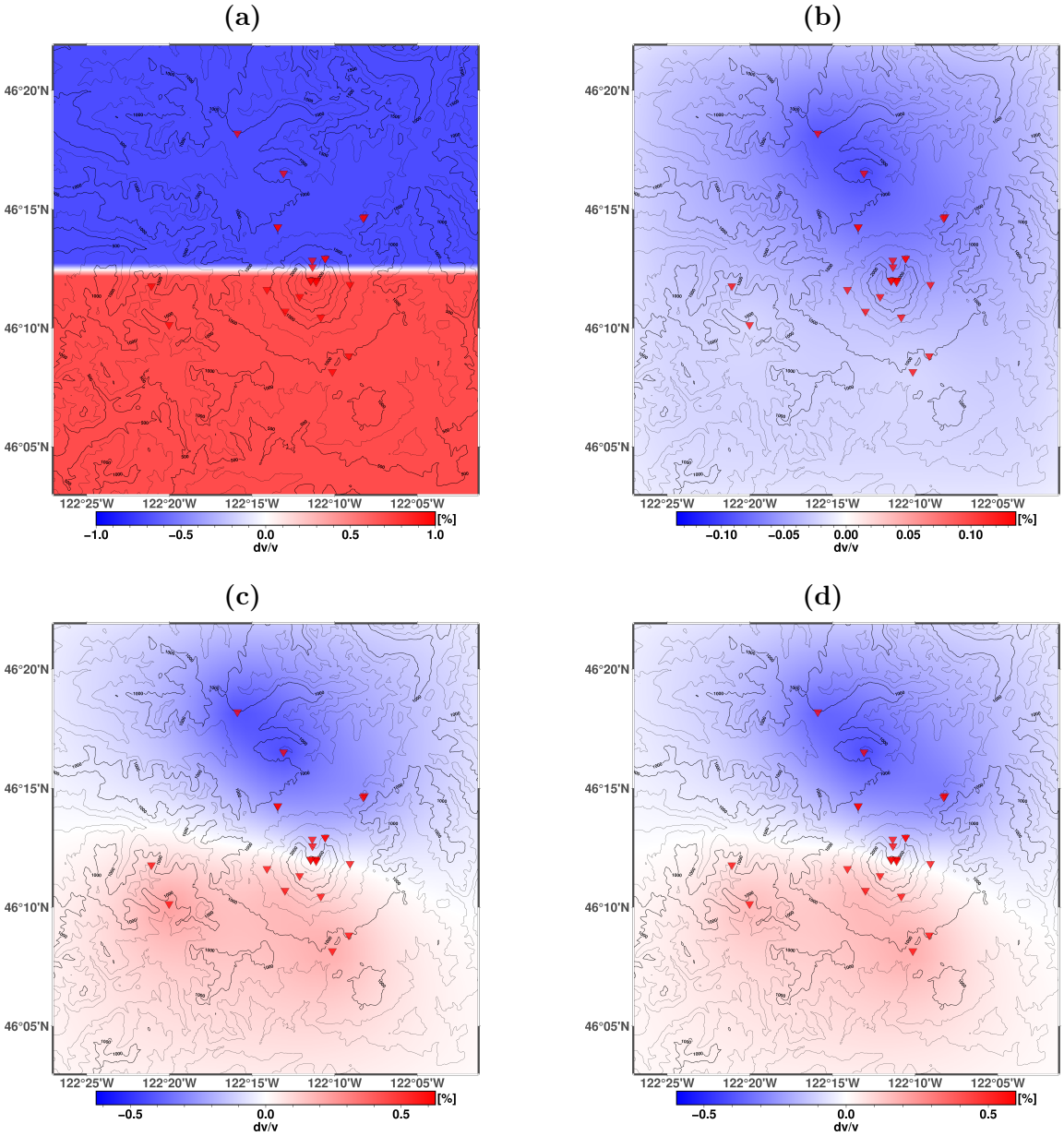

Figure C.13: Recovery of a noise-free synthetic velocity model using the same inversion algorithm, station configuration, and correlation coefficients, and thus σ_d values as in our actual dataset inversion for late 2021 (as Figure 5.4). **(a)** Input velocity model. **(b)** Recovered velocity model using frequencies between 0.25 and 0.5 Hz. **(c)** Recovered velocity model using frequencies between 0.5 and 1 Hz. **(d)** Recovered velocity model using frequencies between 1 and 2 Hz. Red inverse triangles indicate the locations of the seismic stations.

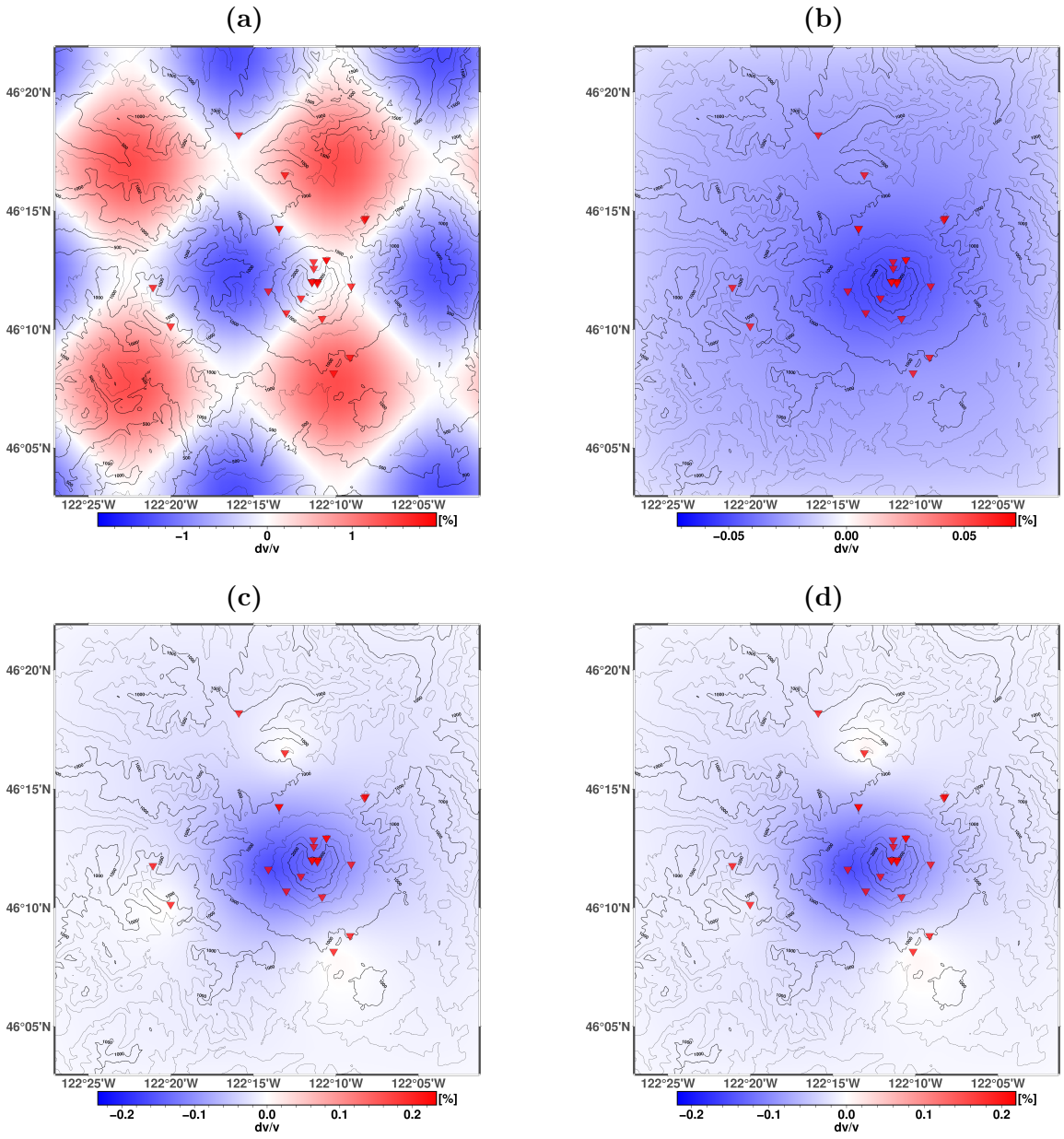

Figure C.14: Recovery of a noise-free synthetic velocity model using the same inversion algorithm, station configuration, and correlation coefficients, and thus σ_d values as in our actual dataset inversion for late 2021 (as Figure 5.4). **(a)** Input velocity model. **(b)** Recovered velocity model using frequencies between 0.25 and 0.5 Hz. **(c)** Recovered velocity model using frequencies between 0.5 and 1 Hz. **(d)** Recovered velocity model using frequencies between 1 and 2 Hz. Red inverse triangles indicate the locations of the seismic stations.

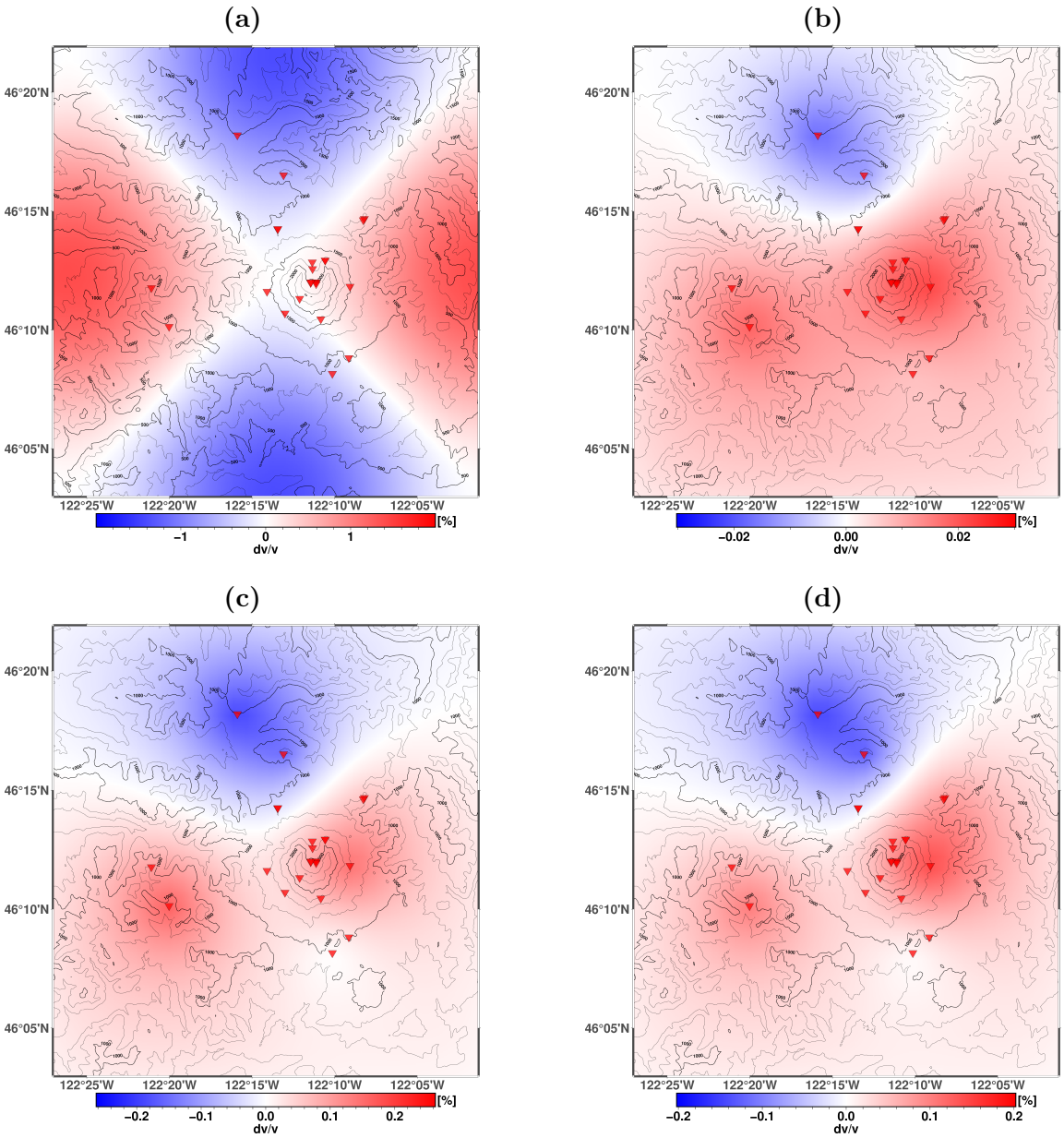

Figure C.15: Recovery of a noise-free synthetic velocity model using the same inversion algorithm, station configuration, and correlation coefficients, and thus σ_d values as in our actual dataset inversion for late 2021 (as Figure 5.4). **(a)** Input velocity model. **(b)** Recovered velocity model using frequencies between 0.25 and 0.5 Hz. **(c)** Recovered velocity model using frequencies between 0.5 and 1 Hz. **(d)** Recovered velocity model using frequencies between 1 and 2 Hz. Red inverse triangles indicate the locations of the seismic stations.

C.6 Environmental Time Series

In Figure C.16, we plot the full-length time series of environmental parameters in conjunction with the two dv/v time series from Figure 5.3. As expected, we see a pronounced seasonal variability in all parameters. Perhaps not so surprisingly, the lake level reaches its peak 20-30 days after the peak in snow load. dv/v is shifted by approximately $\frac{\pi}{4}$ to the the lake level. In 2016, the drainage tunnel of Spirit Lake was out of order, causing an extraordinarily high lake level (Grant et al., 2017), which fortuitously provides us with a better insight into the amount of meltwater supply in the early summer.

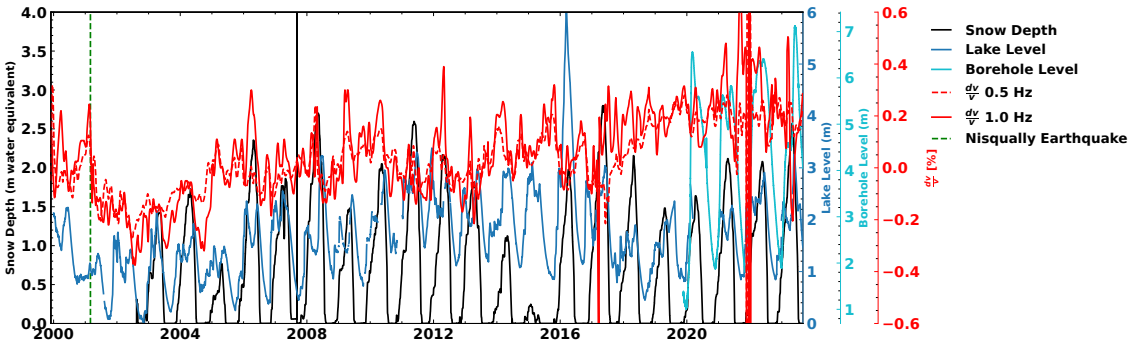

Figure C.16: dv/v time series, Spirit Lake, snow depth, groundwater well level. The velocity change time series shown in this Figure are identical to the ones from Figure 5.3. Here, we set them in context to environmental measurements. The vertical green dash line marks the 2001 Nisqually earthquake.

C.7 Statistical Distribution of Seasonal Variations

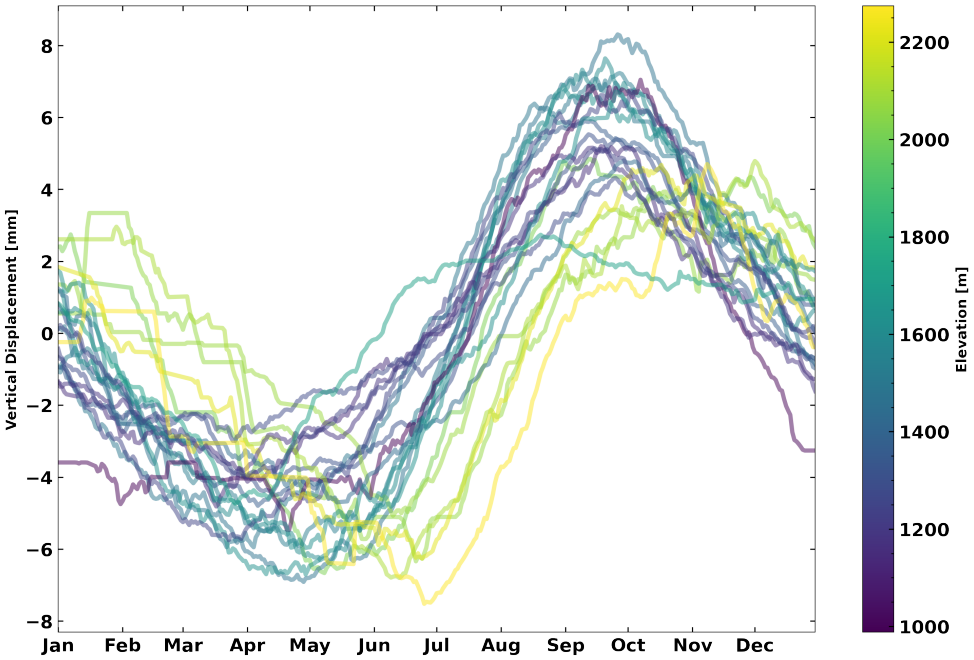

Figure C.17: Seasonal median vertical ground movement for all GNSS stations used in this study. GNSS stations at high altitudes have seasonal cycles that are delayed by up to two months compared to those in the valley.

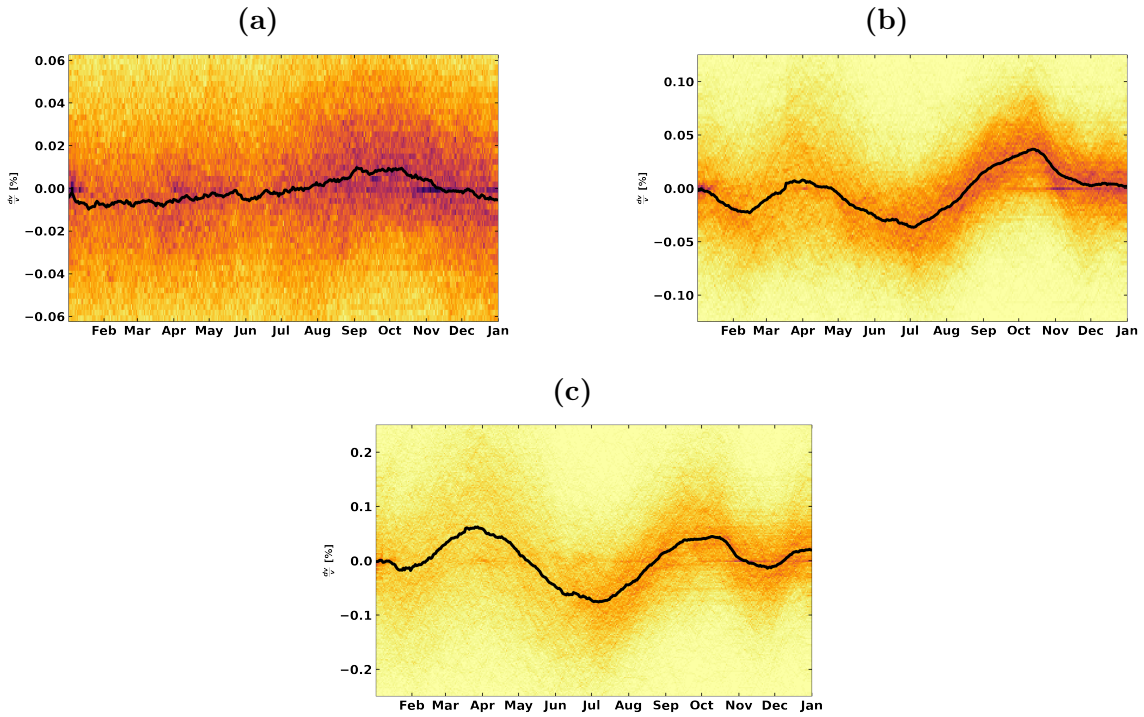

Figure C.18: 2D histograms of median seasonal velocity changes extracted from all ∼1,400 channel combinations. **(a)** for 0.25-0.5 Hz **(b)** for 0.5-1 Hz **(c)** for 1-2 Hz.

C.8 Spatial Distribution of Seasonal Velocity Peaks

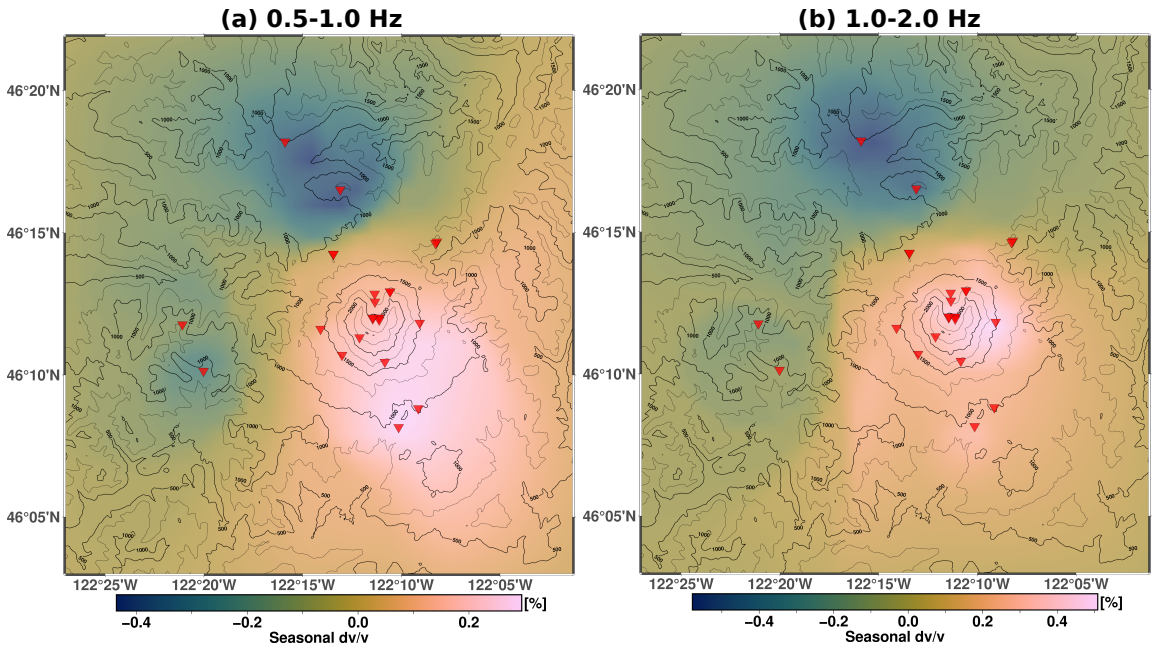

Figure C.19: Median dv/v changes on 30 March. **(a)** for 0.5-1 Hz **(b)** for 1-2 Hz. Median velocity changes corresponding to the time of the first peak in spring. We find positive dv/v anomalies at MSH's peak and negative anomalies in the valley.

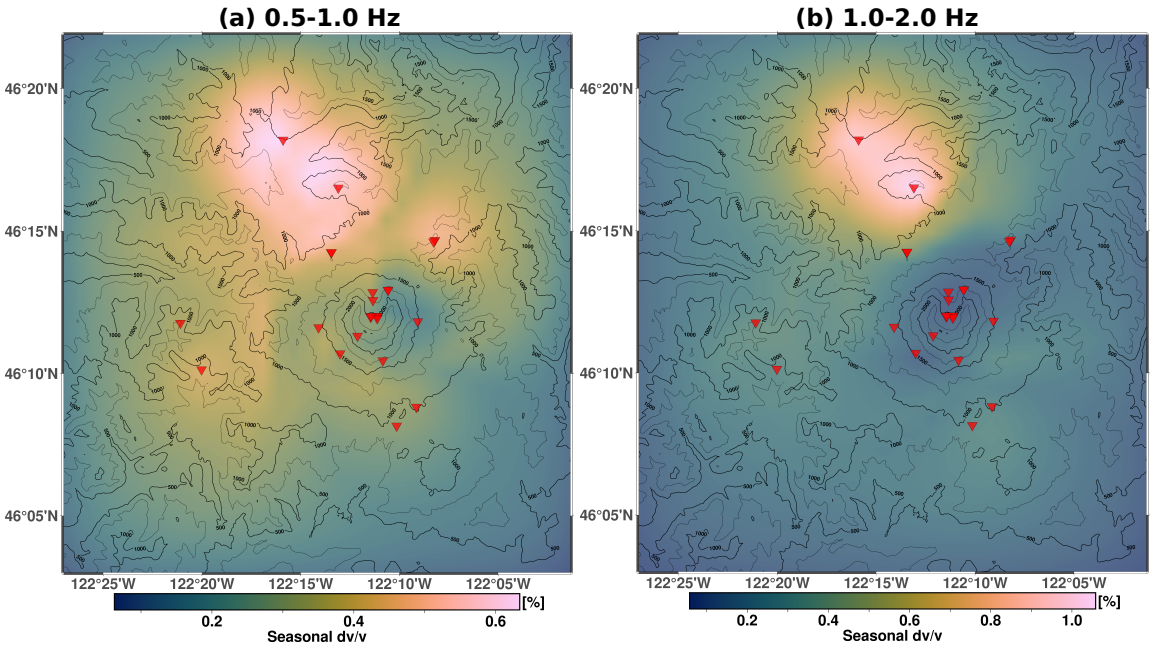

Figure C.20: Median dv/v changes on 30 September. **(a)** for 0.5-1 Hz **(b)** for 1-2 Hz. Median velocity changes corresponding to the time of the second peak in early autumn. We find increased velocities in the whole study area, but stronger increases in the valley, particularly north of the summit.